APPLIED COMPUTATIONAL ELECTROMAGNETICS SOCIETY JOURNAL

March 2020
Vol. 35 No. 3
ISSN 1054-4887

The ACES Journal is abstracted in INSPEC, in Engineering Index, DTIC, Science Citation Index Expanded, the Research Alert, and to Current Contents/Engineering, Computing & Technology.

The illustrations on the front cover have been obtained from the research groups at the Department of Electrical Engineering, The University of Mississippi.

MARCH 2020 REVIEWERS: REGULAR PAPERS

Shobit Agarwal
Otman Aghzout
Iftikhar Ahmed
Mohamed Ahmed
Shahid Ahmed
Shakil Ahmed
Stamatios Amanatiadis
Mohamed Bakr
Emir Baude
Thomas Bauernfeind
Nozhan Bayat
Guan-Yu Chen
Tijana Dimitrijevic
Ozgur Ergul
Andrey Grigoriev
Lu Guo
Taha Imeci
Amir Jafargholi
Reza K. Amineh
Fatih Kaburcuk
Sebastien Lallechere
Gaosheng Li
Yingsong Li
Peyman Mahouti
Hend Malhat
Paolo Manfredi
Andrea Morabito
Sovanlal Mukherjee
Yasemin Oner
Andrew Peterson
Mohammd Pourbagher
C.J. Reddy
Abhishek Sharma
Kapil Sharma
Yan Shi
Javad Soleiman Meiguni
Przemyslaw Syrek
Christopher Trueman
Krushna Kanth V.
Qi Wu
Yongle Wu
John Young
Karam Younus

THE APPLIED COMPUTATIONAL ELECTROMAGNETICS SOCIETY JOURNAL

Vol. 35 No. 3 March 2020

TABLE OF CONTENTS – REGULAR PAPERS

RF Magnetic Field Profiling with a Dielectric Bore Lining for Traveling Waves in a 3-T MRI Scanner: A Computational Study

Milan M. Ilić [1,2], Alexey A. Tonyushkin [3], Pranav S. Athalye [1], Nada J. Šekeljić [1], Andrew J.M. Kiruluta [4], and Branislav M. Notaroš [1]

[1] Electrical & Computer Engineering Department, Colorado State University, Fort Collins, CO
milan.ilic@colostate.edu, athalye@rams.colostate.edu, nada.sekeljic@gmail.com, notaros@colostate.edu

[2] School of Electrical Engineering, University of Belgrade, Serbia
milanilic@etf.bg.ac.rs

[3] University of Massachusetts Boston, Physics Department, Boston, MA
alexey.tonyushkin@umb.edu

[4] Massachusetts General Hospital, Radiology Department, Boston, MA
kiruluta@physics.harvard.edu

***Abstract* —** Traveling-wave magnetic resonance imaging (MRI) can be advantageous over the classical, quasi-static or near-field MRI. However, it is restricted to ultra-high static magnetic fields in the scanner and the correspondingly high RF excitation magnetic field frequencies due to fundamental constraints in cutoff frequencies of the MRI bore, considered as a waveguide. Through a computational study, we propose translating traveling-wave ideas to a 3-tesla scanner, where the RF magnetic field frequency is 127.8 MHz, using a high-permittivity dielectric layer (lining) that is built into the bore. With the lining, we can achieve traveling-wave modes inside the imaging phantoms even at 3 T, where this is generally not possible. We present results obtained using the higher order method of moments in the surface integral equation formulation, previously established as an efficient, accurate, and reliable technique for modeling of RF fields in MRI applications. Our simulations of a simple circularly polarized RF probe and dielectric lining give rise to a considerably uniform circularly polarized RF magnetic field inside phantoms in the clinical scanner.

***Index Terms* —** 3-tesla MRI, bioelectromagnetics, computational electromagnetics, magnetic resonance imaging, RF coils, RF magnetic field profiling, traveling-wave MRI.

I. INTRODUCTION

In magnetic resonance imaging (MRI), the phenomenon of nuclear magnetic resonance (NMR) is employed in order to extract the imaging information. In short, the imaging subject is immersed into a strong, static, homogenous magnetic field, $\mathbf{B}_0$ (e.g., $B_0 = 3$ T in 3-T scanners). This main polarizing field, generated by the main coil, known as the magnet, is axially polarized, i.e., in line with the longitudinal axis (*z*-axis) of the subject. Consequently, the nuclear magnetic moments of the atoms within the imaging subject (typically Hydrogen atoms) practically align with $\mathbf{B}_0$ and precess around it at the Larmor frequency f_0 (proportional to B_0). In the plane perpendicular to the *z*-axis, a circularly polarized RF magnetic field, $\mathbf{B}_1$, is then applied in resonance with the precession, i.e., at f_0, in short pulses. This flips the plane of precession of the nuclei during the pulse duration. By receiving the RF signature emitted during the relaxation of the nuclei, i.e., the return of the precession into the axial direction, the MRI images are generated. For this purpose, a strong, homogeneous, circularly (e.g., right-hand) polarized RF magnetic field $\mathbf{B}_1$ is highly desirable.

Whereas most MRI machines in human medical practice operate at 1.5 T, state-of-the-art clinical MRI scanners are 3-T systems ($B_0 = 3$ T), i.e., high-field (HF) magnets, with MRI bores measuring typically 60 cm in diameter, which allows full-body human subjects. Advanced clinical centers run 3-T scanners because higher B_0 values yield higher signal-to-noise ratio (SNR), that can be traded for higher spatial resolution, which enables imaging of small details or hard to reach areas inaccessible by 1.5-T scanners, and thus considerably improved diagnostics at 3 T over 1.5 T. However, 3-T scanners are yet far from constituting a majority of MRI machines in hospitals, where 1.5-T

Submitted On: October 7, 2019
Accepted On: March 26, 2020

scanners still prevail by a very large margin in part due to higher costs but also due to RF field ($\mathbf{B}_1$) inhomogeneity issues, specific absorption rate (SAR) constraints, etc.

Indeed, one of the main areas of engineering research in advancing HF MRI scanners is in improving exciters generating RF-excitation magnetic fields, $\mathbf{B}_1$, the so-called RF coils at 3 T. For 3-T clinical, preclinical, and research MRI scanners, the RF coils are mostly birdcage coils [1]. Recent developments aimed at improving $\mathbf{B}_1$ field uniformity of body coils in preclinical scanners at 3 T include various modifications of the birdcage coil, such as a birdcage coil with detached endcaps [2], TEM coils [3-5], and spiral coils [6]. Birdcage coils and their variants are, however, designed as close-range or near-field volume coils.

Traveling-wave (TW) magnetic resonance imaging (MRI), unlike a near-field MRI, functions by using the MRI scanner bore as a waveguide in which desired traveling-wave modes are excited. However, TW MRI is primarily reserved for ultra-high-field (UHF) systems, i.e., for MRI scanners with $B_0 > 4$ T, due to fundamental constraints in cutoff frequencies of TW inside hollow waveguides [7]. In 3-T systems, the Larmor frequency, and the frequency of the $\mathbf{B}_1$ field, is $f_0 = 127.8$ MHz [8]. This falls considerably below the cutoff frequency of the bore considered as a cylindrical waveguide, even when loaded with a human body. On the other hand, the potential benefits of TW MRI include large field of view (FOV) coverage, robust RF sources, field profile engineering with a variety of available modes, and a more comfortable open environment. Some of the promising developments for UHF TW MRI are multichannel probes or patch antennas [9], helical-antenna RF coils [10], dielectric linings [11], and meta-bores [12]. At clinical strengths, as the bore becomes wider, it is important to design a homogeneous RF field profile without compromising patient's comfort. Here we propose translating TW MRI ideas to 3-T scanners using a specially designed high-permittivity dielectric layer built into the bore. The TW with dielectric lining may complement a body RF coil inside wide-bore clinical scanners.

II. METHOD AND MATERIALS

For our computational study, we used the higher order method of moments (MoM) in the surface integral equation (SIE) formulation [13,14]. Previously, we had thoroughly verified and validated the higher-order MoM-SIE technique in modeling of RF fields in MRI applications in both HF and UHF MRI regimes by comparisons against two well-established commercial full-wave computational electromagnetics codes [8, 10, 15, 16]. These are a MoM code WIPL-D and a finite element method (FEM) code ANSYS HFSS. The simulations setup of concentric and coaxial three-layers metallic waveguide ($D = 60$ cm) is shown in Fig. 1. The MRI bore is lined with a layer of dielectric from the inside with thickness $T_D = 5$ cm. The dielectric layer (lining) consists of high-permittivity material with $\varepsilon_r = 132$, $\mu_r = 1$, $\sigma = 0.03$ S/m. To investigate RF field profiling, we carried out our simulations with two phantoms of different geometries. The first phantom is a saline-filled uniform cylinder ($L = 1$ m, $D = 15$ cm, $\varepsilon_r = 81$, $\sigma = 0.6$ S/m), as shown in Fig. 1 (a). To eliminate a standing wave, the phantom has an additional saline-filled buffer at the far end of the bore of length $L_C = 40$ cm. The second phantom is a human body model filled uniformly with saline solution ($\varepsilon_r = 81$, $\sigma = 0.6$ S/m), as depicted in Fig. 1 (b). To excite RF fields inside the phantoms, we used a pair of capacitively loaded Tx/Rx loop-coils in orthogonal arrangement, Fig. 1 (c), driven in quadrature that are capable of generating circularly polarized (CP) RF field (needed for MRI) inside the bore [17]. The center of the loops is located at the opening of the bore, Fig. 1 (a).

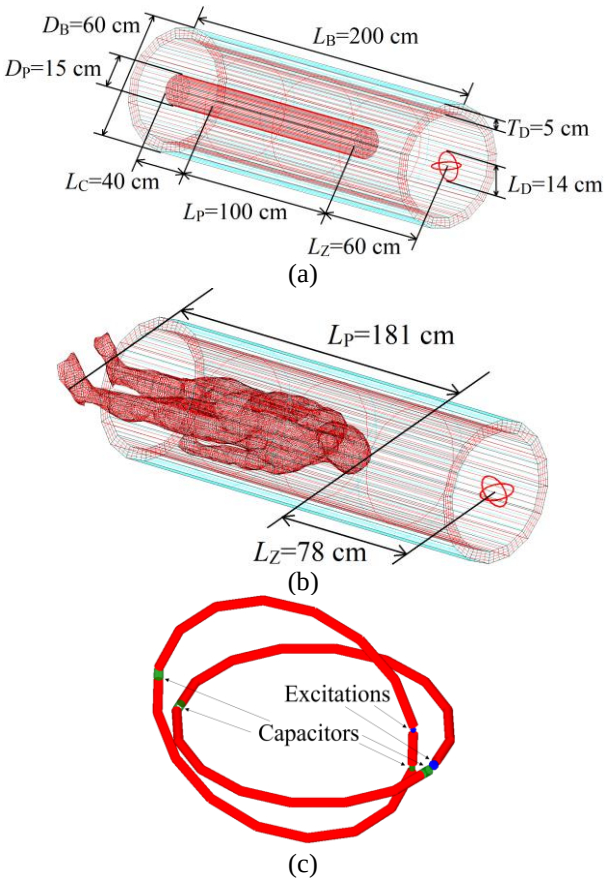

Fig. 1. Simulations setup of lossy-dielectric (saline) phantoms inside a 3-T MRI bore with a dielectric layer (lining): (a) cylindrical phantom; (b) human body phantom; and (c) orthogonal capacitively loaded Tx/Rx loop-coils excited in quadrature, to achieve circular polarization of the magnetic field along the bore axis.

III. RESULTS AND DISCUSSION

The simulations of RF magnetic field (B_1) profiles inside the dielectric cylindrical phantom in the 3-T bore [Fig. 1 (a)] without and with the dielectric lining are shown in Figs. 2 and 3–4, respectively. Note that the scale for B values is adopted to be the same in all graphs in Figs. 2–4, for ease of reference and comparison. With this, the maximum value of 1 nT in the graphs is certainly not optimal (it is too high) for the graphs in Fig. 2 individually, but it enables direct visual comparison of B field intensities between the two distinct cases considered, the structure without and with the dielectric lining, so between the respective graphs in Figs. 2 and 3–4. Figures 2 (a)–(b) and 3 depict the right-hand CP (RCP) RF magnetic field, usually denoted as B_1^+, propagating inside the phantom without and with the lining, respectively, in coronal and axial planes. The longitudinal field profile with the lining, in Fig. 4 (a), produces a slight bump at the entrance of the phantom but stabilizes at a relatively constant initial value. Both longitudinal and transverse profiles, in Figs. 4 (a) and (b), show a very predominant RCP component of the transverse $\mathbf{B}_1$, B_1^+, over the left-hand CP (LCP) component, B_1^-, and hence an excellent B_1^+/B_1^- ratio, desirable for MRI.

From Figs. 2 (a)–(b), the B_1^+ field inside the phantom without dielectric lining is of very low intensity, particularly when compared with the same field when the lining is inserted in the structure, in Figs. 3–4. Also, it produces unfavorable rapid decay along the z-axis, Fig. 2 (c), dropping significantly after distance of $z = 0.25$ m. On the other hand, the same field with the lining, as can be observed from Figs. 3 (a)–(b) and 4 (a), shows excellent propagation along the bore and maintains above one half of its peak strength in the longitudinal plots throughout the entire phantom. In addition, in the bore with the lining (Figs. 3–4) the same field is much stronger, i.e., it is about five times stronger around the peak strength in the longitudinal plot in Fig. 4 (a) than in Fig. 2 (c) (with the same excitation in both figures) and about eight times stronger around the peak strength in the axial cross section at $z = 0.15$ m. This difference increases even further into the phantom where at the center of the phantom the peak strength is about 30 times stronger when the dielectric lining is used. Moreover, the field profile in the axial cross section in Fig. 4 (b) shows symmetric and relatively lower B_1^-, component than in Fig. 2 (d), indicating better B_1^+/B_1^- ratio in the right hand side of the figure. Finally, we note that stronger, non-decaying, and more uniform B_1^+, as well as better B_1^+/B_1^- ratio, in all cross sections in Figs. 3–4 than those in Fig. 2, will ultimately lead to better SNR in the MRI image [1] in the bore with the dielectric lining. Unmodified 3-T scanner may allow propagating TW modes in larger phantoms with appropriate excitations. However, we here choose the parameters (narrow diameter of the cylinder and long distance $L_Z = 60$ cm from the probe) that normally do not support TW.

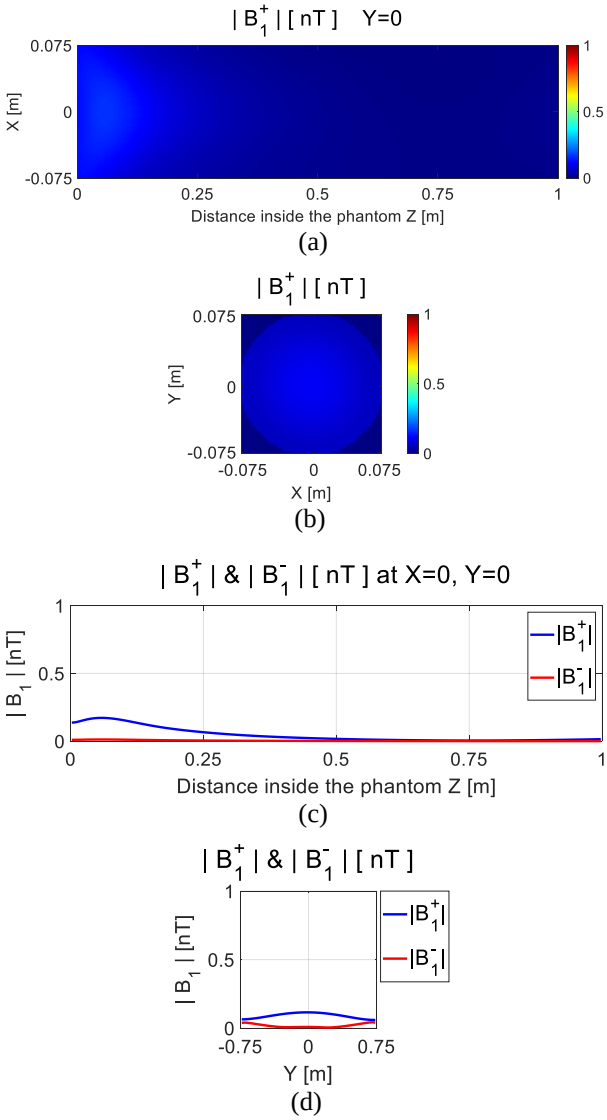

Fig. 2. Simulations of B_1 field in the cylindrical saline phantom in the MRI bore at 3 T [Fig. 1 (a)] without dielectric layer: (a) 2-D B_1^+ field profile in central coronal plane; (b) B_1^+ profile in axial plane at $z = 0.15$ m; (c) B_1^+ (blue) and B_1^- (red) longitudinal field distributions; and (d) transverse field distributions. The scale for B values is adopted to be the same (maximum value 1 nT) as in Figs. 3 and 4 (on the next page), for easier comparison.

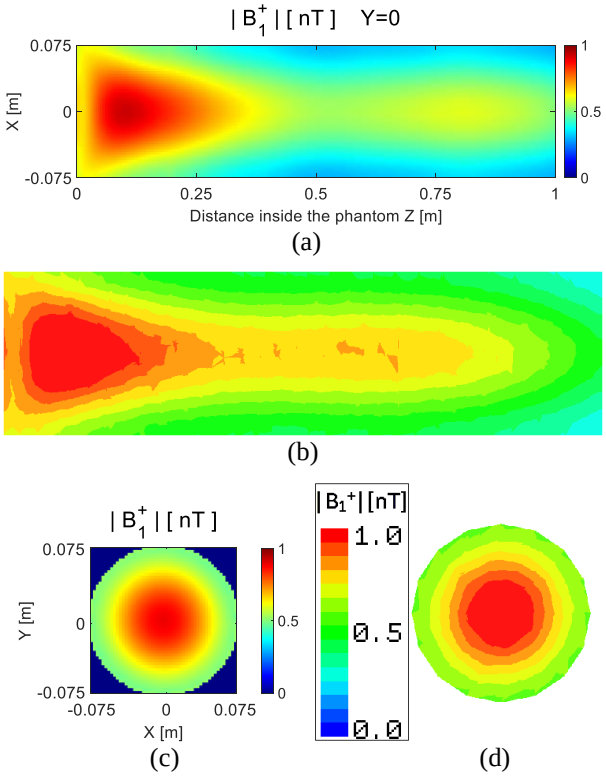

Fig. 3. 2-D B_1^+ field profiles in the cylindrical saline phantom for the MRI bore with dielectric lining as in Fig. 1 (a), to be compared with Figs. 2 (a)–(b): (a) MoM-SIE results for the central coronal plane; (b) ANSYS HFSS (FEM) solution in the coronal plane; (c) MoM-SIE simulation for the axial plane at z = 0.15 m; and (d) HFSS results in the axial plane.

The MoM-SIE simulation model with the cylindrical phantom without the dielectric lining employed 800 elements with 2,640 unknowns and the simulation time was 20.95 seconds. The model with the cylindrical phantom with the dielectric lining had 5,808 elements which yielded 14,416 unknowns and the simulation time was 224.34 seconds. The simulations were run on a desktop computer with Intel i7-3770 CPU (3.4 GHz) and 16 GB RAM. In addition, we show in Figs. 3 (b) and (d) the results obtained by ANSYS HFSS, and an excellent agreement between the MoM-SIE [Figs. 3 (a) and (c)] and HFSS solutions is observed (having in mind the differences of the color maps and unavoidable mesh imprints). Note that the two solution approaches used for comparison are completely different, both conceptually and numerically; the MoM-SIE is a surface modeling technique that solves boundary integral equations for currents, while HFSS is a volumetric modeling technique that solves partial differential equations for fields.

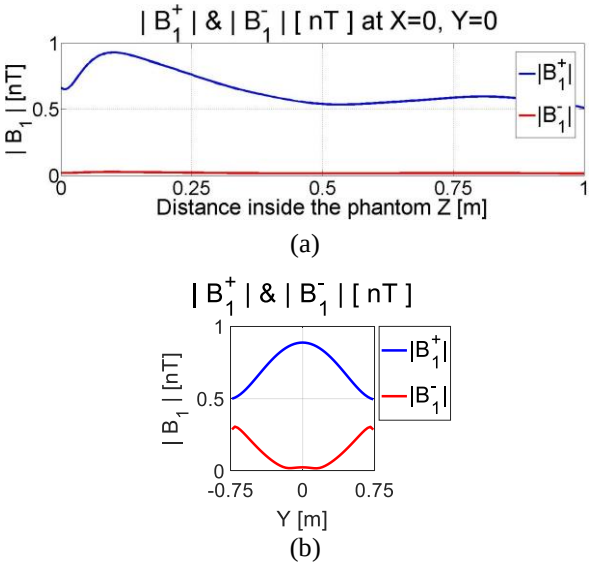

Fig. 4. B_1^+ and B_1^- field distributions for the MRI bore with dielectric lining [Fig. 1 (a)] in (a) longitudinal and (b) transverse directions, for comparison with Figs. 2 (c)–(d).

We extended our simulations to a human body model uniformly filled with saline [Fig. 1 (b)], and the results are given in Figs. 5 and 6 for the bore without and with the dielectric lining, respectively. Overall, we observe a pattern similar to the cylindrical phantom along the human body phantom with the dielectric lining bore (Fig. 6) and rapid decay without lining (Fig. 5).

It can also be concluded from Figs. 5 and 6 that the dielectric lining significantly improves the B_1^+ strength as well as the B_1^+/B_1^- ratio within the imaging subject with all associated benefits already discussed in the first example. The lower B_1^+ at the shoulders corresponds to the Gaussian field profile of the dielectric-lining bore. The MoM-SIE simulations of the structure with the human body phantom model involved 1,566 elements and 6,112 unknowns without the dielectric lining, and simulation time was 220.24 seconds. When the dielectric lining was added, these parameters increased to 2,798 elements, 14,432 unknowns, and 377.92 seconds. Further optimizations of the field profile may include higher dielectric constant material for the lining as well as non-uniform permittivity ε_r along the z-coordinate to compensate for the drop of the field in various body regions, such as the neck. Similar effects, qualitatively, can be achieved using dielectric pads [18] or collars [8].

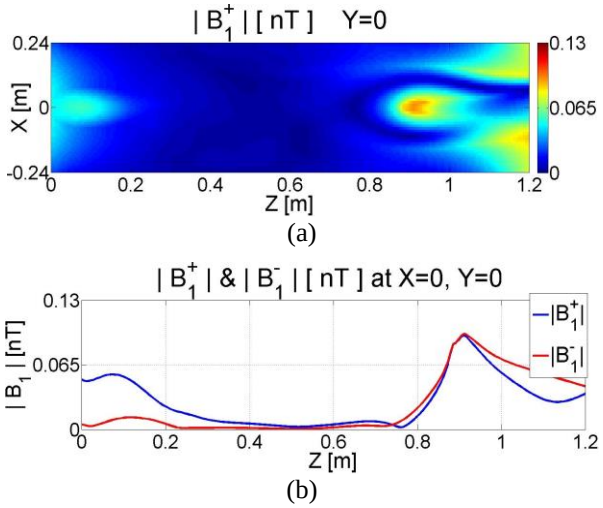

Fig. 5. Simulations of the human body model phantom in the MRI bore at 3 T [Fig. 1 (b)] without dielectric liner: (a) B_1^+ in coronal plane; (b) B_1^+ (blue) and B_1^- (red) profiles along the *z*-coordinate, inside the phantom. The RF coils are located at the opening of the bore (head side); the head of the phantom is at the isocenter, so the lower part of the body is outside of the bore ($z > 1.2$ m).

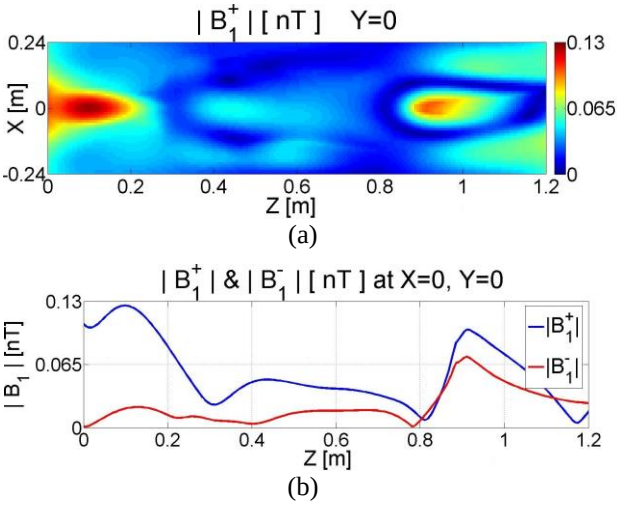

Fig. 6. The same as in Fig. 5 but for the MRI bore with dielectric lining as in Fig. 1 (b).

In terms of realizability and implementation, high-permittivity materials are more available (as opposed to metamaterials, like negative ε and negative μ, and double negative metamaterials, as well as most other metamaterials suggested for lower-field TW MRI [19]). They are widely used in dielectric resonators based on BaTiO3 compounds, where ε_r can be up to 300. Other realizations are possible as well.

IV. CONCLUSIONS

This paper has proposed translating traveling-wave ideas to a 3-T scanner, where the RF magnetic field frequency is considerably below the cutoff frequency of the bore, using a high-permittivity dielectric lining built into the bore. Our simulation model with a dielectric layer and a simple circularly polarized RF probe gives rise to a relatively uniform TW with an excellent RCP/LCP field ratio inside the phantom in the 3-T clinical scanner. The dielectric lining could be incorporated into the wide bore to shape the B_1 field profile from the body RF coil or for TW MRI at lower B_0 fields. Future work will include optimization of dielectric lining parameters and investigation of the impact of a non-uniform layer on a heterogeneous human body model.

ACKNOWLEDGEMENT

This work was supported by the National Science Foundation under grants ECCS-1307863 and ECCS-1810492.

REFERENCES

[1] C. E. Hayes, W. A. Edelstein, J. F. Schenck, O. M. Mueller, and M. Eash, "An efficient, highly homogeneous radiofrequency coil for whole-body Nmr imaging at 1.5-T," *J Magn Reson.*, vol. 63, no. 3, pp. 622-8, 1985.

[2] M. Alecci, C. M. Collins, J. Wilson, W. Liu, M. B. Smith, and P. Jezzard, "Theoretical and experimental evaluation of detached endcaps for 3 T birdcage coils," *Magn Reson Med.*, vol. 49, pp. 363-370, 2003.

[3] J. T. Vaughan, G. Adriany, C. J. Snyder, J. Tian, T. Thiel, L. Bolinger, H. Liu, L. DelaBarre, and K. Ugurbil, "Efficient high-frequency body coil for high-field MRI," *Magnetic Resonance in Medicine: Official Journal of the Society of Magnetic Resonance in Medicine/Society of Magnetic Resonance in Medicine*, vol. 52, no. 4, pp. 851-859, 2014.

[4] C. A. Van den Berg, B. Van den Bergen, J. B. Van de Kamer, B. W. Raaymakers, H. Kroeze, L. W. Bartels, and J. J. W. Lagendijk, "Simultaneous B+ homogenization and specific absorption rate hotspot suppression using a magnetic resonance phased array transmit coil," *Magn Reson Med.*, vol. 57, pp. 577-586, 2007.

[5] J. Tian, L. DelaBarre, J. Strupp, J. Zhang, J. Pfeuffer, M. Hamm, J. Nistler, and K. Ugurbil, "Searching for the optimal body coil design for 3T MRI," *Proceedings of the 21st Annual Meeting, International Society for Magnetic Resonance in Medicine*, Salt Lake City, Utah, USA, pp. 2746,

ACES JOURNAL, Vol. 35, No. 3, March 2020

Application of Barycentric Subdivision Method for Singularity Integration in Method of Moments

Chunwang Xiang [1], Xunwang Dang [2], Maokun Li [1*], Fan Yang [1], and Shenheng Xu [1]

[1] Department of Electronic Engineering
Tsinghua University, Beijing 100084, China
State Key Laboratory on Microwave and Digital Communications
Beijing National Research Center for Information Science and Technology (BNRist)
maokunli@tsinghua.edu.cn

[2] Science and Technology on Electromagnetic
Scattering Laboratory, Beijing 100854, China

Abstract ─ Method of moments (MoM) is an essential tool to model electromagnetic wave interactions with three-dimensional targets. Numerical integration is a key technique in MoM. Due to the singular nature of Green's function, MoM requires special treatment in the calculation of singular integration, which is usually time-consuming. In this study, the barycentric subdivision method is investigated to compute numerical integration in three-dimensional surface integral equations. This method allows a uniform treatment for both singular and non-singular integrals. Numerical examples show that this method could reach the same level of accuracy as the singularity extraction method for RWG basis functions, and the computational time of setting up the matrix can be reduced by half.

Index Terms ─ Barycentric subdivision method, Method of moments (MoM), Rao-Wilton-Glisson (RWG) basis, singular integration, singularity extraction method.

I. INTRODUCTION

Rao-Wilton-Glisson (RWG) basis [1] has been widely used in Method of Moments (MoM) for modeling electromagnetic wave interactions with 3D targets. While setting up the matrix equation of MoM, we usually use numerical integration to evaluate the source integrals and field integrals, both of which contain the Green's function. Because of the singular nature of the Green's function, the integrals need to be treated carefully when the domain of the source integral overlaps with the one of the field integrals. The commonly used techniques include singularity extraction [1,2], Duffy coordinate transformation [3-5], polar co-ordinate transformation, and etc.

The singularity extraction method was proposed by Wilton et al. [1]. This method evaluates the non-singular part of the integral by numerical quadrature and the singular part by analytical formula [2]. Khayat and Wilton proposed a simple and efficient numerical procedure, which uses singularity cancellation scheme [6]. Khayat et al. further optimized this method for the integration scheme [7]. Vipiana and Wilton presented a purely numerical procedure to evaluate strongly near-singular integrals in the gradient of Helmholtz-type potentials for observation points at small distances from the source domain [8]. Popovic [9], Geng and Tong [10, 11] also applied potential integral method to computing singular integrals based on bilinear surface modeling. Wang and Nie et al. used the singularity transferring method to calculate the integral with 1/R singularity in its integrand and remove the small area, which makes zero contribution to the numerical integration [12]. Hua and Xu reduced the order of singularity and avoided the coincidences between the source and field points [13]. Wu et al. extracted the strong singularity of Magnetic Field Integral Equation (MFIE) and used the integral domain transform to eliminate the residual mild singularity [14]. Vipiana and Wilton presented a simple and efficient numerical procedure for evaluating singular and near-singular source vector potential integrals involving junction basis functions based on a double transformation, which could cancel singularities [22]. Jarvenpaa presented recursive formulas by which they can extract any number of terms from the singular kernel and generalize the singularity extraction technique for surface and volume integral equation with high-order basis functions [23]. These methods can compute the singular integral with good accuracy. However, we have to carefully separate the singular and non-singular integral so that they can be treated differently. Also, compared with non-singular integrals, the singular integrals are more expensive to compute. It can become

Submitted On: March 21, 2019
Accepted On: September 7, 2019

a bottleneck in computing time for method of moments.

The Duffy coordinate transform method was proposed by Duffy [3]. This is a simple transformation that facilitates the evaluation of integrals with singular integrands at a vertex. Zhao and Nie et al. used domain decomposition and Duffy coordinate transformation to remove the singularity in the integrand [4]. Botha presented a new family of systematically constructed near-singularity cancellation transformations, which yields quadrature rules for integrating near-singular kernels over triangular surfaces based on Duffy transformation [5]. Zhang and Sun constructed a general variable transformation based on the idea of diminishing the difference of the orders of magnitude, which can remove the near singularity efficiently by eliminating the rapid variations of the integrand in nearly singular integrals, and improve the accuracy of numerical results [23]. Duffy transformation eliminates the singularity in the integral through coordinate transformation and evaluates the integral numerically. But the non-singular and singular integrations are still treated separately. Besides, the errors of the numerical quadrature would increase for triangles with small aspect ratios. Because Duffy transformation requires coordinate transform and computation of quadrature points, fast evaluation of the singular integrals is still a challenge.

In this work, we studied the barycentric subdivision method, which is also known as the nine-point numerical integration, for computing integrals in MoM. It was originally applied to image rendering in computer science [15]. Makarov introduced the method into RWG-MoM [16], and he stated in his works that this technique was not very accurate. Hence, this method has not been widely used. Xiang et al. also studied this method in 2017 [21]. In this method, the singular integrals are evaluated in the same fashion as the non-singular ones, which allows a uniform treatment of the numerical integrals. Therefore, the time of setting up the MoM matrix equation can be reduced. Numerical examples showed that the accuracy is still in remained in the results.

Compared with [16], more details of the barycentric method are studied in this paper, especially its numerical accuracy, which is compared with one of the singularity extraction schemes. The accuracy is important in the application of the scheme for solving electromagnetic problems. Based on both derivation and numerical examples, we found that the accuracy of this scheme is comparable to the singularity extraction scheme. A more detailed convergence analysis of the numerical accuracy of this scheme is presented. It is proved that the integral will converge when the triangle gets smaller, similar as other integration schemes. This scheme is only applied to EIFE in reference [16], we also investigated its applicability for MFIE, PMCHWT and FEM-BI formulations. It seems to work as well.

This paper is organized as follows: Section II describes the formulation. In Section III, numerical examples are given to show the efficiency and accuracy of this method. In Section IV, a convergence analysis is carried out. Section V summarizes this work.

II. FORMULATION

A. Electric field integral equation (EFIE) for PEC targets

The electric field on the surface of a perfect electric conductor (PEC) target satisfies the following integral equation [17, 18]:

$$\hat{n} \times \overline{\overline{L}}(\bar{\mathbf{J}}) = \hat{n} \times \mathbf{E}^{inc}(\mathbf{r}), \mathbf{r} \in S_0, \tag{1}$$

where

$$\overline{\overline{L}}(\bar{\mathbf{J}}) = jk_0 \iint_{S_0} \bar{\mathbf{J}}(\mathbf{r}')G(\mathbf{r},\mathbf{r}')dS' + \frac{j}{k_0}\iint_{S_0} \nabla' \cdot \bar{\mathbf{J}}(\mathbf{r}')\nabla G(\mathbf{r},\mathbf{r}')dS', \tag{2}$$

where G(**r**,**r**') denotes the Green's function in free space, $\bar{\mathbf{J}}$ denotes the scaled electric current density on the surface of the target. Discretizing $\bar{\mathbf{J}}$ by RWG basis and applying the Galerkin's method, we can setup a matrix of MoM with elements as [18]:

$$Z_{mn} = jk_0 \iint_{S_0} \mathbf{f}_m(\mathbf{r}) \cdot \left[\iint_{S_0} \mathbf{f}_n(\mathbf{r}')G(\mathbf{r},\mathbf{r}')dS'\right]dS - \frac{j}{k_0}\iint_{S_0} \nabla \cdot \mathbf{f}_m(\mathbf{r})\left[\iint_{S_0} \nabla' \cdot \mathbf{f}_n(\mathbf{r}')G(\mathbf{r},\mathbf{r}')dS'\right]dS, \tag{3}$$

where Z_{mn} represents the electric field generated by the *n-th* basis function and tested by the *m-th* basis function. $\boldsymbol{f}_m(\mathbf{r})$ and $\boldsymbol{f}_n(\mathbf{r})$ represent the RWG basis functions, which can be written as:

$$\mathbf{f}_m(\mathbf{r}) = \begin{cases} \dfrac{l_n}{2A_m^+}\boldsymbol{\rho}_m^+(\mathbf{r}), \mathbf{r}\ in\ \mathrm{T}_m^+ \\ \dfrac{l_n}{2A_m^-}\boldsymbol{\rho}_m^-(\mathbf{r}), \mathbf{r}\ in\ \mathrm{T}_m^- \\ 0, \quad otherwise \end{cases}, \tag{4}$$

where $\mathrm{T}_m^{\pm}$ denote the two triangles associated with the *m-th* edge, $\mathrm{A}_m^{\pm}$ are the areas of triangles $\mathrm{T}_m^{\pm}$, and $\rho_m^{\pm}$ are the vectors defined in Fig. 1, other symbols are the same as those in reference [1].

The integral in Eq. (3) then becomes:

$$Z_{mn} = jk_0\frac{l_m}{2A_m^+}\iint_{T_m^+}(\mathbf{r}-\mathbf{r}_i)\cdot\tilde{\mathbf{A}}[\mathbf{r}, f_n(\mathbf{r}')]dS + jk_0\frac{l_m}{2A_m^-}\iint_{T_m^-}(\mathbf{r}_j-\mathbf{r})\cdot\tilde{\mathbf{A}}[\mathbf{r}, f_n(\mathbf{r}')]dS - \frac{jl_m}{k_0A_m^+}\iint_{T_m^+}\tilde{\Phi}[\mathbf{r}, f_n(\mathbf{r}')]dS + \frac{jl_m}{k_0A_m^-}\iint_{T_m^-}\tilde{\Phi}[\mathbf{r}, f_n(\mathbf{r}')]dS, \tag{5}$$

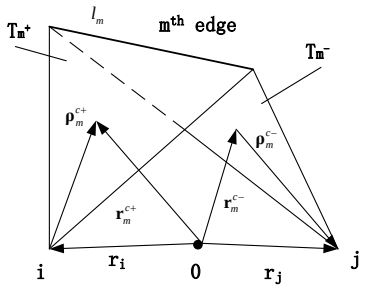

Fig. 1. RWG basis function defined on the *m-th* edge.

In this method, we can use one-point quadrature for the field integral. The barycenter of the *m-th* triangle elements is chosen as the testing point. The matrix element $\mathbf{Z}_{mn}$ can then be written as:

$$\begin{aligned} \mathbf{Z}_{mn} &= jk_0 \frac{l_m}{2}(\mathbf{r}_m^{c+} - \mathbf{r}_i)\cdot\tilde{\mathbf{A}}[\mathbf{r}_m^{c+}, f_n(\mathbf{r}')] \\ &+ jk_0 \frac{l_m}{2}(\mathbf{r}_j - \mathbf{r}_m^{c-})\cdot\tilde{\mathbf{A}}[\mathbf{r}_m^{c-}, f_n(\mathbf{r}')] \\ &- \frac{jl_m}{k_0}\tilde{\Phi}\left[\mathbf{r}_m^{c+}, f_n(\mathbf{r}')\right] + \frac{jl_m}{k_0}\tilde{\Phi}\left[\mathbf{r}_m^{c-}, f_n(\mathbf{r}')\right]. \end{aligned} \quad (6)$$

Here $\mathbf{r}_m^{c\pm}$ is the barycenter of triangle in the *m-th* basis function, $\tilde{\mathbf{A}}$ and $\tilde{\Phi}$ represent the source integrals, which can be written as:

$$\begin{aligned} \tilde{\mathbf{A}}[\mathbf{r}, f_n(\mathbf{r}')] &= \frac{1}{4\pi}\frac{l_n}{2A_n^+}\iint_{T_n^+}(\mathbf{r}' - \mathbf{r}_i')\frac{e^{-jk_0R}}{R}dS' \\ &+ \frac{1}{4\pi}\frac{l_n}{2A_n^-}\iint_{T_n^-}(\mathbf{r}_j' - \mathbf{r}')\frac{e^{-jk_0R}}{R}dS', \end{aligned} \quad (7)$$

$$\tilde{\Phi}\left[\mathbf{r}, f_n(\mathbf{r}')\right] = \frac{1}{4\pi}\frac{l_n}{A_n^+}\iint_{T_n^+}\frac{e^{-jk_0R}}{R}dS' - \frac{1}{4\pi}\frac{l_n}{A_n^-}\iint_{T_n^-}\frac{e^{-jk_0R}}{R}dS', \quad (8)$$

where $R = |\mathbf{r} - \mathbf{r}'|$. The source integration in the *n-th* patch can be calculated by the barycentric subdivision method.

B. Magnetic field integral equation (MFIE) for PEC targets

The magnetic field on the surface of a perfect electric conductor (PEC) target satisfies the following integral equation [17, 18]:

$$\frac{1}{2}\bar{\mathbf{J}} + \hat{n}\times\bar{\bar{K}}(\bar{\mathbf{J}}) = \hat{n}\times\mathbf{H}^{inc}(\mathbf{r}), \mathbf{r}\in S_0, \quad (9)$$

where $\bar{\bar{K}}(\bar{\mathbf{J}}) = \iint_{S_0}\bar{\mathbf{J}}(\mathbf{r}')\times\nabla G(\mathbf{r},\mathbf{r}')dS'$. Using the same method as EFIE, we can get the impedance matrix elements for MFIE as:

$$\begin{aligned} \mathbf{Z}_{mn} &= \frac{1}{2}\iint_{S_0}\mathbf{f}_m(\mathbf{r})\cdot\mathbf{f}_n(\mathbf{r}')dS \\ &+ \iint_{S_0}\mathbf{f}_m(\mathbf{r})\cdot\left[\hat{n}\times\iint_{S_0}\mathbf{f}_n(\mathbf{r}')\times\nabla G(\mathbf{r},\mathbf{r}')dS'\right]dS, \end{aligned} \quad (10)$$

here, $\nabla G(\mathbf{r},\mathbf{r}') = (-jk_0 - \frac{1}{R})\frac{e^{-jk_0R}}{4\pi R^2}\mathbf{R}$.

Now the source integral for the singular point is extracted for separate analysis. We defined the $\mathbf{H}_i(r)$ as:

$$\begin{aligned} \mathbf{H}_i(\mathbf{r}) &= \iint_{S_0}\mathbf{f}_n(\mathbf{r}')\times\nabla G(\mathbf{r},\mathbf{r}')dS' \\ &= -\frac{1}{2A_n}\iint_{S_0}(-jk_0 - \frac{1}{R})\frac{e^{-jk_0R}}{4\pi R^2}\mathbf{R}\times\boldsymbol{\rho}_i'dS'. \end{aligned} \quad (11)$$

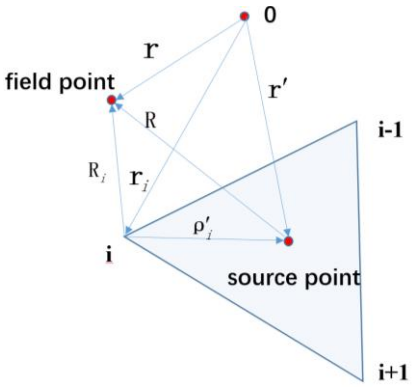

Fig. 2. The related vector and scalar location relationship between the field point and the source point coordination.

Figure 2 depicts the geometric relationship between the vector and the scalar, which are involved in the formula; substituting $\mathbf{R} = \mathbf{R}_i - \boldsymbol{\rho}_i'$ into equation (11), which will take the cross product out of the integral. Equation (11) can be written as:

$$\mathbf{H}_i(\mathbf{r}) = \frac{1}{2A_n}\mathbf{R}_i\times\iint_{S_0}(jk_0 + \frac{1}{R})\frac{e^{-jk_0R}}{4\pi R^2}\boldsymbol{\rho}_i'dS'.$$

The integral of impedance matrix element, which is related to the *m-th* and *n-th* edges, can be written as:

$$\begin{aligned} Z_{mn} &= I_0(m^+, n) + I_0(m^-, n) \\ &+ \frac{l_m}{2A_m^+}\iint_{T_m^+}(\mathbf{r} - \mathbf{r}_i)\cdot\tilde{\mathbf{V}}[\mathbf{r}, f_n(\mathbf{r}')]dS \\ &+ \frac{l_m}{2A_m^-}\iint_{T_m^-}(\mathbf{r}_j - \mathbf{r})\cdot\tilde{\mathbf{V}}[\mathbf{r}, f_n(\mathbf{r}')]dS, \end{aligned} \quad (12)$$

where,

$$I_0(m^+, n) = \begin{cases} \frac{l_m l_n}{8A_n^+}(\mathbf{r}_m^{c+} - \mathbf{r}_i)\cdot(\mathbf{r}_n^{c+} - \mathbf{r}_i'), \mathbf{r}_m^{c+}\in T_n^+ \\ \frac{l_m l_n}{8A_n^-}(\mathbf{r}_m^{c+} - \mathbf{r}_i)\cdot(\mathbf{r}_j' - \mathbf{r}_n^{c-}), \mathbf{r}_m^{c+}\in T_n^- \\ 0, \quad otherwise \end{cases}, \quad (13)$$

$$I_0(m^-, n) = \begin{cases} \frac{l_m l_n}{8A_n^+}(\mathbf{r}_j - \mathbf{r}_m^{c-})\cdot(\mathbf{r}_n^{c+} - \mathbf{r}_i'), \mathbf{r}_m^{c-}\in T_n^+ \\ \frac{l_m l_n}{8A_n^-}(\mathbf{r}_j - \mathbf{r}_m^{c-})\cdot(\mathbf{r}_j' - \mathbf{r}_n^{c-}), \mathbf{r}_m^{c-}\in T_n^- \\ 0, \quad otherwise \end{cases}, \quad (14)$$

$$\begin{aligned} \tilde{\mathbf{V}}[\mathbf{r}, f_n(\mathbf{r}')] &= \frac{l_n}{2A_n^+}\hat{n}_m\times(\mathbf{r} - \mathbf{r}_i')\times\iint_{T_n^+}(\mathbf{r}' - \mathbf{r}_i')(jk_0 + \frac{1}{R})\frac{e^{-jkR}}{4\pi R^2}dS' \\ &+ \frac{l_n}{2A_n^-}\hat{n}_m\times(\mathbf{r} - \mathbf{r}_j')\times\iint_{T_n^-}(\mathbf{r}_j' - \mathbf{r}')(jk_0 + \frac{1}{R})\frac{e^{-jkR}}{4\pi R^2}dS', \end{aligned} \quad (15)$$

here, $\hat{n}_m$ is the outer normal on the patch of the *m-th* edge.

After using the one-point quadrature for the field integral about $\boldsymbol{r}$, the matrix element $\mathbf{Z}_{mn}$ can be written as:

$$\begin{aligned} Z_{mn} &= I_0(m^+, n) + I_0(m^-, n) \\ &+ \frac{l_m l_n}{16\pi A_n^+}(\mathbf{r}_m^{c+} - \mathbf{r}_i)\cdot\hat{n}_m \times (\mathbf{r}_m^{c+} - \mathbf{r}_i') \times \iint_{T_n^+}(\mathbf{r}' - \mathbf{r}_i')\tilde{G}(R)dS' \\ &+ \frac{l_m l_n}{16\pi A_n^+}(\mathbf{r}_m^{c+} - \mathbf{r}_i)\cdot\hat{n}_m \times (\mathbf{r}_m^{c+} - \mathbf{r}_j') \times \iint_{T_n^-}(\mathbf{r}_j' - \mathbf{r}')\tilde{G}(R)dS' \\ &+ \frac{l_m l_n}{16\pi A_n^-}(\mathbf{r}_j - \mathbf{r}_m^{c-})\cdot\hat{n}_m \times (\mathbf{r}_m^{c-} - \mathbf{r}_i') \times \iint_{T_n^+}(\mathbf{r}' - \mathbf{r}_i')\tilde{G}(R)dS' \\ &+ \frac{l_m l_n}{16\pi A_n^-}(\mathbf{r}_j - \mathbf{r}_m^{c-})\cdot\hat{n}_m \times (\mathbf{r}_m^{c-} - \mathbf{r}_j') \times \iint_{T_n^-}(\mathbf{r}_j' - \mathbf{r}')\tilde{G}(R)dS', \end{aligned} \quad (16)$$

where, $\tilde{G}(R) = (jk_0 + \frac{1}{R})\frac{e^{-jk_0R}}{R^2}$.

The remaining source integrals about $\mathbf{r}'$ in the above equations can be calculated with the following nine-point integration method.

C. Barycentric subdivision method for numerical integration

We can apply the barycentric subdivision method (the nine-point quadrature) to the source integral in Eq. (6) and Eq. (16). Each edge of a triangle is equally partitioned into three parts to construct small triangles as shown in Fig. 3, and the small circle "∘" in the figure represents the barycenter of the triangle element.

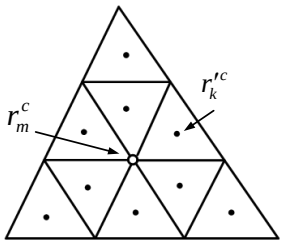

Fig. 3. Nine-point subdivision of a triangle element, where the small circle "∘" denotes the barycenter of the triangle element, "." denotes the barycenter of the sub-triangle elements.

Each triangle is divided into nine equal-sized sub-triangles as shown in Fig. 3. The source integral of the patch can then be approximated by the nine sub-triangles with the same weights. Since these nine triangles have the same area, the integral can be written as:

$$\iint_{T_n} G(\mathbf{r},\mathbf{r}')dS' = \frac{A_n}{9}\sum_{k=1}^{9} G(\mathbf{r},\mathbf{r}'^c_k), \quad (17)$$

By using similar process, the integral in MFIE can be written as:

$$\iint_{T_n}(\mathbf{r}' - \mathbf{r}_\mathbf{i})\tilde{G}(\mathbf{r},\mathbf{r}')dS' = \frac{A_n}{9}\sum_{k=1}^{9}(\mathbf{r}_k'^c - \mathbf{r}_\mathbf{i})\tilde{G}(\mathbf{r},\mathbf{r}_k'^c), \quad (18)$$

where $\mathbf{r}'^c_k$ denotes the quadrature points shown as Fig. 3. The quadrature point of the field integral resides on the barycenter of the patch (triangle), so the quadrature point of the field integral will not coincide with the one of the source integral. Therefore, the value of the integrand will not become singular.

III. NUMERICAL EXAMPLES

A. Computation of radar cross section (RCS)

Case 1: We consider the plane wave scattering of a PEC sphere with radius of 1*m*. We use the Mie series result as benchmark. The incident plane wave has frequency of 300MHz, ϕ^{inc}=0°, θ^{inc}=90°, and vertical polarization. The surface current is computed using the nine-point numerical integration method. The bistatic RCS with VV polarization (vertical polarization excitation and vertical polarization reception) is computed with EFIE and MFIE respectively when the observation angle at ϕ=0° and $\theta \in$ [0°, 180°]. In the computation, the current on the sphere is partitioned into 4527 unknowns.

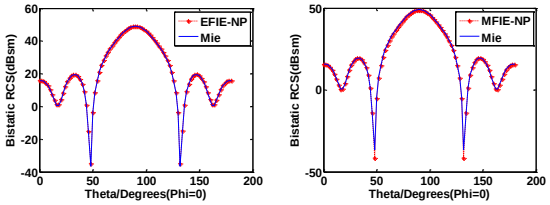

(a) (b)

Fig. 4. The calculation on bistatic RCS: (a) bistatic RCS for PEC sphere solved by EFIE, and (b) bistatic RCS for PEC sphere solved by MFIE.

From Fig. 4 (a) and Fig. 4 (b), we can see that the numerical results have a good agreement with the Mie series results [17, 18, 20]. We can also see that the proposed method works not only for the EFIE equation but also for the MFIE equation.

Case 2: In order to further validate the efficiency of this method to other integral equation and structures, a dielectric sphere and a dielectric cube are computed with PMCHWT and FEM-BI equation, respectively.

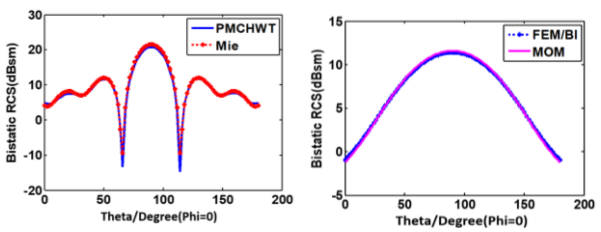

(a) (b)

Fig. 5. Bistatic RCS: (a) dielectric sphere solved by PMCHWT, and (b) dielectric cube solved by FEM-BI.

The dielectric sphere has ε_r=2.5, radius = 1m, the number of unknowns after discretization is 6875. The dielectric cube has ε_r=2.5, side length = 1m, the number of unknowns is 4440. The incident plane wave has the same parameters as Case 1.

From Fig. 5 (a) and Fig. 5 (b), we can see that the numerical results agree well with the Mie series results.

From the above two examples, we can see that this method can be applied to various integration equation and complex structures.

B. Matrix setup time

Using the parameters of Case 1, a comparison of matrix setup time between the nine-point numerical integration and the singularity extraction method is shown in Table 1.

Table 1: Comparison of Matrix setup time

Unknowns	Matrix Setup Time (seconds)	
	Nine-point Numerical Integration	***Singularity Extraction***
1197	10s	17s
4527	2m20s	4m26s
6993	5m45s	10m34s
18297	46m30s	88m12s
50886	367m20s	700m40s

In Table 1, the previous four models are computed on a PC with Intel(R) Core(M) i5-4690K, CPU@3.5GHz/64, RAM 32G, and the last example is a server with Intel(R) Xeon(R) E7-8857v2@3.0GHz, 4 cores, RAM 1.5T.

From Table 1, we can see that the barycentric subdivision method can save nearly half of the setup time compared with the singularity extraction method.

IV. CONVERGENCE ANALYSIS

A. Theory on the barycentric subdivision method

In this section, we will study the convergence of numerical integration using the barycentric subdivision method.

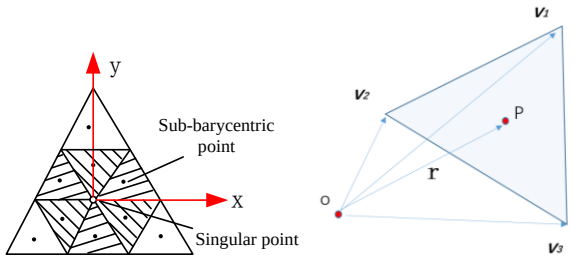

(a) (b)

Fig. 6. Six sub-triangles around the singular point in a triangle element and vector in a sub-triangle. (a) The six small sub-triangles (the shaded area) around the singular point (barycenter of triangle), and (b) the vector for three vertices and quadrature point in a sub-triangle.

The source integral becomes singular when its integration domain overlaps with the field integral. In this case, the source integrals over 6 small triangles around the barycenter "∘" in Fig. 6 (a) will have singularity at one of their corners, i.e. the barycenter"∘" of the triangle.

We can analyze these singular integrals based on the Duffy transform. It transforms from the original barycenter coordinate system (ξ_1,ξ_2,ξ_3) to a new coordinate (u,v), as shown Fig. 6 (b) below (here $\mathbf{v}_1$ is the vector of the singular point"∘"when the field point O is overlapped with $\mathbf{v}_1$):

$$\begin{aligned}\mathbf{r} &= \xi_1\mathbf{v}_1 + \xi_2\mathbf{v}_2 + \xi_3\mathbf{v}_3 \\ &= u\mathbf{v}_1 + v(1-u)\mathbf{v}_2 + (1-v)(1-u)\mathbf{v}_3,\end{aligned} \tag{19}$$

here $\mathbf{v}_1$ is the vector of the singular point, ξ_3=1-ξ_1 –ξ_2, then the singular integral for one sub-triangle can be transformed into:

$$\begin{aligned}I &= \int_S \frac{e^{-jk_0R}}{R}dS = A\int_S \frac{e^{-jk_0|\mathbf{r}-\mathbf{v}_1|}}{|\mathbf{r}-\mathbf{v}_1|}d\xi_1 d\xi_2 \\ &= A\int_0^1\int_0^1 \frac{e^{-jk_0(1-u)|v\mathbf{v}_2+(1-v)\mathbf{v}_3-\mathbf{v}_1|}}{|v\mathbf{v}_2+(1-v)\mathbf{v}_3-\mathbf{v}_1|}dvdu,\end{aligned} \tag{20}$$

where A denotes the area of one sub-triangle S. The integral on S is then converted to a 2-fold integral of u and v, respectively. Now we can define the function $a(v)$:

$$\begin{aligned}a(v) &= k_0\left|v\mathbf{v}_2+(1-v)\mathbf{v}_3-\mathbf{v}_1\right| \\ &= k_0\left|v(\mathbf{v}_2-\mathbf{v}_3)+(\mathbf{v}_3-\mathbf{v}_1)\right|.\end{aligned} \tag{21}$$

From Eq. (21), we can see $a(v)$ is linear with the size of triangle, As the mesh of the target becomes denser, $a(v)$ will be smaller, so the analytical expression I_D of integral I for v is:

$$I_D = A\int_0^1 \frac{dv}{a(v)}\frac{1-e^{-ja(v)}}{ja(v)} \approx Ak_0\int_0^1 \frac{dv}{a(v)}(1+o(a)) = Ak_0/a(\zeta), \tag{22}$$

where $a(\zeta)$ is derived from the mean value theorem for definite integrals [19].

Since the Duffy transformation can eliminate the singularity when the field point overlaps with the singular point as shown in Fig. 6 (a), we can try to eliminate the singularity when the field point at the sub-barycentric point, and further compare these two integral value. The quadrature for the above integral on each sub-triangle samples the domain of integration at (ξ_1,ξ_2) =(1/3,1/3), namely (u,v)=(1/3,1/2) in the new coordinate, substituting the u=1/3, v=1/2 into Eq. (20), the numerical integration on the sub-barycentric point is:

$$I_c \approx Ak_0/a(1/2). \tag{23}$$

The numerical difference between I_D (based on Duffy transform at the singular point) and I_c (based on Duffy transform at the sub-barycentric point) is:

$$I_D - I_c \approx Ak_0\left[1/a(\zeta) - 1/a(1/2)\right]. \tag{24}$$

This difference is only related to the area A. When the area A of triangle tends to zero, the numerical difference $I_D - I_c$ will converge to zero as well. This can ensure that the error is only related to the mesh density,

and convergence of the integral has a good agreement with the traditional Duffy method.

B. Convergence analysis based on numerical experiments

To verify the convergence of the barycentric subdivision method, we compute the bistatic RCS for a PEC sphere with EFIE and MFIE, respectively.

We compute the RCS with the nine-point method and traditional singularity extraction method (S-E) respectively. These two method are compared with Mie series results respectively. The results are shown in Fig. 7.

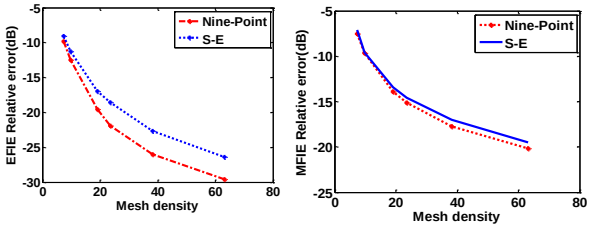

(a) (b)

Fig. 7. Comparison of relative error in RCS. (a) EFIE and (b) MFIE.

The relative error is defined as:

$$error = 10\log\left(\left\|RCS_{\_cal} - RCS_{\_mie}\right\| / \left\|RCS_{\_mie}\right\|\right), \quad (25)$$

and the mesh density is defined as:

$$\text{mesh density} = \sqrt{\frac{N}{S}} \cdot \lambda, \quad (26)$$

where N denotes the numbers of unknowns, S denotes the surface area of the sphere, and λ denotes the wave length of the incident wave. From Fig. 7, we can observe that the error decreases as the mesh density increases.

C. Computation of integrals of 1/R

To check the convergence, we also study the singular integration on a triangle as the below:

$$I = \oiint_{S_m}\left[\oiint_{S_n}(1/R)dS'\right]dS, \quad (27)$$

where R denotes the distance between the source and field point.

In Fig. 8, the size of the area zooms step by step, and the side length L declines by half every time. The value of integration for Eq. (27) is shown in Table 2.

It can be seen from Table 2 that the results of the nine-point method agree well with those of the analytical method. Besides, the two methods diverge at the same time when the area of the triangle becomes too small due to the limited machine precision. In summary, this illustrates that our method is applicable to the cases where the mesh size is small enough.

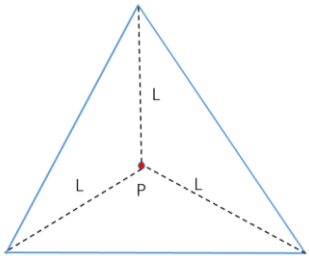

Fig. 8. The area of the triangle changes with L.

Table 2: Comparison of integral value

The Size of Area (L)	The Value of Integral for 1/R	
	The Nine-point	Analytical
1	4.218747139	5.132335663
0.5	0.527344286	0.641542614
0.25	6.59E-02	8.02E-02
0.125	8.24E-03	1.00E-02
0.125/2	1.03E-03	1.25E-03
0.125/2/2	1.29E-04	1.57E-04
0.125/2/2/2	1.61E-05	1.96E-05
0.125/2/2/2/2	2.01E-06	2.45E-06
0.125/2/2/2/2/2	2.51E-07	3.06E-07
0.5/2/2/2/2/2/2/1000	2.17E-16	2.64E-16
0.5/2/2/2/2/2/2/1000/2	NaN	NaN

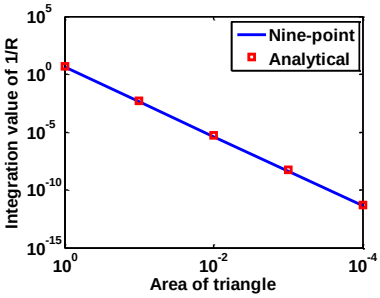

Fig. 9. Convergence for 1/R

The above integral is computed by both the nine-point integration and the analytical method [1], respectively. Figure 9 shows the values of I with respect to mesh density using the two methods. They agree well with each other.

V. CONCLUSION

In this study, we investigated the barycentric subdivision method. We studied the numerical convergence of this method for singular integration by both theoretical analysis and numerical examples. We observe that this method converges at the same level of accuracy as other method such as the singularity extraction. This method avoids the complex treatment of singular integrals and allows a uniform procedure for both singular and non-singular integrations in method of

moments. Numerical examples show that this method can reduce the matrix setup time by half. We hope this study could help us to further understand this method and extend its applications in solving 3D scattering problems using method of moments.

ACKNOWLEDGMENT

This work is supported by National Science Foundation of China under contract 61490693 and 61571264, and the National Basic Research Program of China under contract 2013CB329002, and in part by Beijing National Research Center for Information Science and Technology (BNRist), Guangzhou Science and Technology Plan (201804010266), Beijing Innovation Center for Future Chip, and Research Institute of Tsinghua, Pearl River Delta.

REFERENCES

[1] S. M. Rao, D. R. Wilton, and A. W. Glisson, "Electromagnetic scattering by surfaces of arbitrary shape," *IEEE Trans. Antennas and Propagation*, vol. 30, no. 3, pp. 409-418, 1982.

[2] D. R. Wilton, S. M. Rao, A. W. Glisson, D. H. Schaubert, O. M. Al-Bundak, and C. M. Butler, "Potential integrals for uniform and linear source distributions on polygonal and polyhedral domains," *IEEE Trans. Antennas and Propagation*, vol. 32, no. 3, pp. 276-281, 1984.

[3] M. G. Duffy, "Quadrature over a pyramid or cube of integrands with a singularity at a vertex," *SIAM J. Numer. Anal*., vol. 19, no. 6, pp. 1260-1262, 1982.

[4] Y. W. Zhao, Z. P. Nie, J. H. Xu, and S. B. Wu, "Accurate and efficient calculation of singular integrals in Galerkin method with RWG basis functions," *ACTA Electronica Sinica*, vol. 33, no. 6, pp. 1019-1023, 2005.

[5] M. M. Botha, "A family of augmented Duffy transformations for near-singularity cancellation quadrature," *IEEE Trans. Antennas and Propagation*, vol. 61, no. 6, pp. 3123-3134, 2013.

[6] M. A. Khayat and D. R. Wilton, "Numerical evaluation of singular and near-singular potential integrals,"*IEEE Trans. Antennas and Propagation*, vol. 53, no. 10, pp. 3180-3190, 2005.

[7] M. A. Khayat, D. R. Wilton, and P. W. Fink, "An improved transformation and optimized sampling scheme for the numerical evaluation of singular and near-singular potentials," *IEEE Antennas and Wireless Propagation Letters*, vol. 7, pp. 377-380, 2008.

[8] F. Vipiana and D. R. Wilton, et al., "Numerical evaluation via singularity cancellation schemes of near-singular integrals involving the gradient of Helmholtz-type potentials," *IEEE Trans. Antennas and Propagation*, vol. 61, no. 3, pp. 1255-1265, 2013.

[9] B. D. Popovic and B. M. Kolundzija, *Analysis of Metallic Antennas and Scatters*, The Institution of Electrical Engineers, London, pp. 58, 1988.

[10] F. Z. Geng and C. M. Tong, "An efficient method of singular integrals in hybrid basis MoM solutions," *Journal of Air Force Engineering University (N.S.E.)*, vol. 7, no. 3, pp. 65-68, 2006.

[11] C. W. Xiang and C. M. Tong, et al., "Modeling method of reduced dimension for complex targets and application in electromagnetic scattering analysis," *Chinese Journal of Radio Science*, vol. 20, no. 2, pp. 189~192, 2005.

[12] H. G. Wang and Z. P. Nie, et al., "Singularity analysis of the integral equation for three dimension vector fields scattering," *ACTA Electronica Sinica*, vol. 27, no. 12, pp. 68-71, 1999.

[13] Y. H. Hua and J. P. Xu, et al., "Integration singularity reduction by the locally continuous functions used in moment method with EFIE," *Journal of Electronics and Information Technology*, vol. 25, no. 10, pp. 1436-1440, 2003.

[14] J. H. Wu, X. Y. Cao, H. B. Yuan, and J. Gao, "Effective method to solve magnetic field integral equation with method of moment," *Chinese Journal of Radio Science*, vol. 28, no. 5, pp. 974-978, 2013.

[15] Y. Kamen and L. Shirman, "Triangle rendering using adaptive subdivision," *IEEE Computer Graphics and Application*, pp. 95-103, Mar.-Apr. 1998.

[16] S. N. Makarov, *Antenna and EM Modeling with Matlab*. NY: Wiley-Interscience, New York, pp. 128, 2002.

[17] W. C. Chew, E. Michielssen, J. M. Song, and J. M. Jin, *Fast and Efficient Algorithms in Computational Electromagnetics*. MA: Artech House, Boston, 2001.

[18] J. M. Jin, *Theory and Computation of Electromagnetic Fields*. John Wiley & Sons, Inc., Hoboken, New Jersey, USA, 2010.

[19] AdiBen-Israel and R. Gilbert, *Computer-Supported Calculus*. pp. 224-278, Springer-Verlag Wien, 2002.

[20] X. Q. Sheng, J. M. Jin, J. M. Song, C. C. Lu, and W. C. Chew, "On the formulation of hybrid finite-element and boundary-integral methods for 3-D scattering," *IEEE Trans. Antennas and Propagation*, vol. 46, no. 3, pp. 303-311, 1998.

[21] C. W. Xiang, X. W. Dang, M. K. Li, F. Yang, and S. H. Xu, "The application of barycentric subdivision method for numerical integration in method of moments," *2018 IEEE International Conference on Computational Electromagnetics (ICCEM)*, Chengdu, pp. 1-3, 2018.

[22] F. Vipiana and D. R. Wilton, "Optimized numerical evaluation of singular and near-singular potential

integrals involving junction basis functions," *IEEE Trans. Antennas and Propagation*, vol. 59, no. 1, pp. 162-171, 2011.

[23] S. Jarvenpaa, M. Taskinen, and P. Y. Oijala, "Singularity extraction technique for integral equation methods with higher order basis functions on plane triangles and tetrahedral," *Int. J. Numer. Meth. Eng*., vol. 58, pp. 1149-1165, Aug. 2003.

Chunwang Xiang received the B.S. degree from Air Force Engineering University, Xi'an, China, in 2002. He is now a Ph.D. student at Tsinghua University, Beijing, China. His current research interests include finite element method (FEM), time-domain finite element method (FETD), finite element boundary integral method (FE-BI), and design on Radar antenna and etc.

Xunwang Dang received the B.S. degree from Tsinghua University, Beijing, China, in 2013, and the Ph.D. degree from the same university in 2018.

His current research interests include reduced basis method (RBM), equivalent principle algorithm (EPA), fast algorithms in the method of moments, deep learning techniques in electromagnetics etc.

Maokun Li received his B.S. degree in Electronic Engineering from Tsinghua University, Beijing, China, in 2002, and the M.S. and Ph.D. degrees in Electrical Engineering from University of Illinois at Urbana-Champaign in 2004 and 2007, respectively. After graduation, he joined Schlumberger-Doll Research as a Post-doc Research Scientist, and later as a Senior Research Scientist. In June 2014, he joined the Department of Electronic Engineering in Tsinghua University as an Associate Professor. His research interests include fast algorithms in computational electromagnetics and electromagnetic inverse problems.

Fan Yang received the B.S. and M.S. degrees in Electronic Engineering from Tsinghua University, Beijing, China, in 1997 and 1999, respectively, and the Ph.D. degree in Electrical Engineering from the University of California, Los Angeles (UCLA), Los Angeles, CA, USA, in 2002. From 2002 to 2004, he was a Postdoctoral Research Engineer and Instructor with the Electrical Engineering Department, UCLA. In 2004, he joined the Electrical Engineering Department, The University of Mississippi as an Associate Professor in 2009. In 2011, he joined the Electronic Engineering Department, Tsinghua University as a Professor, and has served as the Director of the Microwave and Antenna Institute since then. He has authored or coauthored more than 300 journal articles and conference papers, 6 book chapters, and 5 books. His research interests include antennas, surface electromagnetics, computational electromagnetics and applied electromagnetic systems.

Yang served as an Associate Editor for the IEEE Transactions on Antennas and Propagation (2010–2013) and an Associate Editor-in-Chief for Applied Computational Electromagnetics Society Journal (2008–2014). He was the Technical Program Committee Chair of 2014 IEEE International Symposium on Antennas and Propagation and USNC-URSI Radio Science Meeting. He is a Fellow of IEEE and ACES. He is also an IEEE APS Distinguished Lecturer for 2018–2020.

Shenheng Xu received the B.S. and M.S. degrees in 2001 and 2004, respectively, from the Southeast University, Nanjing, China, and the Ph.D. degree in Electrical Engineering in 2009 from the University of California, Los Angeles (UCLA), CA, USA. From 2000 to 2004, he was a Research Assistant with the State Key Laboratory of Millimeter Waves, Southeast University, Nanjing, China. From 2004 to 2011, he was a Graduate Student Researcher and later a Postdoctoral Researcher with the Antenna Research, Analysis, and Measurement Laboratory, UCLA. In 2012, he joined the Department of Electronic Engineering, Tsinghua University, Beijing, China, as an Associate Professor. His research interests include novel designs of high-gain antennas for advanced applications, artificial electromagnetic structures, and electromagnetic and antenna theories.

Analysis of Infrared Nano-antennas Material Properties for Solar Energy Collection

Wided Amara [1], Taoufik Aguili [1], Abdulsalam Alghamdi [2,3], Donia Oueslati [2], Nermeen Eltresy [2,4], Muntasir Sheikh [2], and Hatem Rmili [1,2]

[1] SysCom Laboratory, ENIT, University of Tunis El Manar, Tunis, Tunisia

[2] Electrical and Computer Engineering Department, Faculty of Engineering
King Abdulaziz University, Jeddah, Saudi Arabia

[3] King Salman bin Abdulaziz Chair for Energy Research, King Abdulaziz University, Jeddah, Saudi Arabia

[4] Microstrip Department, Electronics Research Institute, Giza, Egypt

Abstract ─ This work presents the effect of material properties on three infrared nano antennas that are rectangular, bowtie, and elliptical-shaped designed to collect a maximum field in the gap between the two dipole arms over a frequency band of 28-29THz. The dipole shapes are comprised of conducting dipoles printed on a dielectric substrate. The bowtie is designed to be curved with an exponential shape, and itis found to collect a higher value of the electric field in the gap than do the other two shapes. The above antennas are investigated with different materials for the dipoles and the substrate to study the effect of material variation on the electric field collected in the dipole gap. Three different types of conducting materials, namely, gold, chromium, and titanium are used. It is found that the collected gap field intensity is directly proportional to the conductivity of the dipole material. The effect of three different types of substrates; quartz (GaAs), silicon, and SiO2 on the collected gap field is also investigated.

Index Terms ─ Electric field, energy harvesting, infrared, nano-antenna.

I. INTRODUCTION

Solar energy has recently been viewed as one of the most accessible sources of renewable energy [1], and it can be harvested by using antennas that operate at infrared or visible frequency bands [2]. Several infrared antennas with different geometrical shapes have been investigated in the literature including rectangular [3, 4]; circular [4] spiral; bowtie [5, 6, 7, and 8]; dipole [9, 10, and 11]; elliptical [12]; and Vivaldi [13].

Optical antennas are currently being used for various medical applications such as breast cancer treatment [14]. To treat cancer, optical antennas are placed in contact with the malignant breast. The antenna is excited by a near infrared plane wave. The intense field in the antenna gap resulting from the excitation causes arises in the distribution of local temperature, which helps destroy the cancerous cells. Additionally, these antennas are also used as biological sensors [15].

The infrared rectenna (antenna+rectifier) is comprised of a receiving antenna, designed for infrared frequencies, together with a rectifying diode, which converts the infrared waves into electric power. Optical and infrared rectennas are superior to the photovoltaic cells, whose conversion efficiencies are limited [7]. The rectennas use the natural energy of the sun (lights), and in contrast to the photovoltaic cells, their conversion efficiency can reach up to 100% [7]. Generally, the rectenna needs to be designed such that it harvests the maximum amount of energy from the impinging electromagnetic wave. In addition, good impedance match between the rectifier and the antenna is required [7] to achieve a maximum power transfer. Nano-antennas should be optimized to realize the maximum field intensity for the specific operating frequency. Finally, the electromagnetic study and numerical simulations of the nano-antennas designed with real and special materials, dimensions, and substrate thickness is actually a challenge. The simulation of nano-antennas with thin substrate layers such as nanometers and without substrate is already have been performed to obtain the maximum field intensity at an operating frequency. The objective of this paper is twofold; the first one is to study the effect of the conducting material of the nano-antennas based on the structures presented in [21], in order to collect maximum energy at the resonance frequency of 28.3 THz. The second is to study the effect of the substrate material on maximizing the electric field intensity across the antenna gap. Analysis of the obtained simulated results shows that the using of

Submitted On: October 19, 2019
Accepted On: February 15, 2020

the high conductor material, Gold, leads as to have the highest gap electric field intensity for any structure. The choice of the Quartz as a substrate for these nano-antennas allow a better collection for the electric field in comparison with the most used substrate material; Silicon (Si) and Silicon oxide (SiO2).

This paper is organized as follows: Section II describes the geometries of three proposed antennas in detail, using the Drude model to describe the conductors' properties in terahertz frequency band. Following this, Section III presents the simulation results and discussions.

II. ANTENNAS DESIGN

The proposed IR nano-antennas were designed for harvesting of solar energy over the frequency range of 28-29 THz. The three different antenna shapes presented in [21] are optimized to realize a maximum level of the electric field intensity at 28.3 THz. The antennas are printed on a dielectric substrate and placed on a conducting ground plane. The ground plane has a thickness of 0.2µm which may improve the antenna coupling of the substrate.

Each of the three shapes are investigated to determine the effect of choosing the dipole shape as well as its material properties on the level of energy that is possible to collect in the gap.

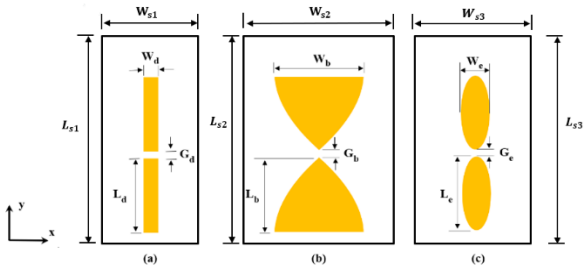

Fig. 1. The structure of the proposed dipole optical antenna: (a) rectangular, (b) bowtie, and (c) elliptical.

First, we start to study a simple rectangular dipole di to its advantages related to its small dimension, low cost, light weight and its manufacturing feasibility. The proposed rectangular dipole antenna is shown in Fig. 1 (a). We note that each rectangular arm has a length L_d=1.8µm, width of W_d=0.15µm, separation gap of Gd= Wmin=0.05µm and conductor thickness of 0.08µm. The dimension of the substrate is Ls1=3.8µm and Ws1=1.2 µm.

Next, we studied a modified bowtie antenna. Usually the bowtie antenna consists of two triangularly shaped arms. However, here the two arms of the bowtie are designed to have a curved exponential shape, represented by (1), where V is the curvature coefficient, W_{max} and W_{min} are the maximum and the minimum widths of the tapered arm respectively, and B is given by (2). Figure 1 (b) shows the proposed curved bowtie nano-antenna. The conductor thickness is 0.1µm and its gap size is 0.05 µm. The geometrical parameters of this structure are W_{s2}=4 µm, L_{s2}=7µm, W_b=2.52µm, L_b=2.5µm, Wmin=G_b=0.05µm, W_{max}=5.05µm, and V=0.8µm:

$$g(x) = B(e^{Vx} - e^{-Vx}) + \frac{W_{min}}{2}, \quad (1)$$

$$B = \frac{W_{max} - W_{min}}{2(e^{V\frac{W_b}{2}} - e^{-V})}. \quad (2)$$

The third proposed shape is an elliptical dipole, whose conductor thickness is 0.1µm. As shown in Fig. 1 (c) the dimensions of the structure for the elliptical dipole are L_{s3}=17µm, W_{s3}=4 µm, W_e=1.6µm, L_e=8µm and the gap width is G_e=0.05 µm.

All three dipoles were printed on a substrate that has an area of 3.8×0.2µm^2 and thickness of 100µm.

While the metal is considered as a perfect electric conductor at lower frequencies, e.g., RF. This is not the case at infrared frequencies in which it is plasmonic in nature [16] and is typically represented by the Drude model to describe the transport properties of electrons in materials [17]. The complex permittivity ε_c is given by:

$$\varepsilon_c = \varepsilon_1 + i\varepsilon_2. \quad (3)$$

The Drude model of ε_c is represented via the expression:

$$\varepsilon_c = \varepsilon_\infty - \frac{{\omega_{p1}}^2}{\omega^2 - i\Gamma\omega} + \frac{{\omega_{p2}}^2}{{\omega_0}^2 - \omega^2 + i\gamma\omega}. \quad (4)$$

In (4), where $\omega_0 = \frac{2\pi c}{\lambda_0}$, and ε_∞ is the contribution of the bound electron to the permittivity, γ denotes the damping frequency, ω_p is the plasma frequency, ω represents the angular frequency and ω_0 corresponds to the angular frequency. It is shown in [17] that expression in (4) agrees well with the experimentally measured dielectric properties of metal. Figures 2 (a) and (b) show that the variation of real and imaginary parts of permittivity for different metals, such as gold, copper, silver, chromium and titanium, still have good conductivity and low losses at the frequency range of 1 to 30 THz. It can be seen that the electrical permittivity varies from one metal to another and it decreases as the frequency is increased.

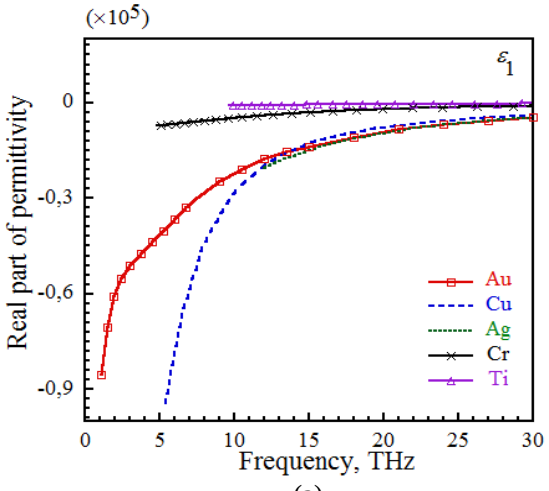

(a)

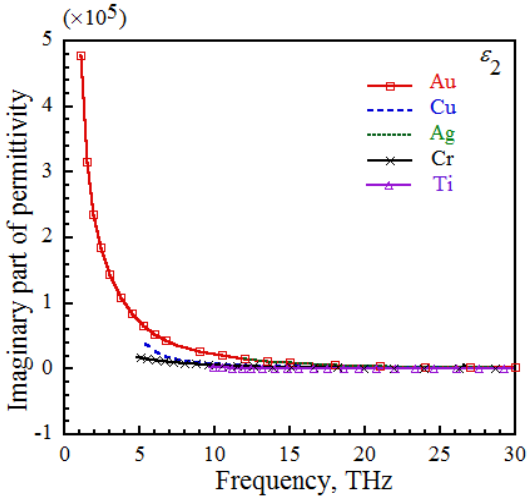

(b)

Fig. 2. The variation of the real and imaginary parts of relative permittivity for various metals.

Table 1: Real and imaginary part of relative permittivity at 28.3 THz

Conductor	ε_1	ε_2
Gold (Au)	–5605.6	2243.2
Copper (Cu)	–4261.8	1186.2
Silver (Ag)	–5061.3	1566.1
Chromium (Cr)	–1132.5	563.18
Titanium (Ti)	–306.94	301.73

The three antennas mentioned above, are simulated by using the Computer Simulation Technology (CST) [18] program package, where the metal properties of the gold are calculated by using the Drude model and are inserted in the CST Microwave Studio. The imaginary part of the permittivity is associated with the ohmic losses, which should be as low as possible. Alternatively, we can maintain the ohmic losses to be low by choosing a metal that has a significant real negative part. Table 1 lists the real and imaginary parts of the relative complex permittivity for five conductors of gold, copper, silver, chromium, and titanium.

III. RESULTS AND DISCUSSIONS

A. Effect of the conductor

Gold, silver, aluminum and copper are the three widely used materials in optical applications [19]. Gold and copper have almost the same dielectric and conduction properties with similar responses to Drude at less than 2.1 eV, and the beginning of inter-band transitions occurring around 2.3 eV (530-550 nm). These two types of materials generally have a good conductivity in the infrared region, whereas Titanium has a low conductivity compared to other metals previously studied. In the terahertz frequency band, the conductivity of the metal is complex, given by:

$$\sigma = \sigma_1 + i\sigma_2, \quad (5)$$

where σ_1 and σ_2 can be calculated by using the following equations:

$$\sigma_1 = \varepsilon_0 \varepsilon_2 \omega, \quad (6)$$

$$\sigma_2 = \varepsilon_0 (\varepsilon_1 - 1)\omega. \quad (7)$$

The conductivity of different metals is calculated at different frequencies by using the above expressions. Figures 3 (a) and (b) show the variations of the conductivities of different metals vs frequency. It is obvious that the conductivity of the metals reduces as we increase the frequency. Also, the real and imaginary values of the conductivity for gold are higher than those of other metals because gold is characterized by its high absorption of radiation at terahertz frequencies [7]. Silver and copper have conductivity values that are near – but less than – that of gold. This can be noticed in Table 2.

Since the conductivity of titanium is the least among the selected metals, we can anticipate that the titanium antennas will collect less electric field than would the others. This can be seen from Figs. 4 (a), (b) and (c), which present the results for the three different dipole shapes.

The gold is chosen for the rectangular, curved bowtie and elliptical dipole shaped antennas which realize field strengths of 350.75, 429.858, and 330.01 V/m, respectively, at 28.35 THz. This choice is based on the results obtained from the simulation of these antennas and are shown in Fig. 3. A set of conductors are used for each dipole, instead of a single conductor for each arm. By combining gold with chromium, gold with titanium, and chromium with titanium. Figures 4 (d), (e), and (f) show the effect of the conductors on the collected electric field in the gap for the three different dipole shapes. It can be seen that the structures with the gold collect the higher electric field than the other structures.

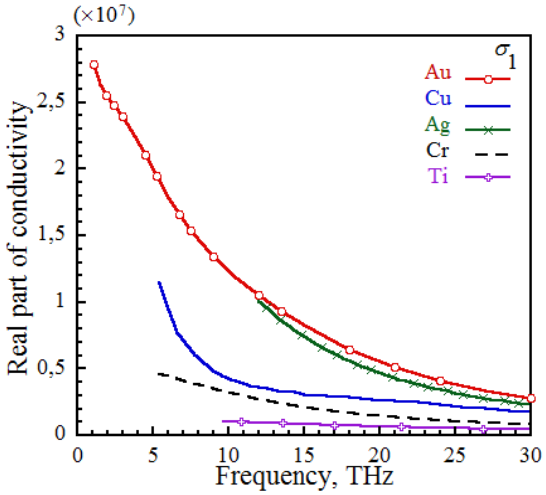

(a)

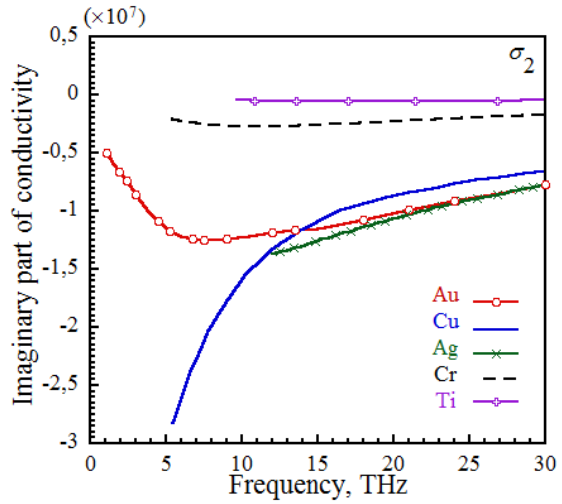

(b)

Fig. 3. Variation of metal conductivity versus frequency band [0...50THz].

Table 2: Real and imaginary part of conductivity at 28.3 THz [20]

Conductor Type	σ_1 (S/m)	σ_2 (S/m)
Gold(Au)	0.33728×10^7	-0.84305×10^7
Copper (Cu)	0.18855×10^7	-0.67762×10^7
Silver (Ag)	0.25012×10^7	-0.80856×10^7
Chromium (Cr)	0.08889×10^7	-0.17893×10^7
Titanium (Ti)	0.047507×10^7	-0.04848×10^7

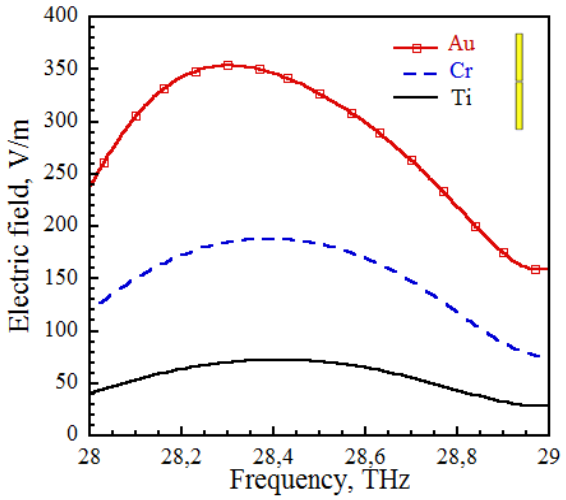

(a)

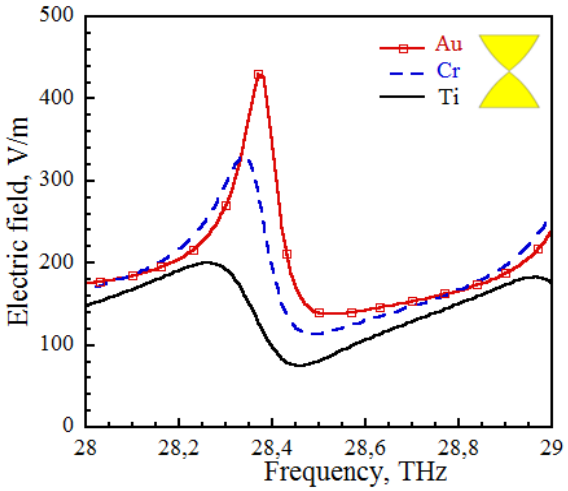

(b)

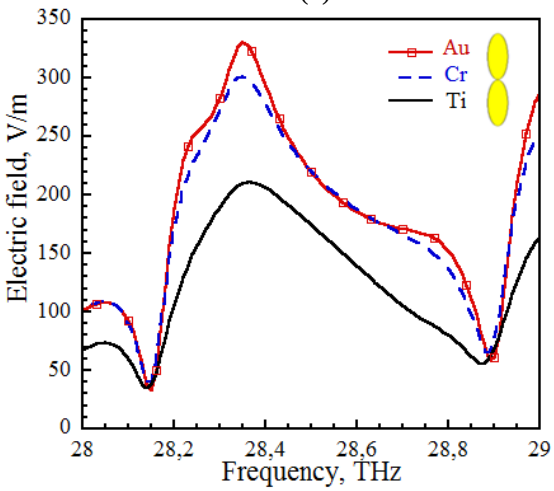

(c)

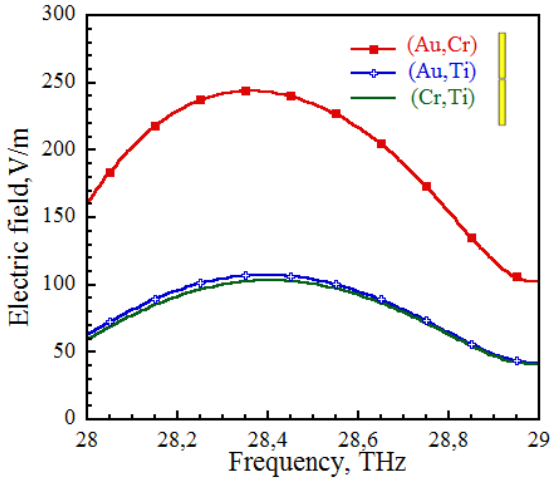

(d)

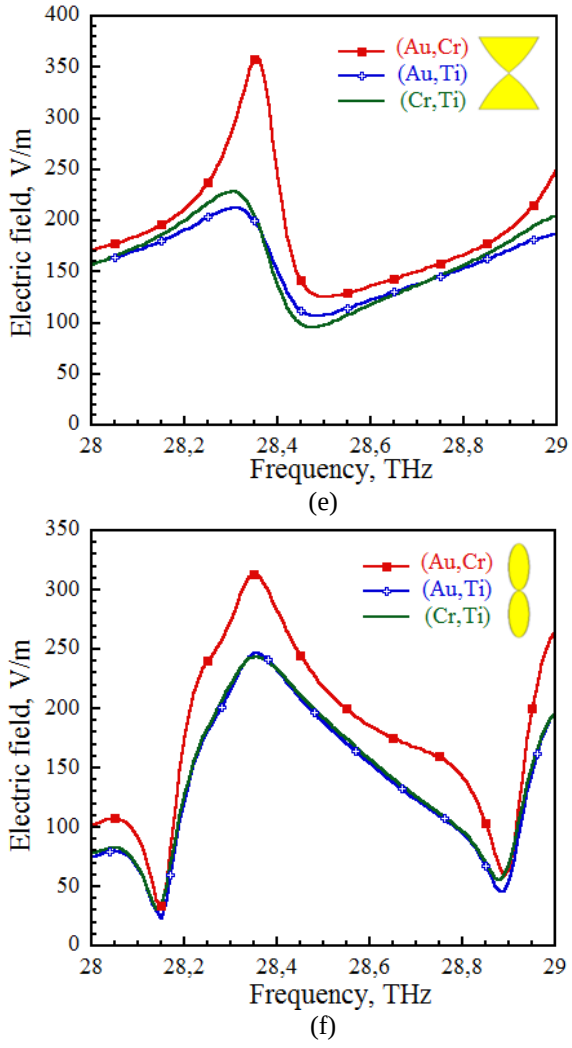

Fig. 4. The effect of metal type on electric field variation versus frequency for (a,d): rectangular, (b,e): curvature bowtie, and (c,f): elliptical antenna.

B. Effect of the substrate

The choice of the dielectric material plays an important role in the design of antennas. The best strategy is obviously to choose a substrate that has a low loss. At infrared, the type of the substrate plays a very important role where we attempt to improve the electric field amplitude in the gap of the antenna structure. We have investigated three different substrates to see which one has the best performance. The three substrates are: Quartz (GaAs, $\varepsilon_r = 3.75$, silicon (Si, $\varepsilon_r = 11.68$, and silicon oxide (SiO2, $\varepsilon_r = 4.71$ at 28.3 THz). Figures 5 (a) and (b) show variations of the real and imaginary parts of relative permittivity for the three different substrate materials versus frequency range of 28-29 THz. These three different substrates are used to evaluate their effect on the electric field captured in the gaps of the dipoles. The results are presented in Fig. 6, where we observe that the nano-antenna with quartz substrate achieved the highest gap electric field. The maximum field value obtained for the rectangular dipole antenna with the quartz substrate is at 353.743 V/m at 28.3 THz; for the bowtie dipole antenna, the maximum value is 429.858 V/m at 28.37 THz; and for the elliptical dipole antenna, the maximum value of electric field reaches 327.202 V/m at 28.35 THz. It should be noted that the substrate permittivity affects both the maximum value of the captured gap field and the resonance frequency. Additionally, we note, from Figs. 6 (a, b, c), that the quartz substrate allows for capturing a higher level of the field in the entire band.

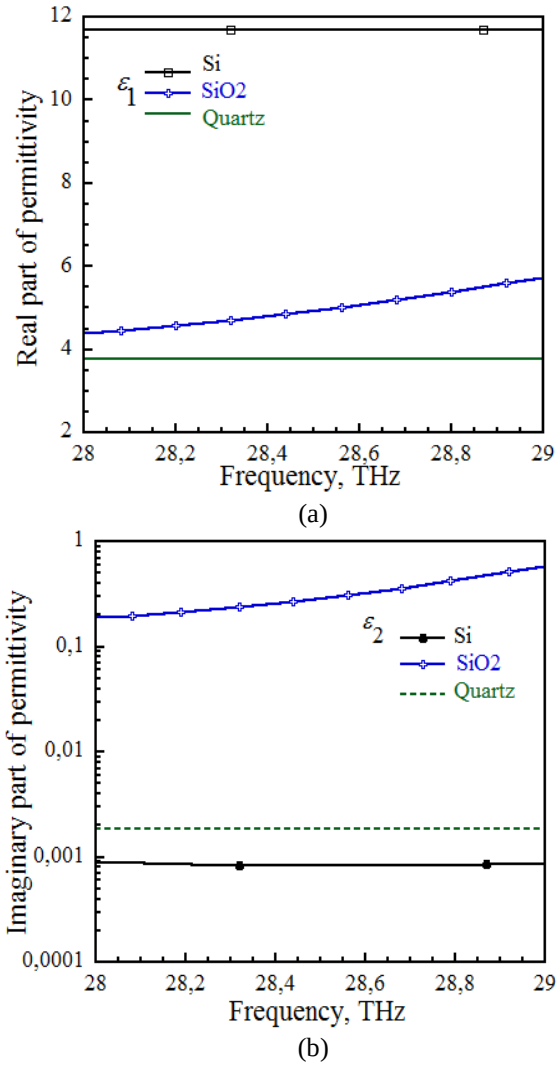

Fig. 5. Real and imaginary part of relative permittivity of studied substrates [20].

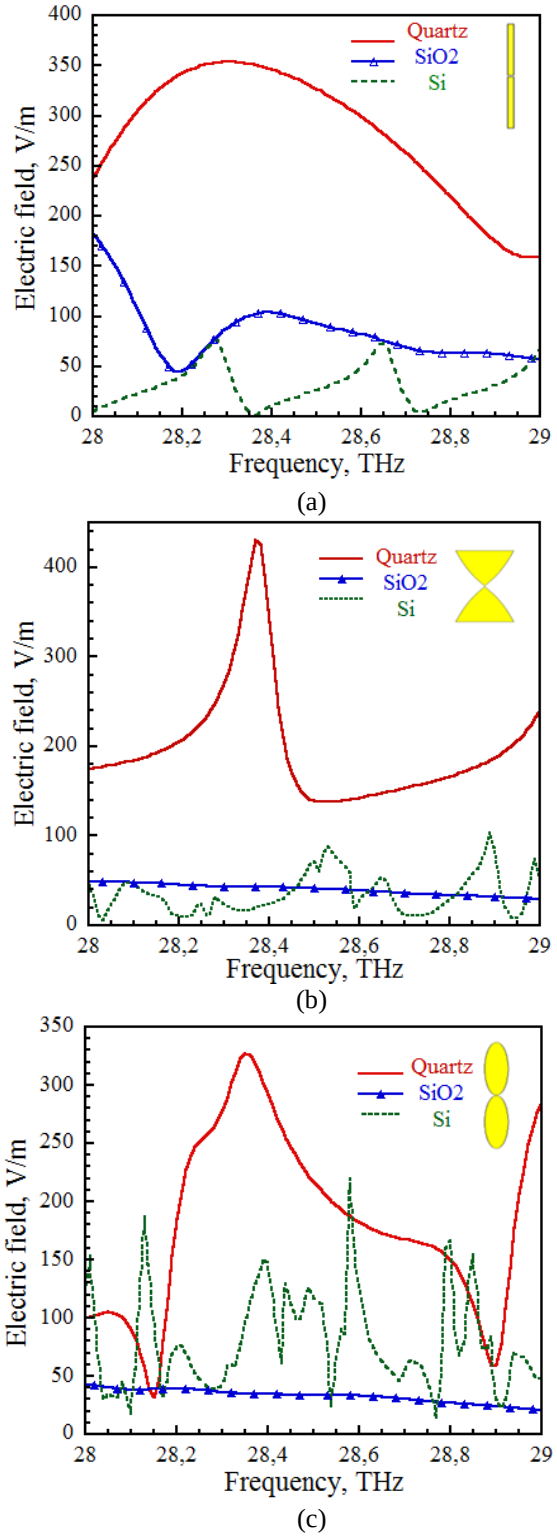

Fig. 6. Effect of substrate type and thickness on electric field distribution for the different structures.

We now compare the three different shapes of the studied dipole antennas. It is evident that the curved bowtie antenna has the highest value of the captured field at 28.3 THz, as compared to the dipole designs with elliptical and the rectangular shapes (See Fig. 7). Moreover, Table 3 summarizes the maximum field values realized by antennas with different metal types. It is evident that gold-based antennas provide the maximum electric field for rectangular, elliptical, and bowtie dipole shapes at 28.30, 28.32 and 28.33 THz, respectively.

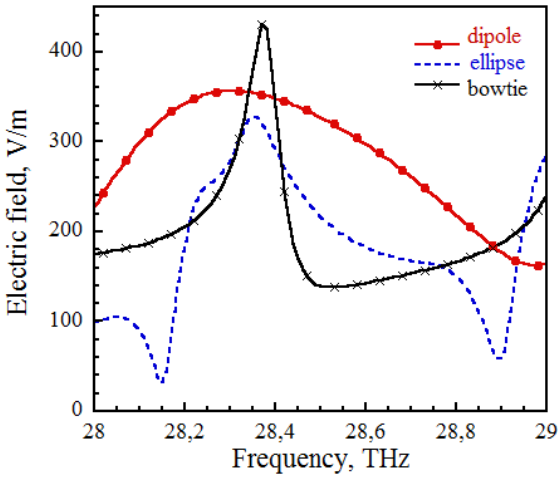

Fig. 7. Variation of electric field versus frequency for the optimum case of different dipole antenna shapes.

Table 3: E_{Max} at resonance frequencies for different conductor type

Dipole Shape	Type of Metal	Resonant Frequency (THz)	E_{Max} (V/m)
Rectangular	Au	28.30	353.75
	Cr	28.37	188.00
	Ti	28.42	72.67
	(Au,Cr)	28.36	244.032
Bowtie	Au	28.33	429.85
	Cr	28.34	331.52
	Ti	28.26	200.67
	(Au,Cr)	28.35	357.63
Elliptical	Au	28.32	327.20
	Cr	28.35	301.39
	Ti	28.32	200.03
	(Au,Cr)	28.35	313.22

IV. CONCLUSION

In this paper, a set of Ultra-Wideband optical nano-antennas operating in the infrared region were proposed and optimized to collect the maximum energy. A combination of three different dipole shapes, three different metals and three types of substrates were investigated. It was shown that using goldas a conductor achieved the highest gap electric field intensity for any

dipole/substrate combination, and so did quartz for any dipole/conductor combination.This is due to gold having the highest conductivity and quartz having the lowest loss. We propose a future similar investigative study where a metal-insulator-metal (MIM) diode with a thin insulator layer of Al_2O_3 inserted in the antenna gap.

ACKNOWLEDGMENT

This work was supported by King Salman bin Abdulaziz Chair for Energy Research, King Abdulaziz University, Jeddah, Saudi Arabia, under grant no. PSCE-4. The authors gratefully acknowledge the technical and financial support for this project.

REFERENCES

[1] P. Bosshard, W. Hermann, E. Hung, R. Hunt, and A. Simon, "An assessment of solar energy conversion technologies and research opportunities," *GCEP Energy Assessment Analysis*, 2006.

[2] G. Moddel and S. Grover, *Rectenna Solar Cells*. Springer, New York, 2013.

[3] A. M. A. Sabaawi, C. Tsimenidis, and B. S. Sharif, "Infra-red nano-antennas for solar energy collection," Loughborough, UK, 14-15 Nov. 2011.

[4] A. M. A. Sabaawi, C. Tsimenidis, and B. S. Sharif, "Infra-red spiral nano-antennas," Loughborough, UK, 12-13 Nov. 2012.

[5] G. Jayaswal, A. Belkadi, A. Meredov, B. Pelz, G. Moddel, and A. Shamim, "Optical rectification through an Al2O3 based MIM passive rectenna at 28.3 THz," *Materials Today Energy*, 7, pp. 1-9, 2018.

[6] A. Haque, A. W. Reza, N. Kumar, and H. Ramiah, "Slotting effect in designing circular edge bow-tie nano antenna for energy harvesting," *2015 IEEE Conference on Open System (ICOS)*, Melaka, Malaysia, Aug. 2015.

[7] M. N. Gadalla, M. Abdel-Rahman, and A. Shamim, "Design, optimization and fabrication of a 28.3 THz nanorectenna for infrared detection and rectification," *Scientific Reports*, 4, 2014.

[8] A. M. A. Sabaawi, C. C. Tsimenidis, and B. S. Sharif, "Planar bowtie nanoarray for THz energy detection," *IEEE Transactions on Terahertz Science and Technology*.

[9] I. E. Hashem, N. H. Rafat, and E. A. Soliman, "Dipole nantennas terminated by traveling wave rectifiers for ambient thermal energy harvesting," *IEEE Transactions on Nanotechnology*, vol. 13, no. 4, July 2014.

[10] N. A. Eltresy, H. A. Malha, S. H. Zainud-Deen, and K. H. Awadalla, "Dual-polarized nanoantenna solar energy collector," *33rd National Radio Science Conference (NRSC 2016)*, Aswan, Egypt, Feb. 2016.

[11] W. Amara, D. Oueslati, H. Rmili, A. Alghamdi, and T. Aguili, "Numerical analysis of a modified-dipole optical antenna for solar energy harvesting," *The 2018 International Conference on Innovative Trends in Energy (ITE'18)*, Hammamet-Tunisia, May 10-12, 2018.

[12] W. Amara, D. Oueslati, H. Rmili, A. Alghamdi, and T. Aguili, "Ultra-wideband elliptical-dipole optical antenna for solar energy harvesting," *The 2018 International Conference on Sensors, Systems, Signals and Advanced Technologies*, (SSS'18), Hammamet-Tunisia, May 10-12, 2018.

[13] W. Amara, N. Elresty, A. Yahyaoui, H. Rmili, T. Aguili, and J. M. Floch, "Design of ultra-wideband nano-antennas for solar energy harvesting," *The Loughborough Antennas and Propagation Conference, LAPC*, Nov. 2017.

[14] A. Vial, T. Laroche, and M. Roussey, "Crystalline structure's influence on the near-field optical properties of single plasmonic nanowires," *Applied Physics Letters*, 91, 123101, 2007.

[15] J. Schuller, R. Zia, and M. Brongersma, "Near-field characterization of guided polariton propagation and cutoff in surface plasmon waveguides," *Physical Review B*, 74, pp. 1-12, 2006.

[16] R. W. Alexander, Jr. and C. A. Ward, "Optical properties of the metals Al,Co, Cu, Au, Fe, Pb, Ni, Pd, Pt, Ag, Ti, and Win the infrared and far infrared," *Appl. Opt.*, vol. 22, p. 1099, 1983.

[17] P. B. Johnson R. W. Christy, "Optical constants of the noble metals," *Phys. Rev. B*, 6:4370-9, 1972.

[18] CST Microwave Studio, ver. 2012, Computer Simulation Technology, Framingham, MA, 2012.

[19] P. Biagioni, J.-S. Huang, and B. Hecht, "Nano-antennas for visible and infrared radiation," *Rep. Prog. Phys.*, 75, 024402 (40pp), 2012. doi:10.1088/0034-4885/75/2/024402

[20] https://refractiveindex.info/

[21] W. Amara, D. Oueslati, N. Elestry, A. Alghamdi, K. Sedraoui, T. Aguili, and H. Rmili, "Parametric study of modified-dipole nano-antennas printed on thick substrates for infrared energy harvesting," *Int. J Numer Model*, 2019. e2704. https://doi.org/10.1002/jnm. 2704.

Wided Amara received her B.S. in Industrial Electronics Engineering in October 2015, and the M.S. in Smart Systems for Communication in November 2016, from the National Engineering School of Sousse (ENISO, Tunisia). She is actually preparing her Ph.D. in Telecommunications within the SysCom Laboratory,

ENIT, Tunis, Tunisia. She has published 3 international conference papers in the area of IR energy harveesting by using nano-antennas.

Taoufik Aguili received his Engineering degree in Electrical Engineering and his Ph.D. degree in Telecommunications from INSA, France. He is working as Professor at the National Engineering School of Tunis (ENIT). He is actually the Head of the SysCom Laboratory, at ENIT, Tunis, Tunisia.

Abdulsalam S Alghamdi is an Associate Professor of Electrical Engineering at King Abdulaziz University (KAU), and the Director of King Salman ben Abdulaziz Chair for Energy Research (KSCER). He received his B.Sc. from KAU, Saudi Arabia, in 1988. He received a M.Sc. degree in Electrical Power and Energy from the University of Manchester Institute of Science and Technology (UMIST), UK, in 1990. In 1993, he was granted a Ph.D. from the University of Manchester, UK, in Electrical Engineering. He held many academic and administrative roles as a Vice-Dean and Dean, and a Director for Jeddah Board for Technical Education and Vocational Training, from 1994 to 2006. In 2006, he spent a one-year sabbatical leave in Tony Davis High Voltage Lab at the University of Southampton; and has been there as a Visiting Academic several times since then.

His subspecialty is High Voltage Engineering. His research interest and publications are in Electrical Power Systems and Energy, Electrical High voltage Insulating Materials and Renewable Energy, especially the Solar Energy Systems.

Donia Oueslati received a degree in Electronics, Computer and Information Science from the University Tunis El Manar, Tunisia in 2008 and the Master thesis in System of Communications from National Engineering School of Tunis, Tunisia in 2011. She received the Ph.D. in Engineering Sciences from Université Catholique de Louvain, Belgium and in Telecommunication from UTM in 2017. From April 2017 to August 2018, she was a Post-Doctoral Researcher with Antenna Lab, Université Catholique de Louvain, in collaboration with HEC research center, EMC Lab, University of central Florida, Orlando, Florida, USA, and ECE Department, King Abdulaziz University, Saudi Arabia. Since September 2018, she is working as Research Assistant at University Catholique de Louvain.

Her research mainly focuses on the development of a modal analysis methods for printed structures based on the Method of Moments and singular decomposition to identify a chipless Radio Frequency Identification (RFID) and to localize a reader. Her research interests include Ultra-Wideband (UWB) optical rectennas for Solar Energy Harvesting, investigation of irregular fractal antennas, as well as on low profile antenna array and array optimization for 5G applications.

Nermeen Eltresyreceived the B.S. and M.S. from Menoufia University, Menoufia, Egypt, in May 2012 and January 2016, respectively. Her Master's thesis was about study and design of nanoantennas element and arrays for different applications. She is Assistant Researcher from 2016 until now in the Microstrip Department, Electronics Research Institute. She has published 7 papers in periodical Journals and 9 papers in conferences and a book chapter in the area of nanoantennas design and applications. Actually, she is collaborating with King Abdulaziz University (KAU), Jeddah in Saudi Arabia in the research area related to IR energy haveresting by using nano-antennas.

Muntasir Sheikh received his B.Sc. from King Abdulaziz University, Saudi Arabia, in Electronics and Communications Engineering, M.Sc. in RF Communications Engineering from the University of Bradford, U.K., and PhD from the University of Arizona, U.S.A.

Since then he has been teaching in the Electrical and Computer Engineering Dept. in KAU. His research interests are Antenna Theory and Design, Radar applications, and electromagnetic metamaterials.

Hatem Rmili received the B.S. degree in General Physics from the Science Faculty of Monastir, Tunisia in 1995, and the DEA diploma from the Science Faculty of Tunis, Tunisia, in Quantum Mechanics, in 1999. He received the Ph.D. degree in Physics (Electronics) from both the University of Tunis, Tunisia, and the University of Bordeaux 1, France, in 2004. From December 2004 to March, 2005, he was a Research Assistant in the PIOM Laboratory at the University of Bordeaux 1. During March 2005 to March 2007, he was a Postdoctoral Fellow at the Rennes Institute of Electronics and

Telecommunications, France. From March to September 2007, he was a Postdoctoral Fellow at the ESEO Engineering School, Angers, France. From September 2007 to August 2012, he was an Associate Professor with the Mahdia Institute of Applied Science and Technology (ISSAT), Department of Electronics and Telecommunications, Tunisia. Actually, he is Full Professor with the Electrical and Computer Engineering Department, Faculty of Engineering, King Abdulaziz University, Jeddah, Saudi Arabia.

Professor Rmili's research interests concern applied electromagnetic applications involving antennas, metamaterials and métasurfaces. The main targeted applications are reconfigurable antennas for multi-standard wireless communications systems, security of chipless RFID systems with fractal tags, terahertz photoconductive antennas for infra-red energy harvesting, UWB nano rectennas for collection of solar energy, phase shifters for low-cost 5G communication systems, and microwave absorbing materials for stealth technologies.

Radar Cross Section Reduction using Characteristic Mode Analysis

Marcelo Bender Perotoni [1], Felipe A. A. da Silva [1], Kenedy Marconi G. dos Santos [2], and Danilo Brito Almeida [2]

[1] UFABC
Santo Andre, SP,09210-580, Brazil
Marcelo.perotoni@ufabc.edu.br

[2] IFBA
Vitória da Conquista, BA, 45078-900, Brazil
kenedymarconi@gmail.com

Abstract ─ This article covers the application of Characteristic Mode Analysis to reduce the Radar Cross Section of a canonical object, a metallic cylinder. Electrically small, non-resonant slots are added to the structure and loaded with complex impedances, positioned on hot spots found after mode analysis based on the Method of Moments. Two critical frequencies with higher amplitude radar cross-section, 400 and 450 MHz, were analyzed. Results showed monostatic reductions on average of 5 dB, in both frequencies for two different sets of loads and at two different incident angles. Radar cross-section patterns were found to be affected by the load impedances, thereby offering a low profile and low drag solution to control the backscattering signature pattern.

Index Terms ─ Characteristic-mode analysis, electromagnetic simulation, radar cross section reduction.

I. INTRODUCTION

Reduction of the RCS (Radar Cross Section) of an aircraft can increase the survivability rate in combat cases since its detection becomes more difficult due to the reduced energy reflected back to the radar antenna. That means the enemy detection can only occur when the aircraft is deep into the enemy lines, which can be a game-changer in the context of aerial dominance. Conversely, for small civilian boats and ships, metallic structures based on corner reflectors help increase the RCS response so that they become more visible in operation [1], which renders their operation safer. When the incoming wave hits the target, the total energy is scattered in multiple directions and partially converted in heat, the echo is the part the hits back the radar. Given the fact that the echo response is related to the aircraft type, it is sometimes called its signature [2]. The scattering response of an aircraft depends on its geometry and its materials, as well as the incoming wave characteristics (polarization, frequency) [3]. Several different approaches are commonly used to reduce the RCS in aircraft, notably on the design of stealthy vehicles [4], which have lower amplitude backscattered responses than those expected from their actual dimensions. Extensive use of electromagnetic simulation allows the test of alternative geometries (a practice also known as shaping) which scatter back the incoming energy in directions other than that of the incoming wave [5]. Another technique involves radar absorbing materials (RAM), specifically designed to operate within radar frequency ranges, coating parts of the vehicles that are responsible for the high scattering (hot spots). A specific RAM case designed to operate within the X-band (10 to 12 GHz) was proved to reduce the RCS response in the average of 10 dB on a modified F5 fighter, analyzed by means of electromagnetic simulation [6]. Metamaterials (artificially engineered materials) are usually employed to reduce the RCS of antennas, which in virtue of their resonant nature can be responsible for a large part of the backscatter energy. For instance, artificial magnetic materials (AMC) were imprinted on a patch antenna as a kind of load, so that the overall RCS is reduced, within the band of 9.66 GHz to 11.50 GHz [7]. Another investigation had two AMC arrays operating in overlapped frequency ranges, mounted in a chessboard fashion, operating in the frequency range of 5.8 GHz [8]. Another chessboard-like structure, made out of a matrix of copper and high-permittivity dielectric material enabled the control of RCS for the frequency of 18.45 GHz, achieving reductions around 15 to 30 dB [9]. The use of plasma as an electromagnetic shield has also been proposed as a means to achieve RCS reduction, shown in one example at the 10 GHz range, simulated with an FDTD (Finite Difference Time Domain) code [10]. Other techniques to achieve a stealthy operation worth

Submitted On: December 3, 2019
Accepted On: February 28, 2020

mention are passive and active cancellation [4],[11], the latter relying on heavy high-speed data processing and phased arrays. This article covers the RCS analysis of a canonical structure, a metallic cylinder, and investigate the impact of small loaded slots on its response at two different close frequencies (400 and 450 MHz). The impact on the RCS is analyzed using computer simulation, based on the CMA (Characteristic Mode Analysis). The proposed technique, without the use of shaping and/or RAM, achieves a reduction and modification on the RCS signature. Due to its structural nature it can be made switchable, enabling a dynamical modification of the electromagnetic response and therefore turning the target detection and identification more complicated. Placement of inductive loadings on locations found after a CMA analysis was a way devised to reduce unwanted out of band antenna coupling, a similar approach to a different goal observed in this study [12].

II. RCS EVALUATION

A hollow metallic cylinder (1 meter long and with a radius of 0.2 m, zero thickness), made of PEC (perfect electric conductor) is analyzed according to Fig. 1. The worst case scenario in terms of radar signature, i.e., a plane wave with its electric field parallel to the cylinder axis is modeled with FEKO MoM (Method of Moments) solver. MoM offers good advantages for the simulation of metallic structures, given the fact the mesh is done only on the surface, in contrast to volumetric meshes of Finite Element Method (FEM) or Finite-difference Time-domain (FDTD). The MoM impedance matrix is also the basis for the CMA computation, therefore this numerical method is directly tied to the characteristic modes computation [13]. For simulation of a real object, more complicated than the present canonical cylinder, the Multi-Level Fast Multipole Method (MLFMM) can be used to reduce the coupling on the MoM matrix and turn the matrix sparse, easing the numerical solution. The cylinder monostatic radar response is simulated and the results with the frequency swept from 200 MHz to 700 MHz are shown in Fig. 2, for the angle Θ=90° - angle whose response is the largest in terms of backscattered energy.

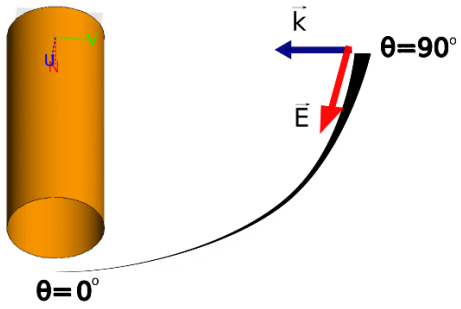

Fig. 1. Simulation setup.

It can be seen from Fig. 2 that the range around 400-450 MHz has the largest return amplitude, the respective surface current distributions are shown in Fig. 3. The surface current absolute values refer to a plane wave whose absolute amplitude is 1 V/m, constant over the entire frequency range, default within the FEKO suite.

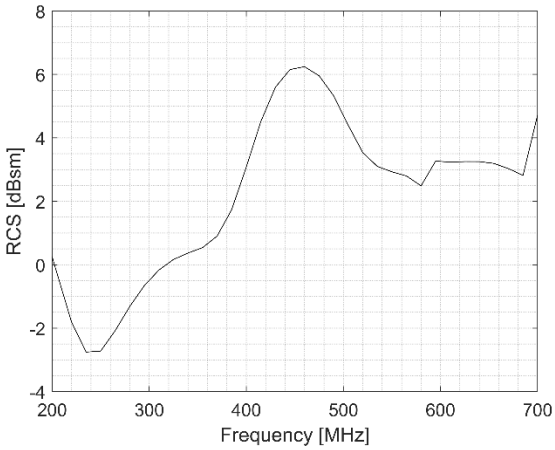

Fig. 2. Simulated RCS for the angle Θ=90°.

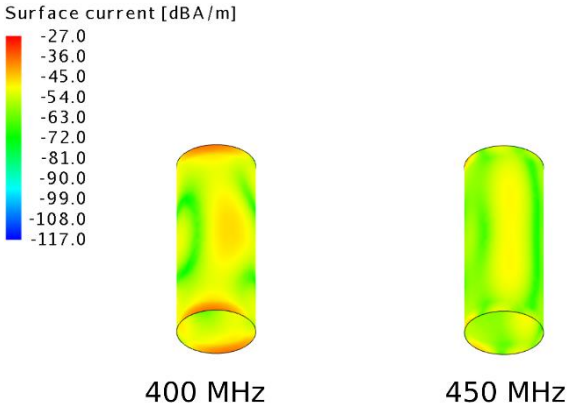

Fig. 3. Surface currents distribution for two different frequencies, incident angle Θ=90°.

From the current distribution at 400 MHz and 450 MHz it is possible to see that the area around the cylinder edges concentrates their maximum amplitudes, therefore they are backscattering hot spots. These areas should be possible options for having a RAM coating. This particular frequency range (C-band) is used by Early Warning Radars, for long-range detection, and each one of the two individual frequencies will be dealt with individually. The range resolution parameter of the target depends on the frequency span of the incoming signal, whereas the cross-range resolution depends on different angles scattered from the object [14]. Both domains – frequency and angular range, are therefore covered in the study.

III. CHARACTERISTIC MODE ANALYSIS

Characteristic Mode Analysis computes the natural modes on a metallic structure, described in terms of eigenvalues λ_n. A set of orthogonal current modes is found, and the individual modes existence and respective weight on the final current shape depend upon their individual excitation. Some modes might be good radiators in some frequencies whereas others might only store reactive energy. This analysis has been used as a tool for antenna placement, taking advantage of the natural resonant modes of chassis of vehicle or mobile phones to achieve better performances [15]. There is also a relation between CMA and the RCS of a metallic structure [16] – the RCS can be computed as the summation of all characteristic modes inside a structure [17]. An application involved a computer model of a jet aircraft, that in simulation showed a reduction in the RCS response by loading it with resonant antennas positioned in hot spots pointed out by a CMA study [13] - the antennas dissipated in their loads the high intensity currents generated by the plane wave excitation, thereby reducing the backscattering energy.

Several different parameters related to the eigenvalues describe their relative importance on the electromagnetic response of the structure, one of them is the Modal Significance (MS), that represents the normalized amplitude of the current modes. MS depends only on the shape and size of the structure, without influence on the excitation [18]. Figure 4 shows the computed MS for the three first modes of the cylinder – MS values closer to one indicate that the mode resonates. For the frequency range close to 400 MHz the mode 2 has the largest importance, whereas 450 MHz has mode 4 as the most significant. It can be seen in Fig. 5 that these modes have a current surface pattern similar to the one generated after a plane wave illumination. It indicates that the frontal illumination from a plane wave excites currents that accommodate/resonate in these specific modes, a scenario that reproduces the radar illuminated target.

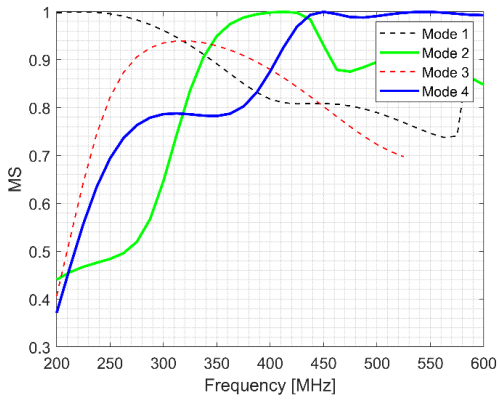

Fig. 4. Computed modal significance for the three first modes. Bold/solid lines represent the modes responsible for the large RCS values.

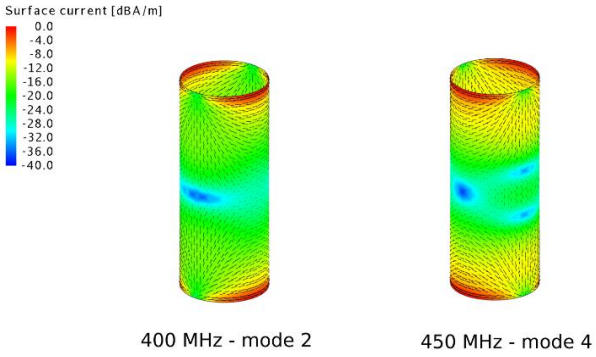

Fig. 5. Normalized current distribution relative to the modes at frequencies 400 MHz and 450 MHz.

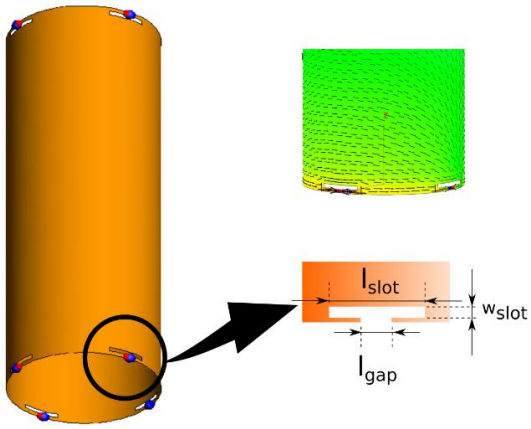

Fig. 6. Slots geometry and detail of the developed current surface shape (top right), excited by the ports (blue/red dots in the zoomed area). The dimensions are l_{slot}=10 cm, w_{slot} = 1 cm and l_{gap}=1.16 cm.

Once CMA provides an indication of which frequencies are more likely to radiate the next step consists of the proper selective excitation of these modes. Two basic formats are offered in the literature [19],[20], capacitive and inductive. The first uses a metallic patch placed where the mode has a current minimum; the latter has a loop where the mode current peaks, both are supposed to be electrically small, acting as a coupling to the source so that the large structure itself radiates. It is worth mentioning that these coupling structures are not necessarily matched, in general, due to their small electrical dimensions they have large imaginary parts which need to be dealt with in case of matched antennas or systems (50 Ω). In regard to the choice between capacitive or inductive excitation, since the interest is in a flying object, due to aerodynamic constraints a loop excitation was chosen – an electrical patch floating above the cylinder would induce an aerodynamic drag and the loop, being of a slot type, does not impose this sort of constraint. The main idea consists in directing the incoming plane wave energy into the

slots so that it is dissipated by the loads and/or scattered in other directions, in order to reduce the monostatic backscatter energy. The chosen excitation is depicted in Fig. 6. A total of eight symmetrical slots were distributed along the edges of the cylinder, to capture both 2nd and 4th modes, depending on the direction of the plane wave excitation. The input impedance at the gap is approximately 20 + j350 Ω (400 MHz) and 60 + j434 Ω (450 MHz).

IV. RCS REDUCTION

Complex impedances ($Z_{slot} = R_{slot} + jX_{slot}$) were added as loads to each one of the slots, and it was evaluated their influence on the RCS response. Figure 7 shows the RCS response (direction Θ=90°) for different values of Z_{slot}, for both 400 MHz and 450 MHz. It can be seen that the optimum real part (R_{slot}) is close to a short whereas the optimum X_{slot} is larger for the case of 450 MHz than that of 400 MHz, and also that the set of possible load values that decrease the RCS is larger for the higher frequency than to the lower one. In terms of load type, a capacitive part should be added to achieve lower RCS values for both individual frequencies. It was observed a strong sensitivity on the RCS signature on the Z_{slot} value, suggesting a possible means of scrambling radar detection by means of emulating targets with different PDFs (Probability Density Function) and reconstructed SAR/ISAR images [21]. Electronically switching of different loads can be implemented dynamically as an incoming radar signal is detected in case of evasive or stealthy operations. The size and relative position of the slots were not seen to have a large influence on the RCS reduction, given their small electrical size.

In terms of spatial angular responses, two particular sets of optimized Z_{slot} values, $Z_{slot}1$= (0.1 - j240) Ω and $Z_{slot}2$ = (0.1 - j330) Ω are shown in a polar plot format, Fig. 8, alongside with the baseline (no slots) case. The angle 90° had reductions of 4.2 dB (for $Z_{slot}1$, 400 MHz) and 3.3 dB (with $Z_{slot}2$, 450 MHz). The 0° direction had a reduction of 9.4 dB (400 MHz) and 4.2 dB (450 MHz), both with the $Z_{slot}2$ load impedance. The cut slots represented only 0.7% of the total cylinder area, so they do not impose a large modification on the original structure given the small electrical size of the exciters.

Figure 9 shows the PDF for the original and modified cylinder, with the two sets of impedances Z_{slot}. It can be seen that the inclusion of slots and the respective impedances modify the statistical distribution of the backscatter energy. For the case of $Z_{slot}2$ it shifts the distribution towards smaller RCS values. $Z_{slot}1$ minimizes the RCS for 400 MHz but the PDF still resembles the original object without slots whereas $Z_{slot}2$ provides a more substantial modification on the shape of the PDF function, for both frequencies. This modification turns the vehicle detection more difficult given that the PDF acts as a sort of electromagnetic signature.

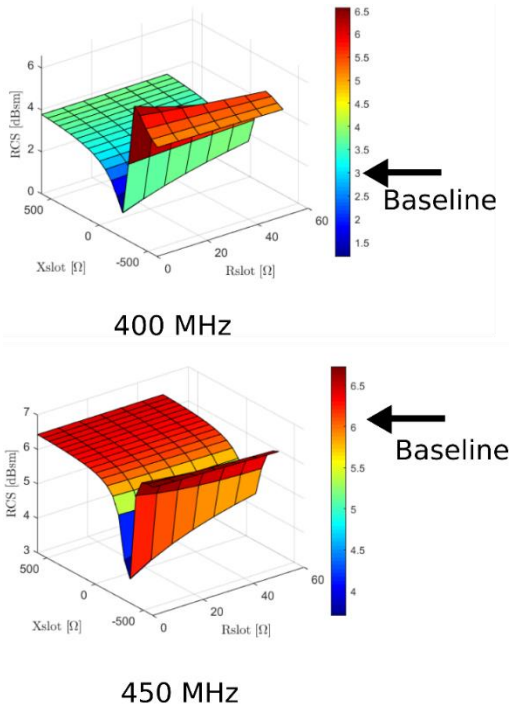

Fig. 7. Simulated monostatic RCS (Θ=90°) for 400 MHz and 450 MHz, with different loads connected to the slots. The baseline original RCS, without the slots, is shown in the black arrows by the colorbars.

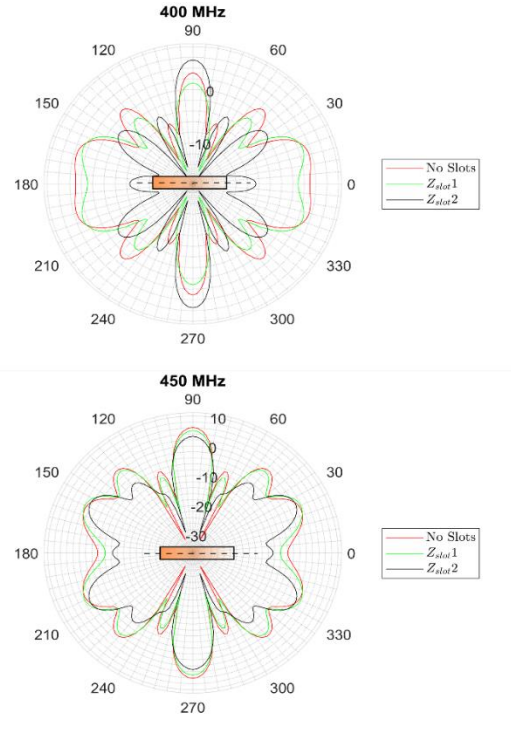

Fig. 8. Simulated monostatic RCS, in dBsm. Angle Θ swept, with the cylinder left for reference on the center of the figures.

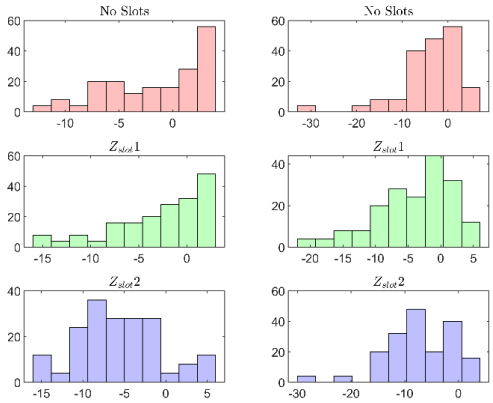

Fig. 9. Probability Density Functions for 400 MHz (left column) and 450 MHz (right column).

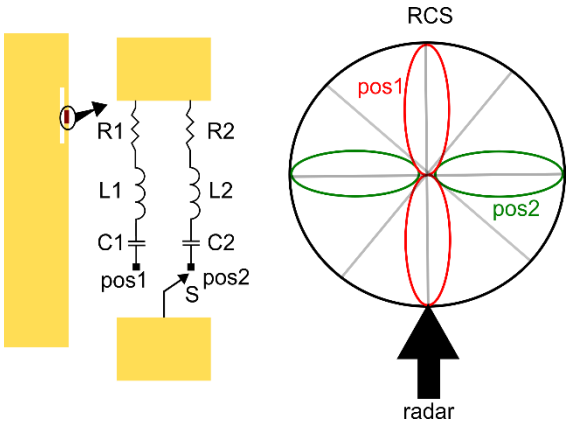

Fig. 10. Description of the switching load approach. Polar plot shows an example only, not related to this work.

The procedure for achieving the CMA reduction of the RCS can then be synthesized is as follows:

1. Determine the frequencies of interest. It can be VHF or low UHF for Early Warning Systems or X band for missile and aircraft radars, for instance.
2. Find out within the specific frequency range the most significant modes, running a CMA evaluation.
3. For these modes, investigate their current distribution pattern.
4. On the found hot spots (high amplitude surface current) deploy non-resonant slots, and add complex loads to them. The initial estimate of the load impedance should be the conjugate input impedance of the slot, at the frequency of interest. Alternatively, capacitive patches can be used as exciters, but these should instead be placed on points where the modes present maximum voltages.
5. Run a plane wave excitation and evaluate the RCS response after a sweep on the load impedance. Optimum load impedances can be chosen as a compromise between different frequencies, or as a way to create a different RCS signature.

Dynamic switching of the loads allows the on-the-fly electromagnetic signature scrambling, as Fig. 10 shows. The radar is positioned as shown on the polar plot, and it detects the target at the maximum backscatter direction. Upon switching the load from position S1 to S2 the main lobe moves to another direction, scrambling the proper vehicle detection.

V. CONCLUSION

This article covered the use of CMA analysis of a metallic cylinder and the respective loading of the excited modes in order to modify its RCS signature. Without traditional RCS reduction techniques, like absorbing materials or shaping, this technique changes the RCS of a canonical object with minimal structural modifications, given the fact the slots are electrically small and do not introduce aerodynamic drag to an aircraft. It also enables the modification to be implemented dynamically, by switching different sets of loads. Moderate RCS reductions (around 5 dB) were found after numerical simulations.

REFERENCES

[1] R. L. Haupt, D. Aten, and S. E. Haupt, "Modeling maritime radar reflectors using FEKO," *ACES Conference*, 2009.

[2] J. Paterson, "Overview of low observable technology and its effects on combat aircraft survivability," *Journal of Aircraft*, vol. 36, no. 2, pp. 380-388, 2012.

[3] C. A. Balanis, *Antenna Theory: Analysis and Design.* 3rd Edition, SJ: John Wiley and Sons, 2012.

[4] E F. Knott, J. Shaeffer, and M. Tuley, *Radar Cross Section.* Raleigh: Scitech, 2004.

[5] D. Liu, J. Huang, L. Song, and J. Ji, "Influence of aircraft surface distribution on electromagnetic scattering characteristics," *Chinese Journal of Aeronautics*, vol. 30, no. 2, pp. 759-765, 2017.

[6] L. A. de Andrade, L. S. C. dos Santos, and A. M. Gama, "Analysis of radar cross section reduction of fighter aircraft by means of Computer Simulation," *J. Aerosp. Technol. Manag.*, vol. 6, no. 2, pp. 177-182, 2014.

[7] Y. Zheng, J. Gao, H. Yang, Y. Zhou, and L. Cong, "A wideband gain enhancement and RCS reduction patch antenna using improved loading method," *2017 Int. Appl. Comput. Electromagn. Soc. Symp. China, ACES-China*, 2017.

[8] M. E. de Cos, Y. Alvares, and F. de Las-Heras, "A novel approach for RCS reduction using a combination of artificial magnetic conductors," *Prog. Electromagn. Res.*, vol. 107, no. 7, pp. 147-159, 2010.

[9] S. Simms and V. Fusco, "Chessboard reflector for RCS reduction," *Electron. Lett.*, vol. 44, no. 4,pp. 316-317, 2008.

[10] B. Chaudhury and S. Chaturvedi, "Three-dimensional computation of reduction in radar cross section using plasma shielding," *IEEE Trans. Plasma Sci.*, vol. 33, no. 6 II, pp. 2027-2034, 2005.
[11] M. Yi, L. Wang, and J. Huang, "Active cancellation analysis based on the radar detection probability," *Aerosp. Sci. Technol.*, vol. 46, pp. 273-281, 2015.
[12] Q. Wu, W. Su, Z. Li, and D. Su, "Reduction in out-of-band antenna coupling using characteristic mode analysis," *IEEE Trans. Antennas Propag*., vol. AP-64, no. 7, pp. 2732-2742, 2016.
[13] M. Vogel, G. Gampala, D. Ludick, U. Jakobus, and C. J. Reddy, "Characteristic mode analysis: Putting physics back into simulation," *IEEE Antennas Propag. Mag*., vol. 57, no. 2, pp. 307-317, 2015.
[14] C. Özdemir, *Inverse Synthetic Aperture Radar Imaging with MATLAB Algorithms.* Hoboken: Wiley, 2012.
[15] Y. Chen and C. F. Wang, *Characteristic Modes : Theory and Applications in Antenna Engineering.* Hoboken: Wiley, 2015.
[16] R. Harrington and J. Mautz, "Control of radar scattering by reactive loading," *IEEE Trans. Antennas Propag*., vol. 20, no. 4, pp. 446-454, 1972.
[17] R. F. Harrington and J. R. Mautz, "Theory of characteristic modes for conducting bodies," *IEEE Trans. Antennas Propag*., vol. AP-19, no. 5, pp. 622-628, 1971.
[18] M. Cabedo-Fabres, E. Antonino-Daviu, A. Valero-Nogueira, and M. F. Bataller, "The theory of characteristic modes revisited: A contribution to the design of antennas for modern applications," *IEEE Antennas Propag. Mag*., vol. 49, no. 5, pp. 52-68, 2007.
[19] R. Martens, E. Safin, and D. Manteuffel, "Inductive and capacitive excitation of the characteristic modes of small terminals," *LAPC 2011 Loughbrgh, Antennas Propag. Conf*., 2011.
[20] R. Martens, E. Safin, and D. Manteuffel, "Selective excitation of characteristic modes on small terminals," *Proc. 5th Eur. Conf. Antennas Propagation, EUCAP*, 2011.
[21] X. Wang, C. Wang, and Y. Liu, "RCS computation and Analysis of target using FEKO," *Proc. 3rd Asia-Pacific Conf. Antennas Propagation, APCAP*, 2014.

Marcelo B. Perotoni Electrical Engineer (UFRGS, Porto Alegre, Brazil), Ms.C. and Ph.D. in Electrical Engineering from USP (Sao Paulo, Brazil). He has been involved with electromagnetic simulation, RF and EMC since 2002. He is currently a professor at UFABC.

Felipe A. A. da Silva Electronic Technician and Bachelor in Science and Technology, currently in the Information Engineering program at UFABC. He was a visiting student at Montana Tech and has interests in Propagation and RF design.

Kenedy Marconi G. dos Santos is B.Sc. in Electrical Engineering (2006) – PUC MG, M.Sc. in Electrical Engineering (2011)-UFMG, Ph.D. in Electrical Engineering (2018) – UFBA. Currently is professor at the IFBA. He has experience in Electrical Engineering with emphasis on EMC, Microwave and Antennas.

Danilo B. Almeida is B.Sc. in Electrical Engineering (2005) – UNIP – SP. He is a Specialist in Occupational Safety and Energy Efficiency. Currently is professor at the IFBA and FAINOR.

Array Pattern Reconfiguration Using Pixel Method

Karam M. Younus and Jafar R. Mohammed

College of Electronics Engineering
Ninevah University, Mosul, 41002, Iraq
karam.younus@uoninevah.edu.iq, jafarram@yahoo.com

Abstract ─ In this paper, the array elements are considered as pixels and their magnitude excitations are assigned to the values of 1 (i.e., active or turned ON) or 0 (i.e., inactive or turned OFF). Thus, each element either exists at its position in the considered array or not. The proposed pixel method can be applied to different planar array configurations such as square, rectangular, triangular, circular, or any other shape to achieve the required pattern reconfigurability. Moreover, by turning OFF some of the selected elements, the main beam of the array pattern can be switched to specify directions without using any phase shifters or any other RF components. Therefore, its practical implementation is simpler and cheaper than any other existing method. However, when comparing with arrays in which all their elements are turned ON, the gain of the considered arrays will be reduced when some selected elements are turned OFF. The array pattern reconfiguration using the pixel method has been designed and its parameters have been optimized using computer simulation Technology (CST-MWS), which uses the Finite Integration Technique (FIT). It's also verified by High-Frequency Surface Structure (HFSS) commercial software (based on the FEM method). Numerical results obtained under full-wave modeling CST environment demonstrate the effectiveness of the described method.

Index Terms ─ Beam steering, magnitude excitation, pattern configuration, pixel arrays, planar arrays.

I. INTRODUCTION

Currently, the array pattern reconfiguration becomes one of the important issues in the satellite and terrestrial communication systems, where the radiating parts of the transmitting and/or receiving devices in such systems need to be continuously reconfigured to assure reliable link over dynamic channels or environmental conditions. The design of the antenna arrays has been developed toward compact and simple architectures such as conventional beamforming [1], smart arrays [2-4], and re-configurable array patterns [5-11].

The array pattern configurability and beam steering capability of such types of antenna arrays are traditionally accomplished by using phase shifters, variable attenuators, and other RF components that connected to each element of the array in the feeding network which exhibits a complex circuitry. In addition, the use of phase shifters in such arrays exhibit scans loss and errors which lead to performance degradation [12].

Recently, the radiation characteristics of the reconfigurable arrays can be changed by using switches such as PIN diodes to connect the required elements and to achieve the desired radiation patterns [13].

Very recently, the array pattern configuration has been achieved by means of parasitic elements [14]. In such approaches, the need for phase shifters has been overcome. Therefore, the loss and error problems associated with the progressive phase shift between array elements are alleviated.

In this paper, the radiation characteristics such as beamwidth, gain, sidelobe level, and main beam direction of planar arrays can be controlled by turning ON/OFF a certain number of the array elements by selecting their magnitude excitations to be either 1 or 0. This type of array is known as Pixel Array. It can offer a great reduction in the cost and weight of the feeding network circuitry. Further, the method is capable to provide a narrow beamwidth that is approximately equal to that of the fully active array elements under the condition of keeping the same array size. Also, the elements that turned ON (active) with magnitude excitation selected to be 1, in an array is able to provide a lower sidelobe level with respect to that of the fully uniform array where all of its elements are active [15]. In this type of arrays, the directivity will depend directly on the number of turned on elements. The key feature of the proposed planar array is its ability to switch the main beam to some pre-specified directions in the azimuth plane without using any phase shifters or any other RF components.

Since the simplicity and versatility of the proposed pixel planar array are assured, thus, it can be recognized as a good candidate for 5G technologies in which the communication efficiency is of great importance [16].

Furthermore, the performance of the proposed array has been investigated and verified using (CST-MWS)

Submitted On: December 11, 2019
Accepted On: December 28, 2019

software. The Time-Domain solver was used to obtain the required results [17]. Parametric studies and optimization using the built-in Trust Region Framework Algorithm which is a numerical optimization for solving nonlinear programming problems have been used. Section II describes the concept of designing the proposed array starting from a single patch, while section III presents the results. Section IV presents a numerical comparison of the results achieved by CST and HFSS [18]. Finally, the conclusions are listed in Section V.

II. THE PLANAR PIXEL ARRAY

In this work, the shape of the considered planar array is chosen to be triangular which is derived from an original square planar array with (NxN) elements. However, the proposed pixel method can be straight forwarded to any other planar shape. To illustrate the concept of the pixel elements, first the proposed planar array with assigned magnitude values is shown in Fig. 1. It consists of two sets of elements. The first set contains the active elements, while the second set contains only inactive elements. Here, each element in the considered array is chosen to be a small circular patch. Then an array of such patches is formed. The details of each part are shown in the next sections.

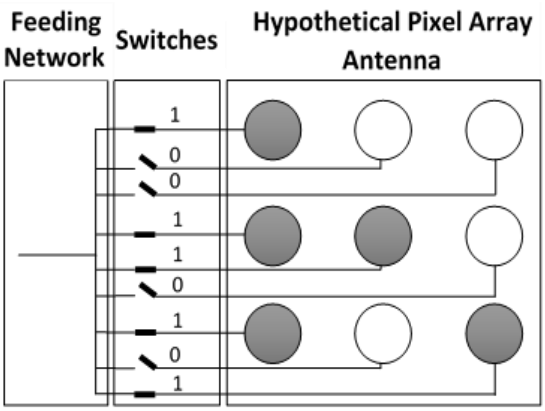

Fig. 1. Pixel array feeding network: gray (active elements) and white (inactive elements).

A. Single element circular patch antenna

The substrate of such a Patch element is chosen to be FR-4 with thickness h=1.6 mm, relative permittivity εr=4.3, and dielectric loss tangent of 0.025. The proposed antenna has been chosen to work at 2.4 GHz, which then designed, simulated and optimized. The structure of a single element circular patch antenna is shown in Fig. 2, where R represents the radius of the patch which is chosen to be 19 mm and F represents the feeding point. The procedure for designing the circular patch is illustrated below.

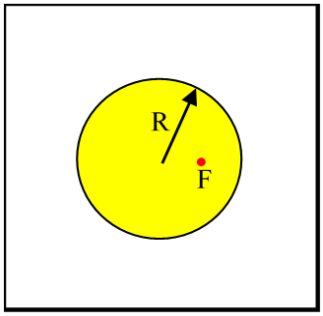

Fig. 2. Structure of the single element circular patch antenna.

The actual radius of the patch R at the resonant frequency f_0 can be calculated as in the following equations [19]:

$$f_0 = \frac{1.8412 \times V}{2\pi R\sqrt{\varepsilon_r}}, \quad (1)$$

where V is the speed of light in the Freespace. The fringing effect does not take into account when calculating the f_0 in (1). Consequently, an effective radius R_e has been considered to replace the actual radius R as:

$$R_e = R\left\{1 + \frac{2h}{\pi\varepsilon_r h}\left[ln\left(\frac{\pi R}{2h}\right) + 1.7726\right]\right\}^{0.5}. \quad (2)$$

Therefore, and based on (2), the resonant frequency of (1) can be given as:

$$f_0 = \frac{1.8412 \times V}{2\pi R_e\sqrt{\varepsilon_r}}. \quad (3)$$

Then, a first-order approximation to the solution of (2) for R is given by:

$$R = \frac{F}{\left\{1+\frac{2h}{\pi\varepsilon_r F}\left[ln\left(\frac{\pi R}{2h}\right)+1.7726\right]\right\}^{0.5}}, \quad (4)$$

where F:

$$F = \frac{8.791 \times 10^9}{f_0\sqrt{\varepsilon_r}}. \quad (5)$$

The excitation of the circular patch can be achieved by more than one technique such as a coaxial probe, a microstrip line, electromagnetic coupling or aperture coupling. A coaxial probe has been used as the feeding network of the antenna. The position of the feeding point with the patch must be equal to the characteristic impedance of the probe which is 50 Ω. The optimization tool of the CST-MWS has been used to specify the exact point which is matched the feeder characteristic impedance. It has been found that the feeding point that matches the characteristic impedance is F=7 mm from the circular patch center. The SMA connector has been mounted on the antenna back-side. Figure 2 shows the antenna feeding point. Figure 3 shows the Reflection Coefficient (S_{11}) of the designed circular patch antenna which is optimized to be < -10 dB. It is clear that the CST and HFSS simulators are giving almost the same results corresponding to the bandwidth, and deeper S_{11} for the CST at the operating frequency.

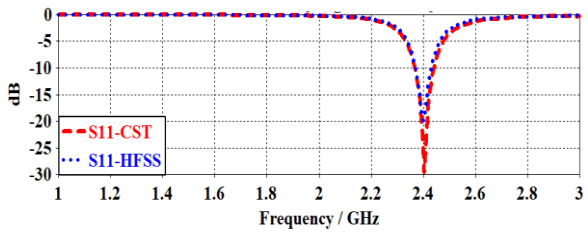

Fig. 3. S_{11} for the designed single element circular patch antenna.

B. Design of the triangular planar array

The geometry of the proposed planar array is shown in Fig. 4, the design consists of a number of single circular patch elements arranged in a right-angle triangle shaped planar array.

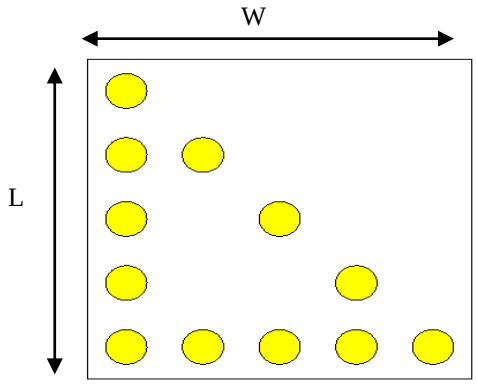

Fig. 4. Proposed planar antenna array, *W=L=312 mm*.

The design procedure of such a planar array has been divided into three steps as follows; in the first step, a single element circular patch antenna has been designed. In order to obtain the best performance, the patch has been optimized using CST built-in Trust Region Framework Algorithm. In the second step, a planar array or 5 × 5 elements are designed. Then, the active elements of the designed array have been reduced. Finally, to measure the performance, a comparison between the fully active array elements and the proposed array is presented.

C. Array configurations

A planar array of 5 × 5 circular patch antennas has been formed as shown in Fig. 5 (I). In order to keep the mutual coupling between the elements as small as possible, the spacing between any successive elements in the considered planar array is set to be as $\lambda_e/2$ in both *X* and *Y* direction, then it is optimized to have the best performance.

The main idea of this paper is to minimize the number of active elements and simplify the feeding network circuitry. Also, the performance of the designed array should be kept as close as possible to that of the fully active arrays. Thus, the removal of the active elements from the planar array has been applied in two steps. The first one is by removing the upper right six elements as in Fig. 5 (II). Then, removing another three elements from the center of the triangle as in Fig. 5 (III). The structure that is shown in Fig. 5 (III) has many important features where it consists of three sides (vertical, horizontal, and diagonal (sloped by 45 degrees)). These three sides can be used to generate different radiation patterns with different main beam direction as can be seen in the next section.

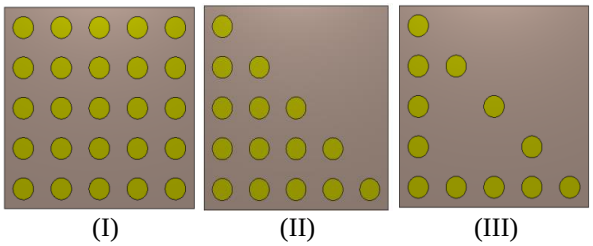

Fig. 5. Array configuration: (I) fully 5 × 5 array antenna, (II) array after removing the upper right six elements, and (III) the proposed planar antenna array.

III. SIMULATION RESULTS

Each side of the right-angle triangle shaped planar array can be considered as separate linear sub-array elements. Their corresponding radiation patterns can be configured in different directions with different polarization. The main beam directions can be switched toward any of the following three cases. In all these cases, it is worthy to mention that the directivity of the original fully active array elements (i.e., all of 25 elements in 5 × 5 array are set to be on and active) is (19.8 dB). Certainly, this value of the directivity cannot be maintained when switching OFF some of the array elements as can be seen in the following cases. The three cases have been simulated using CST then the results have been further verified using HFSS, the results show great similarities. For simplicity, the CST has been chosen to present the remaining results.

A. Case1

In this case, the lower (or horizontal) side elements of the triangle array are chosen to be active (i.e., their magnitudes are set to 1) while all other remaining elements are switched OFF as shown in Fig. 6 (see Type 3). This figure also shows two other types as shown in the second and third columns of Fig. 6. Type 1 represents an original 5 × 5 square planar array with only lower side elements were selected to be active. This type is considered here for only comparison purposes. Figure 7 shows the 2D radiation patterns of the three types.

	Type 1	Type 2	Type 3
Surface Current	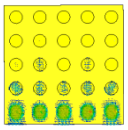	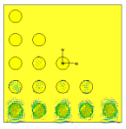	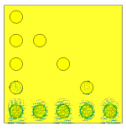
Farfield Pattern	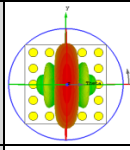	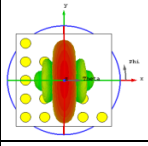	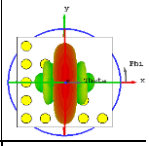
Directivity (dBi)	12.8	12.8	12.9
HPBW (Deg)	19.6	19.7	20
Efficiency (%)	92	90	89

Fig. 6. Results of Case1.

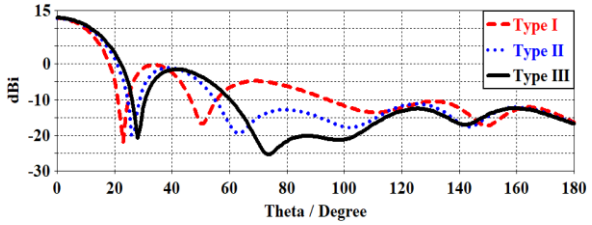

Fig. 7. The corresponding 2D radiation patterns.

From Fig. 6 and Fig. 7, it's clear that the radiation pattern of the array in type 3 is almost the same as those in type 2 and type 3. Indeed, the directivity of the three types is around 12.8 dBi and the HPBW is around 19.7˚. From this result, it can be seen that the Type 3 configuration, represents the most efficient configuration in terms of a smaller number of overall elements while maintaining the same performance. Indeed, the efficiency is perfect for the proposed array 89%, compared with the other two array types.

B. Case2

In this case, the vertical side elements of the triangle array are chosen to be active while all other remaining elements are switched OFF as shown in Fig. 8. This figure shows the various configuration and their corresponding array patterns. Again, the result of the array in Type 3 represents the cheaper design in terms of containing the smaller number of elements while achieving the same performance. In this case, the main beam direction is pointed toward 90˚. Figure 9 shows the 2D radiation patterns of the three types. The directivity of the three types is around 12.2 dBi and the HPBW is almost the same 20.1˚. Indeed, the efficiency is perfect for the proposed array 89.5%, compared with the other two array types.

	Type 1	Type 2	Type 3
Surface Current	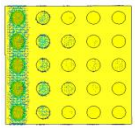	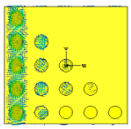	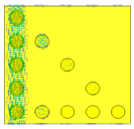
Farfield Pattern	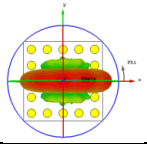	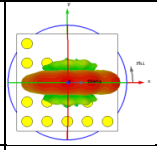	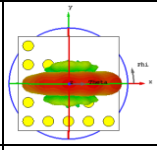
Directivity (dBi)	12.3	12.2	12.2
HPBW (Deg)	20	20.1	20.1
Efficiency (%)	93	91	89.5

Fig. 8. Results of Case2.

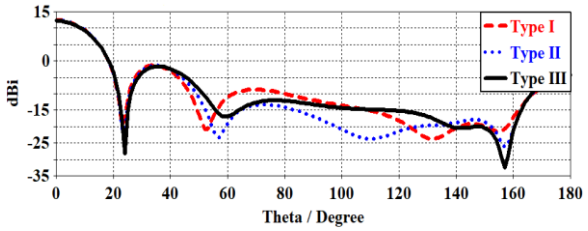

Fig. 9. The 2D radiation patterns for Case2.

	Type 1	Type 2	Type 3
Surface Current	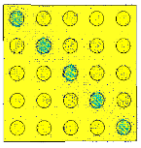	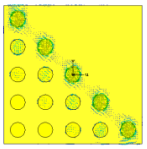	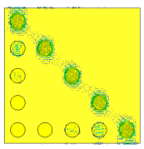
Farfield Pattern	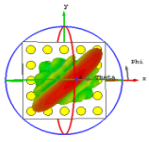	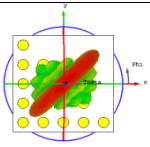	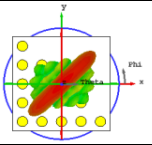
Directivity (dBi)	13.5	13.6	13.6
HPBW (Deg)	19.9	19.9	20
Efficiency (%)	90	89	88

Fig. 10. Results of Case3.

C. Case3

In this case, the elements located on the main diagonal of the triangle array are chosen to be active while all other remaining elements are switched OFF as shown in Fig. 10. Figure 11 shows the 2D radiation patterns of the three types. Again, the result of the array

in Type 3 represents the cheaper design in terms of containing the smaller number of elements while achieving the same performance as compared to the other two types. In this case, the main beam direction is pointed toward 45°. The directivity of all the types is around 13.6 dBi which is lower than that of the fully active array elements 19.1 dBi and the HPBW is almost the same 19.9°. However, this reduction comes at a profit of many advantages including a lower number of active elements and a simplified feeding network. Again, the efficiency is perfect for the proposed array 88%, compared with the other two array types.

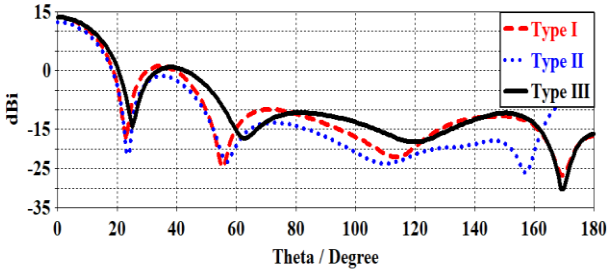

Fig. 11. The 2D radiation patterns for Case3.

From the above-mentioned three cases, it has been found that the antenna bandwidth is almost the same for the proposed antenna (Type 3) as can be seen in Fig. 12.

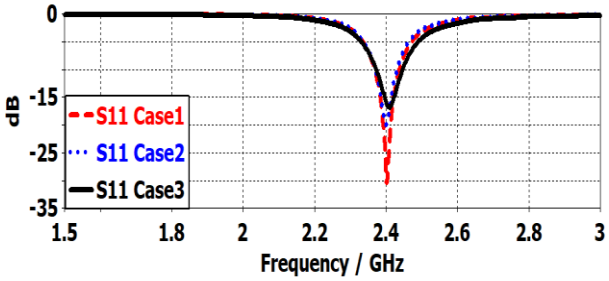

Fig. 12. S_{11} for the proposed antenna for the three cases.

Table 1: Comparison between CST and HFSS results

	Case1		Case2		Case3	
	CST	HFSS	CST	HFSS	CST	HFSS
Directivity (dBi)	12.9	12.7	12.2	12.1	13.6	13.5
HPBW (Deg)	20	20.5	20.1	20	20	19
Efficiency (%)	89	88	89.5	88	88	89

IV. DESIGN VERIFICATION WITH HFSS

To verify the proposed antenna array, the HFSS simulation program has been used. The results show great matching between the two programs in terms of Directivity, HPBW, and Efficiency. Table 1 shows the obtained values for the proposed array (Type 3) in the previous three cases using both CST and HFSS.

V. CONCLUSION

This work showed that the elements in the planar arrays could be considered as pixels, where their magnitude excitations were assigned to the values of either 1 or 0, depending on which elements need to exist at its position in the array. The pixel method can be applied to the different array configuration such as square, rectangular, triangular, or any other shape. To switch the main beam direction, only the magnitude of the selected elements can be altered from 1 to 0 or vice versa. Thus, the proposed approach needs only switches rather than phase shifters or attenuators to achieve the main beam scanning capability. Moreover, the polarization can be also easily altered from vertical to horizontal or vice versa without any mechanical movement of the array. Therefore, the proposed pixel array is simpler and cheaper to implement. Simulation results showed that the directivity and the efficiency of the proposed pixel array are almost the same as those of the fully planar array. Nevertheless, the proposed array enjoys many advantages such as a smaller number of active elements.

In the future work, the method may be further extended by using an optimization algorithm such as a genetic algorithm to optimally choose which elements should be switched OFF such that the array pattern reaches the desired configuration.

REFERENCES

[1] V. Venkateswaran, F. Pivit, and L. Guan, "Hybrid RF and digital beamformer for cellular networks: algorithms, microwave architectures, and measurements," *IEEE Transactions on Microwave Theory and Techniques*, vol. 64, no. 7, pp. 2226-2243, 2016.

[2] R. L. Haupt, *Antenna Arrays: A Computational Approach*, John Wiley & Sons, 2010.

[3] J. R. Mohammed, "Obtaining wide steered nulls in linear array patterns by controlling the locations of two edge elements," *AEU - International Journal of Electronics and Communications*, vol. 101, pp. 145-151, Mar. 2019.

[4] J. R. Mohammed, "Element selection for optimized multi-wide nulls in almost uniformly excited arrays," *IEEE Antennas and Wireless Propagation Letters*, vol. 17, iss. 4, pp. 629-632, Apr. 2018.

[5] W. S. Yoon, J. W. Baik, H. S. Lee, S. Pyo, S. M. Han, and Y. S. Kim, "A reconfigurable circularly polarized microstrip antenna with a slotted ground plane," *IEEE Antennas and Wireless Propagation Letters*, vol. 9, pp. 1161-1164, 2010.

[6] A. Kalis, A. G. Kanatas, and C. B. Paradias, *Parasitic Antenna Arrays for Wireless MIMO Systems*, Springer, New York, NY, USA, 2014.
[7] S. J. Lee, W. S. Yoon, and S. M. Han, "Planar directional beam antenna design for beam switching system applications," *Journal of Electromagnetic Engineering and Science*, vol. 17, no. 1, pp. 14-19, 2017.
[8] M. Farkharzadehet, *et al.*, "The effects of imbalanced phase shifters loss on phased array gain," *IEEE Antennas Wireless Propag. Lett.*, vol. 7, pp. 192-196, 2008.
[9] M. Gao, B. Wang, Y. Li, and B. Tian, "A novel pattern reconfigurable antenna composed of electric dipole vector antenna," *2017 International Applied Computational Electromagnetics Society Symposium (ACES)*, Suzhou, pp. 1-2, 2017.
[10] Y. Li, W. Li, and W. Yu, "A compact reconfigurable antenna using SIRs and switches for ultra-wideband and multi-band wireless communication applications," *ACES Journal*, vol. 28, no. 5, May 2013.
[11] M. Gao, B. Wang, Y. Li, and B. Tian, "A novel pattern reconfigurable antenna composed of electric dipole vector antenna," *2017 International Applied Computational Electromagnetics Society Symposium (ACES)*, Suzhou, pp. 1-2, 2017.
[12] P. Lotfi, S. Soltani, and R. D. Murch, "Broadside beam steerable planar parasitic pixel patch antenna," *IEEE Trans. Antennas and Propagation*, vol. 64, iss. 10, pp. 4519-4524, Oct. 2016.
[13] D. Akimu, D. Aliou, T. P. Le, and S. Robert, "Directive and reconfigurable loaded antenna array for wireless sensor networks," *Progress In Electromagnetics Research C*, vol. 84, pp.103-117, 2018.
[14] S.-J. Lee, W.-S. Yoon, and S.-M. Han, "Planar beam steerable parasitic array antenna system design based on the Yagi-Uda design method," *International Journal of Antennas and Propagation*, vol. 2019, Article ID 8023712, pp. 1-9, 2019.
[15] J. R. Mohammed and K. M. Younus, *Modern Printed Circuit Antennas: Radiation Pattern Synthesis of Planar Arrays Using Parasitic Patches Fed by a Small Number of Active Elements*, IntechOpen, 2019.
[16] Y. I. A. Al-Yasir, *et al.*, *Modern Printed Circuit Antennas: New Radiation Pattern-Reconfigurable 60-GHz Antenna for 5G Communications*, InTechOpen, ISBN 978-1-83880-858-7, 2019.
[17] CST Microwave Studio, ver. 2017, *CST*, Framingham, MA, USA, 2018.
[18] High Frequency Surface Structure (HFSS) (15 ed.), Available: http://www.ansys.com, 2019.
[19] C. A. Balanis, *Antenna Theory, Analysis and Design*, 4th Ed., Wiley, 2016.

Karam Mudhafar Younus was born in Mosul, Iraq, in 1986. He received the B.Eng. degree in Communication Engineering from the University of Mosul, Iraq, in 2010, and an M.Sc. degree in Communication Engineering, University of Bradford, U.K., in 2015. He is currently an Assistant-Lecturer in the Communication Engineering Department, College of Electronics Engineering, Ninevah University. His research interest includes beam steering, reconfigurable antennas, and antenna design.

Jafar Ramadhan Mohammed received the B.Sc. and M.Sc. degrees in Electronics and Communication Engineering in 1998, and 2001, respectively, and the Ph.D. degree in Digital Communication Engineering in Nov. 2009. He was a Visiting Lecturer in the Faculty of Electronics and Computer Engineering at the Malaysia Technical University Melaka (UTeM), Melaka, Malaysia in 2011 and Autonoma University of Madrid, Spain in 2013. He is currently an Assistant Professor and Vice Chancellor for Scientific Affairs at Ninevah University, Mosul. He authored more than 50 papers in international refereed journals and conference proceedings. Also, he edited the book titled "Array Pattern Optimization" published by IntechOpen in 2019. His main research interests are in the area of Digital Signal Processing and its applications, Antenna, and Adaptive Arrays. In 2011, He is listed in Marquis, Who's Who in Science and Engineering (Edition 28). In 2018, he has been selected for the Marquis Who's Who Lifetime Achievement Award.

Design and Analysis of Reactive Load Dipole Antenna using Genetic Algorithm Optimization

K. Kayalvizhi and S. Ramesh

Department of Electronics and Communication Engineering
SRM Valliammai Engineering College, Kattankulathur, Chennai - 603203, Tamil Nadu, India
kayal_sacet@yahoo.co.in, rameshs.ece@valliammai.co.in

Abstract ─ This article presents a reactive load dipole antenna and it is working in the frequency range from (10 MHz- 600 MHz). The LR Load can improve the antenna characteristics to produce maximum gain. The loads are in the combination of parallel and series LR circuits. Genetic Algorithm is used to obtain the optimum values of loads and their optimum position along the dipole. The proposed design is simulated using 3D EM CST Microwave Studio tool. In the working band, the S_{11} parameter and gain of the loaded antenna are -15.73 dB at 328 MHz and from -15 dBi at 10 MHz to 2.80 dBi at 600 MHz. An optimized reactive load dipole antenna were fabricated and tested. Good agreement were attained among the measured and simulated results.

Index Terms ─ dipole antenna, genetic algorithm, loading antenna, reactive loading.

I. INTRODUCTION

Recent advances in broadband communication system are generating a great interest in miniature, efficient and broadband antennas. Antenna designers used a lumped element to improve impedance matching and the antenna bandwidth. A loaded wire antenna can be obtained by placing reactive element on wire radiator such as bifold monopole [1], long wire stub loading [2], in order to modify the current distribution along the conductors to enhance the antenna performance. In [3], an inductor and resistor is loaded wire monopole antenna with a matching network were designed by using genetic algorithm optimization with VSWR less than 3. In [4], an antenna consists of loaded wire monopole, a sleeve pedestal and an on body matching network and they are optimized by using Genetic algorithm to enhance the system gain and increase the antenna bandwidth. In [5], presents a new technique for wideband impedance matching of short monopole antenna in HF/VHF band is designed to improve VSWR of antenna and a resistor is located between the two parts of the antenna.

Discretely loaded resistive dipoles [6], were implemented and analyzed for use of short pulse radiation and reception application. Discretely loaded Vee dipole [7], and durable 2-arm resistor cross dipole antenna [8] were designed for use of Ground penetrating Radars. In [9], a non-foster matching network using an operational amplifier is designed to reduce the reflection in resistive loaded Vee dipole antenna. In [10], to broader an antenna input impedance bandwidth, a frame work based on reactive loading using NCM is presented. In [11-13], designed a dipole with left handed topology to realize matched input impedance values and a miniaturized antenna with enriched performance. In [14], discussed about the single feed cross dipole antenna loaded with different NFPR element to implement compact polarized reconfigurable antenna which is used in wireless communication. In [15,16], investigates to achieve circular polarization operating bandwidth between of the broad band cross over dipole antenna loaded with parasitic elements will be used for broadband wireless communication system. In [17], designed a RL loaded dipole antenna by using genetic algorithm. In [18-20], present a dual polarized linear TCDA loaded with resistive loops and to achieve a wide bandwidth and low profile, a resistors were introduced in the array to reduce a ground plane interference. In [21], an antenna design method based on genetic algorithm optimization and it is applied to the wire antenna loaded with lumped components. In [22], a broadband six LR loaded dipole antenna is designed and the load values and position are optimized by using Genetic Algorithm. In [23], an antenna with resistive loading is designed on a printed circuit board and the performances were realized for pulse radiation. In [24], a planar sleeve monopole antenna is designed and its antenna performance is enhanced by using passive lumped element loading. In [25], a mode matching analysis of dipole antenna loaded with metamaterial inclusion has been examined analytically.

In this article, we consider the use of genetic algorithm optimization for a dipole antenna with matching network. The designed antenna consist of a loaded wire dipole and matching network, in which loads and matching network are optimized by the genetic algorithm in order to enhance the antenna performance. The article is prepared as follows. In Section II, it

Submitted On: December 27, 2019
Accepted On: March 18, 2020

deliberate about the antenna design. Section III, discuss about the antenna optimization, modelling and component. Section IV, discuss about results and its performance. Section V discuss about antenna fabrication and measurements results and finally conclusion of the paper are discussed in Section VI.

II. ANTENNA DESIGN

The steps for designing an initialized unloaded and optimized loaded dipole antenna, as described in Fig. 1 in detail, are summarized in the following: Design an initialized unloaded dipole antenna and it is operated over frequency range from 10 MHz - 600 MHz is simulated using 3D EM CST Microwave studio tool to evaluate the performance of S_{11} parameter, gain and radiation pattern of the antenna. The reactive load is employed in the dipole antenna to improve the antenna characteristics performance with respect to the desired frequency range. The optimized loaded and unloaded dipole antenna are symmetrical in its length (h) and diameter (D) [17]. The loaded dipole antenna is designed by using two different software's, simulation done by using 3D EM CST Microwave studio software and the load values and their position are optimized by using MATLAB Genetic Algorithm optimization technique. Then the optimized antenna parameters are updated to 3D EM CST Microwave studio software to extract the antenna performance of the simulated result.

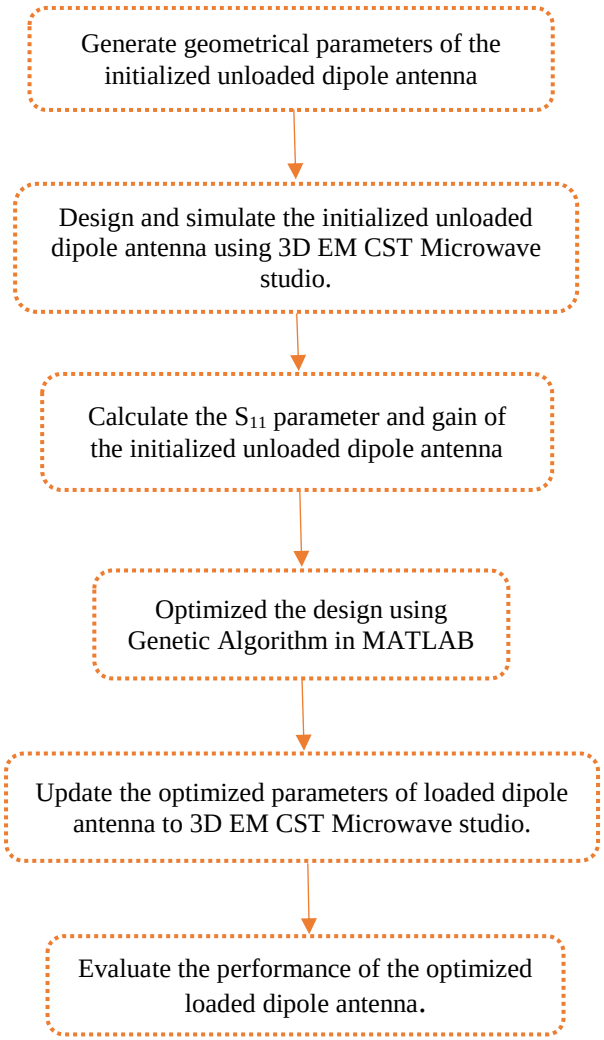

Fig. 1. Steps for designing an initialized unloaded and an optimized loaded dipole antenna.

III. GENETIC ALGORITHM BASED ANTENNA OPTIMIZATION

The Fig. 2 (a) illustrate the geometry and dimension of the unloaded dipole antenna, Fig. 2 (b) illustrates the geometry of the proposed LR loaded dipole antenna and the Fig. 2 (c) represents the geometry of the LR loaded antenna which, has a single inductor as a load 1, one parallel LR circuit for load 2, a matching network that is 1:4 impedance transformer connected to an inductor in parallel with the antenna

terminal and two series LR circuits for load 3 and load 4.The dipole length and diameter is h and D. Reactive loads of definite partition of the dipole antenna is effort to adjust the characteristics performance with esteem to a desired frequency band. Designing a loaded dipole antenna system to satisfy certain requirements generally entails the solution of a nonlinear optimization problem. The optimizer has to determine the large set of optimal parameter such as position, parameter values of the LR circuits and the element of the equivalent network.

In our design, an antenna loaded with four LR circuits and matching network involves a simultaneous optimization of parameters. The number of loads, their location and the load parameter values are specified using Genetic Algorithm Optimization. Genetic algorithm is used to solve the number of electromagnetic problem and finding optimum antenna design that maximize or minimize the certain radiation property. It is prevalent for its perception, experimentation, easiness and the competency to crack nonlinear and optimum problem.

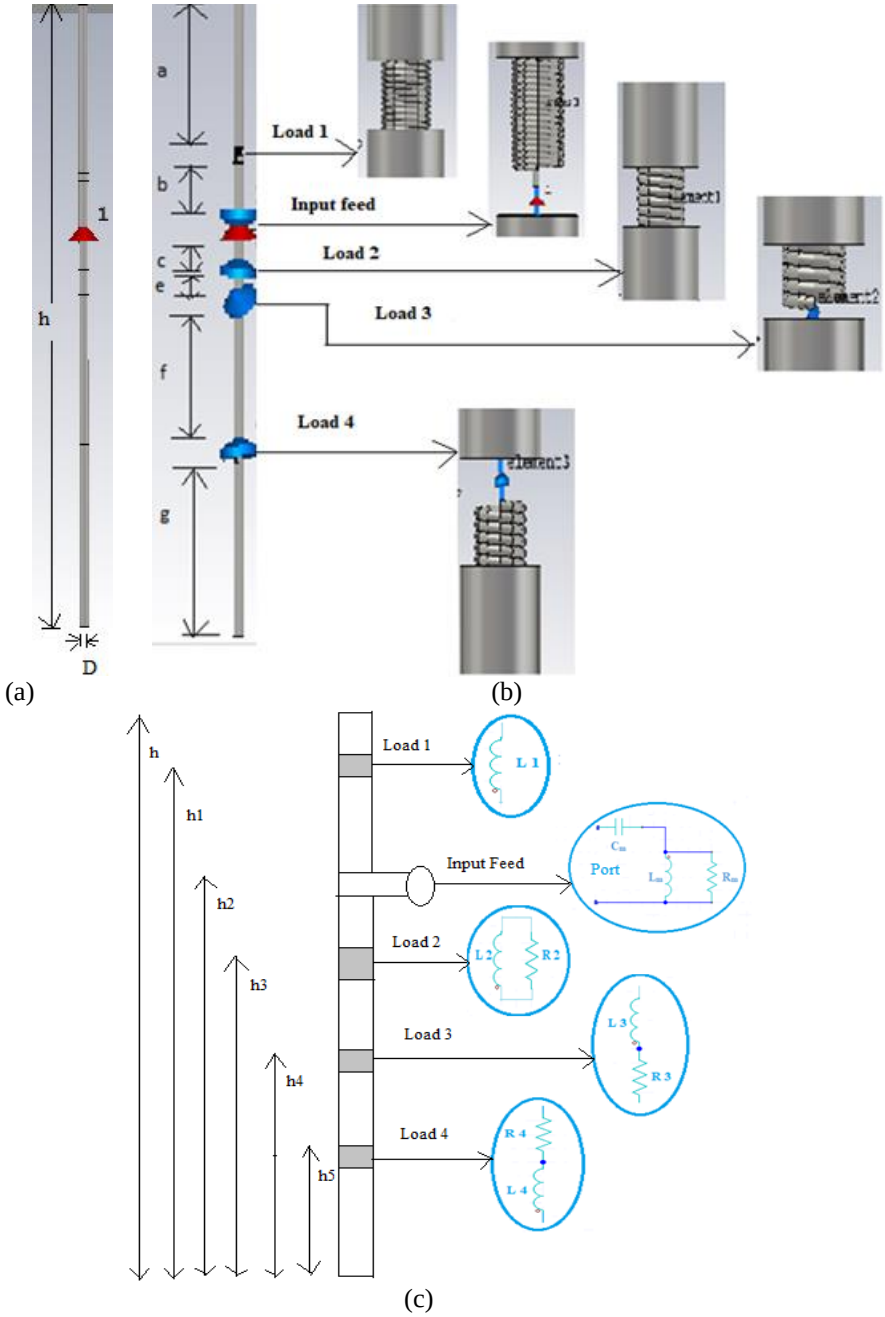

Fig. 2. Geometry of the: (a) top view of unloaded dipole antenna, (b) proposed LR loaded dipole antenna, and (c) LR loaded antenna, matching network and 1:4 impedance transformer.

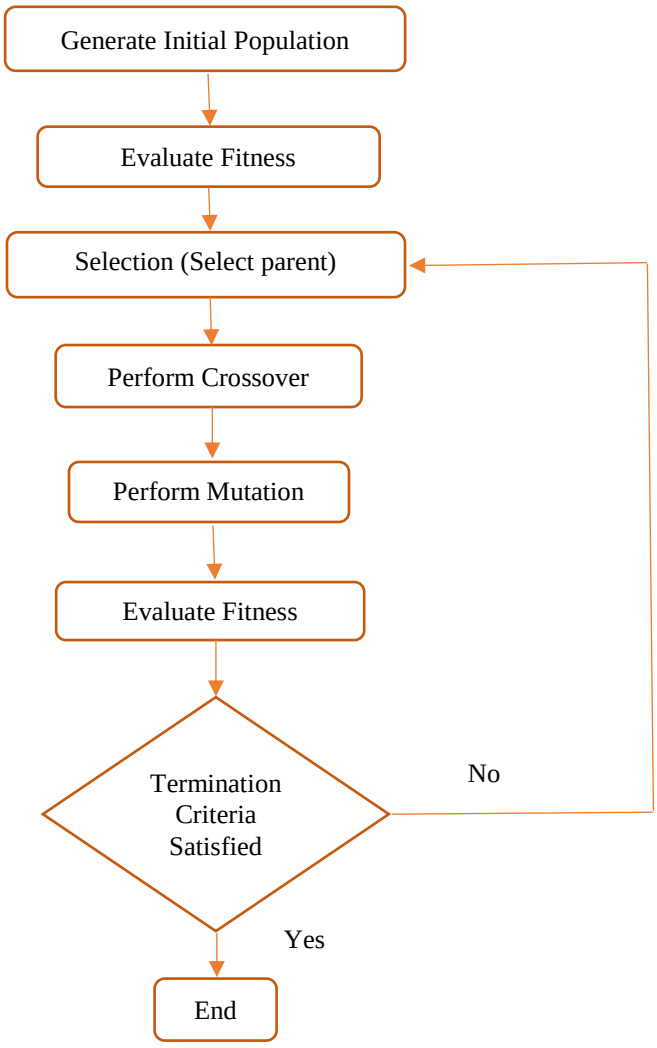

Fig. 3. A data flow for optimizing the dipole antenna using genetic algorithm optimization.

The Fig. 3 illustrate the data flow for optimizing the dipole antenna using Genetic Algorithm. The Genetic Algorithm is a search procedure and provide optimal solution by successively creating population that improve over many generation. Genes are the binary encoding of each problem variable and all the genes are referred as chromosomes. A set of chromosomes are named as population. Chromosomes are the main concern of genetic algorithm. Every chromosomes have two fragments. Segment chromosomes tagging the load position and a value chromosomes tagging the load value in genetic algorithm execution, every one of the alignment entailing N connected fragments are encrypted into 0 and 1 chromosomes. If the LR circuits positioned in any of the N fragments the identical fragments will fixed as 1 else 0. Mutation is permitted to transpire at a small possibility.

Synchronously each component value X, being either capacitance or inductance or resistance [19], is given:

$$X = X_{min} + \frac{X_{max} - X_{min}}{2^{N^X - 1}} \sum_{n=o}^{N^X} b_N^X \; 2^n \,. \qquad (1)$$

Where, N^X is a bit string:

$b_0^X \ldots b_{N^X}^X - 1$ is the binary representation of X.

X_{max} and X_{min} are the maximum and minimum value for X.

The objective function [3], is given by:

$$ObjV = \frac{1}{N_f} \sum_{n=1}^{N_f} \left[C_g w_g^{(n)} F_g^{(n)} + C_b w_b^{(n)} F_b^{(n)} \right]. \qquad (2)$$

Where, N_f is the total number of frequency samples in the selected ranges and $F_g^{(n)}$ and $F_b^{(n)}$ are the function which controlling antenna bandwidth and gain [3] is given by:

$$F_b^{(n)} = \begin{cases} 0, & \text{if } VSWR^{(n)} < B_0 \\ \frac{VSWR^{(n)} - B_0}{VSWR^{(n)}}, & \text{Otherwise} \end{cases}, \qquad (3)$$

$$F_g^{(n)} = \begin{cases} 0, & \text{if } G^{(n)} > G_0 \\ \frac{G_0 - G^{(n)}}{G_0}, & \text{otherwise} \end{cases} . \quad (4)$$

In these functions, B_0 and G_0 are frequency independent constants, VSWR has to be constrained under B_0 and gain has to be confined above G_0. $w_g^{(n)}$, $w_b^{(n)}$ are selective weights. $F_b^{(n)}$ and $F_g^{(n)}$ are indifferent part of band. Coefficient C_g and C_b are frequency independent weights.

Table 1: Parameter ranges for GA optimization of antenna

	Min	Max	# Bits	Resolution
L	0.23 µH	1.5 µH	8	0.0025 µH
R	0 Ω	1 KΩ	8	390 Ω
L_m	0.23 µH	1 µH	8	0.35 µH
R_m	0 Ω	1 KΩ	8	680 Ω
C_m	0.01 pF	50 pF	8	20 Pf

Table 2: GA settings and resulting number of objective function evaluation

Genetic Algorithm Parameters	Genetic Algorithm
Number of Individual	100
Crossover Probability	0.8
Mutation Rate	0.1
Generation Gap	0.9
Number of Generation	480

IV. RESULTS AND DISSCUSSION

Based on the Genetic algorithm optimization, the load parameter value, location and matching network element value has to be determined. Listed in Table 1 are the range and resolution of each of the ten parameters in the loaded antenna. Table 2 shows the how to set the Genetic Algorithm parameters, which include number of individual, crossover probability, mutation rate, generation gap and the number of generation. The 3D EM CST Microwave Studio tool is used for all simulation works to calculate the antenna performance.

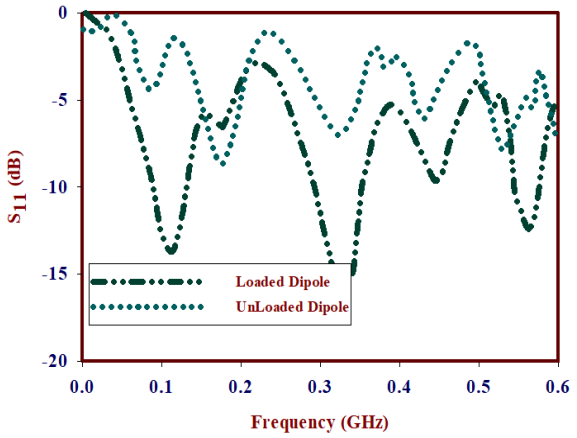

Fig. 4. Computed results comparison of S_{11} for LR loaded and unloaded dipole antenna.

The S_{11} parameter diagram of an unloaded dipole antenna is compared with LR loaded dipole antenna is shown in Fig. 4. The unloaded dipole antenna is same to the LR loaded dipole antenna with identical length and diameter. As it is shown, the prior explain the result of S_{11} parameter for loaded dipole antenna is -15.73 dB at 328 MHz [17].

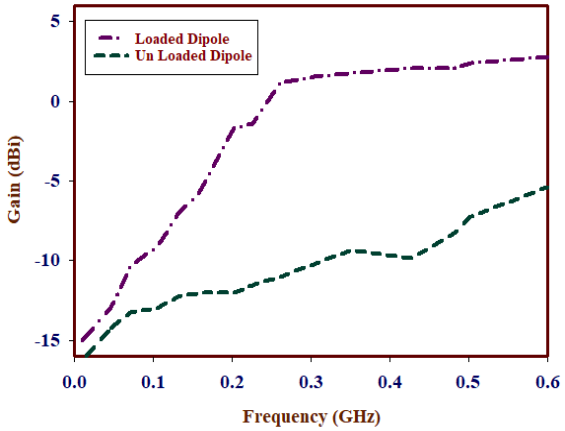

Fig. 5. Computed results comparison of gain for loaded and unloaded dipole antenna.

The Fig. 5 which illustrate the computed gain of loaded and unloaded dipole antenna. The gain of unloaded dipole antenna is decreases at higher frequencies. This problem can be solved by Genetic Algorithm optimization of the antenna profile and these drops at higher frequencies are considerably increased in the loaded dipole antenna. The maximum value for antenna gain can be achieved at higher frequencies and in this case at 600 MHz. For this loaded dipole antenna gain is gradually increasing from -15 dBi at 10 MHz to 2.80 dBi at 600 MHz.

V. ANTENNA FABRICATION AND MEASUREMENT RESULTS

Table 3 shows the antenna parameter values for the Genetic Algorithm optimization. The resulted load parameter are presented in Fig. 2 (b). A loaded dipole antenna is fabricated from the thin wall copper tubing with 10 mm diameter are shown in Fig. 6. In the antenna, the helical coil can be modeled as a series of parallel wire loops and the coil used in this article were constructed by winding 14 American Wire Gauge (AWG) wire with 2 mm diameter. The ½ W resistors were used in the LR circuits. The loads for the numerical design of Table 1 were constructed based on the optimization algorithm.

Table 3: Parameter values for the Genetic Algorithm optimization of dipole antenna and matching network of Fig. 2. (h = 169 cm, D = 10 mm, a = 40 cm, b = 13 cm, c = 6 cm, e = 3 cm, f = 35 cm, g = 40 cm, h1 =129.1cm, h2=110.9 cm, h3=96.9 cm, h4 = 88.8 cm, h5 = 47.8 cm)

Load Parameters	**Load 1**	**Input**	**Load 2**	**Load 3**	**Load 4**
Load position (cm)	6.10	8	5.10	6	7.8
No. of turns	5	18	4.5	6	6
Winding Gauge (AWG)	14	14	14	14	14
Core material	Air	Air	Air	Air	Air
Wire diameter (mm)	2	2	2	2	2
Coil diameter (mm)	9.8	13	9.8	9.8	20.4
Length of the coil (mm)	19	35	13.2	15	15
Resistor value	-	680 Ω	390 Ω	56 Ω	390 Ω
Capacitor value	-	20 pF	-	-	-

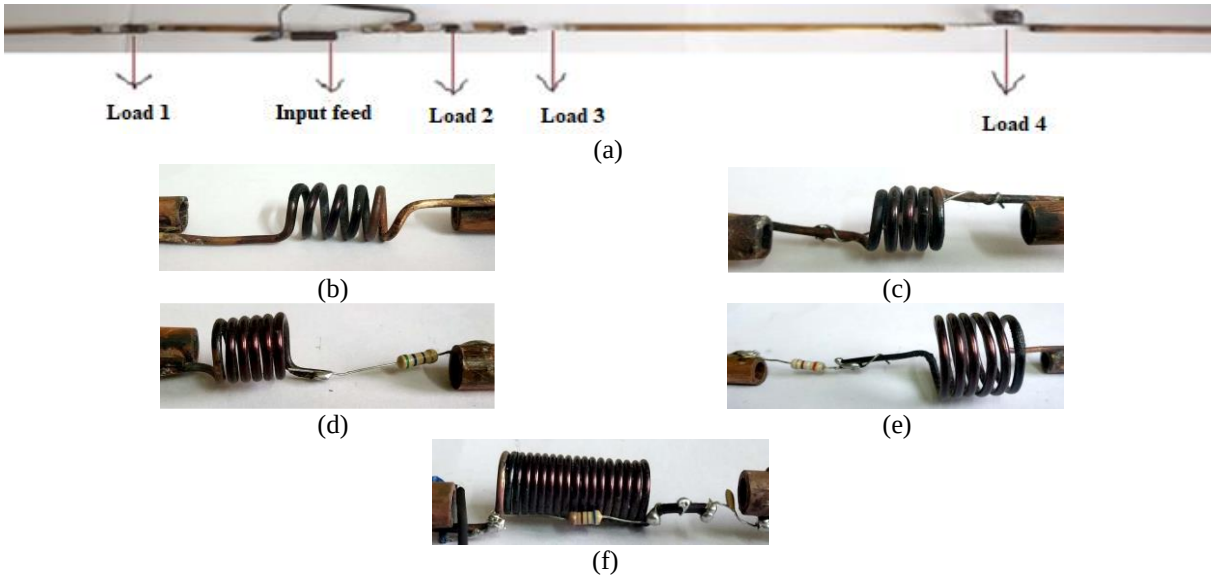

Fig. 6. Fabricated Loaded Dipole Antenna, (a). Antenna with load which listed in the Table 3, (b). Load 1, (c). Load 2, (d). Load 3, (e). Load 4 and (f). Input feed.

A prototype of loaded dipole antenna is shown in Fig. 6 (a). In Load 1 the inductor was realized in air core coil made up of 6 turns of 14 AWG wire with 2 mm diameter which is shown in Fig. 6 (b). In Load 2, the inductor and resistor are in parallel .The inductor that was realized in air core coil made up of 4 turns of 14 AWG wire with 2 mm diameter, which is shown in Fig. 6 (c). In Load 3 and Load 4 the inductor and resistor are in series, in which inductor was apprehended in air core and coil is made up of 6 turns of 14 AWG wire with 2 mm diameter, which is shown in Fig. 6 (d) and 6 (e).The input feed region is shown in Fig. 6 (f), which consists of balun and 1:4 impedance transformer. The S_{11} parameter and gain of the loaded dipole antenna were measured.

The measured and computed results of S_{11} parameter and gain for the proposed antenna is shown in Fig. 7 and Fig. 8. The good agreement was achieved between measured and computed results. As a result the measured antenna operate in 10 MHz – 600 MHz. Moreover the antenna gain has a maximum gain of 2.80 dBi at 600 MHz while minimum gain -15 dBi at 10 MHz [17].

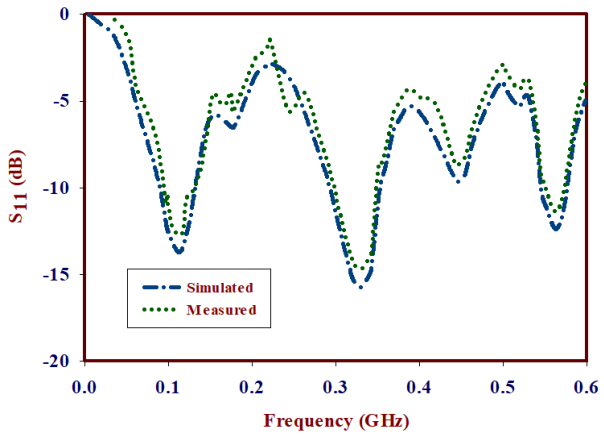

Fig. 7. Comparison of S_{11} parameter for the proposed dipole antenna.

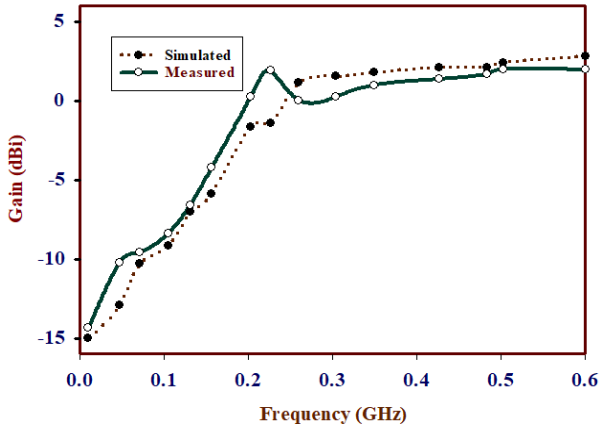

Fig. 8. Comparison of gain for the proposed dipole antenna.

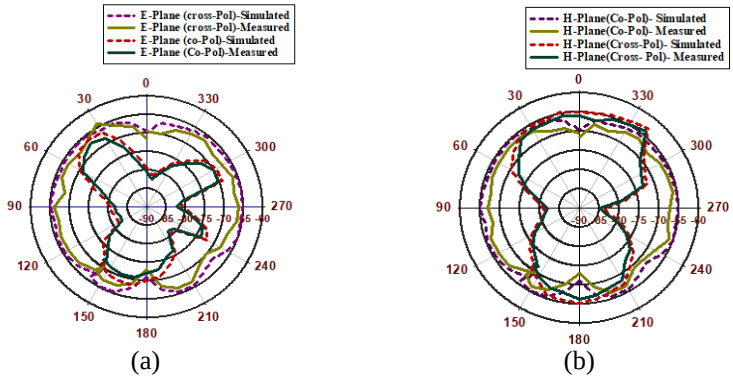

Fig. 9. Measured and computed radiation pattern for proposed dipole antenna at frequency of 305 MHz: (a) XZ plane and (b) YZ Plane.

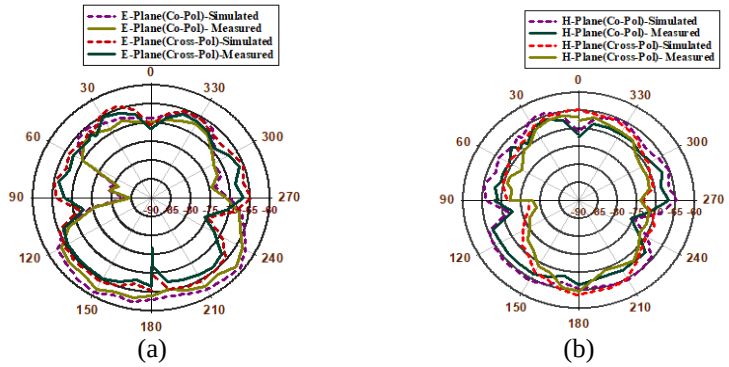

Fig. 10. Measured and computed radiation pattern for proposed dipole antenna at frequency of 600 MHz: (a) XZ plane and (b) YZ Plane.

The measured and computed radiation pattern in the E-plane and H-plane of dipole antenna in two selected frequencies (305 MHz and 600 MHz) are shown in Figs. 9 and 10.The results demonstrate both in co-polarization (Co-pol) and cross- polarization (Cross-pol). Thus it can be seen that the loaded dipole antenna radiation patterns are almost omni-direction in H-Plane and the maximum gain is also at the horizontal radiation direction

VI. CONCLUSION

In this article, a Genetic Algorithm is used to optimize a HF/VHF/UHF antenna for improving gain of

straight wire dipole antenna loaded with single inductor, one parallel LR circuit and two series LR circuits and it is driven through an equivalent network. Guided by optimization and realization techniques discussed, the authors constructed dipole antenna system with gain from -15 dBi at 10 MHz to 2.80 dBi at 600 MHz. A reactive loaded dipole antenna is fabricated and measured, which shows good agreement with simulated results. The designed antenna can be used in Portable Applications.

ACKNOWLEDGEMENT

The authors wish to acknowledge DST-FIST supporting department of Electronics and Communication Engineering, SRM Valliammai Engineering College, Chennai, Tamil Nadu for Measurement Support.

REFERENCES

[1] L. Mattioni and G. Marrocco, "Design of a broadband HF antenna for multimode naval communication-Part II: Extension on VHF/UHF ranges," *IEEE Antennas Wireless Propagation Letters*, vol. 6, pp. 83-85, 2007.

[2] P. L. Werner, Z. Bayraktar, B. Rybicki, D. H. Werner, K. J. Schlager, and D. Linden, "Stub-loaded long-wire monopoles optimized for high gain performance," *IEEE Transactions on Antennas and Propagation*, vol. 56, no. 3, pp. 639-645, 2008.

[3] X. Ding, B. Z. Wang, G. Zheng, and X. M. Li, "Design and realization of a GA-optimized VHF/UHF antenna with 'on-body' matching network," *IEEE Antennas Wireless Propagation Letters*, vol. 9, pp. 303-306, 2010.

[4] S. D. Rogers, C. M. Butler, and A. Q.Martin, "Design and realization of GA-optimized wire monopole and matching network with 20:1 bandwidth," *IEEE Transaction on Antennas and Propagation*, vol. 51, no. 3, pp. 493-502, 2003.

[5] M. KarimiMehr and A. Agharasouli, "A miniaturized non-resonant loaded monopole antenna for HF-VHF band," *International Journal of Scientific & Engineering Research*, vol. 8, no. 4, pp. 1092-1096, 2017.

[6] W. Kang, K. Kim, and I. Kim, "Implementation and analysis of discretely loaded resistive dipoles using planar resistor technology," *IEEE Transactions on Antennas and Propagation*, vol. 63, no. 11, pp. 5088-5093, 2015.

[7] K. Kim and W. R. Scott Jr., "Design and realization of a discretely loaded resistive Vee dipole for ground-penetrating radars," *Radio Science*, vol. 39, pp. 1-9, 2004.

[8] E. Noh, J. Kang, B. Kim, S. Choi, and K. Kim, "Durable 12-arm resistive cross-dipole for use in ground-penetrating radar," *IET Journals & Magazines*, vol. 53, pp. 1235-1236, 2017.

[9] H. Yang, I. Kim, and K. Kim, "Non-foster matching of a resistively loaded Vee dipole antenna using operational amplifiers," *IEEE Transactions on Antennas and Propagation*, vol. 64, no. 4, pp. 1477-1482, 2016.

[10] E. A. Elghannai, B. D. Raines, and R. G. Rojas, "Multiport reactive loading matching technique for wide band antenna applications using the theory of characteristic modes," *IEEE Transactions on Antennas and Propagation*, vol. 63, no. 1, pp. 261-268, 2015.

[11] H. Iizuka and P. S. Hall, "Left-handed dipole antennas and their implementations," *IEEE Transaction on Antennas and Propagation*, vol. 55, no. 5, pp. 1246-1253, 2007.

[12] W.-P. Cao, L. Shafai, B.-Z. Wang, S.-M. Li, and B.-B. Li, "A small and bandwidth-extended dipole antenna with nonperiodic left-handed transmission line loading," *IEEE Antennas and Wireless Propagation Letters*, vol. 13, pp. 1019-1022, 2014.

[13] L. Borja, "Dipole antenna with left-handed loading operating at a zero order mode," *Progress in Electromagnetics Research C*, vol. 19, pp. 85-92, 2011.

[14] S. X. Ta, "Polarizations of crossed-dipole antenna loaded with different NFRP elements," *Progress in Electromagnetics Research M*, vol. 75, pp. 131-140, 2018.

[15] L. Chang, L. L. Chen, J. Q. Zhang, and D. Li, "A broadband dipole antenna with parasitic patch loading," *IEEE Antenna and Wireless Propagation Letters*, vol. 17, pp. 1717-1721, 2018.

[16] G. Feng, L. Chen, X. Wang, X. Xue, and X. Shi, "Broadband circularly polarized crossed bowtie dipole antenna loaded with parasitic elements," *IEEE Antenna and Wireless Propagation Letters*, vol. 17, pp. 114-117, 2018.

[17] N. Amani, A. Jafargholi, and R. Pazoki, "A broadband VHF/UHF loaded dipole antenna in the human body," *IEEE Transaction on Antennas and Propagation*, vol. 65, no. 10, pp. 5577-5582, 2017.

[18] S. Ramesh and T. Rama Rao, "Dielectric loaded exponentially tapered slot antenna for wireless communication at 60 GHz," *Progress in Electromagnetics Research*, vol. 38, pp. 43-54, 2013.

[19] H. Zhang, S. Yang, S. Xiao, M. Huang, L. Zhou, Y. Chen, and S. Qu, "A compact wideband dual-polarized linear array with hybrid structure and resistive loadings," *International Journal of RF and Microwave Computer-Aided Engineering*, pp. 1-10, 2019.

[20] S. Ramesh and T. Rama Rao, "Indoor radio link characteristics wireless communication utilizing dielectric loaded exponentially tapered slot antenna," *Taylor & Francis-Journal of Electromagnetic Waves and Applications*, vol. 29, no. 4,

pp. 551-564, Apr. 2015.
[21] A. Boag, A. Boag, E. Michielssen, and R. Mittra, "Design of electrically loaded wire antenna using genetic algorithm," *IEEE Transactions on Antennas and Propagation*, *vol.* 44, no. 5, pp. 687-696, 1996
[22] M. Bod, M. Ahmadi-Boroujeni, and K. Mohammadpour-Aghdam, "Design of a low-cost broadband loaded dipole antenna for VHF/UHF frequency range," *IET Microwaves, Antennas & Propagation*, vol. 13, pp. 1983-1988, 2019.
[23] W. Kang and K. Kim, "Design and implementation of complementary dipoles with continuous resistive loading," *Journal of Electromagnetic Waves and Applications*, pp. 1583-1595, 2017.
[24] Y. Xia, Y. Li, and W. Xue, "A low profile miniaturization low frequency wideband antenna using passive lumped elements loading," *ACES Journal*, vol. 35, no. 1, pp. 31-37, Jan. 2020.
[25] A. Jafargholi and M. Kamyab, "Fullwave analysis of loaded dipole antenna using mode matching theory," *ACES Journal*, vol. 26, no. 11, pp. 915-921, Nov. 2011.

K. Kayalvizhi received the B.E. degree in Electronics and Communication Engineering from Shri Angalamman College of Engineering and Technology, Trichy, in 2009, and M.E. degree in Communication Systems from Saranathan College of Engineering, Trichy, in 2011. She is currently pursuing the Ph.D. degree at Anna University, Chennai. Her current research interests include Antennas and Wireless Communication.

S. Ramesh received his B.E. in Electronics and Communication Engineering from University of Madras, M.Tech. in Communication Engineering from VIT University, Vellore and received his Ph.D. degree on from SRM University, Chennai, in 2001, 2004 & 2015 respectively. He is currently, working as an Associate Professor in the Department of Electronics and Communication Engineering, SRM Valliammai Engineering College, Chennai with experience of 16 years. He is a senior member (S'10-M'17-SM'18) of IEEE Antennas & Propagation Society, Life member in IETE, ISTE, SEMCE, BES. He authored papers in reputed journals and international/national conferences. His area of interest includes Antennas & Propagation and Wireless Communications. He is guiding research scholars in the field of antennas & RF Filter under Anna University, Chennai. He is associated with IEEE AP-S Madras chapter as a member in executive committee during 2018-2019 and IEEE MTT-S Madras Chapter for the year 2017.

A Design of OAM Metal-only Transmitarray Antenna Using High-Transmission Slot-Type Jerusalem Elements

Li Yu [1,2,3], Xiuping Li [1,2,3], Hua Zhu [1,2,3], and Zihang Qi [1,2,3]

[1] School of Electronic Engineering Beijing University of Posts and Telecommunications, Beijing, 100876, China

[2] Key Laboratory of Universal Wireless Communications Ministry of Education
Beijing University of Posts and Telecommunications, Beijing

[3] Beijing Key Laboratory of Work Safety Intelligent Monitoring
Beijing University of Posts and Telecommunications, Beijing 100876, China
hi_yuli@163.com, xpli@bupt.edu.cn, judy-cool@163.com, qizihang@bupt.edu.cn

Abstract ─ In this paper, an orbital angular momentum transmitarray antenna based on high-transmission slot-type Jerusalem elements is proposed. The equivalent circuit model of the proposed element is analyzed by the transmission line theory. Theoretical results calculated by MATLAB show that a four-layer element with non-identical layers can realize a similar phase range and a much higher transmission efficiency as that with identical layers. Using this method, the transmission magnitude is greater than −0.45 dB within a 360° transmission phase range. Based on the proposed element, a round aperture orbital angular momentum transmitarray composed of 648 elements is designed and simulated by HFSS. The results confirm that orbital angular momentum waves with l=+1 are successfully generated. The divergence angle and maximum gain are about 6° and 19.2 dBic, respectively. And the aperture efficiency with l=+1 is 11.3%.

Index Terms ─ High-transmission, metal-only, orbital angular momentum (OAM), transmitarray, transmission line theory.

I. INTRODUCTION

In recent years, wireless communication technology has been developed rapidly, which poses unprecedented challenges to the limited spectrum resources. As a new method to improve the spectrum efficiency, orbital angular momentum (OAM) [1-3] has aroused extensive attention, which has infinite eigen modes with transmission orthogonality.

To date, fruitful methods for generating OAM waves have been continuously proposed, such as spiral phase plates [4], parabolic antennas [3], and circular array antennas [5]. However, due to the disadvantages such as large size, complex structure, high cost, and narrow bandwidth, their further development and application are restricted. Recently, transmitarray antennas [6] have gradually become a hot candidate for OAM generation, which combine optical theory and array synthesis theory. By adjusting the transmission phase of each element in the array, the spherical waves radiated by the feed source can be converted into OAM waves in a specific direction.

In [7], a planar spiral phase plate composed of double-layer split-ring transmitarray elements was proposed to generating OAM waves with l=+1. In [8], a transmitarray was designed to generated dual-mode OAM beam waves, which implemented the elements formed by two dual-polarized wideband microstrip antennas. In [9], a transmitarray for generating OAM beam waves was proposed by employing three-layer elements. Although these transmitarray antennas have successfully produced OAM waves, the element transmission loss of these transmitarray is up to 1 dB, even 3.9 dB, which may deteriorate the antenna radiation performance. Thus, it is necessary to design an OAM transmitarray with ultralow transmission loss.

In this paper, an OAM meta-only transmitarray antenna is presented by employing high-transmission slot-type Jerusalem elements with non-identical layers. The impedance matching condition based on the transmission line theory is applied to the element design, and hence a complete 360° transmission phase range with low transmission loss is obtained. An antenna prototype is designed, and simulated. The results confirm that OAM waves with l=+1 is successfully generated.

II. HIGH-TRANSMISSION ELEMENT DESIGN

A. Design principle

Inspired by [10], a general model of the four-layer element with non-identical layers which is described as

Submitted On: November 29, 2019
Accepted On: February 23, 2020

a combination of four metal layers and three dielectric layers with dielectric constant of ε_r, as shown in Fig. 1 (a). Metal layer 1 and 4 are the same, while metal layer 2 and 3 are the same. To simplify analysis, metal layers 1, 4 and 2, 3 are modelled as normalized pure susceptance jb_1 and jb_2, respectively. And the dielectric layers between two metal layers are modelled as the transmission line with the characteristic admittance of Y_1/Y_0 and the length of d_1, d_2 and d_3, respectively, as presented in Fig. 1 (b). Y_0 and Y_1 are the normalized characteristic admittance of free space and the dielectric layer, respectively. In addition, the air on the top and bottom sides of the four-layer element are equivalent to normalized susceptance Y_s and Y_L, respectively, and $Y_s = Y_L = 1$.

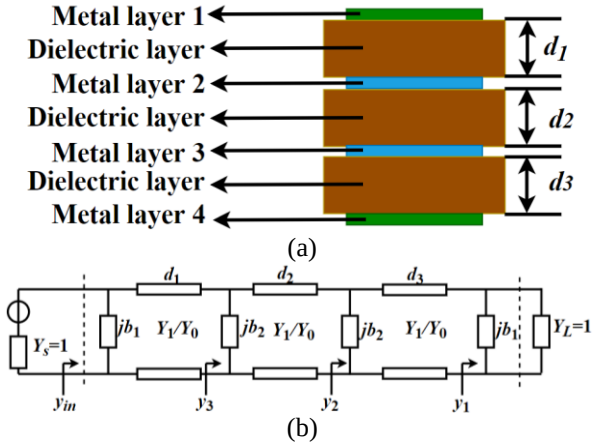

Fig. 1. The four-layer element: (a) the general model, and (b) the equivalent circuit model.

In the above design, according to the transmission line theory, it can be obtained:

$$y_1 = 1 + jb_1, \tag{1}$$

$$y_2 = (Y_1/Y_0) * \frac{y_1 + j(Y_1/Y_0)\tan(\beta d_3)}{(Y_1/Y_0) + jy_1\tan(\beta d_3)} + jb_2, \tag{2}$$

$$y_3 = (Y_1/Y_0) * \frac{y_2 + j(Y_1/Y_0)\tan(\beta d_2)}{(Y_1/Y_0) + jy_2\tan(\beta d_2)} + jb_2, \tag{3}$$

$$y_{\text{in}} = (Y_1/Y_0) * \frac{y_3 + j(Y_1/Y_0)\tan(\beta d_1)}{(Y_1/Y_0) + jy_3\tan(\beta d_1)} + jb_1, \tag{4}$$

$$\beta = \omega\sqrt{\mu_0\varepsilon_0\varepsilon_r}, \tag{5}$$

$$Y_1 = \sqrt{\mu_0/\varepsilon_0\varepsilon_r}, \tag{6}$$

$$Y_0 = \sqrt{\mu_0/\varepsilon_0}. \tag{7}$$

Where μ_0 and ε_0 are the dielectric constant and permeability in the free space. When $y_{in} = y_s = 1$, the impedance matching condition is satisfied. Assume that $d_1 = d_2 = d_3 = \lambda_0/4$ and ε_r=1 (λ_0 is the wavelength at center frequency), i.e., the dielectric layer is filled with air, then the relationship between b_2 and b_1 can be obtained:

$$b_2 = \left\{ {Y_1}^2 b_1 \pm jY_1 \left[-\left({Y_1}^2 - \left(Y_0 {b_1}^2 + Y_0 \right) \right)^{1/2} \right] \right\} / \left({Y_0}^2 {b_1}^2 + {Y_0}^2 \right). \tag{8}$$

The transmission matrix of the normalized equivalent circuit between the dashed line in Fig. 1 (b) can be written as a cascade form of transmission matrices of a plurality of two-port networks, as follows:

$$\begin{bmatrix} a & b \\ c & d \end{bmatrix} = \begin{bmatrix} 1 & 0 \\ jb_1 & 1 \end{bmatrix}^2 \begin{bmatrix} 1 & 0 \\ jb_2 & 1 \end{bmatrix}^2 \begin{bmatrix} 0 & j\frac{Y_1}{Y_0} \\ j\frac{Y_0}{Y_1} & 0 \end{bmatrix}^3, \tag{9}$$

$$S_{21} = \frac{2}{a + b + c + d}. \tag{10}$$

Then the transmission magnitude and the corresponding transmission phase are calculated by equation (9) and (10) in MATLAB, as shown in Fig. 2. Since there is no linear relationship between b_1 and b_2, there are two matching trajectories. One matching trajectory is with $|b_1|$ lower than 2 and $|b_2|$ lower than 0.58 and another is with $|b_1|$ lower than 2 and $|b_2|$ lower than 1.5, which form the red area in Fig. 2 (a). Seen from Fig. 2 (c), a 360° phase range with transmission magnitude greater than −0.45 dB is achieved. Thus, it is necessary to design a one-layer structure whose equivalent susceptance b can cover the variation range from -2 to 2.

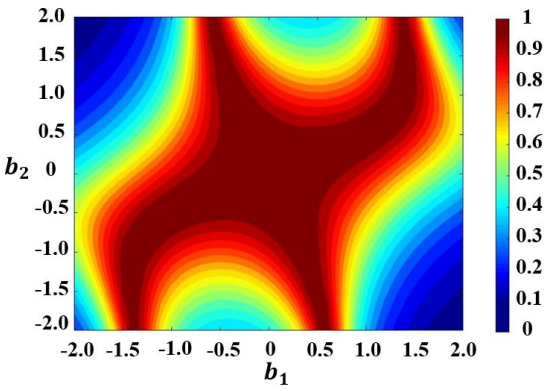

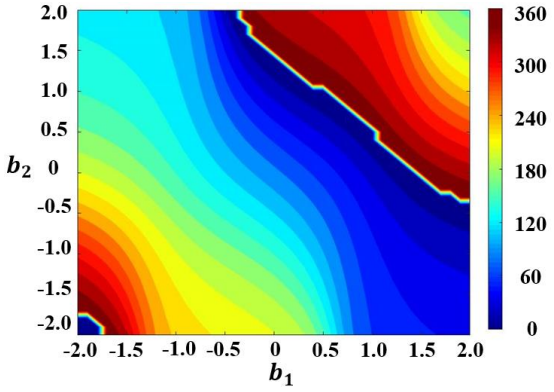

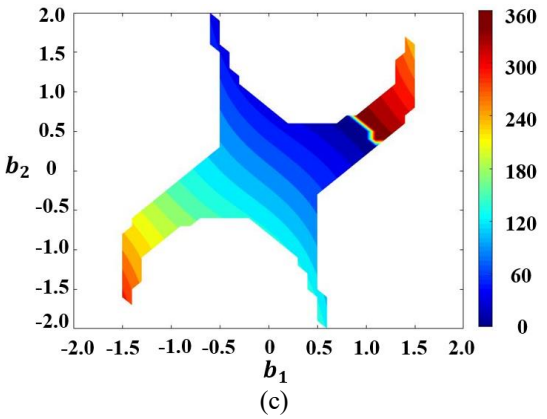

(c)

Fig. 2. The transmission characteristic of four-layer elements calculated by MATLAB: (a) transmission magnitude, (b) transmission phase, and (c) transmission phase for magnitude > - 0.45 dB.

B. Element design

Due the advantages of the metal-only structure [11], such as low cost and low loss, a metal-only slot-type Jerusalem metal layer etched on the 0.2 mm aluminum plate is designed, as shown in Fig. 3 (a). The operation frequency is 6 GHz and the period are 15 mm ($0.3\lambda_0$). Full wave electromagnetic simulation software (HFSS) is used to analyze the proposed metal layer which is surrounded by the periodic boundary conditions and illuminated by Floquet port. The capacitive and inductive equivalent susceptance can be realized by changing the size of the designed metal layer. As plotted in Fig. 3 (b), it can be seen that the equivalent susceptance changes from -3.3 to 2.3 when L varies from 11 mm to 14.5 mm, which meet the design requirements of the metal layer.

The simulation of the proposed element composed of four non-identical slot-type Jerusalem metal layers is also conducted in HFSS. The element is divided in two groups, the middle two layers form a group, and the other two layers form another group, as shown in Fig. 4. The structures in two group are exactly the same, but the sizes are different. In this design, d=$\lambda_0/4$, p = 15 mm, $a_1 = 0.8 \times L_1$, $a_2 = 0.8 \times L_2$, s = 2 mm, w = 1 mm. And L_1 and L_2 range from 12 to 14 mm with a step size of 0.1 mm. The transmission coefficient distribution when L_1 and L_2 change from 12 to 14 mm is shown in Fig. 5, it can be concluded that the proposed element is able to cover the transmission phase range of 360° with transmission amplitude greater than -0.45 dB.

To investigate the difference between the transmission characteristics of elements obtained by equivalent circuit model in MATLAB and that obtained by full wave simulation in HFSS, some elements with different sizes are picked out, as shown in Table 1. Obviously, the transmission magnitude and phase obtained by full wave simulation in HFSS are slightly different from that obtained by equivalent circuit model in MATLAB. This is because the input impedance of the one-layer slot-type Jerusalem element may not be ideal pure susceptance, and the existence of conductance will lead to the increase in transmission loss.

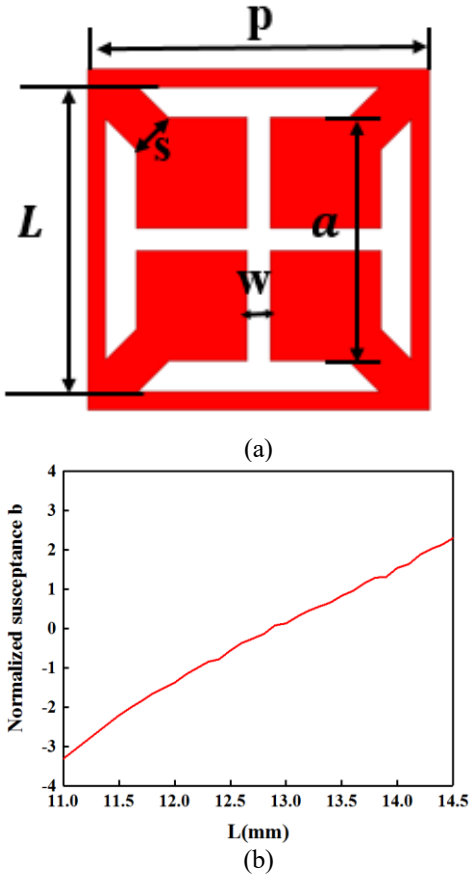

(a)

(b)

Fig. 3. The slot-type Jerusalem metal layer: (a) the model and (b) the equivalent susceptance *b* versus L.

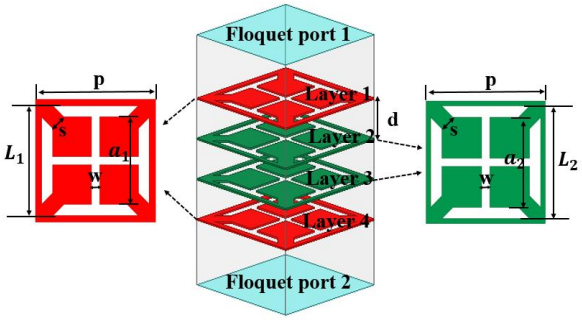

Fig. 4. The structure of the designed element.

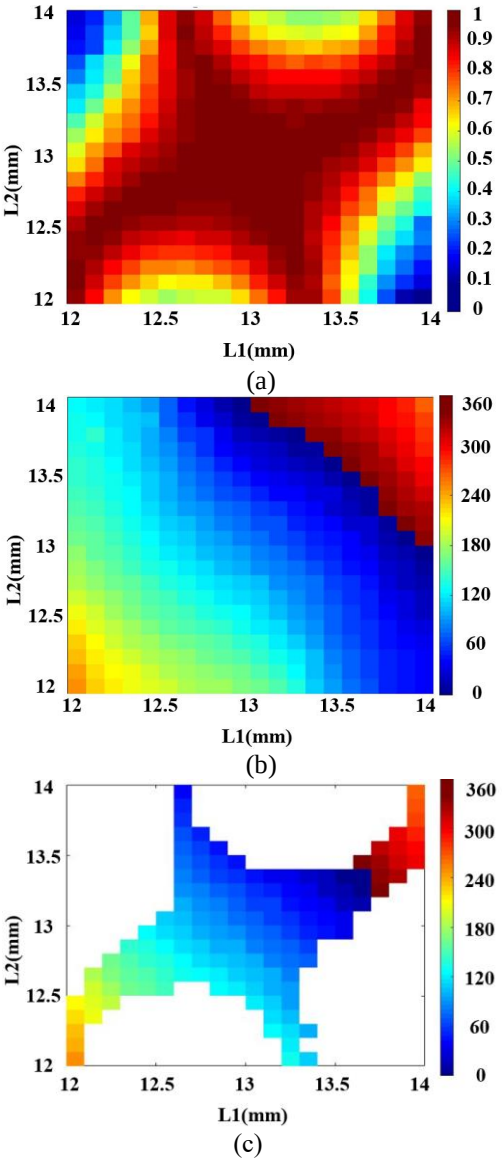

Fig. 5. The transmission coefficient of the proposed element when L_1 and L_2 change from 12 to 14 mm: (a) transmission amplitude distribution, (b) transmission phase distribution, and (c) transmission amplitude > -0.45 dB.

In particular, for OAM transmitarray antenna, because the far field radiation pattern of 3-bit quantization transmitarray is very close to the continuous ones [12], these eight elements in Table 1 are sufficient to form a transmitarray. Thus, to reduce the simulation time, in actual design, the theoretical dimension values L_1 and L_2 to achieve desired phase can be obtained by the corresponding relationship between dimension size and equivalent susceptance value in Fig. 3 (b), where the equivalent susceptance value is calculated by equivalent circuit model in MATLAB. Then the full wave simulation analysis of the designed element is carried out in HFSS.

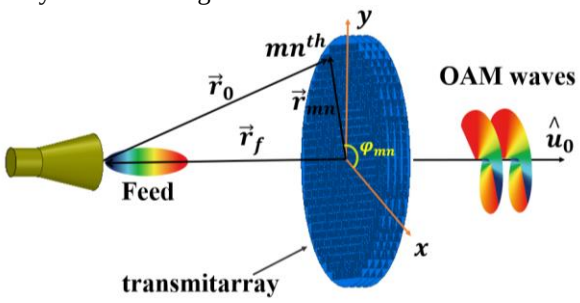

Fig. 6. The schematic of OAM transmitarray antenna.

Table 1: The transmission characteristics of some elements

	Circuit Model				Full-wave Simulation	
	b_1	b_2	$\lvert S_{21}\rvert$ (dB)	Phase (deg)	$\lvert S_{21}\rvert$ (dB)	Phase (deg)
1	0.5	1.0	0	0	-0.12	3.1
2	0.1	0.6	-0.09	48.8	-0.15	49.4
3	0	0	0	90	-0.09	90.2
4	-0.3	-0.5	0	136.4	-0.11	140.4
5	-0.5	-1	0	180	-0.12	178.4
6	-1	-1.2	0	222.6	-0.45	222.2
7	-1.5	-1.4	0	272.3	-0.23	272.2
8	0.9	1.3	0	312.7	-0.19	301.6

III. OAM TRANSMITARRAY DESIGN

Consider a planar circular aperture transmitarray that are illuminated by a horn at position vector $\vec{r}_f$, as shown in Fig. 6. $\vec{r}_{mn}$ is the position vector of the mn^{th} element, l is the desired OAM mode number which can be an arbitrary integer, and $\varphi(x_{mn}, y_{mn})$ is the azimuth angle of the mn^{th} element. To generate OAM beam waves, the phase compensation can be accomplished by varying the transmission phase $\phi(x_{mn}, y_{mn})$ of each element, which can be calculated as follows:

$$\phi(x_{mn}, y_{mn}) = k_0\left[\left|\vec{r}_{mn} - \vec{r}_f\right| - \vec{r}_{mn} \cdot \hat{u}_0\right] + l\varphi(x_{mn}, y_{mn}). \quad (11)$$

Based on the proposed element and the phase compensation equation (11), a transmitarray with circular aperture composed of 648 elements is designed to generate OAM beam waves with l=+1. $\hat{u}_0 = (0°, 0°)$ and a left-hand circular polarization horn antenna whose E-plane pattern can be represented as $cos^{8.5}\theta$ at 6 GHz is used as a feeding source. Its maximum gain is 15.2 dBi. And the distance between the phase center of the horn and transmitarray is about 490 mm. The corresponding phase distribution of the designed transmitarry is shown in Fig. 7.

Table 2: The comparison of the proposed antenna with other published designs

Refs.	Frequency (GHz)	Element			Array			
		Phase Range	Maximum Transmission Loss (dB)	Dielectric Layers	Size	OAM Mode	Gain (dBic)	Aperture Efficiency with l=+1
[9]	10	360°	1.94	With	$21.7\lambda_0^2$	+1	14.8	11%
[14]	60	360°	1	With	$144\lambda_0^2$	+1	21.5	7.8%
[15]	13.58	360°	1.5	Without	$45.7\lambda_0^2$	0	23.9	——
This work	6	360°	0.45	Without	$58.32\lambda_0^2$	+1	19.2	11.3%

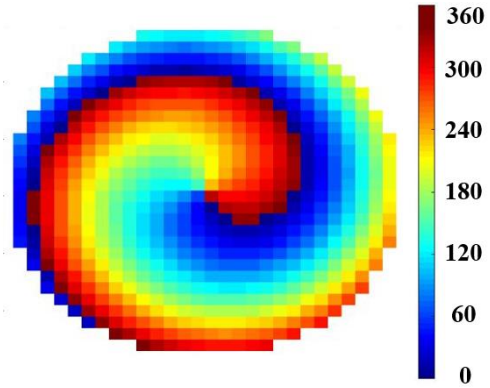

Fig. 7. The corresponding phase distributions of the designed transmitarray.

IV. SIMULATED RESULTS

The full-wave electromagnetic simulation software Ansys HFSS is used to analyze the proposed transmitarray antenna. To observe the characteristics of near-field *E*-field of the generated OAM beam waves, a test plane is set at a distance of 1 m in front of the transmitarray. The *E*-field characteristics of the OAM beam waves on the test plane is shown in Fig. 8. It is revealed that a doughnut-shaped magnitude is obtained in the generated OAM beam waves and a phase distribution varying from -180° to 180° is also observed, which is accord with the property of OAM waves of l=+1. The simulated two-dimensional (2-D) far-field radiation patterns at 6 GHz are plotted in Fig.9. It is clear that a zero-depth structure appears in the center of the beam which agrees well with the characteristics of OAM waves. The maximum gain is about 19.2 dBic and the divergence angle is 6°.

In addition, the OAM mode purity which can be calculated in [13] for the proposed transmitarray is shown in Fig. 10. It can be seen that OAM purity with l=+1 can reach up to around 90%. Besides, the maximum aperture efficiency of the antenna can be calculated by the following formula:

$$\eta = \frac{\lambda^2 G}{4\pi A}. \tag{12}$$

Where G represents the maximum gain of the antenna, and A represents the aperture area. Thus, the maximum aperture efficiency of the designed antenna is 11.3%, which is higher than that of 11% in [9] and 7.8% in [14].

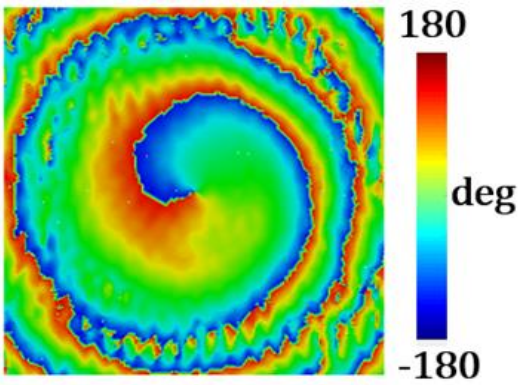

(a)

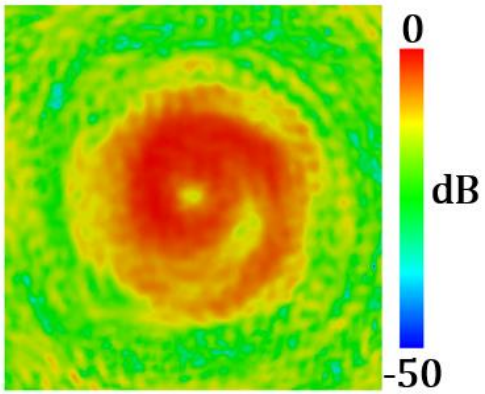

(b)

Fig. 8. The simulated *E*-field characteristics of the OAM beam on the test plane: (a) phase distribution and (b) magnitude distribution.

Finally, the element and array performances of the proposed transmitarray antenna are compared with other published designs, as summarized in Table 2. It can be clearly seen that the proposed element can achieve a 360° phase range with a much lower transmission loss.

Compared with [9] and [14], the proposed transmitarray antenna can generate OAM beam waves with much higher aperture efficiency.

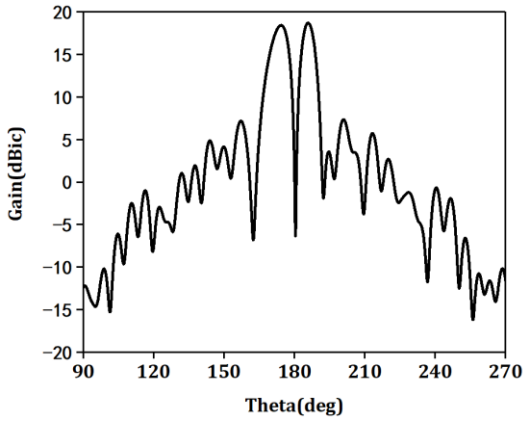

Fig. 9. The simulated 2-D far-field radiation patterns.

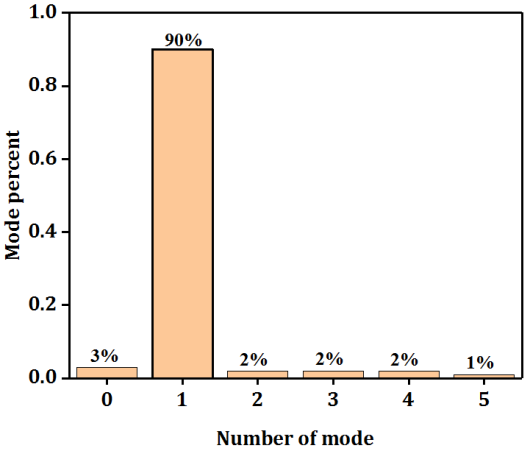

Fig. 10. The OAM mode purity for the proposed transmitarray.

V. CONCLUSION

In this paper, a transmitarray composed of 648 elements is designed to generate OAM beam waves with l=+1. A full 360° phase shift with transmission magnitude greater than -0.45 dB is obtained by using wavelength slot-type Jerusalem elements with non-identical layers. The full-wave electromagnetic simulation is used to analyze the proposed transmitarray and the simulated results confirm that OAM beam waves of l=+1 with high gain and small divergence angle have been successfully generated. The proposed design is an effective method to generate OAM beam waves for wireless communication applications.

ACKNOWLEDGMENT

This work is supported by the project 61971051 from the National Natural Science Foundation of China (NSFC) and the Central University Fundamental Research Fund.

REFERENCES

[1] L. Allen, M. W. Beijersbergen, R. J. C. Spreeuw, and J. P. Woerdman, "Orbital angular momentum of light and the transformation of Laguerre-Gaussian laser modes," *Physical Review A*, vol. 45, no. 11, p. 8185, 1992.

[2] F. Tamburini, E. Mari, B. Thidé, C. Barbieri, and F. Romanato, "Experimental verification of photon angular momentum and vorticity with radio techniques," *Applied Physics Letters*, vol. 99, no. 20, p. 204102, 2011.

[3] F. Tamburini, E. Mari, A. Sponselli, B. Thidé, A. Bianchini, and F. Romanato, "Encoding many channels on the same frequency through radio vorticity: First experimental test," *New Journal of Physics*, vol. 14, no. 3, p. 033001, 2012.

[4] X. Hui, S. Zheng, Y. Hu, C. Xu, X. Jin, H. Chi, and X. Zhang, "Ultralow reflectivity spiral phase plate for generation of millimeter-wave OAM beam," *IEEE Antennas and Wireless Propagation Letters*, vol. 14, pp. 966-969, 2015.

[5] Z. G. Guo and G. M. Yang, "Radial uniform circular antenna array for dual-mode OAM communication," *IEEE Antennas and Wireless Propagation Letters*, vol. 16, pp. 404-407, 2016.

[6] J. R. Reis, M. Vala, and R. F. Caldeirinha, "Review paper on transmitarray antennas," *IEEE Access*, vol. 7, pp. 94171-94188, 2019.

[7] D. Zelenchuk and V. Fusco, "Split-ring FSS spiral phase plate," *IEEE Antennas and Wireless Propagation Letters*, vol. 12, pp. 284-287, 2013.

[8] F. Qin, S. Gao, W. C. Cheng, Y. Liu, H. L. Zhang, and G. Wei, "A high-gain transmitarray for generating dual-mode OAM beams," *IEEE Access*, vol. 6, pp. 61006-61013, 2018.

[9] F. Qin, L. Wan, L. Li, H. Zhang, G. Wei, and S. Gao, "A transmission metasurface for generating OAM beams," *IEEE Antennas and Wireless Propagation Letters*, vol. 17, no. 10, pp. 1793-1796, 2018.

[10] J. Luo, F. Yang, S. V. Hum, S. Xu, and M. Li, "Study of a low-profile transmitarray element using 3 non-identical layers," *2018 IEEE MTT-S International Wireless Symposium (IWS)*, 2018.

[11] A. H. Abdelrahman, A. Z. Elsherbeni, and F. Yang, "Transmitarray antenna design using cross-slot elements with no dielectric substrate," *IEEE Antennas and Wireless Propagation Letters*, vol. 13, pp. 177-180, 2014.

[12] D. Zhang, X. Cao, H. Yang, and J. Gao, "Radiation performance synthesis for OAM vortex wave generated by reflective metasurface," *IEEE Access*, vol. 6, pp. 28691-28701, 2018.

[13] E. Yao, S. Franke-Arnold, J. Courtial, S. Barnett, and M. Padgett, "Fourier relationship between angular position and optical orbital angular momentum," *Optics Express*, vol. 14, no. 20, pp. 9071-9076, 2006.

[14] Y. Chen, S. Zheng, Y. Li, X. Hui, X. Jin, H. Chi, and X. Zhang, "A flat-lensed spiral phase plate based on phase-shifting surface for generation of millimeter-wave OAM beam," *IEEE Antennas and Wireless Propagation Letters*, vol. 15, pp. 1156-1158, 2015.

[15] G. Liu, H. J. Wang, J. S. Jiang, F. Xue, and M. Yi, "A high-efficiency transmitarray antenna using double split ring slot elements," *IEEE Antennas and Wireless Propagation Letters*, vol. 14, pp. 1415-1418, 2015.

Li Yu received the B.S. degree from Xidian University in 2017. She is currently pursuing the M.S. degree with the Beijing University of Post and Telecommunications.

Her current research interests include OAM antennas, reflectarray and transmitarray.

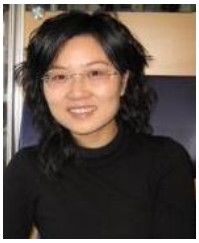

Xiuping Li received B.S. degree from Shandong University, Jinan, Shandong, P. R. China, in 1996, and the Ph.D. degree from Beijing Institute of Technology, Beijing, P.R. China, in 2001. She has been a Professor at Beijing University of Posts and Telecommunications, P.R. China.

Her research interests include microwave devices for communications, antennas, and microwave circuit design for millimeter wave/Terahertz applications.

Hua Zhu received the M.S. degree from Guilin University of Electronic Technology, P. R. China, in 2010, and the Ph.D. degree from Beijing Institute of Technology, Beijing, P.R. China, in 2015. She has been a Postdoc at Beijing University of Posts and Telecommunications, P.R. China.

Her research interests include UHF RFID beam scanning antenna array design in complex environment and millimeter wave/Terahertz antenna design.

Zihang Qi received the B.E. degree in Electronic and Information Engineering from China Three Gorges University, Yichang, China, in 2013, and the Ph.D. degree in Electronic Science and Technology from the Beijing University of Posts and Telecommunications, Beijing, China, in 2019. He is currently a Post-Doctoral Fellow with the Beijing University of Posts and Telecommunications.

His current research interests include OAM antennas, millimeter-wave/THz antennas and microwave filters. Qi was a recipient of the 2018 National Scholarship of China for Doctoral Students.

Arbitrary Shaped Objects Detection and Reconstruction through Overset Grid Generation Method with B_2-spline Interpolation in Forward-Backward Time-Stepping Inverse Scattering

Bong S. Wee [1, 2], Kismet A. H. Ping [1], Shafrida Sahrani [1], and Toshifumi Moriyama [3]

[1] Applied Electromagnetic Research Group, Department of Electrical and Electronic Engineering
Faculty of Engineering, Universiti Malaysia Sarawak, Kota Samarahan, 94300, Malaysia
bongsw@pmu.edu.my, hpkismet@unimas.my, sshafrida@unimas.my

[2] Department of Electrical Engineering
Politeknik Mukah, Mukah, 96400, Malaysia
bongsw@pmu.edu.my

[3] Department of Electrical and Electronic Engineering, Graduate School of Engineering
Nagasaki University 1-14 Bunkyo-machi, Nagasaki, 852-8521, Japan
t-moriya@nagasaki-u.ac.jp

Abstract ─ Finite-Difference Time-Domain (FDTD) method is a simple and powerful tool used to solve electromagnetic (EM) problems. However, the drawbacks of FDTD method are difficult to model the curved boundaries and small features due to its restriction to inherent orthogonal grids. We have previously proposed that the B_2-spline or biquadratic spline interpolation technique for Overset Grid Generation and Finite-Difference Time-Domain (OGG-FDTD) method be utilised to overcome the limitations of FDTD method. This proposed method has the ability to accurately measure a scattered field around an unknown object. In this paper, the OGG-FDTD method with B_2-spline interpolation in Forward-Backward Time-Stepping (FBTS) inverse scattering technique was proposed for the detection and reconstruction of arbitrary shaped objects in Case A and malignant breast tumour detection in Case B. The results showed that the Mean Square Error (MSE) of reconstructed dielectric profiles by using the proposed method has achieved significantly lower values than the FDTD method in FBTS. In Case A, the accuracy difference between the two methods was 26.67% for relative permittivity and 27.63% for conductivity, respectively. In Case B, it was found that the implementation of the proposed method increased the accuracy of reconstructed the relative permittivity image by 50.54%, and conductivity by 74.42% as compared to the FDTD method in FBTS technique. Furthermore, the values of normalised error function for the proposed method were also lower than the FDTD method in FBTS. Hence, it is proven that this numerical method can provide clearer and better reconstructed images to improve the quality of retrieve the dielectric profiles of the investigation area.

Index Terms ─ B_2-spline interpolation, buried object detection, inverse scattering problem, overset grid generation method.

I. INTRODUCTION

Microwave tomography is the new technology which evaluates buried or embedded objects in a medium by using EM waves. The main applications of microwave tomography are ground-penetrating radar [1-3], buried object detection applications in remote sensing [4-6], non-destructive evaluation [7-9], and medical diagnostic for biomedical engineering [10-13]. Microwave imaging technique (MWT) for non-destructive evaluation utilises frequency-domain [14] or time-domain [15] to solve the electromagnetic (EM) scattering problems. The EM scattering problems can be classified into two, which are direct and inverse scattering problems, respectively. The inverse scattering problem is the problem of determining characteristics of an unknown objects from the measurement data of a scattered field based on the actual objects detected [16].

Several methods have been reported in literature for solving the inverse scattering problem such as Bojarski-Lewis method [17], Linear Sampling method [18], and Lagrange Multipliers method [19]. However, those methods have some limitations such as instability, fails to estimate the target support for certain frequencies, and needed a large number of data for images reconstruction. Therefore, the Forward-Backward Time-Stepping (FBTS)

Submitted On: February 7, 2019
Accepted On: October 23, 2019

inverse scattering technique by Takenaka et al. [20] is utilised in this paper. The FBTS technique (also known as an iterative inversion technique) can be used to obtain the unknown electrical properties of objects by inverting measure scattered-field data. Furthermore, the useful quantitative information of the objects (e.g., its shapes, dimensions, locations and dielectric properties) also can be determined by utilising FBTS technique.

Finite-Difference Time-Domain (FDTD) method is a simple and powerful tool by which to solve Electromagnetic (EM) problems such as scattering from metal objects and dielectrics, microstrip circuits, antenna analysis, electromagnetic wave propagation, and human exposure to EM waves [21, 22]. It can investigate multiple frequencies without any extra computational effort. However, the limitations of the FDTD method are difficult to model the curved boundaries and small features due to its restriction to inherent orthogonal grids [23, 24]. Several methods have been reported in literature to improve the efficiency of the FDTD method, such as sub-gridding, non-uniform, and sub-cell algorithm [25-27]. However, those methods still have some drawbacks such as: requiring high computation time and more memory; as well as time step or cell size being restrictive by the Courant-Friedrichs-Lewy (CFL) stability condition [28]. Previously, we proposed the B_2-spline interpolation technique for Overset Grid Generation and Finite-Difference Time-Domain (OGG-FDTD) method to overcome these limitations [29]. This method has the ability to accurately measure the EM scattered field for an unknown object in a different medium.

In this paper, the OGG-FDTD method with B_2-spline interpolation in Forward-Backward Time-Stepping (FBTS) inverse scattering technique is proposed for the detection and reconstruction of arbitrary shaped objects and realistic breast composition. The performance of the proposed method is evaluated by investigating the characteristics of arbitrary shaped objects in transverse magnetic z-plane (TM_z) mode. The conjugate gradient minimisation method by Fletcher-Reeves and Polak-Ribiere-Polyak was used in this work for optimisation technique in order to reconstruct the microwave images.

II. OVERSET GRID GENERATION METHOD WITH B_2-SPLINE INTERPOLATION IN FORWARD-BACKWARD TIME-STEPPING INVERSE SCATTERING TECHNIQUE

Figure 1 (a) shows the actual image of two homogenous arbitrary shaped objects. These objects are embedded in the Region of Interest (ROI) with free space as the background medium. Figure 1 (b) shows the reconstructed image by utilising the OGG-FDTD method with B_2-spline interpolation in FBTS inverse scattering technique. The OGG-FDTD lattice consists of two meshes, namely, main-mesh and sub-mesh. The sub-mesh was set to overlap on top and centre of the main mesh and used to model the arbitrary shaped objects.

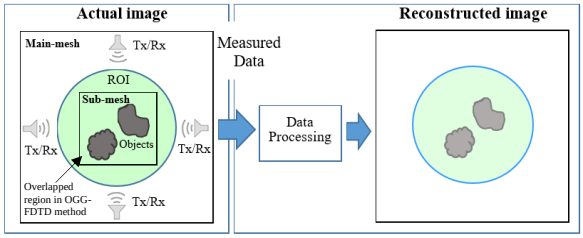

Fig. 1. Configuration of OGG-FDTD method with B_2-spline interpolation in FBTS inverse scattering technique. 'Tx/Rx' indicates the transmission and receiving antennas.

The FBTS technique can be separated into two steps: forward step and backward step [20]. The forward step of the FBTS method begins with the excitation of Gaussian pulse signal to the estimated profile of the arbitrary shaped objects. The OGG-FDTD method with B_2-spline interpolation was used to calculate the scattered fields for forward time-stepping. The B_2-spline interpolation was used to interpolate the EM field for the overlapped region in OGG-FDTD lattice as shown in Fig. 2. B_2-spline interpolation is using a set of lower order polynomials between known values data points at main mesh to determine the unknown value data point at sub-mesh.

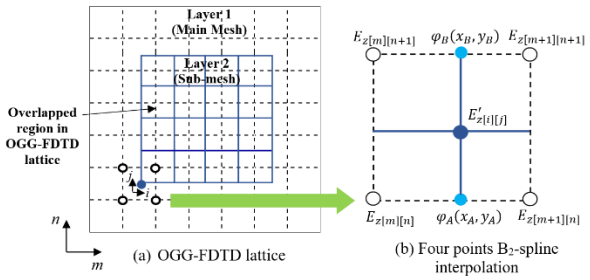

Fig. 2. The overlapped region in OGG-FDTD method with B_2-spline interpolation.

The EM field components on the main mesh are set as E_z, H_x, and H_y while on the sub-mesh are set as E'_z, H'_x and H'_y. The electric field on main mesh (E_z) is interpolated to sub-mesh (E'_z) through B_2-spline interpolation technique. $Ez_{[m][n]}(x_1, y_1)$, $Ez_{[m+1][n]}(x_2, y_2)$, $Ez_{[m][n+1]}(x_3, y_3)$, and $Ez_{[m+1][n+1]}(x_4, y_4)$ are the four known value points at the main-mesh, while $E'_{z_{[i][j]}}(x_s, y_s)$ is the unknown value point at the sub-mesh. Where, m and n are the number of cell grids for main-mesh, whereas i and j are the number of cell grids for sub-mesh. The

unknown value of $\varphi_A(x_A, y_A)$ is interpolated by using the known values of $Ez_{[m][n]}(x_1, y_1)$ and $Ez_{[m+1][n]}(x_2, y_2)$ whereas the unknown value of $\varphi_B(x_B, y_B)$ is interpolated by using the known values of $Ez_{[m][n+1]}(x_3, y_3)$ and $Ez_{[m+1][n+1]}(x_4, y_4)$ at the x-axis. Then, the unknown value of $E'_{Z_{[i][j]}}$ can be calculated by using the φ_A and φ_B at y-axis as follows:

$$E'_{Z_{[i][j]}} = \left[\frac{d_{y1_{[m][n+1]}} - d_{y1_{[m][n]}}}{2(y_B - y_A)}\right](y_s - y_A)^2 + \left[d_{y_{[m][n]}}\right](y_s - y_A) + \varphi_A, \quad (1)$$

$$i = 0,1,2, \ldots \text{ and } j = 0,1,2 \ldots$$

where,

$$d_{y1_{[m][n]}} = 0, \; d_{y1_{[m][n+1]}} = \frac{2(\varphi_B - \varphi_A)}{(y_B - y_A)} - d_{y1_{[m][n]}},$$

$$\varphi_A = \left[\frac{d_{x1_{[m][n+1]}} - d_{x1_{[m][n]}}}{2(x_2 - x_1)}\right](x_A - x_1)^2 + \left[d_{x1_{[m][n]}}\right](x_A - x_1) + E_{Z_{[m][n]}},$$

$$\because d_{x1_{[m][n]}} = 0, \; d_{x1_{[m][n+1]}} = \frac{2\left(E_{Z_{[m+1][n]}} - E_{Z_{[m][n]}}\right)}{(x_2 - x_1)} - d_{x1_{[m][n]}},$$

$$\varphi_B = \left[\frac{d_{x2_{[m][n+1]}} - d_{x2_{[m][n]}}}{2(x_4 - x_3)}\right](x_B - x_3)^2 + \left[d_{x2_{[m][n]}}\right](x_B - x_3) + E_{Z_{[m][n+1]}},$$

$$\because d_{x2_{[m][n]}} = 0, d_{x2_{[m][n+1]}} = \frac{2\left(E_{Z_{[m+1][n+1]}} - E_{Z_{[m][n+1]}}\right)}{(x_4 - x_3)} - d_{x2_{[m][n]}},$$

$$m = 0,1,2, \ldots \text{ and } n = 0,1,2 \ldots .$$

Similarly, the H_x and H_y fields for the overlapped region in OGG-FDTD lattice were interpolated by using the same interpolation process.

Then, the E_z' fields on the sub-mesh were interpolation back into the main mesh, so that the electric fields (E_z) on the main mesh are updated. This algorithm continued until the time-stepping was concluded. The details regarding OGG-FDTD method with B_2-spline interpolation can be found in [29].

The forward time-stepping reconstructions data at the receiving point were collected and compared with the measurement data. The backward step of the FBTS method was used to calculate the adjoint field in OGG-FDTD lattice. The adjoint field is the field which radiates from the equivalent impressed currents of the different of the forward time-stepping reconstructions data and measurement data. Then, the backward time-stepping reconstructions data at the receiving point were collected and compared with the measurement data. The difference between measured and calculated scattered fields was utilised as a source by which to irradiate the original profile.

The cost functional, $Q(p)$ was used to minimise the number of iterations for the FBTS reconstruction as shown in (2):

$$Q(p) = \int_0^T \sum_{m=1}^{M} \sum_{n=1}^{N} K_{mn}(t) \, |V_m(p; r_n^r, t) - \tilde{V}_m(r_n^r, t)|^2 dt, \quad (2)$$

where, $K_{mn}(t)$ is a non-negative weighting function, and T is the time duration of measurement. $V_m(r_n, t)$ is the calculated electromagnetic fields vector for an estimate's medium parameter vector p, and $\tilde{V}_m(r_n, t)$ is the measured EM fields vector for the m^{th} source. The cost functional was computed by comparing the estimated profiles to the actual profiles until the different between both profiles are lower.

Following this, the estimated permittivity values for the next iteration are as shown in (3):

$$\varepsilon_r^{k+1}(r) = \varepsilon_r^k(r) + \alpha^k d_\varepsilon^k(r), \quad (3)$$

where, k is the current optimisation iteration number in the FBTS optimisation, $\varepsilon_r^k(r)$ indicates permittivity values in the reconstruction region, $d_\varepsilon^k(r)$ is search direction, r represents variation in space (i.e., r gives the x, y spatial coordinate), and α^k is the approximate step-size.

An analytical approximation approach is used to calculate the step size, α by substituting the term $p = \varepsilon_r + \alpha d_\varepsilon$ from (3) into (2). The cost functional, $Q(p)$ for current iteration can be calculated as follows:

$$Q(p) = \int_0^T \sum_{m=1}^{M} \sum_{n=1}^{N} K_{mn} \, |v_m(\varepsilon_r + \alpha d_\varepsilon) - \tilde{v}_m|^2 dt. \quad (4)$$

Then, calculate the cost functional $Q(p)$for the 1st iteration as reference:

$$Q_{Vm}(p) = \int_0^T \sum_{m=1}^{M} \sum_{n=1}^{N} K_{mn} |\tilde{v}_m|^2 \, dt. \quad (5)$$

The normalisation of $Q(p)$ can be calculated by utilizing (4) and (5) as:

$$\text{Normalisation of } Q(p) = \frac{Q(p)}{Q_{Vm}(p)}. \quad (6)$$

The conjugate gradient minimisation methods by Fletcher-Reeves and Polak-Ribiere-Polyak were used as optimisation techniques for optimal control of machine computation problems and also to minimise the functional error. The gradient functional can be obtained by introducing the Fréchet derivative to (2). The gradient vectors are then found with respect to the permittivity and conductivity as demonstrated in (7) and (8).

$$g_{\varepsilon_r}(r) = \int_0^T \sum_{m=1}^{M} \sum_{i=1}^{2} w_{mi}\begin{pmatrix} p; \\ r, \\ t \end{pmatrix} \frac{\partial}{\partial(t)} \, v_{mi}\begin{pmatrix} p; \\ \mathrm{r}, \\ t \end{pmatrix} dt, \quad (7)$$

$$g_\sigma(r) = \int_0^T \sum_{m=1}^{M} \sum_{i=1}^{2} w_{mi}(p; r, t) v_{mi}(p; \mathrm{r}, t) d\mathrm{t}. \quad (8)$$

The terms $v_{mi}(p; r, t)$ and $w_{mi}(p; r, t)$ refer as the i^{th} component of the EM field, $v_m(p; r, t)$ and adjoint field vector, $w_m(p; r, t)$. The adjoint fields are calculated by propagating the residual scattered signals being reversed in time and utilised as sources. The summation term from $i = 1$ to $i = 2$ represents the fact that in two-dimensional (2D) the gradients are calculated using the x- and y-components of v_{mi} and w_{mi}.

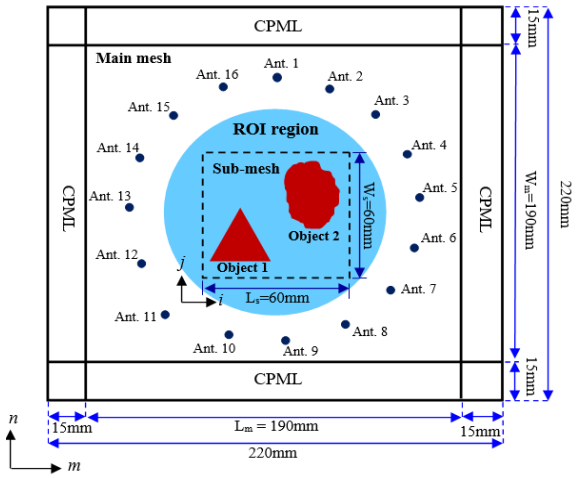

Fig. 2. Configuration of arbitrary shaped objects in 2D OGG-FDTD scheme.

III. NUMERICAL MODEL SETUP

Figure 2 shows the configuration of an active microwave tomography in 2D. The OGG-FDTD method with B_2-spline interpolation in FBTS technique was used to solve the non-dispersive inverse scattering problem in TM_Z. The actual dielectric profiles setting is listed as in Table 1.

Table 1: Actual dielectric profiles setting

Layer	Media Region	ε_r (F/m)	σ (S/m)
Layer 1 (Main-mesh)	Background	1.00	0.00
	ROI	9.98	0.18
Layer 2 (Sub-mesh)	Arbitrary shaped objects	21.45	0.46

The main-mesh was set to 190 mm × 190 mm grids and the sub-mesh was set to 60 mm × 60 mm grids. The Region of Interest (ROI) is a circular shape with a radius of 50 mm and located on the middle of the main-mesh. The dielectric properties of the ROI are assumed to be the fatty tissues, and the arbitrary shaped objects are assumed to be the fibroglandular tissues in the breast. The background of the FDTD lattice is assumed to be free space. Reconstructions were conducted by utilising the 1 mm × 1 mm OGG-FDTD grid size and the optimisation was carried out for 100 iterations. A sinusoidal modulated Gaussian pulse with centre frequency of 2.0 GHz and bandwidth of 1.3 GHz acted as the excitation signal in the simulations. Sixteen (16) points represented as antennas encircle the ROI with a radius of 85 mm. Each of the point source antennas acted as a transmitter that sequentially transmitted a Gaussian pulse. The remaining 15 antennas became the receivers to collect the scattered fields in the OGG-FDTD lattice. The details regarding the effect of different MWT parameters such as the noise of the scattered data, number of antennas, and frequency of operation can be found in [11, 30, 31]. The Convolution Perfectly Matched Layer (CPML) with 15 cells are utilised in this work as absorbing boundary condition (ABC) to absorb the travelling wave without reflections from the edge.

IV. RESULTS AND DISCUSSION

In this section, the performance of OGG-FDTD method with B_2-spline interpolation in Forward-Backward Time Stepping (FBTS) inverse scattering for the detection and reconstruction of buried objects is being evaluated. A homogenous arbitrary shaped object is chosen in this research to validate the competency of the proposed method in Case 1. Then, the efficacy of this proposed method is applied to inhomogeneous realistic breast cancer detection application in Case 2.

A. Case 1: Multiple arbitrary shaped objects

Figure 3 illustrates the actual and reconstructed relative permittivity profiles of the numerical model in Case 1. The actual profile of the relative permittivity is presented in Fig. 3 (a), whereas the reconstructed relative permittivity images are shown in Figure 3(b) for FDTD method in FBTS, and Fig. 3 (c) for OGG-FDTD method with B_2-spline interpolation in FBTS. The curved boundaries and small features of an arbitrary shaped objects cannot be modelled by using the FDTD method in FBTS. In contrast, the OGG-FDTD method with B_2-spline interpolation in FBTS is able to accurately reconstruct the curved boundaries and small features of an arbitrary shaped objects.

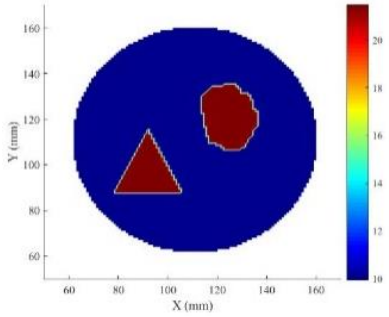

(a) Actual relative permittivity

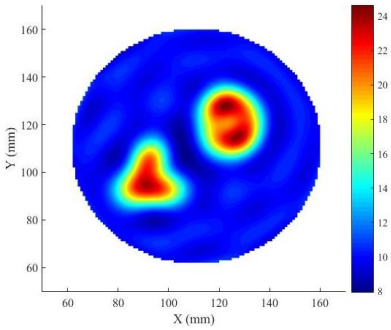

(b) Reconstructed relative permittivity profile for FDTD method in FBTS

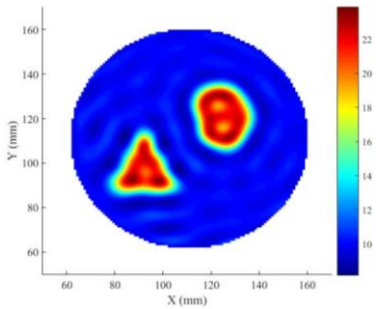

(c) Reconstructed relative permittivity profile for OGG-FDTD method with B_2-spline interpolation in FBTS

Fig. 3. Actual and reconstructed relative permittivity profiles of the arbitrary shaped objects in Case 1.

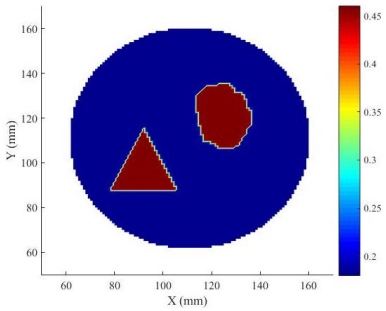

(a) Actual conductivity

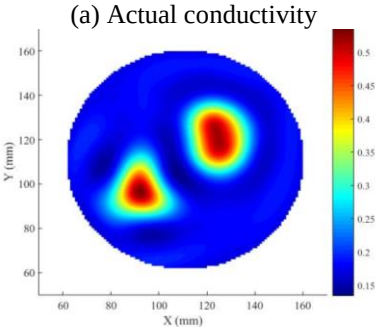

(b) Reconstructed conductivity profile for FDTD method in FBTS

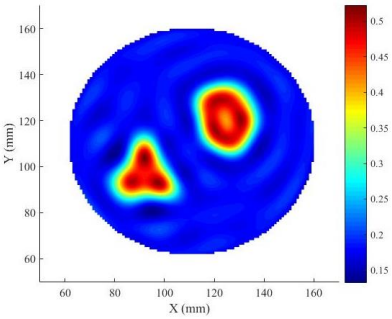

(c) Reconstructed conductivity profile for OGG-FDTD method with B_2-spline interpolation in FBTS

Fig. 4. Actual and reconstructed conductivity profiles of the arbitrary shaped objects in Case 1.

Figure 4 illustrates the actual and reconstructed conductivity profiles of the numerical model in Case 1. Figure 4 (a) depicts the original profile of the conductivity, whereas Fig. 4 (b) shows the reconstructed conductivity image for FDTD method in FBTS, and Fig. 4 (c) shows the reconstructed conductivity image for OGG-FDTD method with B_2-spline interpolation in FBTS. The OGG-FDTD method with B_2-spline interpolation in FBTS inverse scattering technique was successfully detected and accurately reconstructed the conductivity profiles of arbitrary shaped objects. The accuracy of the OGG-FDTD method with B_2-spline interpolation in FBTS was investigated by using the Mean Square Error (MSE) as follows:

$$\text{MSE} = \frac{\sum_{M,N}[P_A(x,y)-P_R(x,y)]^2}{MN}, \quad (9)$$

where, $P_A(x,y)$ is actual dielectric profile, $P_R(x,y)$ is reconstructed profile, and $M \times N$ is an image's dimension. Table 2 shows the MSE analysis for these two methods. The results showed that MSE of reconstructed dielectric profiles by using the proposed method has achieved significantly lower values than the FDTD method in FBTS. The accuracy difference between the two methods was 26.65% for relative permittivity profile and 27.63% for conductivity profile. It has been proven that the OGG-FDTD method with B_2-spline interpolation in FBTS inverse scattering technique can provide accurate results and further improve the quality of reconstructed images such as its location, shape, size and internal composition, respectively.

Table 2: MSE of dielectric profiles

Methods	**MSE**	
	Relative Permittivity Profile	**Conductivity Profile**
FDTD method in FBTS	2.064	1.52×10^{-3}
OGG-FDTD method with B_2-spline interpolation in FBTS	1.514	1.10×10^{-3}

The accuracy of the OGG-FDTD method with B_2-spline interpolation in FBTS inverse scattering technique was further investigated by normalising the functional error. Figure 5 shows the normalised functional error versus the number of iterations. It was found that the normalised functional error decreased when the number of iterations increased. As can be seen, the normalised functional error for the OGG-FDTD method with B_2-spline interpolation in FBTS is lower as compared to the FDTD method. At the 100^{th} iteration, the difference of normalised functional error between these two methods was 6.06×10^{-8}. Hence, the OGG-FDTD method with B_2-spline interpolation in FBTS has the ability to retrieve the dielectric profiles accurately.

B. Case 2: Heterogeneous dense realistic breast

The mammograms for four breast parenchymal density based on BI-RADS [32] are: Class A (mostly fatty breast); Class B (scattered density breast); Class C (heterogeneously dense breast); and Class D (extremely dense breast). In order to analyse the accuracy of the OGG-FDTD method with B_2-spline interpolation in FBTS inverse scattering technique to detect a malignancy tumour embedded in arbitrary shaped of the fibroglandular region, the heterogeneous dense realistic breast was described in Case 2.

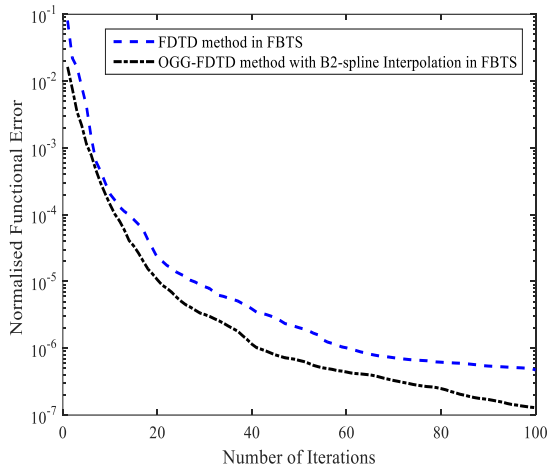

Fig. 5. Normalised functional error versus number of iterations.

The heterogeneously dense breast (also known as Class C breast) has large areas of dense fibrous and glandular breast tissue. Hence, it is difficulties to spot abnormalities in the Class C than in Classes A, and B, respectively. The heterogeneously dense breast phantom from Nagasaki University Hospital was chosen in this research for inhomogeneous breast cancer detection application. The breast tissues in this phantom have realistic ultra-wideband dielectric properties and can be readily used in FDTD computational electromagnetic models. This phantom is derived from a series of T1-weighted magnetic resonance images (MRIs) of patients in a prone position. Each numerical phantom comprised a three-dimensional (3D) grid of cubic voxels, where each voxel measures 0.5 mm × 0.5 mm × 0.5 mm. This 3D anatomical model was transformed into non-dispersive dielectric properties utilising spatial distributions. In order to satisfy the OGG-FDTD grid size, this model needed to resize from 0.5 mm × 0.5 mm × 0.5 mm to 1.0 mm × 1.0 mm × 1.0 mm. The resize process was implemented by using linear interpolation technique. Figure 6 illustrates the 2D numerical setup of an active microwave tomography for breast in OGG-FDTD lattice.

In this research, the non-dispersive heterogeneously dense breast composition was assumed to be immersed in a free space as a background medium. The FDTD lattice as main mesh is consists of 190 mm × 190 mm cells and surrounded by fifteen-cell of Convolution Perfectly Matched Layer (CPML). The sub-mesh is overlapping on top of the main mesh with 90 mm × 130 mm cells. The cell size for main-mesh and sub-mesh is $\Delta x = 1$ mm and $\Delta y = 1$ mm. The sub-mesh was modelled as an entire numerical breast phantom. A radius of 5 mm tumour was added in the fibroglandular region of the numerical breast. The actual setting of numerical measured data is referring to nominal Debye parameters as shown in Table 3. Skin, adipose, fibroglandular, and tumour are the four kinds of breast tissues.

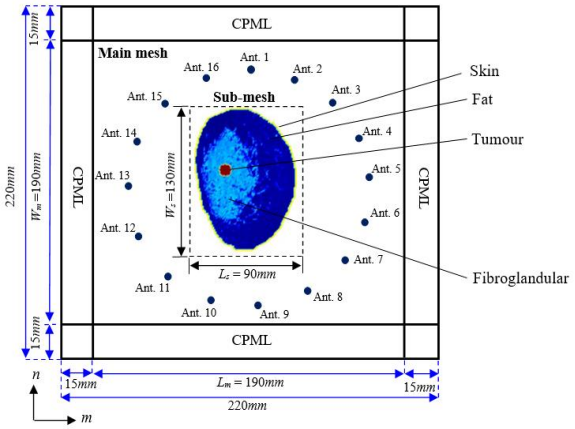

Fig. 6. Configuration of the realistic breast phantom in 2D view.

Table 3: Electronic property parameters utilised for breast tissue [20]

Tissue	ε_r (2 GHz)	σ (2 GHz)
Skin	36.73	0.46
Adipose	9.98	0.18
Fibroglandular	21.45	1.43
Tumour	53.62	1.19

The sinusoidal modulated Gaussian pulse is used as excitation signal with centre frequency of 2.0 GHz and a bandwidth of 1.3 GHz. The OGG-FDTD method with biquadratic spline interpolation in FBTS inverse scattering technique was simulated up to 150 iterations to reconstruct the image of internal breast composition.

Figure 7 (a) shows the actual relative permittivity profile of non-dispersive heterogeneous dense realistic breast. Figure 7 (b) illustrates the reconstructed relative permittivity profile of the FDTD method in FBTS. Figure 7 (c) shows reconstructed relative permittivity profile of the OGG-FDTD method with B_2-spline interpolation in FBTS. These two methods have successfully reconstructed the malignancy tumour placed within the fibroglandular region. However, the reconstructed images

by these two methods are slightly different as compared to the actual distribution image. The curved boundaries and small features of an arbitrary shaped fibroglandular region cannot be modelled by using the FDTD method in FBTS. In contrast, the OGG-FDTD method with B_2-spline interpolation in FBTS was able to accurately reconstruct the curved boundaries and small features of an arbitrary shaped of the fibroglandular region.

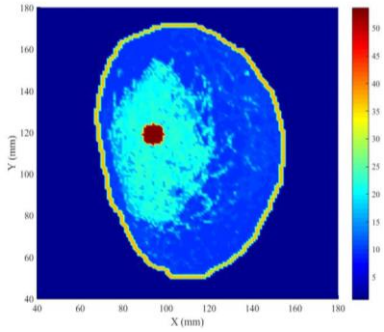

(a) Actual relative permittivity profile

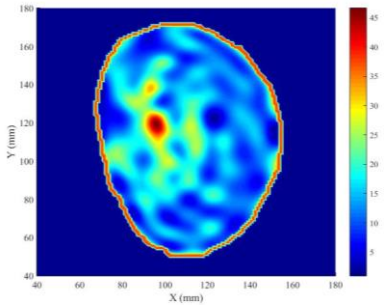

(b) Reconstructed relative permittivity profile for FDTD method in FBTS

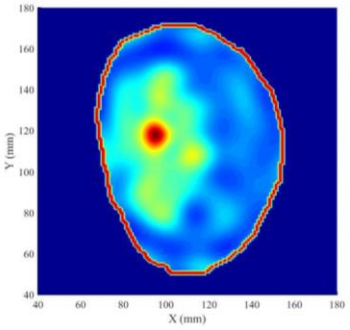

(c) Reconstructed relative permittivity profile for OGG-FDTD method with B_2-spline interpolation in FBTS

Fig. 7. Actual and reconstructed relative permittivity profiles of the breast phantom in Case 2.

Figure 8 (a) shows the actual conductivity profile of a heterogeneous dense realistic breast phantom in Case 2. As illustrated in Fig. 8 (b), the embedded tumour is unable to be detected in conductivity reconstruction by utilising the FDTD method in FBTS. To address this issue, a new numerical method based on the OGG-FDTD method with B_2-spline interpolation in FBTS inverse scattering technique was proposed to determine the presence and location of malignant tumours in the breast. Whereas, the proposed method has successfully detected and reconstructed the breast composition of the conductivity profile as depicted in Fig. 8 (c). Reconstructed image clearly indicates the value of the dielectric parameters as being almost identical to the true values of the tumour located within the fibroglandular region as well as its position and size.

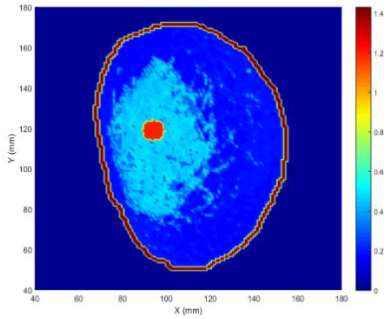

(a) Actual conductivity profile

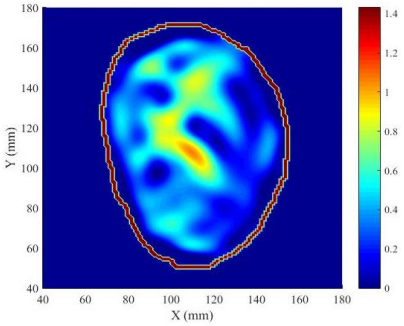

(b) Reconstructed conductivity profile for FDTD method in FBTS

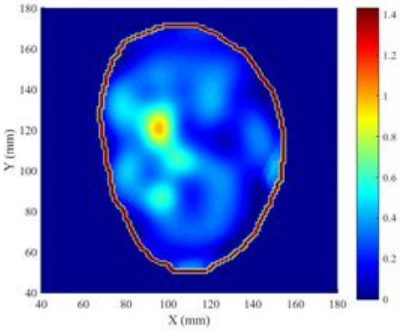

(c) Reconstructed conductivity profile for OGG-FDTD method with biquadratic spline interpolation in FBTS

Fig. 8. Actual and reconstructed conductivity profiles of the breast phantom in Case 2.

The accuracy of actual and reconstructed profiles can be investigated by using Mean Square Error (MSE). In terms of MSE level, the reconstructed relative permittivity profile by the FDTD method in FBTS

attained an accuracy of rating 24.829 while the OGG-FDTD method with B_2-spline interpolation in FBTS attained an accuracy level of 12.279. It was found that the implementation of the OGG-FDTD method in FBTS technique increased the accuracy of reconstructed the relative permittivity image by 50.54% as compared to the FDTD method in FBTS technique. Further, the MSE for reconstructed conductivity profile achieved an accuracy level of 0.043 for the FDTD method in FBTS, while the OGG-FDTD method in FBTS achieved an accuracy rating of 0.011. Hence, the MSE for reconstructed conductivity profile utilising the proposed method achieved significantly lower values than the FDTD method in FBTS.

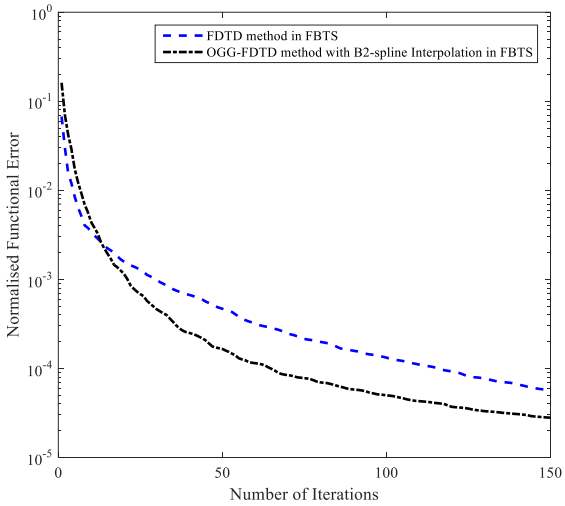

Fig. 9. Normalised functional error versus number of iterations for Case 2.

In this research, the gradient optimization was carried out up to 150 iterations to reconstruct the breast image and minimise the cost functional error. Figure 9 shows that the normalised functional error for OGG-FDTD method with B_2-spline interpolation in FBTS is lower as compared to the FDTD method in FBTS. At 150^{th} iteration, the difference of normalised functional error between these two methods was 2.87×10^{-5}. Numerical results demonstrate the efficiency of the proposed method in providing better reconstructed images as compared with the FDTD method in FBTS. Hence, the numerical simulations were able to demonstrate the ability of the proposed method to accurately determine the quantitative information of a heterogeneous realistic breast.

V. CONCLUSION

In this study, the OGG-FDTD method with B_2-spline interpolation in FBTS inverse scattering technique for reconstruction of arbitrary shaped objects embedded in the ROI and the malignant breast tumour detection in heterogeneous dense realistic breast have been presented as Case 1 and Case 2, respectively. The proposed numerical method provides clearer and better reconstructed images as compared with the FDTD method in FBTS. Hence, it can be concluded that the proposed method was able to determine the quantitative information of arbitrary shaped objects and breast composition accurately. The location, shape, size and dielectric properties of a tumour within an arbitrary shape of fibroglandular region also can be determined. For future work, this numerical method can be applied to reconstruct malignant breast tissues in different breast parenchymal density.

ACKNOWLEDGMENT

This work was supported by *Dana Pelajar Ph.D.* (DPP) Grant F02/DPP/1602/2017, Universiti Malaysia Sarawak (UNIMAS), Ministry of Education Malaysia.

REFERENCES

[1] E. R. Almeida, J. L. Porsani, I. Catapano, G. Gennarelli, and F. Soldovieri, "GPR data analysis enhanced by microwave tomography for forensic archaeology," *in 15th International Conference on Ground Penetrating Radar (GPR), IEEE*, 2014.

[2] R. Persico, G. Pochanin, V. Ruban, A. Orlenko, I. Catapano, and F. Soldovieri, "Performances of a microwave tomographic algorithm for GPR systems working in differential configuration," *IEEE Journal of Selected Topics in Applied Earth Observations and Remote Sensing*, vol. 9, no. 4, pp. 1343-1356, 2016.

[3] A. Fedeli, M. Pastorino, and A. Randazzo, "A two-step multifrequency imaging technique for ground penetrating radar," *in 10th European Conference on Antennas and Propagation (EuCAP), IEEE*, 2016.

[4] C. Estatico, A. Fedeli, M. Pastorino, and A. Randazzo, "Buried object detection by means of a Lp Banach-space inversion procedure," *Radio Science*, vol. 50, no. 1, pp. 41-51, 2015.

[5] P. M. Ibrahim, K. A. H. Ping, N. S. Wei, Y. Guang, N. Rajaee, and M. Anyi, "Elliptic filter and iterative inversion method for buried object detection applications," *Applied Mechanics and Materials*, vol. 833, p. 164, 2016.

[6] S. A. Shah, Z. Zhang, A. Ren, N. Zhao, X. Yang, W. Zhao, J. Yang, J. Zhao, W. Sun, and Y. Hao, "Buried object sensing considering curved pipeline," *IEEE Antennas and Wireless Propagation Letters*, 2017.

[7] M. Benedetti, M. Donelli, A. Martini, M. Pastorino, A. Rosani, and A. Massa, "An innovative microwave-imaging technique for nondestructive evaluation: Applications to civil structures

monitoring and biological bodies inspection," *IEEE Transactions on Instrumentation and Measurement*, vol. 55, no. 6, pp. 1878-1884, 2006.

[8] S. Kharkovsky and R. Zoughi, "Microwave and millimeter wave nondestructive testing and evaluation-Overview and recent advances," *IEEE Instrumentation & Measurement Magazine*, vol. 10, no. 2, pp. 26-38, 2007.

[9] Y. Deng and X. Liu, "Electromagnetic imaging methods for nondestructive evaluation applications," *Sensors*, vol. 11, no. 12, pp. 11774-11808, 2011.

[10] D. W. Winters, J. D. Shea, P. Kosmas, B. D. Van Veen, and S. C. Hagness, "Three-dimensional microwave breast imaging: Dispersive dielectric properties estimation using patient-specific basis functions," *IEEE Transactions on Medical Imaging*, vol. 28, no. 7, pp. 969-981, 2009.

[11] M. A. Elizabeth, K. A. H. Ping, N. B. Rajaee, and T. Moriyama, "Chebyshev filter applied to an inversion technique for breast tumour detection," *International Journal of Research in Engineering and Technology*, vol. 4, no. 6, pp. 210-218, 2015.

[12] E. Porter, M. Coates, and M. Popović, "An early clinical study of time-domain microwave radar for breast health monitoring," *IEEE Transactions on Biomedical Engineering*, vol. 63, no. 3, pp. 530-539, 2016.

[13] S. Vemulapalli, *Early Breast Cancer Diagnosis Using Microwave Imaging via Space-Frequency Algorithm*, University of Missouri-Kansas City, 2017.

[14] Q. Dong and C. M. Rappaport, "Microwave subsurface imaging using direct finite-difference frequency-domain-based inversion," *IEEE Transactions on Geoscience and Remote Sensing*, vol. 47, no. 11, pp. 3664-3670, 2009.

[15] C. Bardak and M. Saed, "Microwave imaging with a time-reversed finite-difference time-domain technique," *Journal of Electromagnetic Waves and Applications*, vol. 28, no. 12, pp. 1455-1467, 2014.

[16] F. Cakoni, D. Colton, and P. Monk, "Qualitative methods in inverse electromagnetic scattering theory: Inverse scattering for anisotropic media," *IEEE Antennas and Propagation Magazine*, vol. 59, no. 5, pp. 24-33, 2017.

[17] W. Perry, "On the Bojarski-Lewis inverse scattering method," *IEEE Transactions on Antennas and Propagation*, vol. 22, no. 6, pp. 826-829, 1974.

[18] M. Erramshetty and A. Bhattacharya, "Shape reconstruction of dielectric and conducting objects using Linear Sampling Method and limitations," *in 2019 URSI Asia-Pacific Radio Science Conference (AP-RASC), IEEE*, 2019.

[19] I. Rekanos, "Time-domain inverse scattering using Lagrange multipliers: An iterative FDTD-based optimization technique," *Journal of Electromagnetic Waves and Applications*, vol. 17, no. 2, pp. 271-289, 2003.

[20] T. Takenaka, H. Jia, and T. Tanaka, "Microwave imaging of electrical property distributions by a Foward-Backward Time-Stepping method," *Journal of Electromagnetic Waves and Applications*, vol. 14, pp. 1609-1626, 2015.

[21] K. S. Yee, "Numerical solution of initial boundary value problems involving Maxwell's in isotropic media," *IEEE Trans. Antennas Propag.*, vol. 14, no. 3, pp. 302-307, 1966.

[22] J. B. Schneide, *Understanding the Finite-Difference Time-Domain Method*, School of Electrical Engineering and Computer Science, Washington State University, 2016.

[23] R. Nilavalan, I. J. Craddock, and C. J. Railton, "Quantifying numerical dispersion in non-orthogonal FDTD meshes," *IEE Proceedings-Microwaves, Antennas and Propagation*, vol. 149, no. 1, pp. 23-27, 2002.

[24] E. Jiménez-Mejía and J. Herrera-Murcia, "Validation of a non-uniform meshing algorithm for the 3D-FDTD method by means of a two-wire crosstalk experimental set-up," *Ingeniería e Investigación*, vol. 35, pp. 98-103, 2015.

[25] C. Xu, Z. Deng, R. Xiong, and F. Deng, "Time-step program for the sub-cell FDTD modeling of apertures with finite depth," *International Journal of Applied Electromagnetics and Mechanics*, vol. 47, no. 1, pp. 255-262, 2015.

[26] Z. Yang and E. L. Tan, "Stability analyses of non-uniform time-step schemes for ADI- and LOD-FDTD methods," *in Computational Electromagnetics (ICCEM), IEEE International Conference on*, 2017.

[27] M. R. Cabello, L. D. Angulo, J. Alvarez, I. D. Flintoft, S. Bourke, J. F. Dawson, R. G. Martín, and S. G. Garcia, "A hybrid Crank-Nicolson FDTD subgridding boundary condition for lossy thin-layer modelling," *IEEE Transactions on Microwave Theory and Techniques*, vol. 65, no. 5, pp. 1397-1406, 2017.

[28] C. A. De Moura and C. S. Kubrusly, "The Courant-Friedrichs-Lewy (CFL) condition," *Commun. Pure Appl. Math*, vol. 10, no. 2, pp. 363-371, 2013.

[29] B. S. Wee, S. Sahrani, and K. A. H. Ping, "B_2-spline interpolation technique for overset grid generation and finite-difference time-domain method," *Progress In Electromagnetics Research C*, vol. 86, pp. 177-190, 2018.

[30] J. Nawawi, S. S Sahrani, K. A. H. Ping, D. A. A. Mat, and D. N. A. Zaidel, "Iterative refinement in inverse scattering technique with median filter," *in 2016 IEEE Asia-Pacific Conference on Applied Electromagnetics (APACE)*, 2016.

[31] E. J. Joseph, K. A. H. Ping, K. Kipli, D. A. A. Mat, S. Sahrani, D. N. A. Zaidel, M. I. Sariphn, and M. H. Marhaban, "Integration of image segmentation method in inverse scattering for brain tumour detection," *Progress In Electromagnetics Research*, vol. 61, pp. 111-122, 2017.

[32] M. Sonnenschein and C. Waldherr, "BI-RADS reporting for breast tomosynthesis (3D-mammography)," *in Atlas of Breast Tomosynthesis, Springer*, pp. 7-57, 2017.

Bong Siaw Wee was born in Kuching, Malaysia, in 1982. She received the B.Eng. (Hons) degree in Electronics Engineering from Universiti Teknikal Malaysia Melaka in 2008, and the M.Eng. degree in Electrical Engineering from Universiti Tun Hussein Onn Malaysia in 2012. She is now working towards Ph.D. degree at the Department of Electrical and Electronic Engineering, Universiti Malaysia Sarawak. Her research interests include electromagnetic direct/inverse scattering, optimisation techniques for microwave imaging, and computational electromagnetic.

Kismet Anak Hong Ping received the B.Eng. (Hons) degree in Electronics and Telecommunication Engineering from Universiti Malaysia Sarawak, Malaysia, M.Sc. in Digital Communication Systems from Loughborough University, England, and Ph.D. from Nagasaki University, Japan in 1999, 2000, and 2009, respectively.

Currently, he is an Associate Professor at the Department of Electrical and Electronic Engineering, Universiti Malaysia Sarawak. His current research interests focus on electro-magnetic direct/inverse scattering, microwave imaging, optimisation techniques, antenna design, and applications of electromagnetic fields to telecommunications and medicine.

Shafrida Sahrani received her B.E. degree in Information Networks, M.E., and Ph.D degrees in Computer Science, from Tokyo University of Technology, Tokyo, Japan in 2005, 2007, and 2013, respectively. She is a Senior Lecturer at the Department of Electrical and Electronic Engineering, Universiti Malaysia Sarawak. Her research interests include computational electromagnetics and microwave imaging.

Toshifumi Moriyama was born in Fukui prefecture, Japan, in 1972. He received B.E., M.E., and D.E. degrees in Information Engineering all from Niigata University, Niigata, Japan, in 1994, 1995, and 1998, respectively. In his theses research, he was engaged in radar polarimetry and polarimetric radar sensing of buried objects. He was with Fujitsu System Integration Laboratories Ltd from 1998 to 2003, the National Institute of Information and Communications Technology, Japan (NICT) from 2003 to 2005, and the Earth Observation Research and Application Center (EORC), Japan Aerospace and Exploration Agency (JAXA) in 2006, respectively. He is now an Associate Professor at the Department of Electrical and Electronic Engineering, Nagasaki University, Japan. He is involved in research activities in collaboration with ELEDIA Research Center, and he is the Director of the ELEDIA@UniNAGA. His interests are in inverse scattering, radar polarimetry, microwave remote sensing, and wireless sensor networks.

A New Method for Predicting Crosstalk of Hand-Assembled Cable Bundles

Chengpan Yang [1], Wei Yan [1,*], Yang Zhao [1], Shishan Wang [2], and Qiangqiang Liu [1]

[1] School of Electrical and Automation
Nanjing Normal University, Nanjing, Jiangsu, 210097, China

[2] Jiangsu Key Laboratory of New Energy Generation and Power Conversion
Nanjing University of Aeronautics and Astronautics, Nanjing, Jiangsu, 210016, China
*61197@njnu.edu.cn

Abstract ─ Hand-assembled cable bundles are random harness whose crosstalk is difficult to obtain accurately. A crosstalk prediction method of hand-assembled cable bundles is proposed in this paper. The harness is modeled by means of the mean pseudo-random number based on the cascade method. The factors considered in the model include the random exchange of wires position in the wiring harness cross section and the random rotation of the cross section to the ground. A mathematical description of the random exchange of wires position is made by using the row and column transformation of the per unit length RLCG parameter matrix. BP neural network with strong nonlinear mapping ability is introduced to describe the random rotation of wiring harness to the ground. Combined with the finite-difference time-domain (FDTD) method, the crosstalk of the wiring harness is predicted. Experimental results show that the new method has good accuracy in predicting crosstalk of hand-assembled cable bundles. The higher the twisting degree of the wiring harness is, the more concentrated the crosstalk is.

Index Terms ─ Crosstalk, finite-difference time-domain (FDTD), multiconductor transmission line (MTL), neural network, random bundles.

I. INTRODUCTION

In the field of aerospace and automobile machinery, transmission lines with some similar characteristics will be tightly fixed by manual binding for the convenience of wiring or aesthetics. A large number of transmission lines are laced together, which increases the possibility of electromagnetic interference (EMI) between wires. With the increase of working frequency, the EMI increases significantly, and the crosstalk between wiring harnesses cannot be ignored [1-2].

The traditional transmission line model is a uniform multiconductor transmission line (MTL). The crosstalk value can be obtained by solving the transmission line equation directly [3]. The wire position changes irregularly along the longitudinal dimension of the hand-assembled cable bundles, and the position of the wires in the section is random and unknown [4-5]. Due to the randomness of the wire position, the per unit length (p.u.l.) RLCG parameter matrix of different spatial locations may be different. It is difficult to predict the crosstalk of hand-assembled cable bundles directly by conventional methods. Broadly speaking, the crosstalk prediction of random wiring harness can be classified into probabilistic model which studies the basic theoretical parameters of crosstalk [6-7], and numerical solution method which simulates the actual random wire trajectories combined with Monte Carlo method [8-10].

In the last two or three decades, a large number of scholars have conducted prediction studies on random wiring harness [11-13], and most scholars have focused their research on the parameter matrix of the harness. In [14], the geometrically symmetrical conventional harness and the irregularly shaped harness are researched. It is verified that the crosstalk between the wires is mainly affected by the position of the generator and the receptor wires. Sun uses the random displacement spline interpolation (RDSI) algorithm to model a random wire harness. The model is used to predict the crosstalk of the harness and evaluate the effectiveness of the method in an experimental environment [15]. In [16-17], the hand-assembled cable bundles are segmented, assuming that the shape of the cross section remains unchanged with the bundle axial direction, and the cross section shape of all the small segments is unchanged. The probability distribution of the inductance and capacitance parameter matrix of a single wire harness cross section is analyzed by using statistical method, and then it is combined with the convolution principle to analyze the "reasonable worst-case" crosstalk of the harness.

The crosstalk of random stranded wiring harness can be predicted by the cascade method [18]. The finite-difference time-domain (FDTD) method is also a special cascade transmission line method in essence. Compared with the conventional cascade method, the FDTD

Submitted On: June 7, 2019
Accepted On: July 29, 2019

algorithm has the advantage of more spatial segments, higher accuracy and better adaptability to solve the crosstalk. The FDTD method can solve the crosstalk in time and frequency domain conveniently. Some scholars have applied the FDTD method to solve crosstalk with nonuniform MTLs [19-20].

The above literature only considers the exchange of wires position. Actually, there may be a change in the angle of the cross section to the ground after the wiring harness is segmented. Accordingly, the effect of the angle on the RLCG parameter matrix is explored in this paper. Furthermore, this paper proposes that the exchange of wires position is equivalent to the elementary transformation of the p.u.l. RLCG parameter matrix, which greatly simplifies the analysis of the influence of the random exchange of wires position on crosstalk. Considering the impact of rotation on the harness, the BP neural network is introduced. BP neural network has a strong non-linear mapping ability [21-23].

This paper is organized as follows. A model of the hand-assembled cable bundles is established in Section II. In Section III, the influence of random exchange of wires position on the parameter matrix is firstly expressed mathematically. Then, the influence of cross section rotation on the RLCG parameter matrix is analyzed by the BP neural network. In Section IV, a specific wiring harness model is analyzed by using the new method, probability method, and the experimental method. Section V gives the conclusions of this paper.

II. MODELING OF HAND-ASSEMBLED CABLE BUNDLES

Hand-assembled cable bundles are the random harness, but the "random" of the harness has its own characteristics. Combining the characteristics of the hand-assembled cable bundles model shown in Fig. 1, the *n*-core harness with length *d* is evenly divided into *N* segments, such as the length of S_1 and S_2 is equal. Therefore, the following assumptions are made for the modeling of the random wiring harness:

1) The parameters of each wire are identical, including the material and radius of the wire and insulation.

2) The transmission line in each segment is regarded as a parallel and uniform transmission line.

3) The wires in the harness are close together, and the geometric shapes of the cross sections at different positions remain unchanged.

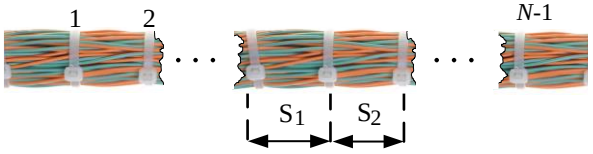

Fig. 1. Photo of the hand-assembled cable bundles.

Hand-assembled cable bundles change irregularly and randomly along the longitudinal dimension of the wiring harness. The randomness of wiring harness can be described by twisting degree β ($\beta \geqslant 0$). The more irregular the wiring harness is, the higher the twisting degree is. The twisting degree represents the number of segments divided per meter, which is obtained from experience. The number of segments *N* of the wiring harness is an integer related to twisting degree β, which satisfies the empirical formula:

$$N = \begin{cases} [\beta d] & \beta > \dfrac{1}{d} \\ 1 & \beta \leq \dfrac{1}{d} \end{cases}, \tag{1}$$

where [] is an integer symbol. The direction of the twisted wiring harness is arbitrary, and the number of twisted wires per segment is unknown (the wires in each segment are divided into twisted wires and untwisted wires).

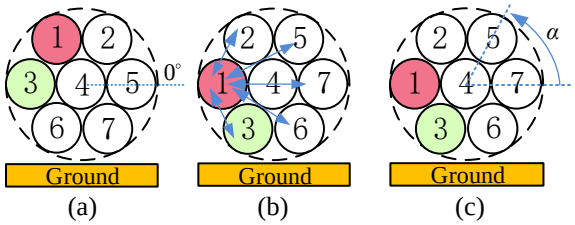

Fig. 2. Cross section of seven-core wiring harness: (a) reference, (b) position exchange, and (c) angle change.

According to the idea of the cascade method of the MTL, hand-assembled cable bundles can be segmented, and the wiring harness in the small segment can be regarded as a parallel MTL. For the convenience of the modeling process description, a seven-core wiring harness is used as an example. Along the axial direction, the wire position change may occur between the different segments, as shown in Fig. 2 (a) and Fig. 2 (b). In addition to the wire position change, the wiring harness may also have a rotation change of angle α ($\alpha \in [0,360°)$) as shown in Fig. 2 (a) and Fig. 2 (c). The effect of rotating a certain degree is similar to that of the wire position change. For example, the wiring harness in Fig. 2 (a) is rotated counterclockwise by 60° and is the same as the effect of Fig. 2 (b). However, only the rotation change cannot make the central wire (No. 4) in Fig. 2 participate in random exchange.

The schematic diagram of random harness modeling is shown in Fig. 3. Figure 3 (a) is a model schematic diagram of parallel MTL. Figure 3 (b) is a model schematic diagram considering only the random exchange of wires position, in which the geometric shapes of the cross section are unchanged relative to the reference ground. In this paper, if there is no special explanation, "random" refers to a random function that obeys uniform

distribution. Figure 3 (c) is a schematic diagram of a random harness model considering both the random rotation angle factor and the wires position exchange. Figure 3 (d) is a wire harness model diagram corresponding to Fig. 3 (c).

Obviously, if the positions of two wires can only be exchanged randomly at a time without considering the change of the rotation, any two cross sections can be converted to each other by n-1 exchange at most.

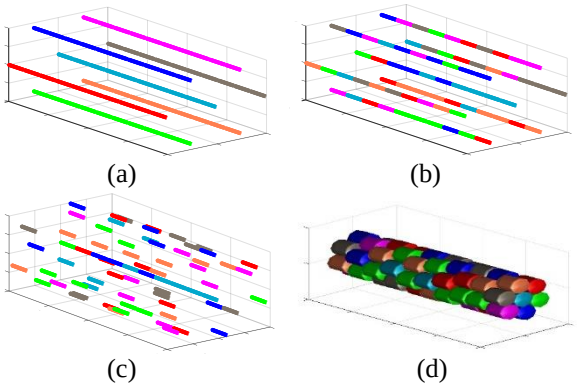

Fig. 3. Model of seven-core wiring harness: (a) parallel, (b) random exchange of wires position, (c) random rotation based the exchange of wires position, and (d) hand-assembled cable bundles.

III. CROSSTALK ANALYSIS OF HAND-ASSEMBLED CABLE BUNDLES

A. The p.u.l. RLCG parameter matrix considering the random exchange of wires position

For ease of study, consider only the changes in Fig. 3 (a) to Fig. 3 (b) in this part. The equivalent circuit of the p.u.l. MTLs is shown in Fig. 4, where dz is expressed as an infinitely short transmission line. The p.u.l. resistances of the circuit are represented by the entries r_i and r_j. The p.u.l. self-inductances and mutual inductances of the circuit are denoted by the entries l_{ii} and l_{ij}. The p.u.l. self-capacitances and mutual capacitances of the circuit are expressed by the entries c_{ii} and c_{ij}. The p.u.l. conductances of the circuit are described by the entries g_{ii} and g_{ij}. The resistance R, the inductance L, the capacitance C and the conductance G parameter matrix of the n-core wiring harness on the return plane are all $n\times n$ order matrices [3]. Specifically expressed as:

$$X=\begin{bmatrix} x_{11} & x_{12} & \cdots & x_{1i} & \cdots & x_{1j} & \cdots & x_{1n} \\ x_{21} & x_{22} & \cdots & x_{2i} & \cdots & x_{2j} & \cdots & x_{2n} \\ \vdots & \vdots & \ddots & \vdots & \vdots & \vdots & \vdots & \vdots \\ x_{i1} & x_{i2} & \cdots & x_{ii} & \cdots & x_{ij} & \cdots & x_{in} \\ \vdots & \vdots & \vdots & \vdots & \ddots & \vdots & \vdots & \vdots \\ x_{j1} & x_{j2} & \cdots & x_{ji} & \cdots & x_{jj} & \cdots & x_{jn} \\ \vdots & \vdots & \vdots & \vdots & \vdots & \vdots & \ddots & \vdots \\ x_{n1} & x_{n2} & \cdots & x_{ni} & \cdots & x_{nj} & \cdots & x_{nn} \end{bmatrix}, \tag{2}$$

where X stands for the R, L, C, and G parameter matrices, and the parameter matrix X is a symmetric matrix. x represents the value of resistance r, the inductance l, the capacitance c and the conductance g corresponding to different parameter matrices.

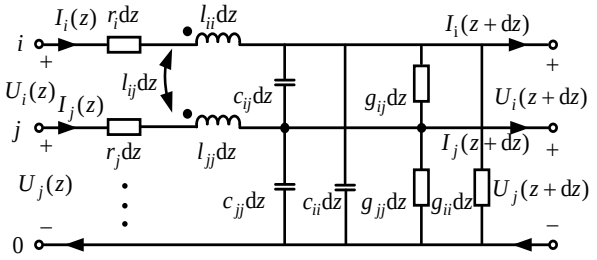

Fig. 4. The equivalent circuit of per unit length MTLs.

The transmission line equations are:

$$\frac{\partial}{\partial z}V(z,t)=-R(z)I(z,t)-L(z)\frac{\partial}{\partial t}I(z,t), \tag{3}$$

$$\frac{\partial}{\partial z}I(z,t)=-G(z)V(z,t)-C(z)\frac{\partial}{\partial t}V(z,t), \tag{4}$$

where $V(z,t)$ and $I(z,t)$ are voltages and currents at different locations and at different times on the MTLs [3]. The $R(z)$, $L(z)$, $C(z)$, and $G(z)$ parameter matrices are variables with respect to the position z of the MTLs, and the MTLs at different positions of the wiring harness may have different parameter matrices. According to the model of hand-assembled cable bundles in the previous section, it can be known that the position of the wires in the cross section of the segmented wiring harness has changed relative to the reference cross section.

Assume that only two wires have exchanged positions which are the i-th and j-th wires, respectively, and the corresponding parameter matrix after the exchange can be expressed as:

$$X'=\begin{bmatrix} x_{11} & x_{12} & \cdots & x_{1j} & \cdots & x_{1i} & \cdots & x_{1n} \\ x_{21} & x_{22} & \cdots & x_{2j} & \cdots & x_{2i} & \cdots & x_{2n} \\ \vdots & \vdots & \ddots & \vdots & \vdots & \vdots & \vdots & \vdots \\ x_{j1} & x_{j2} & \cdots & x_{jj} & \cdots & x_{ji} & \cdots & x_{jn} \\ \vdots & \vdots & \vdots & \vdots & \ddots & \vdots & \vdots & \vdots \\ x_{i1} & x_{i2} & \cdots & x_{ij} & \cdots & x_{ii} & \cdots & x_{in} \\ \vdots & \vdots & \vdots & \vdots & \vdots & \vdots & \ddots & \vdots \\ x_{n1} & x_{n2} & \cdots & x_{nj} & \cdots & x_{ni} & \cdots & x_{nn} \end{bmatrix}. \tag{5}$$

It can be seen from (2) and (5) that the row and column parameters irrelevant to i and j in the two parameter matrices remain unchanged. The parameter matrix in (5) can be obtained by exchanging the parameter matrix in (2) between the i-th row and the j-th row and between the i-th column and the j-th column.

The elementary matrix P_{ij} is defined as the matrix after the exchange of the i-th and the j-th row (or the i-th and the j-th column) of the identity matrix:

$$P_{ij}=\begin{bmatrix} 1 & 0 & \cdots & 0 & \cdots & 0 & \cdots & 0 \\ 0 & 1 & \cdots & 0 & \cdots & 0 & \cdots & 0 \\ \vdots & \vdots & \ddots & \vdots & \vdots & \vdots & \vdots & \vdots \\ 0 & 0 & \cdots & 0 & \cdots & 1 & \cdots & 0 \\ \vdots & \vdots & \vdots & \vdots & \ddots & \vdots & \vdots & \vdots \\ 0 & 0 & \cdots & 1 & \cdots & 0 & \cdots & 0 \\ \vdots & \vdots & \vdots & \vdots & \vdots & \vdots & \ddots & \vdots \\ 0 & 0 & \cdots & 0 & \cdots & 0 & \cdots & 1 \end{bmatrix}. \quad (6)$$

The relationship between X and X' can be expressed as:

$$X' = P_{ij} X P_{ij} . \quad (7)$$

When there are more than two wires exchange positions in the small segment, the parameter matrix after the exchange can be expressed as:

$$X' = P_k \ldots P_1 X P_1 \ldots P_k , \quad (8)$$

where $P_i(i=1,2,...,k)$ is an elementary matrix, k is the number of wire exchanges , $1 \leqslant k \leqslant n$-1.

The p.u.l. RLCG parameter matrix of any small segment in Fig. 3 (b) can be obtained by (8).

B. The p.u.l. RLCG parameter matrix considering the change of rotation angle

The analysis of the previous part only considers the wire position exchange in the small segment, without considering the rotation angle of the small segment to the ground. Since the hand-assembled cable bundles are the random harness, the position of the wires and the rotation angle of the small segments are both random. Different rotation angles correspond to different RLCG parameter matrices. It is difficult to obtain a parameter matrix of an arbitrary rotation angle by a conventional method. Any determined rotation angle of the small segment has its unique corresponding parameter matrix. There is a nonlinear mapping relationship between the rotation angle and the parameter matrix. Therefore, an algorithm with strong nonlinear mapping ability, BP neural network, is introduced in this paper. The specific mapping relationship is shown in Fig. 5.

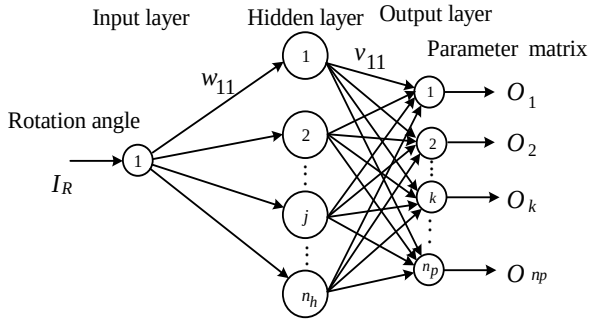

Fig. 5. Mapping topology of rotation degree and parametric matrix based on BP neural network.

In Fig. 5, the input parameter is the degree of rotation I_R, and the number of corresponding neurons is one. The output parameter is the RLCG parameter matrix, which is represented by the array O_P=[O_1, O_2,..., O_{np}], where n_p is the number of corresponding neurons. Its value is equal to the number of elements of the RLCG parameter matrix. According to the actual cross section, samples of the parameter matrix under different rotation degrees are collected and used to train the BP neural network. The BP neural network structure used in Fig. 5 belongs to the small to medium neural network, so one hidden layer can meet the requirements. The number of neurons in the hidden layer n_h is an empirical range value determined by the number of neurons in the input layer and the output layer, specifically:

$$n_h = \sqrt{1+n_p} + n_c , \quad (9)$$

where n_c stands for a constant of the interval [0, 10], and the specific value depends on the specific situation.

The sigmoid function $f_1(x)$ is used for input layer to hidden layer, and the linear function $f_2(x)$ is used for hidden layer to output layer. Respectively,

$$f_1(x) = \frac{1}{1+e^{-x}} , \quad (10)$$

$$f_2(x) = x . \quad (11)$$

After the signal propagates forward through the input layer, hidden layer and output layer of BP neural network, the p.u.l. RLCG parameter matrix output value O_k of the k-th output layer is:

$$O_k = \sum_{j=1}^{n_h} \frac{v_{jk}}{\exp\left(-\left(w_{1j} I_R + \theta_j\right)\right)+1} + b_k , \quad (12)$$

where w_{1j} denotes the weight between the input layer and the j-th hidden layer. The threshold of the j-th hidden layer is represented by θ_j. The weight between the j-th hidden layer and the k-th output layer is denoted by V_{jk}. The threshold of the k-th output layer is indicated by b_k.

The training sample data group is m. The iteration is stopped when the mean square error (MSE) between the output value and the target RLCG parameter matrix value y is less than the error precision E or the training times is not less than the max-epoch. Then the BP neural network outputs the weights and thresholds of each layer. Otherwise, training will continue. The error precision E can be expressed as:

$$E = \frac{1}{2m} \sum_{i=1}^{m} \sum_{j=1}^{n_p} (O_{ij} - y_{ij})^2 , \quad (13)$$

where O_{ij} stands for the value of the RLCG parameter matrix obtained by the j-th neuron of the output layer after the i-th training sample passes through the BP neural network. The sample standard value is represented by y_{ij}.

The training process is the adjustment process of the weights and thresholds. The weights of the two layers are similar to the threshold adjustment method. The weights between the hidden and output layer adjustment are illustrated as an example. The Levenberg - Marquardt (L-M) algorithm is used to adjust the values:

$$w_{k+1} = w_k + \Delta w_k , \tag{14}$$

$$\Delta w_k = -\left[J^T(w_k) J(w_k) + \mu I \right]^{-1} J^T(w_k) * e , \tag{15}$$

where w_k and w_{k+1} are the weights before and after the adjustment of each layer, respectively. And where J denotes the Jacobi matrix of the error e with respect to the weight w, μ is the scalar factor, and I stands for the identity matrix. The L-M algorithm controls the speed of the iteration by changing the value of μ. The error e is the MSE of each layer corresponding to each training sample:

$$e = \frac{1}{2} \sum_{k=1}^{n_p} (O_k - y_k)^2 , \tag{16}$$

where O_k represents the network output value of the hidden layer or the output layer and where y_k is the sample standard value. Through the analysis of this part, we obtain the p.u.l. RLCG parameter matrix considering the rotation angle of the small segment to the ground.

C. Crosstalk analysis

The transmission line equations (3) and (4) are processed by the Wendroff differential format to obtain the FDTD method expression of crosstalk [24]. The FDTD method divides the transmission line into a large number of small segments, and the number of small segments *NDZ* divided by the FDTD method is far more than the wiring harness segments *N*. Therefore, the crosstalk of the hand-assembled cable bundles can be calculated by the FDTD method in this paper.

The flow chart of crosstalk prediction for random wiring harness is shown in Fig. 6. It can be seen from the flow chart that the crosstalk solution of the segmented wiring harness can be divided into two parts, which are the extraction of the parameter matrix of each segment and the crosstalk solution using the FDTD method, respectively. In the process of extracting the parameter matrix for each segment, the RLCG parameter matrix samples with different rotation degrees are extracted by using the ANSYS Q3D software based on the finite element method (FEM) after selecting a reference cross section. The BP neural network that can map any rotation degree is obtained by training samples. Remarkably, the rotation degree of each segment to the ground is generated randomly in the interval [0, 360°), and the corresponding parameter matrix can be quickly solved by combining the trained BP neural network. In wire exchange, the number of exchanges is generated randomly in the interval [1, *n*-1], which corresponds to the number of elementary transformations of the p.u.l. RLCG parameter matrix. The number of two wires exchanged each time is a random number on the interval [1, *n*], which determines the elementary matrix of each transformation. According to the basic idea of the Monte Carlo method, the numerical characteristics of random variables can be used as a reference for the solution of the problem.

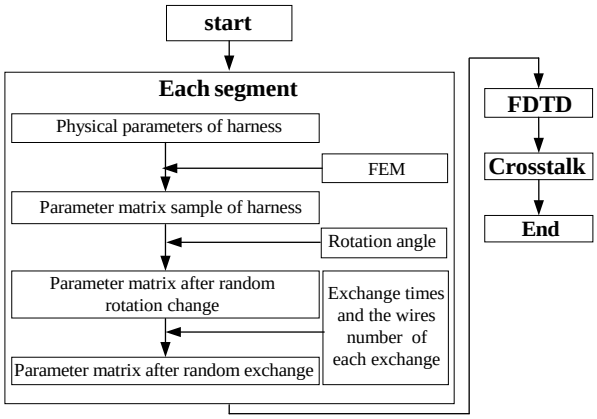

Fig. 6. Flow chart of random wiring harness crosstalk prediction.

IV. VERIFICATION AND ANALYSIS

In this paper, the seven-core hand-assembled cable bundles are used as an example to verify and analyze the new method. The single wire radius in the wiring harness is 0.4 mm and consists of 25 strands of thin copper wire. The insulating material of the wire is the polyvinyl chloride (PVC) with the relative permittivity of 2.7 and the thickness is 0.6 *mm*. The wire length is 3 *m*, and each end is terminated with a 50 Ω resistor. The details are shown in Table 1.

Table 1: Basic parameter of wiring harness

Name	Parameter
Single conductor radius	0.4 *mm*
Insulation thickness	0.6 *mm*
Insulation materials	PVC
Length	3 *m*
Terminated impedance	50 Ω

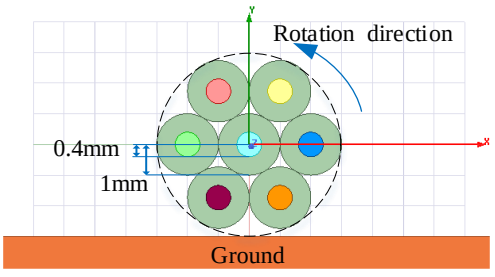

Fig. 7. The cross section and return plane of the seven-core wiring harness.

The cross section showed in Fig. 7 is taken as the reference cross section. The effect of the R and G parameters is ignored because the termination resistance value is much larger than the wire resistance. The inductance L and capacitance C parameter matrices of the reference cross section are:

$$L=\begin{bmatrix} 614.66 & 291.26 & 252.65 & 248.53 & 167.52 & 107.35 & 91.27 \\ 291.26 & 614.62 & 167.56 & 248.51 & 252.51 & 91.34 & 107.24 \\ 252.65 & 167.56 & 533.68 & 211.02 & 116.49 & 147.85 & 81.37 \\ 248.53 & 248.51 & 211.02 & 519.03 & 210.94 & 144.18 & 144.06 \\ 167.52 & 252.51 & 116.49 & 210.94 & 533.51 & 81.40 & 147.67 \\ 107.35 & 91.34 & 147.85 & 144.18 & 81.40 & 378.47 & 92.35 \\ 91.27 & 107.24 & 81.37 & 144.06 & 147.67 & 92.35 & 378.14 \end{bmatrix} \text{nH/m},$$

(17)

$$C=\begin{bmatrix} 64.61 & -21.39 & -21.00 & -15.45 & -1.024 & -0.67 & -0.12 \\ -21.39 & 64.61 & -1.03 & -15.45 & -20.99 & -0.12 & -0.67 \\ -21.00 & -1.03 & 66.10 & -15.41 & -0.19 & -18.80 & -0.51 \\ -15.45 & -15.45 & -15.41 & 93.00 & -15.41 & -15.17 & -15.18 \\ -1.024 & -20.99 & -0.19 & -15.41 & 66.082 & -0.51 & -18.80 \\ -0.67 & -0.12 & -18.80 & -15.17 & -0.51 & 82.01 & -15.41 \\ -0.12 & -0.67 & -0.51 & -15.18 & -18.80 & -15.41 & 82.00 \end{bmatrix} \text{pF/m}.$$

(18)

The parameter matrix of different rotation angles is sampled relative to the reference cross section, and the sampling rotation direction is shown in Fig. 7. All cross sections can be obtained by considering the rotation angle in the range of [0, 60°) and the random exchange of wires since the model discussed is axisymmetric. Samples were collected every 10° for a total of 12 groups.

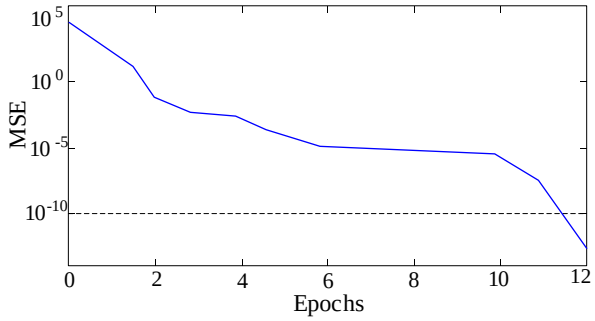

Fig. 8. Iteration number and MSE.

The relationship between the number of iterations and the training MSE of BP neural network is shown in Fig. 8. The training network satisfies the target MSE (E=10^{-10}) when the number of iterations is 12.

In order to verify the correctness and effectiveness of the proposed method, a simple crosstalk test platform is built shown in Fig. 9. The corresponding experimental schematic diagram is shown in Fig. 10. The whole wiring harness is placed on the return plane of the same length, and the width of the return plane is much larger than the distance of the harness from the return plane. The material of the return plane is copper. The Agilent 87511A vector network analyzer (VNA) is used as a measuring device.

The crosstalk comparison results of the seven-core hand-assembled cable bundles with the twisting degree β=6 and β=2 are shown in Fig. 11 (a) and Fig. 11 (b), respectively. The green solid line represents the result of the new method. The blue solid line stands for the result of the experiment. The red dashed line is the outer envelope of the green line. And the black dashed line is the outer envelope of the result of the probability method [25]. It can be observed in Fig. 11 that the experimental results and the method presented in this paper have high consistency. The experimental results are almost within the upper envelope of the results of the proposed method, which means that the proposed method can predict the "worst case" crosstalk of the harness. By comparison, the higher the twisting degree, the more concentrated the crosstalk, and the crosstalk of the low frequency band is more concentrated than the high frequency band. It can be understood that the higher the twisting degree of the wiring harness, the more the crosstalk tends to "average", so the more the crosstalk is concentrated. The more concentrated the curves, the smaller the distance between the upper and lower envelopes of the predicted value.

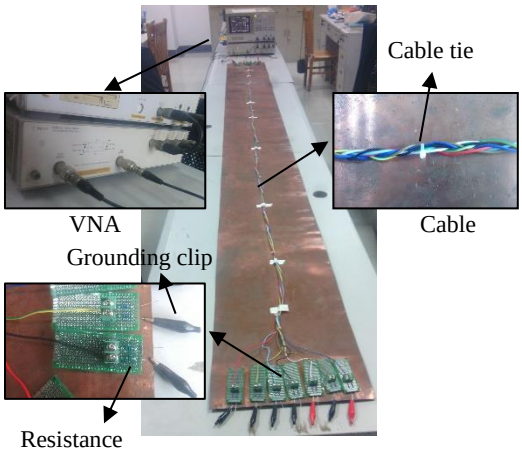

Fig. 9. Crosstalk measurement experimental platform.

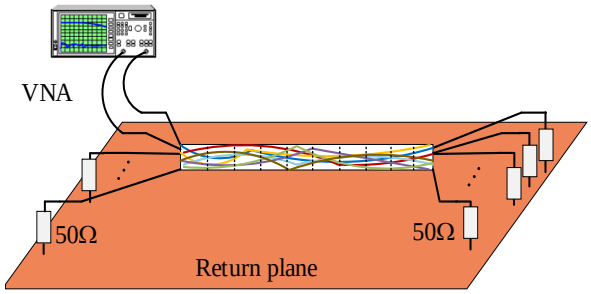

Fig. 10. Schematic diagram of experiment.

In the frequency band of 0.1 MHz - 3 MHz, both the new method and the probability method can predict the "worst case" crosstalk of the harness, but the distance between the lower envelope and upper envelope of the

new method is obviously smaller than that of the probability method. The accuracy of the new method is higher than that of the probability method. In the frequency band of 3 MHz - 40 MHz, the accuracy of the new method is higher than that of the probability method. The lower envelope of the probability method at some frequency points is even larger than the maximum of the experimental results in Fig. 11 (b). Moreover, the prediction range of the probability method in the frequency band of 10 MHz - 25 MHz is too large and has little practical significance. In the frequency band of 40 MHz-100 MHz, the accuracy of the new method and the probability method is not as good as that of the low frequency band, but the trend of the new method is closer to the experimental results. The trend predicted by probability method is not consistent with the experimental results and the range of predicted values is too large.

In [17], it mainly aims at the frequency band less than 10^7 Hz. Compared with [17], the crosstalk frequency band predicted by the new method is wider.

However, it can be clearly seen that at some points of high frequency, the lower envelope and the upper envelope solved by the new method or the probability method are not completely consistent with the experimental test results. The possible reason is that the high frequency characteristics of the components and devices used in the experiment are not completely ideal.

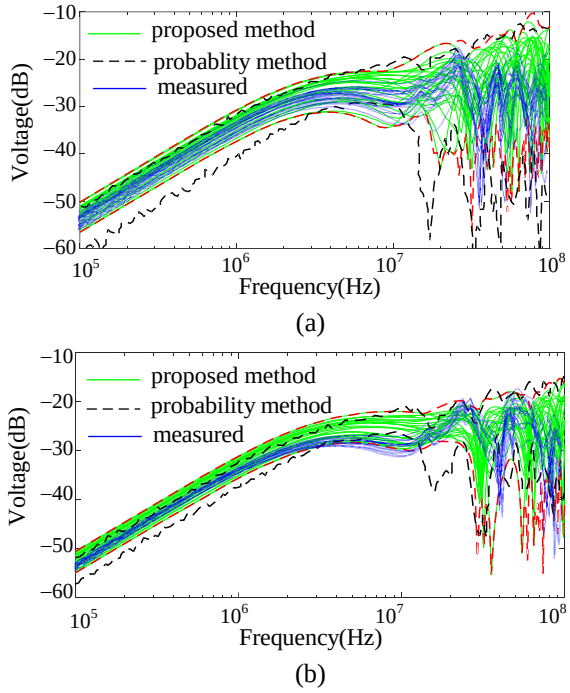

Fig. 11. Comparison of seven-core hand-assembled cable bundles crosstalk solved by different methods: (a) β = 2 and (b) β = 6.

V. CONCLUSION

The crosstalk of hand-assembled cable bundles based on the FDTD method is studied in this paper. The comparison between experiment and simulation shows that after 12 iterations, BP neural network can reflect the mapping of the rotation degree and the p.u.l. RLCG parameter matrix. The proposed method has better prediction accuracy than probability method for the crosstalk of random wiring harness. The crosstalk of wiring harness is widely distributed in high frequency band and relatively concentrated in low frequency band. The higher the twisting degree of the wiring harness, the more concentrated the crosstalk in the whole frequency band.

ACKNOWLEDGMENT

The work was supported by National Natural Science Foundation of China under Grant No.51475246, National Natural Science Foundation of Jiangsu Province under Grant No.BK20161019, and Aviation Science Foundation under Grant No.20172552017.

REFERENCES

[1] S. Chabane, P. Besnier, and M. Klingler, "A modified enhanced transmission line theory applied to multiconductor transmission lines," *IEEE Trans. on Electromagn. Compat.*, vol. 59, no. 2, pp. 518-528, Apr. 2017.

[2] Y. Wang, Y. S. Cao, D. Liu, R. W. Kautz, N. Altunyurt, and J. Fan, "A generalized multiple-scattering method for modeling a cable harness with ground connections to a nearby metal surface," *IEEE Trans. Electromagn. Compat.*, vol. 61, no. 1, pp. 261-270, Feb. 2019.

[3] C. R. Paul, *Analysis of Multiconductor Transmission Lines*. Wiley, New York, 1994.

[4] S. Shiran, B. Reiser, and H. Cory, "A probabilistic method for the evaluation of coupling between transmission lines," *IEEE Trans. Electromagn. Compat.*, vol. 35, no. 3, pp. 387-393, Aug. 1993.

[5] C. R. Paul, "Sensitivity of crosstalk to variations in wire position in cable bundles," *1987 IEEE International Symposium Electromagnetic Compatibility*, Atlanta, GA, pp. 1-5, Aug. 1987.

[6] Z. Fei, Y. Huang, J. Zhou, and Q. Xu, "Uncertainty quantification of crosstalk using stochastic reduced order models," *IEEE Trans. Electromagn. Compat.*, vol. 59, no. 1, pp. 228-239, Feb. 2017.

[7] G. Spadacini, F. Grassi, and S. A. Pignari, "Field-to-wire coupling model for the common mode in random bundles of twisted-wire pairs," *IEEE Trans. Electromagn. Compat.*, vol. 57, no. 5, pp. 1246-1254, Oct. 2015.

[8] S. A. Pignari, G. Spadacini, and F. Grassi, "Modeling field-to-wire coupling in random

bundles of wires," *IEEE Electromagnetic Compatibility Magazine*, vol. 6, no. 3, pp. 85-90, Nov. 2017.

[9] M. Gonser, C. Keller, J. Hansen, and R. Weigel, "Advanced simulations of automotive EMC measurement setups using stochastic cable bundle models," *2010 Asia-Pacific International Symposium on Electromagnetic Compatibility*, Beijing, China, pp. 590-593, Apr. 2010.

[10] A. Ciccolella and F. G. Canavero, "Stochastic prediction of wire coupling interference," *Proceedings of International Symposium Electromagnetic Compatibility.*, Atlanta, GA, pp. 51-56, Aug. 1995.

[11] P. Manfredi, D. De Zutter, and D. V. Ginste, "Analysis of coupled exponential microstrip lines by means of a multi-step perturbation technique," *IEEE 20th Workshop on Signal and Power Integrity (SPI)*, Turin, Italy, pp. 1-4, May 2016.

[12] D. Bellan and S. A. Pignari, "Statistical superposition of crosstalk effects in cable bundles," *China Communications*, vol. 10, no. 11, pp. 119-128, Nov. 2013.

[13] J. C. Pincenti and P. L. E. Uslenghi, "Incident field excitation of random cables," *Radio Science*, vol. 42, no. 06, pp. 1-10, Dec. 2007.

[14] D. Bellan and S. A. Pignari, "Efficient estimation of crosstalk statistics in random wire bundles with lacing cords," *IEEE Trans. Electromagn. Compat.*, vol. 53, no. 1, pp. 209-218, Feb. 2011.

[15] S. Sun, G. Liu, J. L. Drewniak, and D. J. Pommerenke, "Hand-assembled cable bundle modeling for crosstalk and common-mode radiation prediction," *IEEE Trans. Electromagn. Compat.*, vol. 49, no. 3, pp. 708-718, Aug. 2007.

[16] M. Wu, D. Beetner, T. Hubing, Haixin Ke, and S. Sun, "Estimation of the statistical variation of crosstalk in wiring harnesses," *2008 IEEE International Symposium on Electromagnetic Compatibility*, Detroit, MI, pp. 1-7, Aug. 2008.

[17] M. Wu, D. G. Beetner, T. H. Hubing, H. Ke, and S. Sun, "Statistical prediction of "Reasonable Worst-Case" crosstalk in cable bundles," *IEEE Trans. Electromagn. Compat.*, vol. 51, no. 3, pp. 842-851, Aug. 2009.

[18] S. Salio, F. Canavero, D. Lecointe, and W. Tabbara, "Crosstalk prediction on wire bundles by Kriging approach," *IEEE International Symposium on Electromagnetic Compatibility*, Washington, DC, vol. 1, pp. 197-202, Aug. 2000.

[19] A. Tatematsu, F. Rachidi, and M. Rubinstein, "A technique for calculating voltages induced on twisted-wire pairs using the FDTD method," *IEEE Trans. Electromagn. Compat.*, vol. 59, no. 1, pp. 301-304, Feb. 2017.

[20] V. R. Kumar, B. K. Kaushik, and A. Patnaik, "An accurate FDTD model for crosstalk analysis of CMOS-Gate-Driven coupled RLC interconnects," *IEEE Trans. Electromagn. Compat.*, vol. 56, no. 5, pp. 1185-1193, Oct. 2014.

[21] T. Rashid, *Make Your Own Neural Network, Charleston*. Create Space Independent Publishing Platform, Charleston, 2016.

[22] M. Hassoun, *Fundamentals of Artificial Neural Networks*, Bradford Book, Cambridge, 2003.

[23] F. Dai, G. Bao, and D. Su, "Crosstalk prediction in non-uniform cable bundles based on neural network," *Proceedings of the 9th International Symposium on Antennas, Propagation and EM Theory*, Guangzhou, China, pp. 1043-1046, Nov. 2010.

[24] L. Brančík and N. Al-Zubaidi R-Smith, "Comparative simulations of hybrid systems with nonuniform MTLs via Wendroff and NILT based techniques," *2016 Progress in Electromagnetic Research Symposium (PIERS)*, Shanghai, China, pp. 4067-4072, Aug. 2016.

[25] Z. Zhang, S. Wang, and L. Zhao, "Prediction of crosstalk probability distribution in cable bundles," *Transactions of China Electrotechnical Society*, vol. 32, no. 7, pp. 203-214, Apr. 2017.

Chengpan Yang was born in Sichaun Province, China. He received the B.S. degree in School of Automation and Information Engineering from Sichuan University of Science and Engineering, Zigong, China, in 2017. He is currently working toward the Master's degree in electrical engineering at Nanjing Normal University, Nanjing, China. His major research interests include new technology of electrical engineering.

Wei Yan Doctor & Assoc. Professor from Nanjing Normal University. He obtained the Physics and Electronics Ph.D and Electrical Engineering M.S. from Nanjing Normal University in 2014 and 2011. He is the Senior Member of China Electrical Technology Association and the evaluation expert of the Electromagnetic Compatibility Calibration Specification of China.

Yang Zhao received his B.E., M.E., and Ph.D. degree all in Power Electronic Technology from Nanjing University of Aeronautics and Astronautics, Nanjing, China, in 1989 and 1992, and 1995, respectively. He is currently the Professor with Nanjing Normal University. His research interests are in the areas of Electromagnetic Compatibility, Power Electronics and Automotive Electronics.

Shishan Wang received the Ph.D. degree from Xi'an Jiaotong University, Xi'an, China, in 2003. Since 2004, he has been an Associate Professor with the College of Automation Engineering Nanjing University of Aeronautics and Astronautics, Nanjing, China. His main research interests include electromagnetic compatibility in power electronics system and simulation of multiphysics fields for electrical equipment.

Qiangqiang Liu was born in Anhui Province, China. He received the B.S degree in school of Electrical Engineering and Automation from Anhui University of Science and Technology, Huainan, China, in 2018. He is currently working toward the Master's degree in Electrical Engineering at Nanjing Normal University, Nanjing, China. His major research interests include new technology of electrical engineering.

A K-band Spoof Surface Plasmon Polaritons Bandstop Filter with Capacitively Loaded Split-ring Resonator

Peng Chen [1,2], Luping Li [1], Zhijie Wang [1], and Kai Yang [1,2*]

[1] School of Aeronautics and Astronautics
University of Electronic Science and Technology of China, Chengdu, 611731, P. R. China

[2] Aircraft Swarm Intelligent Sensing and Cooperative Control
Key Laboratory of Sichuan Province, Chengdu, 611731, P. R. China
kyang@uestc.edu.cn

Abstract ─ A K-band bandstop filter based on the spoof surface plasmon polaritons (SPP) and the capacitively loaded split-ring resonator (RSS) is proposed in this paper. The capacitively loaded RSS consists of two parts: the traditional rectangle RSS and a T-type stub placed at the center of the arm microstrip line of the rectangle RSS. Thanks to the capacitively loaded RSS, the operating frequency of the resonator is reduced, which is helpful for miniaturizing the circuit size. The dispersion feature of the capacitively loaded RSS is studied by simulation and the geometrical parameters effects on the filter's final performance are discussed. A K-band bandstop filter with spoof SPP and capacitively loaded RSS is designed, fabricated and measured to verify the proposed design methodology. The measured results show that the bandstop filter works at 21.05 GHz-22.95 GHz with more than 40 dB insertion loss.

Index Terms ─ Bandstop filter, capacitively loaded stub, split-ring resonator, spoof surface plasmon polaritons.

I. INTRODUCTION

The classical surface plasmon polariton (SPP) is a kind of electromagnetic (EM) wave which transmits along the metal-air interface in the infrared and visible frequency [1]. Comparing with the traditional microstrip line, the classical SPP has less radiation loss since the EM wave vertical to the metal-air interface attenuates exponentially. It is considered as a promising structure for high-frequency EM wave transmission and widely applied on various optical components design [2-4]. However, the SPP only exists at far-infrared range. In order to make the SPP work at radio frequency (RF) and microwave frequency, various planer spoof SPPs, which have the similar characters of the natural SPP, have been invented in recent years [5].

The bandstop filter, also named as notch filter or reject filter, plays an important role in wireless communication system for its ability to suppress harmonic or unwanted wave, reduce mutual coupling and decrease spurious and leakage transmission [6]. The traditional planer bandstop filter design methods include bandstop stubs, defected ground structures, split-ring resonator, non-resonating nodes filters, extracted pole techniques and coupled resonator and so on. Traditional planer bandstop filters have serious dielectric loss at K-band and even higher-frequency band, resulting large heating in the dielectric material and EM radiation.

As mentioned above, the planer spoof SPP is a low dielectric loss structure and can be designed to pass or stop specified spectrum. The spoof bandstop filter is one of these applications. There are several reported works about the spoof SPP bandstop filter [7-15]. The first reported spoof SPP bandstop filter etched the additional resonator at the backside of the spoof SPP transmission line or at the top side of each stubs of the spoof SPP structure [7]. Soon this work was extended to the tunable metamaterials [8]. A spoof SPP bandstop filter was designed by adding the circular resonator with special holes at the side of the spoof SPP transmission line [9]. Another reported work placed the complementary SRR unit between two stubs of the spoof SPP transmission line for better rejection performance [10]. Furthermore, using the H-shape structures metamaterial particle, the double-side corrugated spoof SPP transmission line also showed bandstop features [11]. Ref [12] verified that by placing a conventional microstrip at the bottom center of a symmetrically periodically corrugated metallic strip showed the similar feature of the localized spoof surface plasmon and can be used to design bandstop filter. The single SRR unit set between two neighboring stubs of the spoof SRR transmission line also was can be applied for

Submitted On: July 25, 2019
Accepted On: February 12, 2020

bandstop filter [13]. Then a spoof SPP bandstop filter with the three different type folded split-ring resonator were presented to design dual-band and tri-band bandstop filter [14]. All these reported spoof SPP bandstop filters have similar performance and design methodologies, such as adding special unit between two neighboring stubs of the spoof SRR transmission line to get the bandstop unit, which is the fundamental base for the bandstop filter design, and controlling the bandstop filter's performance by just adjusting the parameters of their bandstop unit.

Inspired by these above-mentioned works, a novel spoof SPP bandstop filter is proposed in this paper. A capacitively loaded RSS is set between two neighboring stubs of the spoof SRR transmission line. Furthermore, the capacitively loaded RSS and the two neighboring stubs of the spoof SRR transmission line work together as a bandstop unit. The capacitively loaded RSS could reduce the resonating frequency of the bandstop unit and bringing in extra design freedom to optimize the filter's performance.

II. FILTER DESIGN

The traditional spoof SPP filter is displayed in Fig. 1. It consists of three parts. The first part is the standard 50 Ω microstrip line as the input/output port. The third part is the spoof SPP transmission line which is composed of the same height vertical stubs and a horizontal microstrip line connecting these vertical stubs together. The second part is the mode transfer part which transfer the quasi-TEM mode of the microstrip line to the spoof SPP mode of the spoof SPP transmission line.

The traditional spoof SPP unit has the lowpass feature and the cut-off frequency is decided by the height of the stubs. As the stubs become longer, the cut-off frequency becomes lower and vice versa. If an RSS unit is placed between the two neighboring stubs of the spoof SPP transmission line, the new structure performs bandstop feature. This phenomenon can be explained as follows. As the traditional strip-line bandstop filter, the SRR unit is capacitively coupled to the main EM transmission structure. The main EM transmission line is the spoof SPP transmission line in the spoof SPP bandstop filter while it is the microstrip line in the traditional strip-line bandstop filter. The capacitively coupling is realized by the physical circuit gap between the SRR and the main EM transmission line. The SRR performs as the serial LC circuit and often is realized by one quarter open stub.

Since the rejected frequency of the whole bandstop filter is determined by the resonating frequency of the SRR, the circuit miniaturization can be achieved by reducing the resonating frequency of the SRR. The T-type stub is inserted in the center of the horizontal arm of the SRR structure. It brings in three design freedom. The SRR, the T-type stubs and the two neighboring stubs of the spoof SRR transmission line work together to be as a bandstop filter's fundamental resonating unit, which is shown in Fig. 2. The whole bandstop filter is illustrated in Fig. 3.

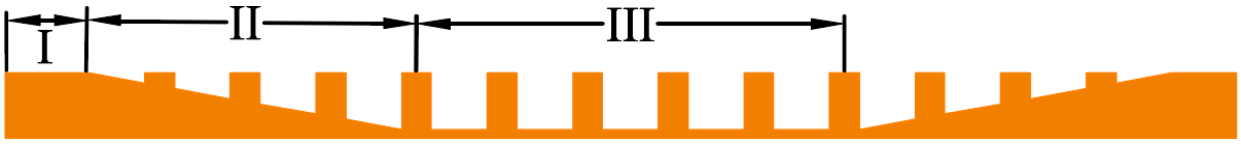

Fig. 1. The schematic of the traditional lowpass spoof SPP filter.

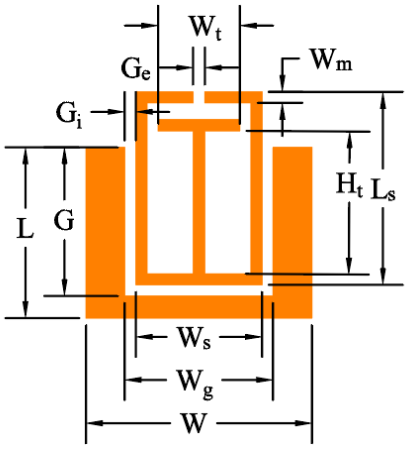

Fig. 2. Schematic of the proposed spoof SPP bandstop filter resonating unit.

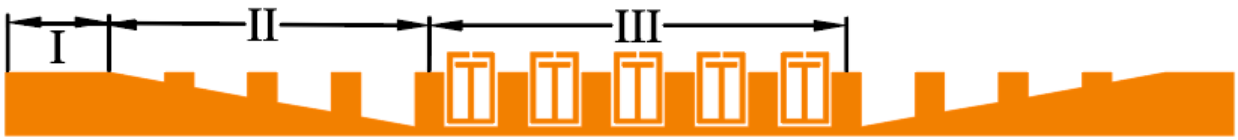

Fig. 3. The schematic of the proposed spoof SPP based bandstop filter with capacitively loaded RSS.

A. Dispersion analysis

To understand the performance of the whole bandstop filter, the dispersion of the single bandstop resonating unit shown in Fig. 2 is analyzed. The initial parameters of this unit are set as follows. The stub height G is 1.34 mm. The height L is 1.54 mm. The length of the comb-shaped unit W_g is 1.34 mm. The length W is 2.04 mm. The length W_s is 1.14 mm. The gap G_i and G_e are both 0.1 mm. The length W_t is 0.74 mm. The height H_t is 1.29 mm. All the line widths of the bandstop resonating unit are 0.1 mm. The dielectric coefficient of the substrate is 2.2 and the height of the substrate is set as 0.508 mm. Back of the substrate is covered by the annealed copper.

The Floquet method in the CST Microwave Studio® full-wave electromagnetic simulating platform is used to study the dispersion of the bandstop resonating unit. The simulated results are shown in Fig. 4. The fundamental, second harmonic and third harmonic modes of the proposed bandstop resonating unit are named as mode 1, mode 2 and mode 3 in Fig. 4, respectively. The black dot line is the dispersion of the calculated EM wave in the vacuum and the black dash line is the fundamental mode of the traditional spoof SPP unit for comparing purpose. There is gray frequency gap between the model 1 and mode 2, which is the bandstop spectrum of the proposed bandstop resonating unit. It is very safe to predict that the filter based on the proposed bandstop resonating unit has a rejection bandwidth between 22 GHz and 23 GHz. Furthermore, the cut-off frequency of the final filter based on the bandstop resonating unit is about 27 GHz since it is determined by the cut-off frequency of the traditional spoof SPP.

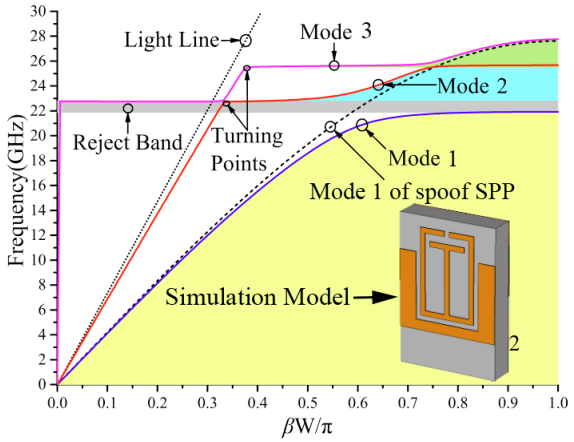

Fig. 4. Dispersion simulation of the spoof SPP unit.

It is note that the cut-off frequency of the proposed bandstop resonating unit is much lower than that of the EM wave in vacuum, which means that this unit behaves slow-wave feature, which is typical feature of the spoof SPP.

B. Equivalent circuit model

To theoretically understand the resonating frequency, the equivalent circuit model is built in Fig. 5, where ML is the microstrip line, CML is the coupling microstrip line, respectively. The ML1 and CML1 are utilized to simulate the performance of the coupling effect between the left-side stub and the left-side rectangle SRR while the ML2 and CML2 are utilized to simulate the feature of the coupling effect between the right-side stub and right-side rectangle SRR. The ML2, ML3 and ML4 are used to simulate the performance of the T-type stubs.

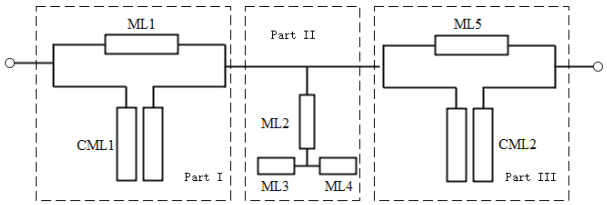

Fig. 5. Equivalent circuit model of the proposed spoof SPP filter unit.

The characteristic impedance of ML1, ML2, ML3 and ML4 is Z_{L1}, Z_{L2}, Z_{L3} and Z_{L4}, the corresponding electric length is θ_{L1}, θ_{L2}, θ_{L3} and θ_{L4}, the even-mode and odd-mode characteristic impedance of CML1 is z_{pe} and z_{po} and the corresponding electric length is θ_{pe} and θ_{po}, respectively. The structure of the whole circuit is centrosymmetric and the parameters of the ML1 and ML5, CML1 and CML2 are the same. Now the part I in Fig. 5 is discussed.

The ABCD matrix of ML1 is:

$$F_1 = \begin{bmatrix} \cos(\theta_{L1}) & jZ_{L1}\sin(\theta_{L1}) \\ j\sin(\theta_{L1})/Z_{L1} & \cos(\theta_{L1}) \end{bmatrix}. \quad (1)$$

The ABCD matrix of CML1 is:

$$F_2 = \begin{bmatrix} \dfrac{Z_{pe}\cot(\theta_{pe})+Z_{po}\cot(\theta_{po})}{Z_{pe}\cot(\theta_{pe})-Z_{po}\cot(\theta_{po})} & -j\dfrac{2Z_{pe}Z_{po}\cot(\theta_{pe})\cot(\theta_{po})}{Z_{pe}\cot(\theta_{pe})-Z_{po}\cot(\theta_{po})} \\ j\dfrac{2}{Z_{pe}\cot(\theta_{pe})-Z_{po}\cot(\theta_{po})} & \dfrac{Z_{pe}\cot(\theta_{pe})+Z_{po}\cot(\theta_{po})}{Z_{pe}\cot(\theta_{pe})-Z_{po}\cot(\theta_{po})} \end{bmatrix}. \quad (2)$$

The ABCD matrix of part II is:

$$F_3 = \begin{bmatrix} 1 & 0 \\ Y_{p2} & 1 \end{bmatrix}, \quad (3)$$

where Y_{p2} is the conductance of ML2, ML3 and ML4. Considering $Z_{L3} = Z_{L4}$ and $\theta_{L3} = \theta_{L4}$, we have:

$$Y_{p2} = \frac{j}{Z_{L2}} \frac{Z_{L2} + Z_{L3}\cot(\theta_{L3})\tan(\theta_{L2})}{Z_{L3}\cot(\theta_{L3}) - Z_{L2}\tan(\theta_{L2})}. \quad (4)$$

The ABCD matrix of the whole circuit is:

$$F = \begin{bmatrix} A & B \\ C & D \end{bmatrix} = F_1F_2F_3F_2F_1. \quad (5)$$

The resonating condition is:

$$Y = \frac{C}{A} = 0, \quad (6)$$

which can be changed as:

$$\begin{cases} \text{Real}(Y) = 0 \\ \text{Imag}(Y) = 0 \end{cases}. \quad (7)$$

For simplification, we set $\theta_{pe} = \theta_{po} = \theta_p$. The real part of Y is identical with 0. We just need to make sure the imaginary part of Y is equal to zero. As a matter of fact, the numerator of the imaginary part of Y can be written as:

$$\begin{aligned} &\tan(\theta_{L3})*((Z_{pe} + Z_{po})Z_{L1}\cos(\theta_{L1}) \\ &+ 2Z_{pe}Z_{po}\cot(\theta_p)\sin(\theta_{L1})Y_{i3} = 0 \end{aligned}, \quad (8)$$

where Y_{i3} is a very complicated function of the above-mentioned parameters and it is impractical to control this complicated express to reach the resonating condition.

i) If θ_{L3} is not equal to 0, the resonating condition is decided as follow:

$$\frac{\tan(\pi - \theta_{L1})}{\tan(\theta_p)} = \frac{(Z_{pe} + Z_{po})Z_{L1}}{2Z_{pe}Z_{po}}, \quad (9)$$

which means that the resonating condition of the proposed bandstop resonating unit is only related with the rectangle SRR and the stubs of the spoof SPP.

ii) If θ_{L3} is equal to 0, the bandstop resonating unit also can resonate.

It is worthy to note that the proposed equivalent circuit model is only roughly simulate the real circuit. It does not mean that the T-type stub is not related with the performance of the proposed filter. It provides import information that the stop bandwidth is mainly predicted by the coupling between the stub from the spoof SPP and the rectangle SRR. We can design the parameters of the stubs of the traditional spoof SPP transmission line and the rectangle SRR and then add the T-type stub for optimizing the final performance.

B. Filter design

As the traditional spoof SPP lowpass filter in Fig. 1, the proposed spoof SPP bandstop filter is also composed of three parts: Part I, Part II and Part III, which is shown in Fig. 3. Part I is a 50 Ohm microstrip line as the input/output port, which transmits the quasi-TEM wave. Part III is the spoof SPP transmission line part which contains five periodically arranged proposed units and transmits spoof SPPs wave. This part is the key of the filter which determines the final feature of the proposed bandstop filter. Part II is a mode conversion part which transforms the quasi-TEM of the microstrip line to the spoof SPPs wave of the spoof SPP part. The whole structure of the proposed filter is centrosymmetric.

The filter is designed on Rogers 5880 substrate with 2.2 dielectric coefficient and 0.508 mm height. It is simulated in CST Microwave Studio® and the simulation results are illustrated in Fig. 5. According to simulated S_{21}, a rejection band is inserted in the low-pass band. Accordingly, the proposed filter has the bandstop feature as previous dispersion analysis. In the bandstop band, 3 dB rejection points are 21.32 GHz and 22.94 GHz, respectively. The center frequency of the bandstop band is 22.13 GHz and 3 dB bandstop bandwidth is 1.62 GHz. The maximal rejection depth is 46.5 dB.

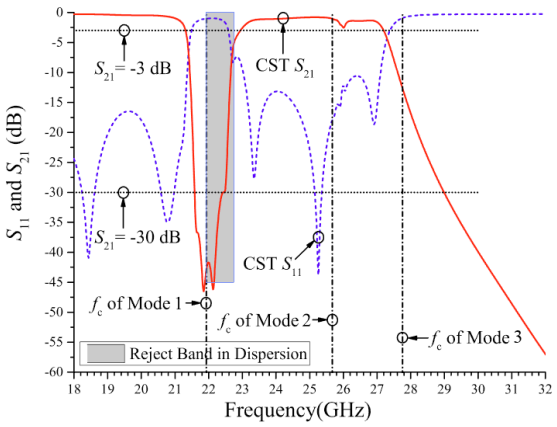

Fig. 5. Simulated S_{11} and S_{21} of the proposed filter. The gray band is bandstop band in dispersion of the proposed unit and f_c is cut-off frequency.

In the first passband, when the frequency increases from 10 GHz to 20.5 GHz, the insertion loss changes from 0.16 dB to 0.52 dB. In the second passband, the maximal insertion loss is 2.5 dB at the depression point and the minimal insertion loss is 0.9 dB. Moreover, 3 dB cut-off frequency of the filter is 27.2 GHz and the out-of-band rejection can reach more than 60 dB.

The gray region in Fig. 5 is the rejection band predicted by the dispersion analysis, which is in the rejection band of the final filter. In addition, the high cut-off frequency of the simulated rejection band is close to the predicted high cut-off frequency of the dispersion analysis while the low cut-off frequency of the simulated rejection band is lower than that of the dispersion results, which may be caused by the added T-type stub. In mode 1 and mode 3, both the cut-off frequencies are in the rejection band, which proves correspondence between

rejection bands of the modes and the filter. In mode 2, depression point in S_{21} is near the cut-off frequency of the mode, which proves that the cut-off effect of mode 2 functions and it degrades S_{21} of the filter. In summary, the bandstop band and the cut-off points of dispersion agree with the filter, which proves effectiveness of the proposed spoof SPPs unit and filter design approach.

C. Performance of capacitively loaded RSS

One of the main differences of the proposed spoof SPP bandstop filter is to add a T-type stub into the rectangle RSS to increase the spurious suppression and reduce the resonating frequency. As illustrated in Fig. 6, the spoof SPP filter with capacitively loaded RSS with T-type stub has lower resonating frequency than the spoof SPP filter with single SRR. Moreover, the spurious of the spoof SPP filter with capacitively loaded SRR with T-type stub has 5 dB lower than the spoof SPP filter with single RSS in the left side of the rejection band while the spurious suppressions of the right sideband keep the same.

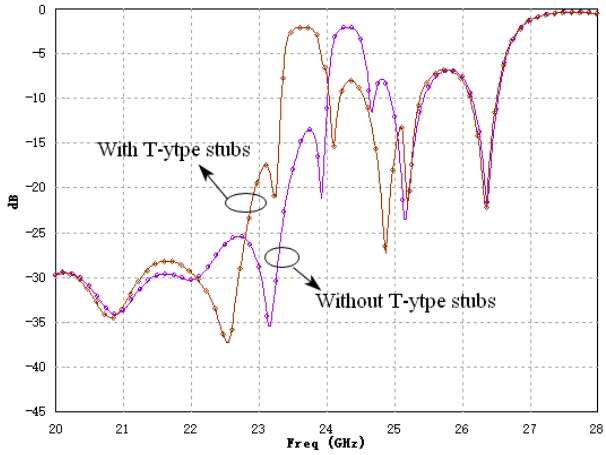

Fig. 6. The simulated results of the spoof SPP bandstop filter with/without the T-type stubs.

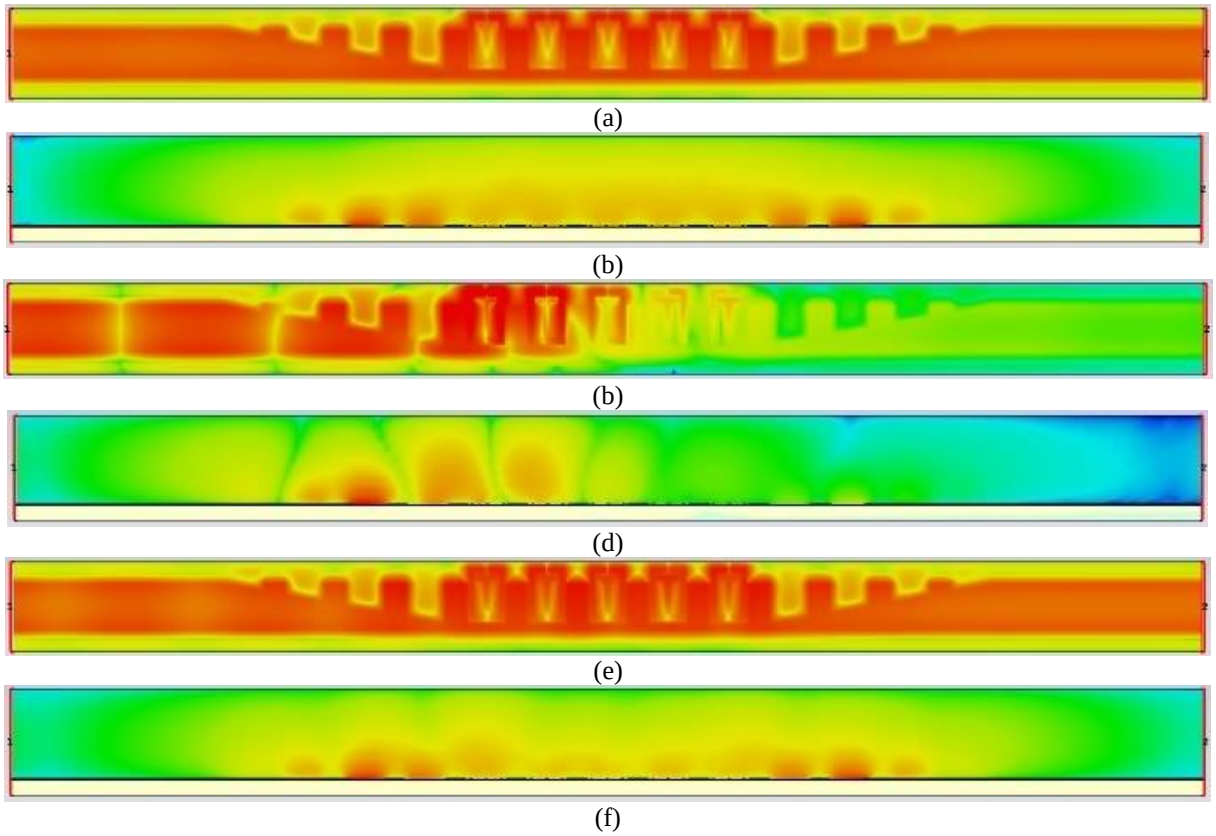

Fig. 7. The simulated electric fields of the spoof SPP filter: (a) top view of the passband at 19 GHz, (b) side view of the passband at 19 GHz, (c) top view of the stopband at 21 GHz, (d) side view of the stopband at 21 GHz, (e) top view of the passband at 24 GHz, and (f) side view of the passband at 24 GHz.

Figure 7 displays the simulated electric field of the spoof SPP filter with capacitively loaded SRR. It can be seen from the two side view figures at 19 GHz, 21 GHz and 24 GHz that most the energy is restricted near the surface of the substrate, which is similar of the natural SPP material. The energy passes through the proposed

spoof SPP filter with capacitively loaded SRR at the passband frequency while the energy reflects to the input port at the stopband frequency. It is proved that the proposed filter performs bandstop feature.

III. FILTER MEASUREMENT

To verify the proposed design method, a bandstop filter based on the proposed spoof SPP transmission line with capacitively loaded SRR is designed and fabricated on Rogers RT/duroid® 5880 with dielectric coefficient of 2.2 and height of 0.508 mm. The photograph of the fabricated filter is displayed in Fig. 8. The whole size of the filter is 40 mm×3 mm. The filter is embedded in a 3.0 mm high aluminum box and connects with 2.92 mm connectors.

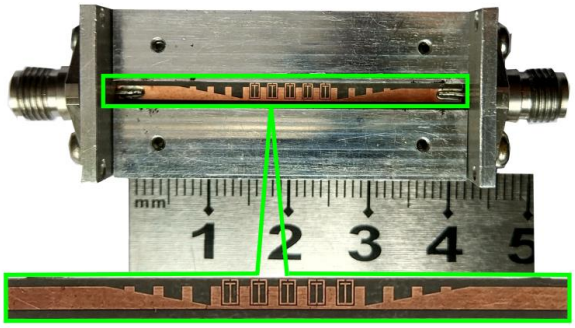

Fig. 8. Photograph of the fabricated filter embedded in an aluminum box.

Measurement results are obtained by the Ceyear® AV3672C vector network analyzer and illustrated in Fig. 9. The simulation results agree with the measurement results except the insertion loss and a little frequency shift to the left side of the designed stopband. As shown by the measured results, the stopband is from 21.05 GHz to 22.95 GHz and the stopband bandwidth is 1.90 GHz. The maximal return loss is 41.8 GHz at 21.8 GHz.

The high insertion loss of the fabricated filter is mainly caused by the substrate dielectric loss. Although the dielectric loss of the spoof SPP transmission line is lower than the microstrip line. However, the length of the fabricated bandstop filter is quite long for adjustment and assembly. In order to proof this point, a microstrip line with the same length of the fabricated bandstop filter and 50 Ohm characteristic impedance is fabricated and measured. The results are illustrated in in Fig. 10. The average insertion losses of simulation and measurement are 0.33 and 1.78 dB, respectively, which has 1.45 dB difference. Also, the worst insertion loss is about 2.5 dB at 21 GHz, which is near the designed stopband. For comparison, the measured S_{21} subtracting the loss of the microstrip line with 50 Ohm impedance is shown in Fig. 11. It is clear that the transmission loss of the spoof SPP near the stopband is very low as predicted.

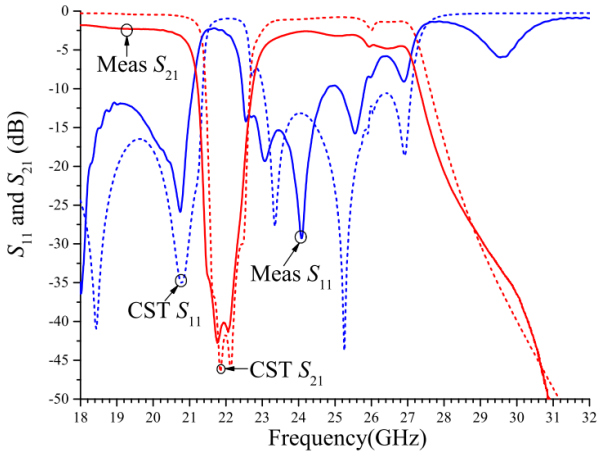

Fig. 9. Measured and simulated S_{11} and S_{21} results of the fabricated filter.

The left and right cutoff frequency of the measured stopband are lower than the measured ones, respectively. The frequency shift is about 0.9% of the central frequency, which is at normal frequency. The difference is mainly caused by the nonideal effect of the substrate and the fabrication tolerance.

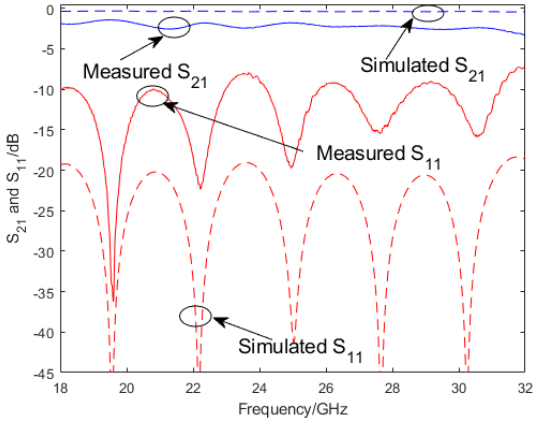

Fig. 10. Measured and Simulated S_{11} and S_{21} of the 50 Ohm microstrip line with the same length of the fabricated filter.

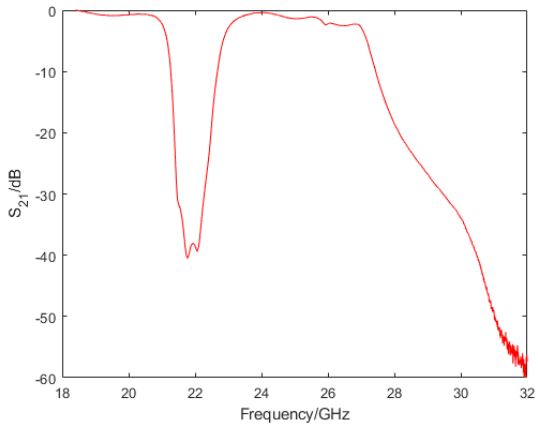

Fig. 11. The measured S_{21} subtracting the loss of the microstrip line with 50 Ohm impedance.

IV. CONCLUSION

This paper presents a novel spoof SPP bandstop filter with capacitively loaded SRR. The dispersion mode is the discussed and the capacitively loaded SRR's effect to the filter feature is studied. In both simulation and measurement, the filter shows a steep and wide rejection band in an ultra-wide low-pass band, which agree with dispersion of the proposed bandstop resonating unit. The fabricated filter has a 1.9 GHz rejection band and 41.8 dB insertion loss at the designed bandwidth. The center frequency of the rejection band is 22.0 GHz.

ACKNOWLEDGMENT

This work was supported by the National Natural Science Foundation of China 61601088 and 61571093 and the Fundamental Research Funds for the Central Universities ZYGX2019J085.

REFERENCES

[1] A. Bostwick, F. Speck, T. Seyller, et al., "Observation of plasmarons in quasi-freestanding doped graphene," *Science*, vol. 328, no. 5981, pp. 999-1002, May 2010.

[2] J. O'Hara, R. Averitt, and A. Taylor, "Terahertz surface plasmon polariton coupling on metallic gratings," *Opt. Lett.*, vol. 12, no. 25, pp. 6397-402, Dec. 2004.

[3] J. B. Pendry, L. M. Moreno, and F. J. Garcia-Vidal, "Mimicking surface plasmons with structured surfaces," *Science*, vol. 305, no. 5685, pp. 847-848, Aug. 2004.

[4] J. T. Shen, P. B. Catrysse, and S. Fan, "Mechanism for designing metallic metamaterials with a high index of refraction," *Phys. Rev. Lett.*, vol. 94, no. 19, p. 197401, May 2005.

[5] X. P. Shen and T. J. Cui, "Planar plasmonic metamaterial on a thin film with nearly zero thickness," *Appl. Phys. Lett.*, vol. 102, no. 21, p. 83, May 2013.

[6] A. D. Vala, A. V. Patel, A. Patel, "Design and analysis of microstrip bandstop filter based on defected ground structure," *Int. J. of Eng. Res. Tech.*, vol. 3, no. 5, pp. 63-66, May 2013.

[7] B. C. Pan, Z. Liao, J. Zhao, et al., "Controlling rejections of spoof surface plasmon polaritons using metamaterial particles," *Opt. Lett.*, vol. 22, no. 11, pp. 13940-50, 2014.

[8] J. Xu, H. C. Zhang, W. X. Tang, et al., "Transmission-spectrum-controllable spoof surface plasmon polaritons using tunable metamaterial particles," *Phys. Rev. Lett.*, vol. 108, no. 19, pp. 824-848, May 2016.

[9] B. G. Xiao, S. Kong, and S. H. Xiao, "Spoof surface plasmon polaritons based notch filter for ultra-wideband microwave waveguide," *Opt. Comm.*, vol. 374, pp. 13-17, Sep. 2016.

[10] Q. Zhang, C. H. Zhang, Y. Y. Jia, et al., "A series of compact rejection filters based on the interaction between spoof SPPs and CSRRs," *Sci. Rep.*, vol. 6, p. 28256, June 2016.

[11] Q. Zhang and T. J. Cui, "Rejection filters based on spoof surface plasmons and complementary meta-material particles," In *IEEE MTT-S Int. Microw. Workshop Series on Adv. Materials and Processes for RF and THz App.*, pp. 1-3, 2016.

[12] B. Z. Xu, Z. Li, L. L. Liu, et al., "Bandwidth tunable microstrip band-stop filters based on localized spoof surface plasmons," *J. Opt. Soc. Am. B*, vol. 33, no. 7, pp. 1388-1391, July 2016.

[13] S. M. Zhao, H. C. Zhang, J. H. Zhao, et al., "An ultra-compact rejection filter based on spoof surface plasmon polaritons," *Sci. Rep.*, vol. 7, no. 1, p. 10576, July 2017.

[14] L. Li, L. Dong, P. Chen, et al., "Multi-band rejection filters based on spoof surface plasmon polaritons and folded split-ring resonators," *Int. J. Microw. Wirel. Tech.*, vol. 11, no. 8, pp. 774-781, Aug. 2019.

Peng Chen received the bachelor's degree and the Ph.D. degree from University of Electronic Science and Technology of China (UESTC), Chengdu, China, in 2009 and 2015, respectively. He then became a Lecturer and an Associate Professor in the School of Aeronautics and Astronautics, UESTC, in 2015 and 2019, respectively. During Nov. 2017 to Nov. 2018, he was a Visiting Researcher in Tohoku University, Sendai, Japan. He is

a member of Chinese Institution of Electronics and a member of IEEE.

His research interests include microwave and wireless communication components design and weak electromagnetic fields detection.

Luping Li received his bachelor's degree from Chengdu University of Information Technology, Chengdu, China in 2016 and master's degree from the University of Electronic Science and Technology of China (UESTC), Chengdu, China in 2019. Now he is studying his Ph.D. degree in UESTC.

His research interests are RF/microwave filters.

Kai Yang received his bachelor's degree and master's degree from University of Electronic Science and Technology of China, Chengdu, P. R. China, in 1993 and 2000, respecttively, where he then became the Associate Professor and the Full Professor in 2001 and 2007, respectively. He is a senior member of Chinese Institution of Electronics.

His research interests are RF/microwave circuits and systems, superconducting microwave application.

Influences of Amplitude Tapering and Feed Blockage on the Radiation Characteristics of Ku-Band Parabolic Reflector Antennas

Nurdan T. Sonmez [1] and Fikret Tokan [2]

[1] The Scientific and Technological Research Council of Turkey
Gebze, Kocaeli, 41470, Turkey
nurdan.sonmez@tubitak.gov.tr

[2] Department of Electronics and Communications Engineering, Yıldız Technical University
Istanbul, 34220, Turkey
ftokan@yildiz.edu.tr

Abstract ─ In this work, the influences of amplitude tapering and feed aperture blocking in gain and first sidelobe level of Ku-band parabolic reflector antennas are investigated. Two different parabolic antenna configuration groups are proposed to determine each of these degradation factors. Designed parabolic reflectors are fed by pyramidal and conic horns to observe the blockage effect of feed type on Ku-band satellite reception applications. In the first examination to designate the influence of illumination loss due to amplitude tapering four parabolic reflectors are designed with 8 dB, 10 dB, 15 dB and 20 dB edge taper values on reflector apertures. Thereafter, thanks to the reflectors designed with the same edge taper value, but having different diameters, it became possible to observe, purely the influence of feed blockage on the radiation characteristics. Both theoretical and simulated patterns of reflector systems are presented.

Index Terms ─ Amplitude tapering, conic horn, feed blockage, illumination loss, parabolic reflector antenna, pyramidal horn.

I. INTRODUCTION

Compared to other antenna configurations, parabolic reflector antennas are well-known for their capabilities to provide highly directive main beam and very low side lobe level (SLL) along with low fabrication costs [1-2]. During the past decade of space exploration, parabolic reflector antennas have been very popular with the increasing demand for high data-rate communications [3]. Increased data rates improve the communication channel signal-to-noise ratio. Obviously, enhancement in the antenna gain results with very high signal-to-noise ratio of the communication channel. Thus, various geometries of high gain reflector antennas have been investigated and developed for satellite applications.

Paraboidal reflectors illuminated by a feed antenna placed at their focus are widely used in many satellite applications [4-5]. However, single reflecting paraboidal surface limits the design flexibility [6]. An alternative design to improve the flexibility is employing an electrically large paraboloidal main reflector illuminated by a relatively smaller hyperboloidal subreflector [7-8]. In such a double reflector antenna system, locating the feed antenna near to main reflector enables to place necessary communications electronics equipment behind the main reflector. This minimizes antenna system dimensions and waveguide losses between the feed antenna and the amplifiers [9].

The main disadvantage of reflector antenna systems is the blockage losses caused by feed apertures. The feed blockage is an important issue concerning the antenna designers occurs when part of the reflected rays impinges upon the feed structure, depending on the feed physical dimensions [10-11].

In double reflector antenna systems, sub-reflector blockage which is characterized by the incidence of main reflector reflected rays upon the hyperboloidal sub-reflector also occurs besides the feed blockage. Although high gain and low SLL are crucial demands in satellite applications, these blockage mechanisms cause deleterious effects on gain and SLL of reflector systems [12-13]. Feed and subreflector blockage problems can be reduced by decreasing the sub-reflector radiation towards the feed and main-reflector radiation towards the subreflector. Axially displaced dual reflector antenna configurations are increasingly used with this aim. [14-16].

Illumination loss due to non-uniform amplitude distribution on the aperture plane of a reflector antenna is another considerable issue in reflector antenna system designs. Illumination loss also has deteriorating effects

Submitted On: August 9, 2019
Accepted On: March 1, 2020

on single or double reflector antenna system radiations [17-18].

In this work, the influences of illumination loss and feed blockage on the radiation characteristics, namely gain and first SLL of single paraboloidal reflector antennas designed for Ku-band satellite applications are investigated [19]. As the first step to determine the illumination loss effects, designed parabolic reflector antennas are fed by pyramidal and conic horns operating at 10.7-14.5 GHz (Ku-band) frequency band. These parabolic reflectors having the same diameter are constituted considering 8 dB, 10 dB, 15 dB and 20 dB amplitude taper distribution on the reflector apertures. Gain and first SLL values regarding each design are analyzed and obtained first SLL values are compared with the theoretical results.

Then, in order to investigate feed blockage effects on the reflector radiation, similarly four different parabolic reflector antennas are designed. This time, these reflectors have different diameters but the same focal length to diameter ratio, *f/D* value. In these designs each reflector has the same edge taper value on their aperture planes. In this way, spillover losses which are associated with the power misses the reflector will be at the same level at each design. These latter designs enable to explore purely the feed blockage effects.

Designed parabolic reflectors fed by Ku-band pyramidal and conic horns are analyzed to observe the blockage effect of feed type on satellite reception applications. The simulations are performed by the Computer Simulation Technology (CST) software using the adaptive mesh refinement to obtain better accuracy with fewer unknowns [20].

II. PYRAMIDAL AND CONIC FEED HORN DESIGNS

Four different parabolic reflector antennas are designed for observing each of loss effects on the radiation. Since horn antennas are widely used in high-gain applications such as satellite communications, [21] constituted parabolic reflectors are fed by two different types of Ku-band horn antennas; a pyramidal horn and a conic horn to observe the blockage effect of feed type on satellite applications. Designed pyramidal and conic horns are shown in Fig. 1 with their physical dimensions.

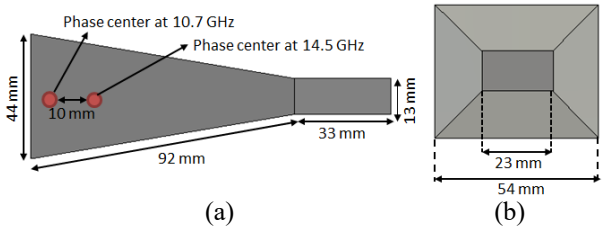

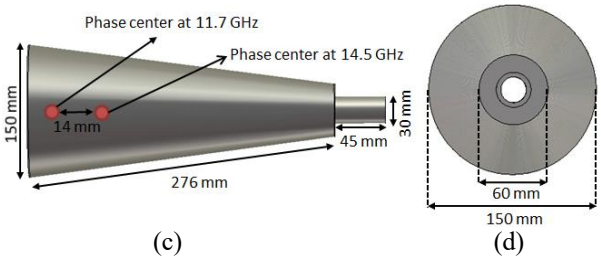

Fig. 1. Feed horn antennas: (a) pyramidal horn side view, (b) pyramidal horn back view, (c) conic horn side view, and (d) conic horn back view.

In general, the phase center positions of wideband antennas move with the change of frequency. Nevertheless, this movement is considerably low in horn antennas [22]. This characteristic enables horn antennas suitable for wideband satellite applications. Indeed, in the whole operating band, the phase centers of both designed feeds exhibit almost a stable behavior as signed in Fig. 1. The phase center locations given in Fig. 1 are determined from radiation pattern simulation results of feed horns considering where the phases of feed antenna beams are nearly constant within the related beam-width. Good matching is achieved at Ku-band with both designed feed horns as given in Fig. 2. It can be seen in Fig. 2 that S_{11} variations of feeds are almost lower than -15 dB in both receive (10.7–12.7 GHz) and transmit (12.7–14.5 GHz) satellite communication bands.

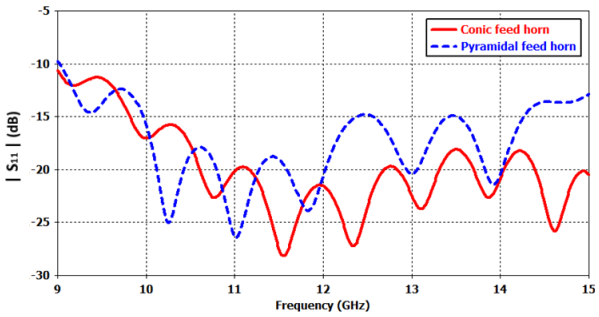

Fig. 2. Reflection coefficient variation of the feed horns with frequency. S_{11} variation of the feed is almost lower than -15 dB in the Ku-band.

Figure 3 exhibits the Co-pol and cross-pol gain patterns of feed horns at 11.7 GHz. Cross-pol isolation of both feed antennas are higher than 50 dB at 11.7 GHz receiving frequency. Due to the almost symmetrical gain patterns in elevation and azimuth planes, only elevation patterns are exhibited. More than 20 dBi gain is obtained by the conic feed horn at 11.7 GHz where the gain of pyramidal horn is 15.2 dBi at the same frequency. The

gain of conic horn is higher than pyramidal horn since electrical length of conic feed is higher than the pyramidal feed as given in Fig. 1.

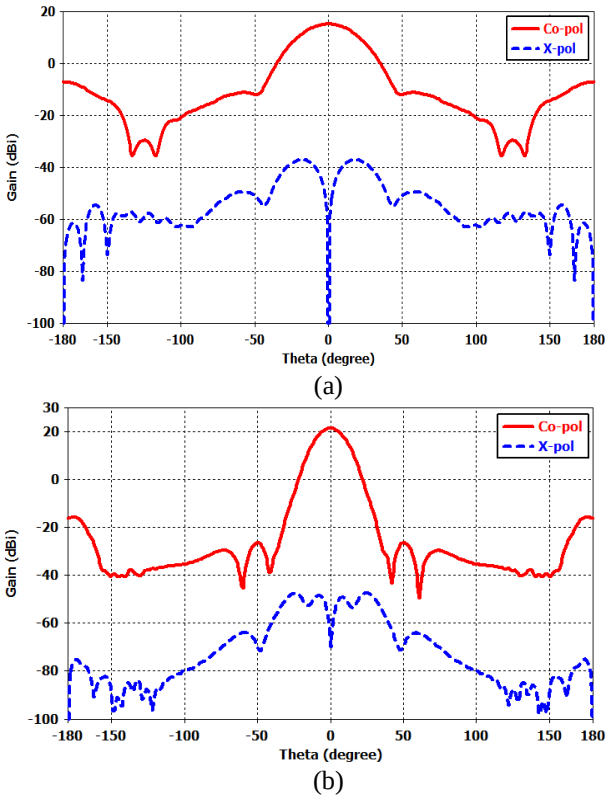

Fig. 3. Co-pol and X-pol gain patterns of feed antennas at 11.7 GHz: (a) pyramidal horn and (b) conic horn.

III. EFFECTS OF AMPLITUDE TAPERING

In this section, the influence of amplitude tapering on gain and first SLL of a parabolic reflector antenna is studied. Kirchoff's scalar formulation is used to obtain the influence of amplitude tapering theoretically on the aperture plane. Then, four parabolic reflector antennas designed considering 8 dB, 10 dB, 15 dB and 20 dB edge taper values on the reflector aperture are fed by Ku-band pyramidal and conic horns. The effective aperture of designed conic feed horn is larger than the pyramidal horn. Thus, the blockage effects of feed type on satellite reception applications are analyzed.

A. Theoretical analysis of amplitude tapering effects

For aperture antennas the source of radiation is the electric-field distribution across the aperture. The electric field of the energy over the reflector aperture is called the electric-field aperture distribution, $E_a(\rho,\phi)$. In Fig. 4, it can be described in terms of an imaginary aperture representing the electric field distribution across a plane in front of the reflector. On the aperture plane, the amplitude of electric field only depends on the distance from the reflector aperture center. Thus, electric-field aperture distribution can be described as $E_a(\rho)$.

Kirchoff's scalar formulation can be used for evaluating the electromagnetic radiation by the aperture plane for large aperture antennas; namely the reflector aperture should be at least several wavelengths along both its principle planes [22].

The aperture plane in Figure 4 is illuminated by the electric field distribution of $E_a(\rho)$. Q is defined as the observation point on the observation plane. Considering the Kirchhoff's scalar diffraction theory, the phasor of radiated electric field from the reflector aperture can be given as:

$$\tilde{E}(r,\theta,\phi)=\frac{j}{\lambda}\left(\frac{e^{-jkr}}{r}\right)\tilde{h}(\theta,\phi), \tag{1}$$

where

$$\tilde{h}(\theta,\phi)=\iint_S \tilde{E}_a(\rho,\phi)\times e^{jk\rho\sin\theta\cos(\phi-\phi')}ds. \tag{2}$$

When the differencial surface area of the aperture is defined as $ds=\rho d\rho d\phi'$ in cylindrical coordinate system. The form factor $\tilde{h}(\theta,\phi)$ of $\tilde{E}(r,\theta,\phi)$ can be defined as follows:

$$\tilde{h}(\theta,\phi)=\int_0^{\rho} E_a(\rho)\times\rho\left[\int_0^{2\pi} e^{jk\rho\sin\theta\cos(\phi-\phi')}\,d\phi'\right]d\rho. \tag{3}$$

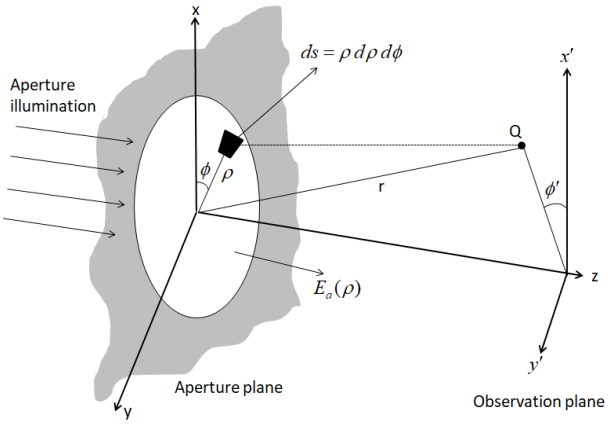

Fig. 4. Radiation by the aperture of a parabolic reflector antenna. Note that standard variables refer to the aperture plane and primed ones denote the observation plane.

The power density of the radiated wave is defined as $S(r,\theta,\phi)=\left|\tilde{h}(\theta,\phi)\right|^2/2\eta_0\lambda^2r^2$. Thus, the radiation pattern of a reflector antenna can be obtained using the square of form factor's amplitude given in (3).

In this work since the diameter of designed parabolic reflector is 45λ at 11.7 GHz frequency, the following amplitude tapering function for the electric

field distribution on the aperture plane is used:

$$E_a(\rho) = \cos^n\left(\frac{\pi \times 10^{-2}}{\lambda} \times \rho\right). \quad (4)$$

Here, n determines the amplitude tapering distribution type on the reflector aperture. The value $n=1$ gives an edge taper of 10 dB and $n=0.8, 1.5$ and 2 corresponds to 8 dB, 15 dB and 20 dB edge taper values, respectively. When $n=1$, for $\rho=0$ the electric field strength reaches its maximum value of 0 dB and this value decreases to -10 dB for $\rho=45\lambda$.

The normalized radiation patterns obtained theoretically using Kirchhoff's scalar formulation in the elevation plane are exhibited in Fig. 5. It should be noted that feed blockage effect is not considered in the radiation patterns. It can be seen in Fig. 5 that the highest first SLL is experienced for the 8 dB edge taper illumination and this value decreases with the increase in the edge taper distributions. Eventually, the first SLL is -31.5 dB for 8 dB edge taper and decreases to -40.6 dB for 20 dB edge taper values on the aperture plane. Thus, the greater amplitude taper on the surface of a parabolic reflector produces lower first side lobes than a more uniform amplitude distribution and consequently reducing the edge taper increases the first SLL. Moreover, it is clear from Fig. 5 that increment in the edge taper results with the 3-dB beamwidth enlargement. Thus, it can be concluded that when the edge taper increases on the reflector aperture the gain of the reflector system decreases.

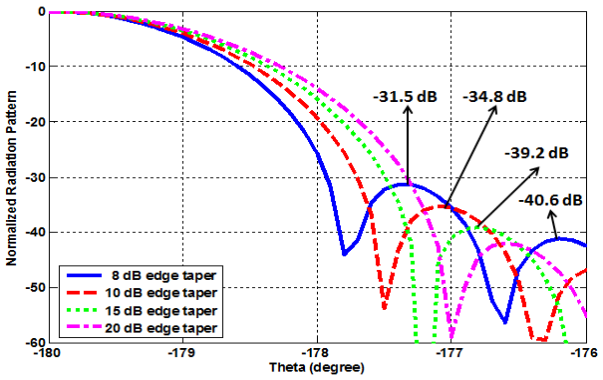

Fig. 5. Evaluated first SLL values as the function of feed tapers using Kirchhoff's scalar formulation.

B. Amplitude tapering effects of feed horn types

This sub-section explains the effects of illumination loss on the radiation characteristics of a parabolic reflector antenna when it is fed by different types of horn antennas. Four different parabolic reflectors fed by pyramidal and conic horns are designed with this aim. All designs have the same diameter since the gain of a reflector system is directly proportional with its collecting effective area. The phase center location of the feed horns at 11.7 GHz frequency are coincided with the reflector focus.

The reflectors illuminated by pyramidal feed considering -8 dB, -10 dB, -15 dB and -20 dB amplitude taper distributions on the reflector apertures results with 1.13, 1.04, 0.87 and 0.74, *f/D* values, respectively. Designed parabolic reflector antennas fed by the pyramidal horn are exhibited in Fig. 6. These values are evaluated regarding the half-subtended angle of the reflector, ψ_0 which is related with *f/D* by:

$$\psi_0 = 2\tan^{-1}\frac{1}{4f/D}. \quad (5)$$

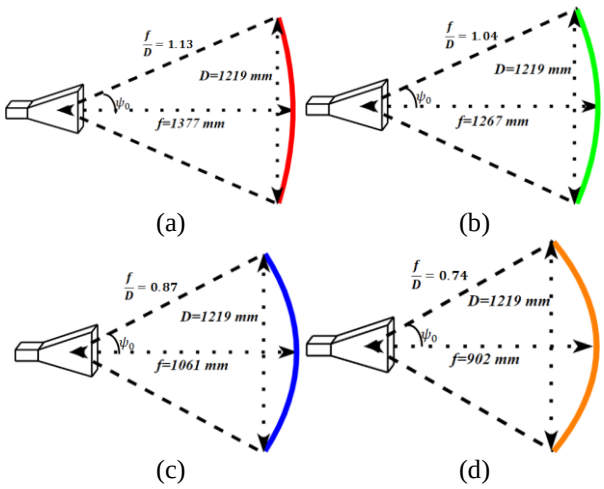

Fig. 6. Pyramidal horn fed parabolic reflector antennas designed with edge taper values of: (a) 8 dB, (b) 10 dB, (c) 15 dB, and (d) 20 dB.

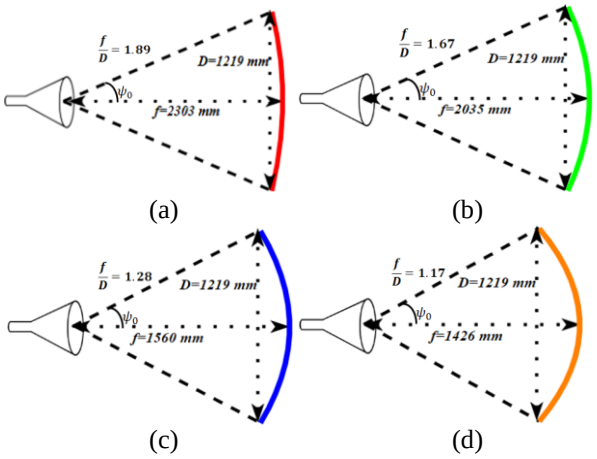

Fig. 7. Conic horn fed parabolic reflector antennas designed with taper values of: (a) 8 dB, (b) 10 dB, (c) 15 dB, and (d) 20 dB.

Four more parabolic reflectors having the same diameter value with the reflectors given in Fig. 6 are

designed. Designed parabolic reflectors are fed by the conic horn to observe the blockage effect of feed type on Ku-band satellite reception applications. *f/D* values of 1.89, 1.67, 1.28 and 1.17 are evaluated considering -8 dB, -10 dB, -15 dB and -20 dB amplitude taper distributions on the reflector apertures, respectively. The parabolic reflector antennas fed by conic horn are highlighted in Fig. 7.

The first SLLs of simulated radiation patterns in the elevation plane regarding to pyramidal and conic horn fed reflector antenna systems are highlighted in Fig. 8 (a) and (b).

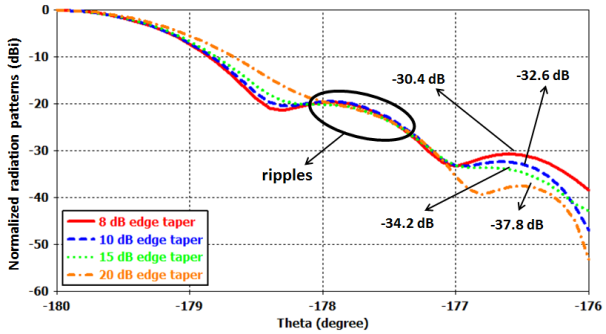

(a)

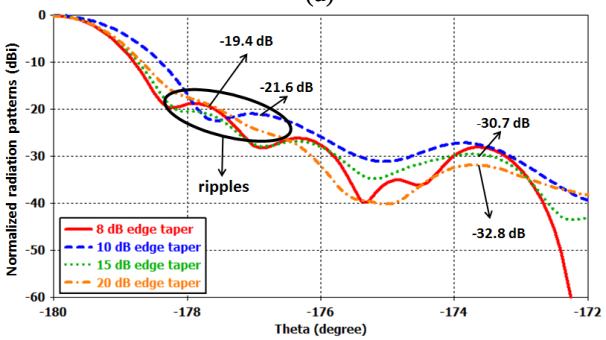

(b)

Fig. 8. The first SLLs as the function of feed tapers for: (a) pyramidal feed horn and (b) conic feed horn.

It can be seen in Fig. 8 (a) that the highest first SLL is experienced for the 8 dB edge taper illumination of reflector aperture when it is fed by the pyramidal horn. The first SLL is decreasing with the increase in the edge taper distribution. Eventually, the first SLL is -30.4 dB for 8 dB edge taper and decreases to -37.8 dB for 20 dB edge taper distribution. Thus, the greater amplitude taper on the surface of a parabolic reflector produces lower first side lobes than a more uniform amplitude distribution and consequently reducing the edge taper increases the first SLL.

When these first SLLs are compared with the theoretical results, it can be said that first SLLs are slightly increased due to the pyramidal feed aperture blocking.

The first SLLs obtained when the reflector antennas are fed by conic horns are given in Fig. 8 (b). Quite higher first SLLs are occurred compared with the levels obtained by pyramidal horn fed reflector antenna.

It is clear from Fig. 8 (a) that small ripples are appeared in the radiation patterns due to the pyramidal feed aperture blocking. Nevertheless, these ripples are small to be considered as SLLs. As it can be seen in Fig. 8 (b), the ripples at the same theta direction are deeper when the blockage is occurred by the conic feed horn. It can be seen in Fig. 1 that the blocking aperture of conic horn is approximately 9 times larger than the pyramidal horn blocking aperture. Thus, the deeper ripples in Fig. 8 (b) can be explained with the higher blockage of radiation by the conic feed horn.

The influence of illumination loss on gain of pyramidal and conic horn fed designed reflector antennas are summarized in Table 1. While the gain is 41.2 dBi for 8 dB edge taper of pyramidal horn fed reflector antennas, it reduces to 38.1 dBi for 20 dB edge taper on the reflector surface. Similar comments can also be made for conic horn fed reflector designs. The highest gain is achieved with the 8 dB edge taper on the reflector surface and this value decreases to 40.25 dBi with the influence of illumination losses. Thus, it can be said from Table 1 that an increase in edge taper results with the decrease in gain. These gain values obtained by the simulation results are compatible with the theoretically obtained normalized radiation patterns given in Fig. 5 where the edge taper results with the 3 dB beam-with enlargement.

Table 1: Gain variations with the edge taper of pyramidal and conic horn fed reflector antennas

Gain (dBi)	8 dB Edge Taper	10 dB Edge Taper	15 dB Edge Taper	20 dB Edge Taper
Pyramidal horn	41.2	40.15	39.4	38.1
Conic horn	41.9	41.65	41.2	40.25

Considering the results presented in Fig. 5, Fig. 8 and Table 1, it can be said that increase of edge taper results with a decrease in the first SLL and in gain. Finally, it can be concluded that the decrease in gain and the increase in the first side-lobe level in a parabolic reflector antenna are highly dependent on the nature of the aperture-distribution function.

IV. EFFECTS OF FEED BLOCKAGE

In this section to dissipate the illumination loss effects on the radiation and so that to specify purely the influence of feed blockage, four different parabolic antennas having the same edge taper value of 20 dB are

designed. These reflector configurations are fed by the pyramidal and conic horns as given in Fig. 9. All parabolic reflector antennas given in Fig. 9 (a) have the *f/D* value of 0.74 and edge taper value of 20 dB on their aperture. Similarly, conic horn fed reflector antennas given in Fig. 9 (b) are also designed considering 1.17 *f/D* value results width 20 dB edge taper on the reflector aperture. Pyramidal horn feed will cast a rectangular and conic horn will cast a circular shadow on the parabolic reflectors as given in Figs. 9 (c) and (d), respectively. The focal length and diameter values of each reflector antenna given in Fig. 9 are summarized in Table 2.

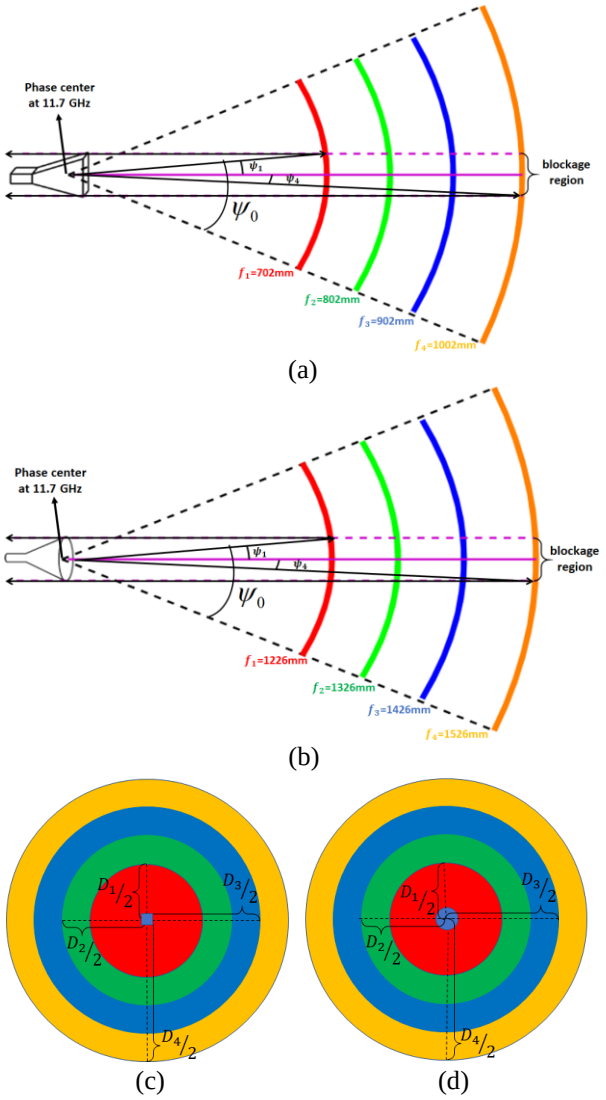

Fig. 9. Parabolic reflector antennas designed with 20 dB edge taper value fed by: (a) pyramidal horn side view, (b) conic horn side view, (c) pyramidal horn back view, and (d) conic horn back view.

Table 2: Focal length and diameter values of the reflector antenna designs given in Fig. 9

Feed Antenna	f_1, D_1	f_2, D_2	f_3, D_3	f_4, D_4
Pyramidal Horn	702, 948	802, 1083	902, 1219	1002, 1354
Conic Horn	1226, 1047	1326, 1113	1426, 1219	1526, 1304

In reflector applications phase error, illumination, spillover and feed blockage losses have deteriorating effects on the antenna radiation characteristics. Since the feed blockage effects are investigated at 11.7 GHz frequency throughout this work, the phase error loss that occurs due to the phase center displacement will not exist. Thanks to the reflector configurations designed with the same edge taper thus with the same *f/D* value as given in Fig. 9, the illumination loss will be at the same level in each reflector configuration. The spillover losses concerning each configuration will also be same since the half-subtended angles, ψ_0 of pyramidal and conic horns are equal for each parabolic reflector groups as given in Figs. 9 (a) and (b).

The first side lobe levels of radiation patterns regarding to the designed reflector configurations are highlighted in Figs. 10 (a) and (b). As explained in Section III, the first SLL of a reflector antenna is strictly related with the edge taper values on the reflector aperture. Thus, as expected first SLLs given in Figs. 10 (a) and (b) have very close values to each other since the edge tapers equal to 20 dB in all reflector apertures. The first SLLs obtained when the reflectors are fed by conic horns given in Fig. 10 (b) are slightly higher. This can be explained with the larger feed blockage aperture of conic feed horn as mentioned in Section III.

In case, the reflector antennas having different diameters are fed by the pyramid horn given in Fig. 9 (a), 35.4 dBi gain is obtained by the smallest reflector (D_1=948 mm). This value increases with the enlargement of the reflector effective areas. The gain values of reflector antennas occur as 36.3 dBi, 38.1 dBi and 38.9 dBi for the reflectors with the diameters of D_2=1083 mm, D_3=1219 mm and D_4=1354 mm, respectively.

Similar comments can be made for the gain values of reflectors fed by conic horn as given in Fig. 9 (b). The lowest gain value of 36.6 dBi is obtained by the smallest reflector antenna (D_1=1047 mm) and this value increases with the enlargement of reflector effective areas to 37.9 dBi for D_2=1113 mm, to 40.25 dBi for D_3=1219 mm and finally to 42.1 dBi for the largest reflector antenna, D_4=1304 mm.

The increment of the gain with the enlargement of the reflector surfaces can be explained with the blockage

amount of the reflected energy by the feed horns. In Fig. 9 (a), it is shown that the pyramidal horn aperture blocks some of the reflected energy from the reflector antennas. The radiation of pyramidal horn with the subtended angle of $\psi_1 = 2^\circ$ is blocked by the smallest reflector and this angle decrease to $\psi_4 = 1.3^\circ$ for the largest reflector. It is clear from Fig. 9 (a) that the enlargement of the reflector surfaces results with smaller ψ angles consequently, decrease in the blocked energy amount of the feed horn.

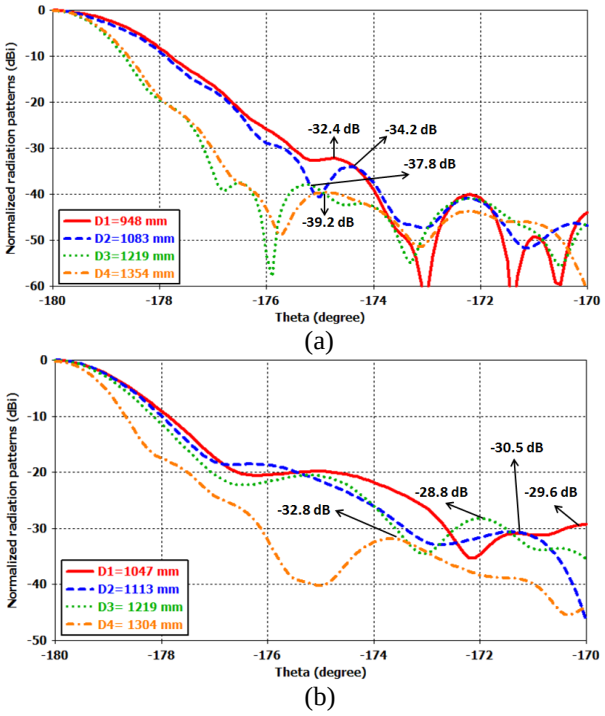

Fig. 10. The first SLL values of various size parabolic reflector antennas fed by: (a) pyramidal horn and (b) conic horn.

When the reflector antennas fed by conic horns given in Fig. 9 (b) are investigated, it can be said that the blocked amount of reflected energy will decrease again with the enlargement of reflector surfaces. Here, ψ_1 value of the blocked energy of the feed horn is 3.5° degree for the smallest reflector and it decreases to $\psi_4 = 2.8^\circ$ for the largest one.

The normalized gain pattern of pyramidal feed horn is given in Fig. 11 (a) to emphasize the 3-dB beam-width of the feed and blocked reflected radiation amount. Similarly, Fig. 11 (b) shows the normalized gain pattern of the conic horn for the 3 dB beam-width and the blocked energy amounts by the feed aperture. According to Fig. 11 (a) the aperture of the pyramidal horn blocks approximately 0.15 dB beam-with of its radiation for the largest reflector surface and this value decreases to 0.1 dB beam-with of its radiation for the smallest reflector antenna. When Fig. 11 (b) is investigated it can be said that due to the larger aperture of conic horn feed, the blocked energy will be higher in these reflector designs. Approximately, 0.4 dB beam-with of conic horn's radiation is blocked with the smallest reflector illumination. This value decreases to 0.6 dB beam-with for the largest reflector illumination.

The higher blockage amount of radiation by the conic feed horn aperture as given in Fig. 11 explains the higher decreases in the gain values of conic horn fed reflector antennas.

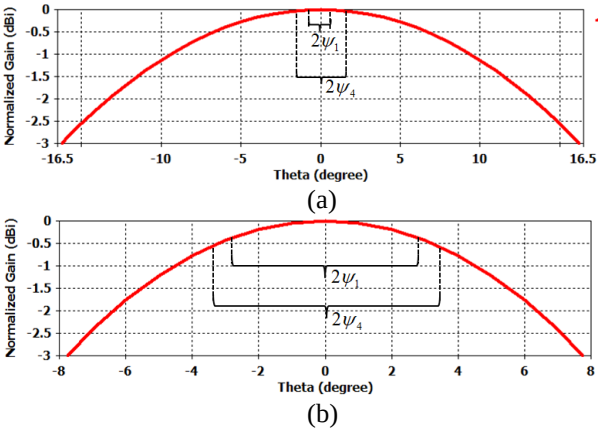

Fig. 11. Normalized gain patterns given within 3-dB beam-widths of the radiation of: (a) pyramidal horn and (b) conic horn. The blocked energy amounts are also marked in the gain patterns.

Thus, it can be concluded that the degradation effects due to the feed blockage on the antenna gain dramatically decrease with the enlargement of the feed antenna aperture.

V. CONCLUSION

High gain and low SLL are crucial demands to provide high signal to noise ratio for satellite applications. The amplitude tapering and feed blockage are considered to have deteriorating effects on reflector antenna radiation patterns. We introduced influences of amplitude taper and feed blockage on the radiation characteristics of Ku-band parabolic reflector antennas by presenting theoretical and simulation results regarding to gain and first SLL.

The role of edge taper in parabolic antennas is studied utilizing four reflectors having the same diameter value, however different edge tapers on their aperture. Designed parabolic reflectors are fed by pyramidal and conic horns to observe the blockage effect of feed type on Ku-band satellite reception applications. It can be concluded that the increase in the first side-lobe level in a parabolic reflector antenna are highly dependent on the

nature of the aperture-distribution function. In fact, the first SLL also increases with a larger aperture blocking.

In order to detect purely the role of feed blockage on the gain similarly, four reflectors are designed. These designed reflectors have the same half subtended angle are fed by pyramidal and conic horns. It is proved that the degradation effects due to the feed blockage on the antenna gain dramatically decrease with the enlargement of the feed antenna aperture.

As a result, to avoid the degradation effects of feed blockage and obtaining higher gain and lower first SLL, greater uniformity of radiation field distribution should be maintained. This can be achieved utilizing electrically larger reflector antennas. However, enlarging the reflector surface results with increase in waveguide losses between the feed antenna and the amplifiers. Designing a planar feed antenna will allow to minimize feed blockage effects but this time, the phase center movement of a planar high gain feed antenna will lead to high level of phase error losses.

REFERENCES

[1] Y. Rahmat-Samii and R. Haupt, "Reflector antenna developments: A perspective on the past, present and future," *IEEE Transactions on Antennas and Propagation Magazine*, vol. 57, no. 2, pp. 85-95, Sep. 2015.

[2] A. Hosseini, S. Kabiri, and F. Flaviis "V-band high-gain printed quasi-parabolic reflector antenna with beam-steering," *IEEE Transactions on Antennas and Propagation Magazine*, vol. 65, no. 4, pp. 1589-1598, Apr. 2017.

[3] J. Huang, W. Lin, F. Qiu, C. Jiang, D. Lei, and Y. J. Guo, "A low profile, ultra-lightweight, high efficient circularly-polarized antenna array for Ku band satellite applications," *IEEE Access Magazine*, vol. 5, no. 18, pp. 356-365, Sep. 2017.

[4] N. Turker Tokan, "Performance of Vivaldi antennas in reflector feed applications," *Applied Computational Electromagnetics Society Journal*, vol. 28, pp. 802-808, Sep. 2013.

[5] V. Manohar, J. M. Kovitz, and Y. Rahmat-Samii, "Synthesis and analysis of low profile, metal-only stepped parabolic reflector antenna," *IEEE Transactions on Antennas and Propagation Magazine*, vol. 66, no. 6, pp. 2788-2798, Apr. 2018.

[6] A. Prata, F. J. S. Moreira, and L. R. Amaro, "Displaced-axis-ellipse reflector antenna for spacecraft communications" *Proceedings of the 2003 SBMO/IEEE MTT-S International Microwave and Optoelectronics Conference*, Brazil, 20-23 Sept. 2003.

[7] N. Fourikis, "A parametric study of the constraints related to Gregorian/Cassegrain offset reflectors having negligible cross polarization," *IEEE Transactions on Antennas and Propagation Magazine*, vol. 36, no. 1, pp. 144-147, Jan. 1988.

[8] R. Lehmensiek, I. P. Theron, and D. I. L. Villiers, "Deriving an optimum mapping function for the SKA-shaped offset Gregorian reflectors," *IEEE Transactions on Antennas and Propagation Magazine*, vol. 63, no. 11, pp. 4658-4666, Sep. 2015.

[9] F. J. S. Moreira and A. Prata, "Generalized classical axially symmetric dual-reflector antennas," *IEEE Transactions on Antennas and Propagation Magazine*, vol. 49, no. 4, pp. 547-554, Apr. 2001.

[10] K. Lee, C. Chen, and R. Lee, "UWB dual-linear polarization dielectric horn antennas as reflector feeds," *IEEE Transactions on Antennas and Propagation Magazine*, vol. 55, pp. 798-804, 2007.

[11] K. Bahadori and Y. Rahmat-Samii, "Estimation of blockage effects of complex structures on the performance of the spacecraft reflector antennas by a hybrid PO/NF-FF method," *Applied Computational Electromagnetics Society Journal*, vol. 22, no. 1, pp. 31-38, Mar. 2007.

[12] A. W. Love, "Central blocking in symmetrical Cassegrain reflectors," *IEEE Transactions on Antennas and Propagation Magazine*, vol. 34, no. 1, pp. 47-49, Feb. 1992.

[13] A. P. Popov and T. Milligan, "Amplitude aperture-distribution control in displaced-axis two-reflector antennas," *IEEE Transactions on Antennas and Propagation Magazine*, vol. 39, no. 6, pp. 58-63, Dec. 1997.

[14] A. Demirci, N. Sonmez, F. Tokan, and N. Turker Tokan, "Phase error analysis of displaced-axis dual reflector antenna for satellite earth stations," *AEU - International Journal of Electronics and Communications*, vol. 110, pp. 1-6, Oct. 2019.

[15] C. Kumar, V. V. Srinivasan, V. K. Lakshmeesha, and S. Pal, "Performance of an electrically small aperture, axially displaced ellipse reflector antenna," *IEEE Antennas and Wireless Propagation Letters*, vol. 8, pp. 903-904, July 2009.

[16] I. Ismatullah, G. Ahmad, and S. A. K. M. Ali, "Design and analysis of ring-focus reflector antenna using method of moments solution of electric field integral equation," *Applied Computational Electromagnetics Society Journal*, N-vol. 33, no. 6, pp. 625-630, June 2018.

[17] H. Kara, and N. Turker Tokan, "Additional losses in ultra-wide band reflector systems," *Applied Computational Electromagnetics Society Journal*, vol. 31, no. 1, pp. 32-38, Jan. 2016.

[18] R. Collin, "Aperture efficiency for paraboloidal reflectors," *IEEE Transactions on Antennas and Propagation Magazine*, vol. 32, no. 9, pp. 997-1000, Sep. 1984.

[19] C. Tienda, J. A. Encinar, M. Barba, and M. Arrebola, "Analysis, design and demonstration of a dual-reflectarray antenna in Ku-band for European coverage," *Applied Computational Electromagnetics Society Journal*, vol. 31, no. 5, pp. 498-507, May 2016.
[20] The homepage of CST Microwave Studio [Online]. Available: http://www.cst.com/
[21] H. T. Chou, C. W. Liu, H. H. Chou, and W. J. Liao, "Optimum horn antenna design based on an integration of HFSS commercial code and genetic algorithms for the feed application of reflector antennas," *Applied Computational Electromagnetics Society Journal*, vol. 25, no. 2, pp. 117-128, Feb. 2010.
[22] S. Manshari, S. Koziel, and L. Leifsson, "A wideband corrugated ridged horn antenna with enhanced gain and stable phase center for X- and Ku-band applications," *IEEE Antennas and Wireless Propagation Letters*, vol. 18, no. 5, pp. 1031-1035, May 2019.
[23] F. T. Ulaby, *Fundamentals of Applied Electromagnetics*. Prentice-Hall, New-Jersey, 2006.

Nurdan T. Sonmez was born in Istanbul, Turkey. She received her B.Sc. and M.Sc. degree in Electronics and Communication Engineering from the Yıldız Technical University, in 2012 and 2014, respectively. She is currently working on her Ph.D. in Communication Engineering at the same university. Her research interests include dielectric lens antennas, automotive radars and reflector antennas.

Fikret Tokan received the M.Sc. and Ph.D. degrees in Electronics and Communications Engineering from Yıldız Technical University, Istanbul, Turkey, in 2005, and 2010, respectively. From 2011 to 2012, he was a Postdoctoral Researcher in the EEMCS Department, Delft University of Technology, The Netherlands, and from 2012 to 2013, he was a Postdoctoral Researcher at the Institute of Electronics and Telecommunications (IETR), University of Rennes 1, France. He is currently an Associate Professor at Yıldız Technical University. His current research interests are UWB antenna design, dielectric lens antennas, electromagnetic waves, antenna arrays, electromagnetic scattering and reflector antennas.

Wideband Low Profile Multi-Polarization Reconfigurable Antenna with Quasi-cross-shaped Coupling Slot

Qun Xu [1,2], Zhiming Liu [1,3], Shaobin Liu [1*], Xiangkun Kong [1], Zhengyu Huang [1], Borui Bian [1], Qiming Yu [1], and Jianghong Qin [1]

[1] College of Electronic and Information Engineering
Nanjing University of Aeronautics and Astronautics, Nanjing, 211106, China
xuqun_jn@126.com, lzmedu@foxmail.com, lsb@nuaa.edu.cn*, xkkong@nuaa.edu.cn, huangzynj@nuaa.edu.cn, bbr@nuaa.edu.cn, yqm1604504@nuaa.edu.cn, 531416050@qq.com

[2] The Aeronautical Science Key Lab for High Performance Electromagnetic Windows
Country the Research Institute for Special Structures of Aeronautical Composite AVIC, Jinan, 250023, China

[3] Department of Electrical and Computer Engineering
University of Victoria, Victoria, BC, V8W 2Y2, Canada

Abstract ─ A wideband low profile multi-polarization reconfigurable antenna with quasi-cross-shaped coupling slot is proposed. The antenna consists of an upper oval radiating patch, the quasi-cross-shaped coupling slot, fork-shaped folded feed lines and a reconfigurable Wilkinson power divider network with four pairs of p-i-n diodes. The antenna reconfigurable polarization modes change among ±45° Linear polarization (LP), dual-LP, left-hand circular polarization (LHCP) and right-hand circular polarization (RHCP) by controlling the ON/OFF states of the p-i-n diodes. The designed prototype has been fabricated and measured. Good agreement between the measured and simulated results is achieved. Measured results show that the antenna has wide impedance bandwidth (over 21.35% for LP and 17.70% for CP) and axial ratio (AR) bandwidth (16.13% for LHCP and 16.88% for RHCP). The average realized gains are about 7.6 dBi for different polarization modes. The proposed antenna has the advantages of multi-polarization reconfigurable ability, wide bandwidth, low profile, and high gains, which make it possible to be applied to wireless communication systems.

Index Terms ─ Low profile, polarization reconfigurable antenna, slot antenna, wideband.

I. INTRODUCTION

Operating characteristics of antennas affect directly the performances of wireless communication systems. With the development of technology, wireless communication systems have been applied to different requirements of wireless services, which causes the limited electromagnetic spectrum resources becoming more and more crowded [1-4]. So, multiple wireless systems are required to be integrated into a single platform for maximum link-up. Therefore, a new generation of antennas that can be adjusted automatically according to environment changes is required.

Reconfigurable antennas not only reduce the size, weight and cost, but also enable the antenna to work in multiple frequency bands and have multiple modes of operation [5-7]. Polarized reconfigurable antennas are the focus of researches on reconfigurable antennas. They can improve the spatial freedom in limited space, which greatly improve the transmission rate and system capacity [8-10]. There are several types of polarizations used in antenna applications: vertical polarization (VP), horizontal polarization (HP), ±45° oblique polarization, [10,11], LHCP and RHCP [12-15]. The first four polarization belongs to LP. Compared with the traditional antennas, the polarization reconfigurable antennas have unparalleled advantages in frequency multiplexing and improving the performance of the polarization control system.

Nowadays, there are mainly two methods to realize electrically controlled polarization reconfiguration: One is to alter feeding network, and the other is to introduce reconfigurability on the radiating elements. The former one achieves the reconfiguration by loading variable reactance to the feeding network or switching the feeding position to generate the phase difference between different operating modes [10, 16, 17]. The latter one is to etch the gap on the proper position of the radiator, which uses RF switches to change the antenna current flow path and generate the phase difference [18-21]. However, most of the proposed antennas have a narrow bandwidth

Submitted On: September 10, 2019
Accepted On: February 23, 2020

especially for the LP and CP polarized reconfigurable antennas. The appearance of the narrow bandwidth is due to two orthogonal LP radiations with same amplitude produce CP mode, while the input impedances between the two LP and CP are different, which will cause the impedance mismatch for LP and CP. Furthermore, it is much harder to overlap the impedance bandwidth and 3-dB AR bandwidth in the broadband range.

In this paper, a novel wideband low profile multi-polarization reconfigurable slot antenna with high realized gains is proposed. The antenna is composed of an upper oval radiating patch, the quasi-cross-shaped coupling slot, fork-shaped folded feed lines and a reconfigurable Wilkinson power divider network with four pairs of p-i-n diodes, which are introduced to change the current flow path to realize the reconfigurable among ±45° oblique LP, dual-LP (VP and HP), LHCP and RHCP. The impedance bandwidth and 3-dB axial-ratio bandwidth are almost overlapped for CP. Also, the average realized gain of the proposed antenna is higher than most of the other reported antennas.

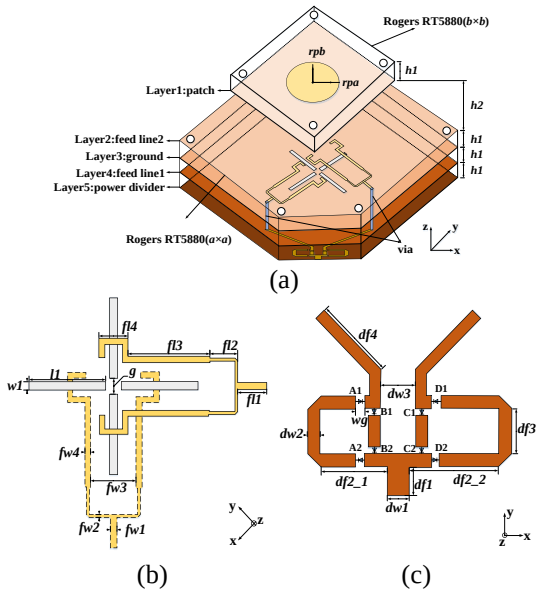

Fig. 1. Structure of the proposed multi-polarization reconfigurable antenna. (a) 3D, (b) Quasi-cross-shaped coupling slot with fork-shaped folded feed lines, and (c) Reconfigurable Wilkinson power divider network.

II. ANTENNA STRUCTURE AND OPERATING PRINCIPLE

The proposed antenna has a multi-layer structure, which consists of four substrates stacked together by nylon screws, and the plastic washers act as a support between the first two layers of substrates as shown in Fig. 1(a). All the substrates are the 0.508-mm thick Rogers RT5880 with a relative permittivity of 2.2 and a loss tangent of 0.0009. The dimensions of the proposed antenna are listed in Table 1.

Table 1: Parameters of the proposed antenna

Parameter	Value (mm)	Parameter	Value (mm)
a	140	*fl4*	7.5
b	80	*w1*	2
h1	0.508	*l1*	19.8
h2	8	*g*	4
rpa	21	*dw1*	3.2
rpb	20	*dw2*	1.8
fw1	1.58	*dw3*	5
fw2	0.9	*df1*	4
fw3	12.65	*df2_1*	10.2
fw4	1.25	*df2_2*	12.6
fl1	4	*df3*	6.4
fl2	7.5	*df4*	36
fl3	24.5	*wg*	0.9

A. Slot antenna

The design of the quasi-cross-shaped coupling slot antenna is based on the antenna proposed in [22]. As shown in Fig. 1 (b), the quasi-cross-shaped coupling slot is etched on the ground which consists of four separated rectangular slots arranged by rotating 90° in turn. The space between two parallel slots reduces the impurity of two linear polarizations and the coupling between two orthogonal polarizations in the center effectively. The fork-shaped folded feed lines are placed on the upper layer and lower layer of the ground plane which avoid the unwanted couplings among the feed line to feed line and feed lines to slots. The purity of two linear polarizations can be improved with the quasi-cross-shaped coupling slot and fork-shaped folded feed lines which provides great help for generating wideband circular polarization. Moreover, the antenna gain is higher than normal slot antennas due to the surface current intensity distributed in the middle and edges of the feed lines is in the same direction which increases the far-field radiation. Besides, the upper oval patch and air gap make a great contribution to the antenna bandwidth, gain and directivity.

B. Reconfigurable Wilkinson power divider network

The structure diagram of Wilkinson power divider with two output ports is shown in Fig. 2. Z_0 is the characteristic impedance of the input port, R_2 and R_3 are the load impedance. Assuming the ratio of output power is $1/k^2$, then:

$$\frac{1}{Z_{in2}}+\frac{1}{Z_{in3}}=\frac{1}{Z_0}, \tag{1}$$

$$k^2=\frac{P_3}{P_2},\ P_2=\frac{U_2^2}{2R_2},\ P_3=\frac{U_3^2}{2R_3},\ U_2=U_3. \tag{2}$$

According to $\lambda/4$ impedance transformation theory, there are:

$$Z_{in2} \times R_2 = Z_{02}^2, \quad (3)$$

$$Z_{in3} \times R_3 = Z_{03}^2. \quad (4)$$

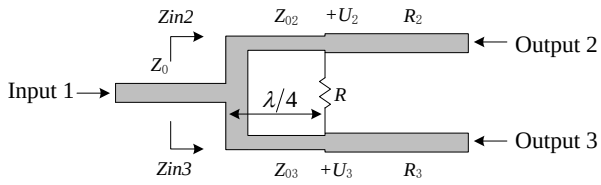

Fig. 2. The structure diagram of Wilkinson power divider with two output ports.

Suppose $R_2 = kZ_0$, then,

$$Z_{02} = Z_0\sqrt{k(1+k^2)}, \; Z_{03} = Z_0\sqrt{\frac{(1+k^2)}{k^3}}, \quad (5)$$

$$R_3 = \frac{Z_0}{k}. \quad (6)$$

The resistance of the isolation resistor R can be expressed as:

$$R = Z_0(k + \frac{1}{k}). \quad (7)$$

When k=1, ports 2 and 3 output the same power signal, $Z_{02} = Z_{03} = \sqrt{2}Z_0$, and the resistance of the isolation resistor is R=2Z_0. In order to reduce the size of the Wilkinson power divider, a Wilkinson power divider network with two λ/4 transmission lines is designed for realizing the polarization reconfiguration, and the schematic is shown in Fig. 1 (c). The network provides phase shifts on different branches by etching separated microstrip lines of different lengths. The microstrip line 2 and line 3 with the same size are located in the middle of the four branches, while the outside microstrip line 1 and line 4 are about λ/4 longer than the inside ones, λ is the guided wavelength at the resonant frequency. The two output ports of the Wilkinson power divider network are connected to the upper feed lines through the vias. Since the upper feed lines are placed on the different layers of the ground plane and the distances to output ports are different, the power divider asymmetric which means the microstrip line 1 is longer than the line 4. Four pairs of p-i-n diodes (A1 and A2; B1 and B2; C1 and C2; D1 and D2) are placed in four different branches respectively to connect the branches with the output ports. By controlling the diodes on and off, different branches can be chosen to generate the phase difference of 0° or ±90°. When diode groups A and C are switched on and others are off, the microstrip line 1 generates a 90° phase delay than the line 3, then the RHCP can be achieved. Similarly, diode groups B and D switched on and others off, the LHCP can be generated. LP can be achieved when just one pair of p-i-n switch on, but only when the diode group A or D switch on could result in a better impedance match. In addition, the ±45° orthogonal dual-LP with high isolation and purity can be generated when diode groups B and C switched on and others off. The corresponding relationship between the diode states and the antenna polarization modes are shown in Table 2. It should be noted that the LP directions are ±45° which is the angle with the positive x-axis.

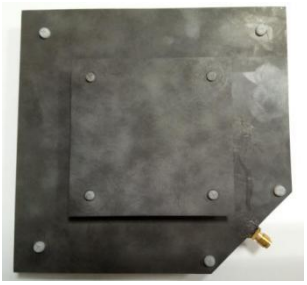

Fig. 3. Photograph of the fabricated antenna.

Table 2: The corresponding relation between diode state and antenna polarization mode

Polarization Mode	Diode State			
	p-i-n A	p-i-n B	p-i-n C	p-i-n D
State 1: +45° LP	ON	OFF	OFF	OFF
State 2: -45° LP	OFF	OFF	OFF	ON
State 3: dual-LP	OFF	ON	ON	OFF
State 4: LHCP	OFF	ON	OFF	ON
State 5: RHCP	ON	OFF	ON	OFF

III. RESULTS AND DISCUSSION

The designed prototype has been fabricated and measured. The simulated and measured results are presented. Figure 3 shows the photograph of the fabricated antenna. The 8 mm M3 nylon bolts are used to support the first layer of the substrate. The simulated results are obtained by CST2017. In the simulation process, the waveguide port was used for feeding, the boundary conditions use open (add space) in all directions, and the time domain solver was applied. The p-i-n diode SMP1345-79 [23] is chosen to connect the different branches of the Wilkinson power divider network. Based on the diode datasheet, the diode is modelled as a 2 Ω resistor for the ON-state and a parallel circuit of a 0.15 pF capacitor and 8000 Ω resistor for the OFF-state. All measurements were performed in a microwave anechoic chamber.

The measured and simulated reflection coefficients for all the modes are shown in Fig. 4. It is observed that the measured 10-dB impedance bandwidths covered wide frequency bands from 2.76 to 3.51 GHz (0.75 GHz, 23.92%) for +45° LP, 2.66 to 3.40 GHz (0.74 GHz, 24.42%) for -45° LP, 2.72 to 3.37 GHz (0.65 GHz, 21.35%) for dual-LP, 2.78 to 3.32 GHz (0.54 GHz, 17.70%) for LHCP and 2.86 to 3.52 GHz (0.66 GHz, 20.69%) for RHCP. The external bias circuit for p-i-n

diodes caused the differences between measured and simulated results. Furthermore, the loading changed since the actual value of the equivalent circuit of the p-i-n diodes may differ from the labeled value. The fabrication and measurement tolerance also affected the results.

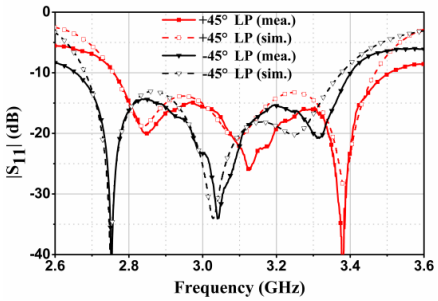

(a)

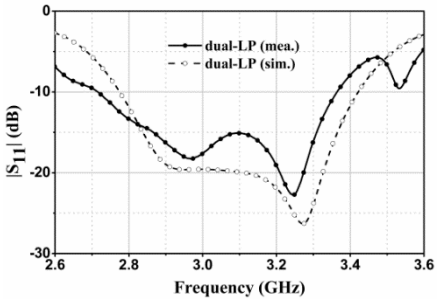

(b)

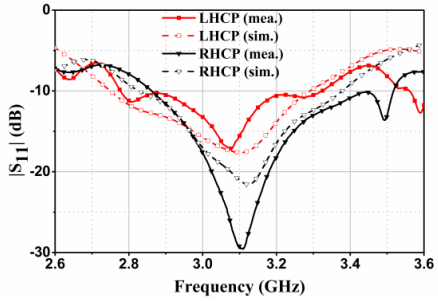

(c)

Fig. 4. Measured and simulated reflection coefficients for all modes: (a) ±45° LP, (b) Dual-LP, and (c) CP.

Figure 5 shows the measured and simulated realized gains of the antenna for LP modes and Fig. 6 presents the realized gains and axial ratios for CP modes which indicates great agreements. It can be seen that the antenna realized gains are quite stable along the operating bandwidth, while the measured peak gains are 8.45 dBi for LP and 8.36 dBi for CP, and the average gains are 7.63 dBi for LP and 7.61 dBi for CP over impedance bandwidth. The measured 3-dB AR bandwidths are 2.85 to 3.35 GHz (0.48 GHz, 16.13%) for LHCP and 2.82 to 3.34 GHz (0.48 GHz, 16.88%) for RHCP, which are wider than most of the proposed polarized reconfigurable antennas.

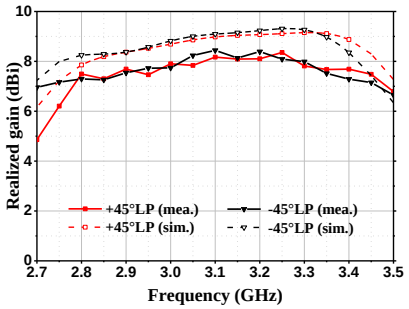

Fig. 5. Measured and simulated realized gains for LP modes.

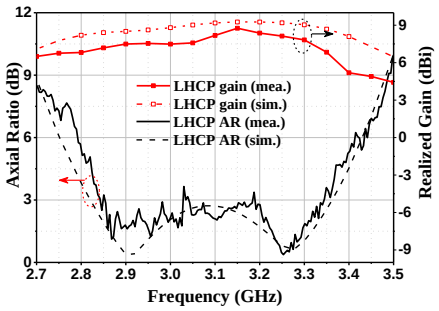

(a)

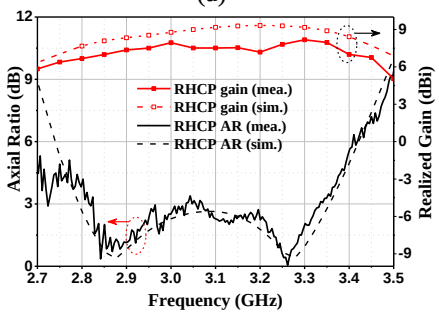

(b)

Fig. 6. Measured and simulated realized gains and axial ratios for CP modes: (a) LHCP and (b) RHCP.

The measured and simulated normalized radiation patterns for LP and CP modes at 2.8, 3.0 and 3.3 GHz are shown in Figs. 7-9. It is observed from Fig. 7 and Fig. 8 that the patterns of the two orthogonal cut-planes (φ=+45° plane and φ=-45° plane) are compared for +45° LP and -45° LP. CP patterns are shown in Fig. 8. The measured cross-polarization levels for all modes are almost below -15 dB. A larger back lobe and unexpected side lobes are found in the measured radiation patterns which are caused by the test environment and affected by the p-i-n diodes with the bias circuit and external DC power device.

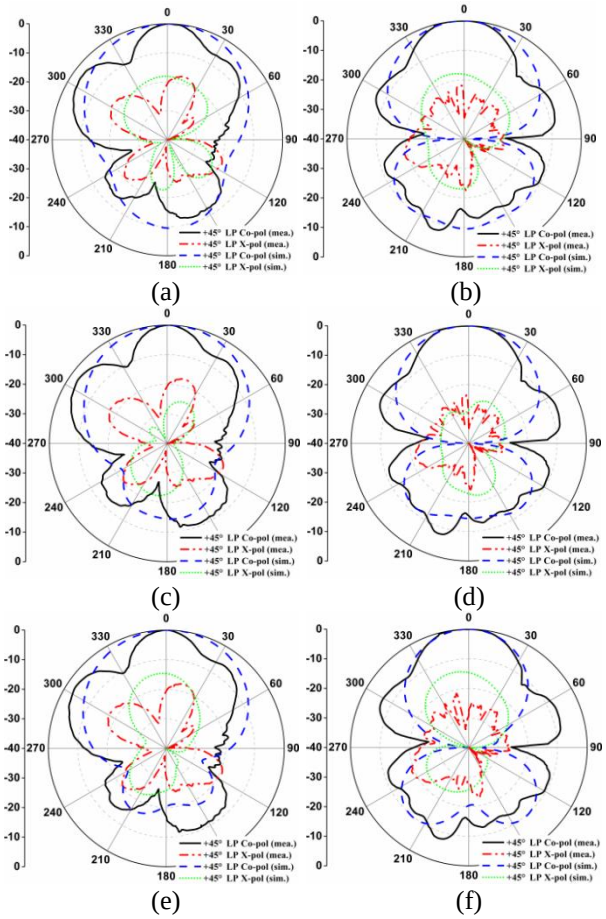

Fig. 7. Measured and simulated radiation patterns for +45° LP mode. (a) φ=+45° and (b) φ=-45° planes at 2.8 GHz, (c) φ=+45° and (d) φ=-45° planes at 3.0 GHz, (e) φ=+45° and (f) φ=-45° planes at 3.3 GHz.

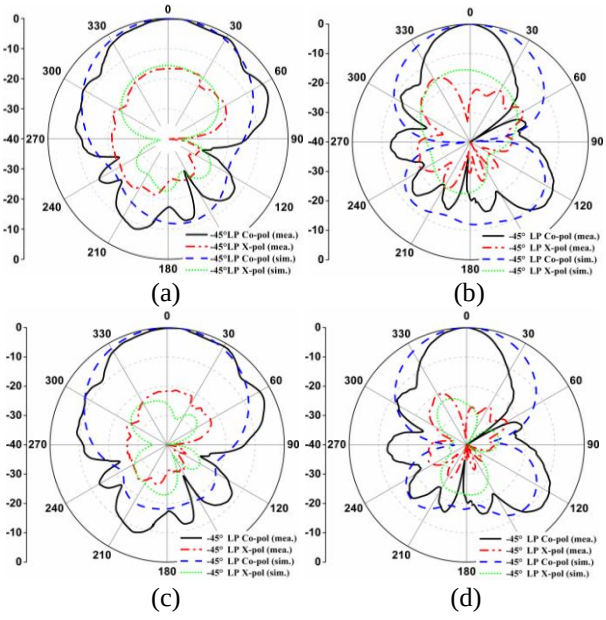

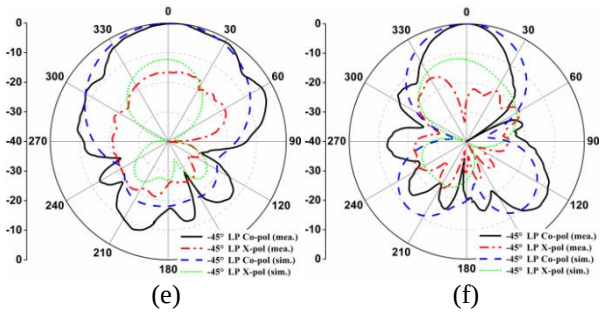

Fig. 8. Measured and simulated radiation patterns for -45° LP mode. (a) φ=-45° and (b) φ=+45° planes at 2.8 GHz, (c) φ=-45° and (d) φ=+45° planes at 3.0 GHz, (e) φ=-45° and (f) φ=+45° planes at 3.3 GHz.

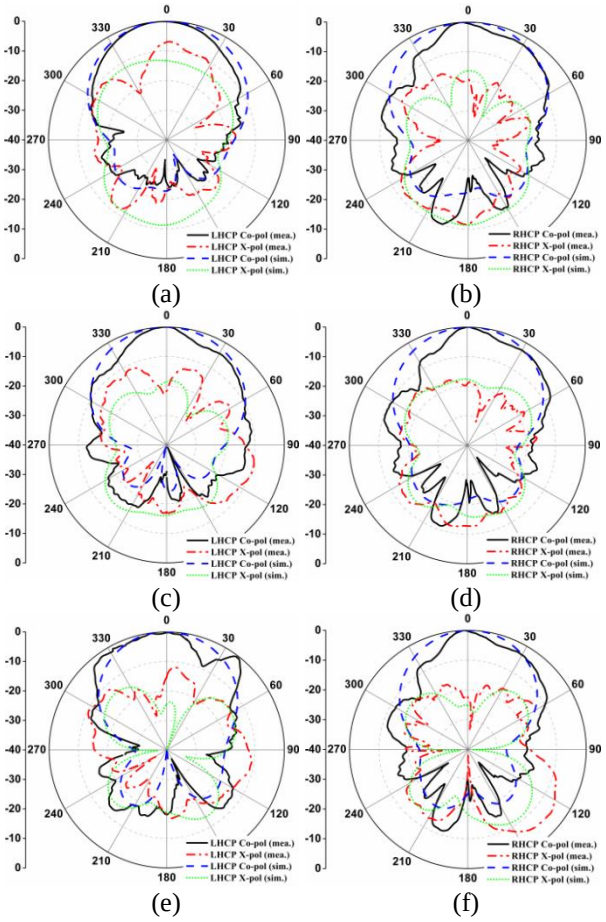

Fig. 9. Measured and simulated radiation patterns for CP modes. (a) LHCP and (b) RHCP at 2.8 GHz, (c) LHCP and (d) RHCP at 3.0 GHz, (e) LHCP and (f) RHCP at 3.3 GHz.

Finally, Table 3 gives the comparisons among reported polarization reconfigurable antennas and the proposed antenna. It can be concluded that the proposed polarization reconfigurable antenna realized wide

impedance bandwidth, AR bandwidth, high realized gains and low profile with five polarization modes.

Table 3: Comparison with reported polarization reconfigurable antennas

0	Polarization States	IMBW (%)	ARBW (%)	Height
[1]	LP LHCP/RHCP	14.2 26.4	- 13.5	$0.60\lambda_0$
[9]	LHCP RHCP	80	37.8 26.9	$0.32\lambda_0$
[14]	LP LHCP/RHCP	27.2 21.9	- 23.5	$0.27\lambda_0$
[22]	LP LHCP/RHCP	7.3	- 1.5	$0.043\lambda_0$
[23]	HP/VP LHCP/RHCP	20 25.6	- 4	$0.10\lambda_0$
Pro.	±45° LP/dual-LP LHCP/RHCP	>23.9 >17.7	- 16.1/16.9	$0.11\lambda_0$

VI. CONCLUSION

A wideband low profile multi-polarization reconfigurable slot antenna with high realized gains has been presented. Four pairs of p-i-n diodes which are placed in four different branches of the reconfigurable Wilkinson power divider network controlling the antenna reconfigurable polarization modes among ±45° LP, dual-LP, LHCP and RHCP. The upper slot antenna with fork-shaped folded feed lines provides two pure orthogonal linearly polarizations, which makes great help for generating wideband circular polarization. The designed prototype was fabricated and measured, showing agreement between the measured and simulated results. Compared to most of the reported antennas, wider impedance bandwidths (over 21.35% for LP and 17.70% for CP) and AR bandwidths (16.13% for LHCP and 16.88% for RHCP) with high realized gains ~7.6 dBi are obtained. Finally, the proposed antenna has the advantages of multi-polarization reconfigurable ability, wide bandwidth, low profile and high gains, which make it possible to be applied to wireless communication systems.

ACKNOWLEDGMENT

This work was supported in part by Chinese Natural Science Foundation (Grant Nos. 61671238; 61471368; 61901217), in part by the Fundamental Research Funds for the Central Universities (No. NJ20160008), in part by Natural Science Foundation of Jiangsu Province (Grant No. BK20190406) in part by China Postdoctoral Science Foundation (Grant Nos. 2016M601802; 2019M661829), in part by the Equipment Advanced Research Foundation of China (Grant No. 61402090103), in part by Jiangsu Planned Projects for Postdoctoral Research Funds (Grant No. 1601009B; 2019K018A), and in part by Aeronautical Science Foundation of China (20161852016). Zhiming Liu greatly acknowledges funding from the China Scholarship Council (CSC) for Grant 201906830035.

REFERENCES

[1] L. Y. Ji, P. Y. Qin, Y. J. Guo, C. Ding, G. Fu, and S. X. Gong, "A wideband polarization reconfigurable antenna with partially reflective surface," *IEEE Trans. Antenna Propag.*, vol. 64, no. 10, pp. 4534-4538, Oct. 2016.

[2] Z.-C. Hao, H.-H. Wang, and W. Hong, "A novel planar reconfigurable monopulse antenna for indoor smart wireless access points' application," *IEEE Trans. Antenna Propag.*, vol. 64, no. 4, pp. 1250-1261, Apr. 2016.

[3] J. S. Row, and M. J. Hou, "Design of polarization diversity patch antenna based on a compact reconfigurable feeding network," *IEEE Trans. Antenna Propag.*, vol. 62, no. 10, pp. 5349-5352, Oct. 2014.

[4] H. Sun and S. Sun, "A novel reconfigurable feeding network for quad-polarization-agile antenna design," *IEEE Trans. Antenna Propag.*, vol. 64, no. 1, pp. 311-316, Jan. 2016.

[5] Z. C. Hao, K. K. Fan, and H. Wang, "A planar polarization-reconfigurable antenna," *IEEE Trans. Antenna Propag.*, vol. 65, no. 4, pp. 1624-1632, Apr. 2017.

[6] M. N. Osman, M. K. Abdul Rahim, M. R. Hamid, M. F. M. Yusoff, and H. A. Majid, "Compact dual-port polarization-reconfigurable antenna with high isolations for MIMO application," *IEEE Antennas Wireless Propag. Lett.*, vol. 15, pp. 456-459, July 2016.

[7] S. W. Lee and Y. J. Sung, "Simple polarization-reconfigurable antenna with T-shaped feed," *IEEE Antennas Wireless Propag. Lett.*, vol. 5, pp. 114-117, 2016.

[8] J.-F. Tsai and J.-S. Row, "Reconfigurable square-ring microstrip antenna," *IEEE Trans. Antennas Propag.*, vol. 61, no. 5, pp. 2857-2860, 2013.

[9] H. Wong, W. Lin, L. Huitema, and E. Arnaud, "Multi-polarization reconfigurable antenna for wireless biomedical system," *IEEE Trans. Biomedical Circuits Syst.*, vol. 11, no. 3, pp. 652-660, 2017.

[10] S.-L. Chen, F. Wei, P.-Y. Qin, Y. Jay Guo, and X. Chen, "A multi-linear polarization reconfigurable unidirectional patch antenna," *IEEE Trans. Antenna Propag.*, vol. 65, no. 8, pp. 4299-4304, 2017.

[11] L. Ge, X. J. Yang, D. G. Zhang, M. J. Li, and H. Wong, "Polarization-reconfigurable magneto-electric dipole a cv antenna for 5G Wi-Fi," *IEEE Antennas Wireless Propag. Lett.*, vol. 16, pp. 1504-1507, 2017.

[12] W. Lin and H. Wong, "Wideband circular

polarization reconfigurable antenna," *IEEE Trans. Antenna Propag.*, vol. 63, no. 12, pp. 5938-5944, 2015.

[13] D. Piazza, J. Kountouriotis, M. D'Amico, and K. R. Dandekar, "A technique for antenna configuration selection for reconfigurable circular patch arrays," *IEEE Trans. Wireless Commun.*, vol. 8, no. 3, pp. 1456-1467, 2009.

[14] M. Fakharian, P. Rezaei, and A. A. Orouji, "Reconfigurable multiband extended U-slot antenna with switchable polarization for wireless applications," *IEEE Antennas Propag. Mag.*, vol. 57, no. 2, pp. 194-202, Apr. 2015.

[15] J. S. Row, W. L. Liu, and T. R. Chen, "Circular polarization and polarization reconfigurable designs for annular slot antennas," *IEEE Trans. Antennas Propag.*, vol. 60, no. 12, pp. 5998-6002, 2012.

[16] W. Lin and H. Wong, "Polarization reconfigurable wheel-shaped antenna with conical-beam radiation pattern," *IEEE Trans. Antennas Propag.*, vol. 63, no. 2, pp. 491-499, 2015.

[17] J. Hu, Z.-C. Hao, and W. Hong, "Design of a wideband quad-polarization reconfigurable patch antenna array using a stacked structure," *IEEE Trans. Antennas Propag.*, vol. 65, no. 6, pp. 3014-3023, 2017.

[18] M. S. Nishamol, V. P. Sarin, D. Tony, C. K. Aanandan, P. Mohanan, and K. Vasudevan, "An electronically reconfigurable microstrip antenna with switchable slots for polarization diversity," *IEEE Trans. Antennas Propag*., vol. 59, no. 9, pp. 3424-3427, 2011.

[19] A. Khidre, K.-F. Lee, F. Yang, and A. Z. Elsherbeni, "Circular polarization reconfigurable wideband E-shaped patch antenna for wireless applications," *IEEE Trans. Antennas Propag*., vol. 61, no. 2, pp. 960-964, 2013.

[20] Z.-X. Yang, H.-C. Yang, J.-S. Hong, and Y. Li, "Bandwidth enhancement of a polarization-reconfigurable patch antenna with stair-slots on the ground," *IEEE Antennas Wireless Propag. Lett.*, vol. 13, pp. 579-582, 2014.

[21] K. M. Mak, H. W. Lai, K. M. Luk, and K. L. Ho, "Polarization reconfigurable circular patch antenna with a C-shaped," *IEEE Trans. Antennas Propag.*, vol. 65, no. 3, pp. 1388-1392, 2017.

[22] J. Lu, Z. Q. Kuai, X. W. Zhu, and N. Z. Zhang, "A high-isolation dual-polarization microstrip patch antenna with quasi-cross-shaped coupling slot," *IEEE Trans. Antennas Propag.*, vol. 59, no. 7, pp. 1713-2717,2011.

[23] Skyworks Datasheet for SMP1345. [Online]. Available: https://www.skyworksinc.com/en/Products/Diodes/SMP1345-Series.

Assessment of Human Exposure in Case of Wireless Power Transfer for Automotive Applications using Stochastic Models

Sahil Deshmukh, Paul Lagouanelle, and Lionel Pichon

GeePs | Group of Electrical Engineering - Paris, CNRS, CentraleSupélec, Université Paris-Saclay
Sorbonne Université, 3 & 11 rue Joliot-Curie, 91192 Gif-sur-Yvette, France
lionel.pichon@geeps.centralesupelec.fr

Abstract ─ In this paper, different non-intrusive stochastic approaches are compared in view of human exposure assessment from an inductive power transfer system at 85 kHz, dedicated to automotive applications. The stochastic approaches are combined with a 3D finite element method to build adequate meta-models based on Kriging and Polynomial Chaos Expansion. These models are used to consider the uncertainty and variability of several parameters defining the electromagnetic problem. Such fast predictions of uncertainties may help to improve the design of shields for inductive power transfer systems considering health and safety standards.

Index Terms ─ Human exposure, Stochastic models, wireless power transfer.

I. INTRODUCTION

During recent years, inductive power transfer (IPT) systems have been widely developed in several fields such as biomedical engineering, consumer electronics and the automotive industry [1-7]. With such increasing use, the human exposure to the radiated electromagnetic fields from these systems in day to day life must be deeply investigated. It is therefore needed to evaluate the compliance to health and safety guidelines [8].

International guidelines for human exposure safety (such as ICNIRP 2010) include two recommendations: reference levels and basic restrictions. The first recommendation to be checked is the reference level. If the reference level is exceeded, then a dosimetry analysis (involving the human body) has to be performed in order to be compliant to the guidelines. The work presented in this paper deals with the reference level. At the standard frequency for inductive power system for wireless charging, 85 kHz, the maximum magnetic flux density allowed according to the ICNIRP in 2010 is 27 μT (reference level).

In order to assess human exposure near IPT systems in automotive applications, adequate modeling methods need to be developed. Nowadays 3D computational models are studied and applied to solve the electromagnetic problem involving the wireless system, the vehicle and the human body (in the vehicle or located beside it) [4-7]. Such full wave computational approaches give reliable results for the radiated fields around the system or the induced quantities in the human body. This may lead to heavy computations that must be repeated for each new configuration. A major point in such problems is that the level of field is highly dependent on various parameters: the shape or size of coils, the geometrical characteristics of the system (structural parts of the vehicle, shielding plates), materials properties (ferrite, frame of the vehicle), the possible misalignment between transmitter and receiver while charging, the position of the human body in case of dosimetry analysis. Moreover, each physical or geometrical parameter may be affected by some uncertainty. For such uncertainty propagation studies, statistical methods based on Monte Carlo simulations may provide reliable results [9]. With this approach, a large set of inputs is considered, and many evaluations of a model response are needed. This leads to a heavy computational cost in case of complex system configurations. To avoid the computational burden and deal with a large variability of data, it can be very useful to build adequate meta-models (or surrogate models). A meta-model is an approximated behavioral model, built with a reduced set of input data, whose behavior is representative of the original model for all data. Metamodeling is a well know procedure in reliability and uncertainty propagation in mechanics. It often relies on stochastic techniques (Kriging, polynomial chaos expansions). In electromagnetics, similar approacheshave been developed and applied to various problems (electromagnetic compatibility problems, microwave devices design, etc.) [10-12]. Recently the quantification of the uncertainty relevant to electrical parameters of a simple wireless transfer system was studied using a polynomial chaos expansion [13]: both the transmitter and receiver units have simple shapes and only consist of a resonant coil (helical or spiral) and a matching loop. Also, Kriging provides an efficient approach that was combined with a finite element software for the design of an inductive power transfer system in [14] and used to verify the compliance of power transfer systems

Submitted On: September 3, 2019
Accepted On: February 22, 2020

regarding human exposure [15].

This paper presents a comparison of surrogate models, Kriging-based and Polynomial chaos-based for the prediction of radiated field in the case of a simplified but realistic 3D inductive power transfer system [16]. In [6] the level of exposure of this system was studied through a parametric analysis involving only the possible misalignment of the two coils. Nevertheless, in practice it is highly desirable to be able to determine the impact of different parameters involved in the electromagnetic analysis. The stochastic techniques used in this paper consider the variability of different parameters defining the 3D configuration in order to evaluate the impact on the radiated magnetic field. In particular, the results show that with a reduced set of input data, accurate predictions can be obtained over a wide range of parameters. These approaches are used to check if the reference levels relevant to the magnetic field are compliant with the recommendations. A sensitivity analysis is performed to evaluate the relative impact of the different parameters.

II. STOCHASTIC MODELING

A. Studied wireless power system

The structure considered in this paper contains two rectangular coils (the transmitter and the receiver), and two ferrite plates [16]. This test case corresponds to an existing inductive power system that has been built in Politecnico di Torino, Italy; the structure studied in this paper involves the main parts of the coupling system. The design also includes a steel plate that represents the chassis of the electric vehicle (Fig. 1). Previous studies [6] have shown that such a simplified chassis is sufficient to evaluate its impact on the results. The dimensions of the system are shown on Table 1. Each coil has 10 turns. This system has been designed for dynamic charging but only static charging is considered in this study. The power electronics controls and keeps the rms value of the current in the transmitter at 36 A and the current in the receiver at 75 A.

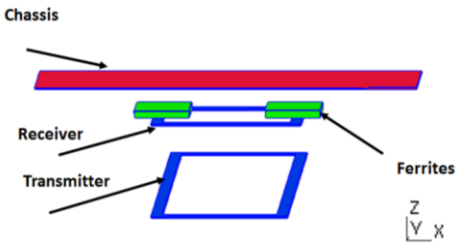

Fig. 1. Wireless power system.

Table 1: Dimensions of the system

	Width (m)	Length (m)
Transmitter	0.5	1.5
Receiver	0.5	0.25
Ferrite	0.2	0.3
Frame	1.5	0.5

B. Kriging

Kriging is a stochastic interpolation algorithm which assumes that the model output M(x) is a realization of a Gaussian process indexed by the input x. A Kriging meta-model is described by the following equation:

$$M(x) \sim M^K(x) = \beta^T f(x) + \sigma^2 Z(x, \omega). \quad (1)$$

The first term in (1), is the mean value of the Gaussian process (trend) and it consists of the regression coefficients β_j (j = 1,…P) and the basis functions f_j (j = 1,…P). Ordinary Kriging has a constant trend. A trend based of linear or quadratic polynomial can also be used. The second term in (1) consists of σ^2, the (constant) variance of the Gaussian process and Z(x, ω), a zero mean, unit variance, stationary Gaussian process. The underlying probability space is represented by ω and is defined in terms of a correlation function R and its hyper-parameters θ. The correlation function R = R(x; x_0 ; θ) describes the correlation between two samples of the input space, *e.g.*, x and x_0 and depends on the hyper-parameter θ. In the context of meta-modelling, it is of interest to calculate a prediction $M^K(x)$ for a new point x, given X = (x_1,…x_n), the experimental design and y = (y_1 =M(x_1),…,y_n = M(x_n)), the corresponding (noise-free) model responses. A Kriging meta-model (Kriging predictor) provides such predictions based on the Gaussian properties of the process.

B. Polynomial chaos expansion

The polynomial chaos is a spectral method and consists in the approximation of the system output in a suitable finite-dimensional basis Ψ(X) made of orthogonal polynomials. A truncation of this polynomial expansion can be written as follows:

$$M(x) \sim M^{PC}(x) = \sum_{j=0}^{P-1} \propto_j \Psi_j(X), \quad (2)$$

where M(x) is the system output, X is the random input vector made of the input parameters x_i, Ψ_j are the multivariate polynomials belonging to $\Psi(X)$, α_j are the coefficients to be estimated, ε is the error of truncation, and P is the size of the polynomial basis $\Psi(X)$. Each multivariate polynomial Ψ_j is built as a tensor product of univariate polynomials orthogonal with respect to the probability density function of each input parameter x_i:

$$\Psi_\alpha(X) = \prod_{i=1}^{N} \Psi_i(x_i). \quad (3)$$

Here, inputs Gaussian distributions are used, and the corresponding polynomial families Ψ_i are the Hermite polynomials families. The coefficients in (2) can be estimated by using spectral projections or least-square regressions [21].

C. Polynomial chaos – Kriging

Kriging interpolates the local variations of the output as a function of the neighbouring experimental design points, whereas PCE approximates well the global behaviour of the output. By combining the global

and local approximation of these techniques, a more accurate meta-model is achieved. Polynomial Chaos-Kriging (PC-Kriging) can be understood as a universal Kriging model the trend of which consists of a set of orthonormal polynomials:

$$M(x) \sim M^{PCK}(x) = \sum_{j=0}^{P-1} \propto_j \Psi_j(X) + \sigma^2 Z(x, \omega), \quad (4)$$

where the first term in the right-hand side is a weighted sum of orthonormal polynomials describing the trend of the PC-Kriging model, and where the second term includes the variance and the zero mean, unit variance, stationary Gaussian process respectively.

The three meta-models summarized above and used in this paper are proposed in the framework for uncertainty quantification are freely available [17]. Kriging (with different trends), Polynomial Chaos Expansion based on the Least Angle Regression (PCE), Kriging combined with Polynomial Chaos Kriging (PCK) are applied to check the compliance regarding the reference levels of radiated magnetic field. For the frequency of interest (85 Hz), the maximum admissible value of the magnetic flux density is 27 µT according to the ICNIRP Guidelines (2010). The experimental design is evaluated by the finite element method using the commercial software COMSOL. The magneto-dynamic problem is solved with a 3D vector potential formulation. The mesh includes around 8000 first order tetrahedral finite elements (Fig. 2). The average size of edges is around 30 mm in coils, ferrite and frame. The mean of the flux density provided by the meta-models in a vertical line, located at 50 cm from the frame representing the possible location of a bystander.

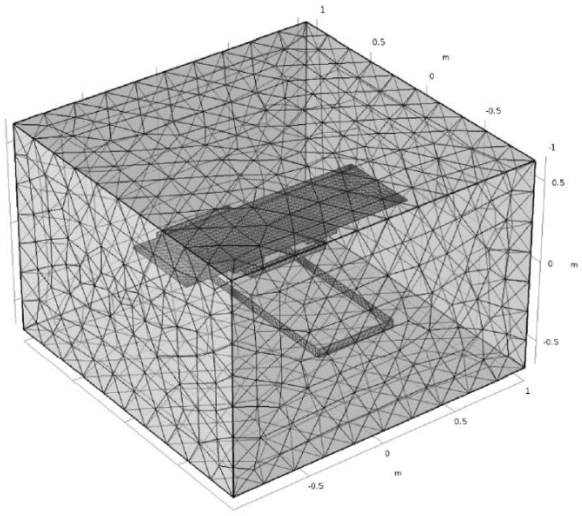

Fig. 2. Finite element mesh used for the computations.

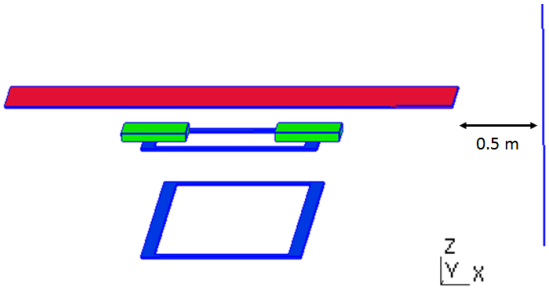

Fig. 3. Position of the observation points (blue line).

III. NUMERICAL RESULTS

A. Configuration with 3 parameters

In the first example, the uncertainty regarding the frame conductivity, distance between coils and length of reception coil is investigated. Here, σ, d, L are the frame conductivity, distance between coils and length of reception coil respectively. The range of variation is shown in Table 1. Regarding the conductivity, the range includes typical values relevant to composite materials which are used in automotive applications [18,19]. These three parameters are important for such analysis since once a park or a road is equipped with defined transmitter coils, different kinds of vehicle may be charged by the system. The level of radiated field then depends on the type of the receiver system (L and d) and car body (σ). They may strongly vary according to the vehicle. The relative permeability of ferrite is 2200.

Table 2: Parameters: Range of variations

Parameter	Min	Max
σ (S/m)	10^4	10^6
d (m)	0.	1.
L (m)	0.2	0.3

The accuracy of the meta-model is checked thanks to the LOO (leave-one-out) cross-validation provided by each meta-model and defined according to [16]:

$$LOO = \sum_{i=1}^{N} (M(x_i) - \hat{M}^{-i}(x_i))^2 / \sum_{i=1}^{N} (M(x_i) - m)^2. \quad (5)$$

This quantity involves N meta-models $\hat{M}^{-i}$, each one created on a reduced experimental design excluding x_i and comparing the prediction to the real value $M(x_i)$. In equation (5), m is the mean of the experimental design response. If the LOO is close to 1, the meta-model is highly modified if one data point is erased, whereas the smaller it is, the least it will be modified.

In order to measure the accuracy of the output model according to the number of sampling points, another

estimate of the accuracy can be defined, the OSE (Out-of-Sample Error):

$$OSE = \frac{1}{N-k}\sum_{i=1}^{N-k}\left(\frac{M(x_i)-M^k(x_i)}{M(x_i)}\right)^2, \quad (6)$$

where M^k is the predictor that was trained using k data-points among the N available.

The OSE is a measure of the accuracy of the meta-model with a reduced set of sampling values.

For the studied case, the meta-model is constructed with 10 randomly selected data points out of 27 (3 samples for each of the three parameters). The computing cost for one simulation (three given parameters) is less than 2 minutes on a work station DELL XEON E5-1630 V3 (64 Go). The number of 27 data inputs points (full wave computations) was chosen as a compromise between accuracy and reasonable computing time in view of an engineering-oriented tool. The accuracy of the meta-model is then calculated on the remaining 17 points out of 27 to get the OSE and the LOO (Table 3). Regarding Kriging, a significant lower LOO is obtained using a linear or quadratic term compared to an ordinary trend. Among the three types of approaches PCK clearly appears as the more accurate.

Table 3: Comparison of different meta-models

	OSE Eq.(5)	**LOO** Eq.(6)
Kriging (ordinary trend)	$2.1\ 10^{-6}$	$2.1\ 10^{-4}$
Kriging (linear trend)	$7.\ 10^{-6}$	$1.7\ 1^{-6}$
Kriging (quadratic trend)	$1.4\ 10^{-5}$	$1.3\ 10^{-5}$
PCK	$7.\ 10^{-6}$	$5.2\ 10^{-11}$
PCE	$7.\ 10^{-6}$	$1.\ 10^{-6}$

In order to study the influence of the number of samples on the predictions, the meta-models were constructed on 8,10,15 randomly selected points out of 27 data points. The values of LOO for different methods and for the three given cases are shown in Table 4. In practice it was shown that using more than 10 points is unnecessary to get a sufficiently accurate surrogate model.

Table 4: LOO values for different numbers of samples

	8 points	**10 points**	**15 points**
Kriging (ordinary trend)	8.8×10^{-6}	$2. \times 10^{-4}$	1.6×10^{-4}
Kriging (linear trend)	1.3×10^{-3}	1.7×10^{-6}	1.2×10^{-8}
Kriging (quadratic trend)	$5. \times 10^{-3}$	1.3×10^{-5}	8.8×10^{-7}
PCK	$1. \times 10^{-3}$	5.2×10^{-11}	3.7×10^{-13}
PCE	2.2×10^{-3}	$1. \times 10^{-6}$	8.1×10^{-7}

B. Configuration with 5 parameters

In this second example, the uncertainty regarding the frame conductivity (σ), distance between coils (d), length of reception coil (L), shift between coils (D) and frame relative permeability (μ) is studied. By increasing the number of parameters, the objective is to evaluate the quality of the meta-models to deal with a larger variability of practical configurations. The distance D refer to a possible misalignment between the transmitter and receiver due to the vehicle position, while charging. The permeability of the frame refers to different type of steel material of the car body. The range of variation of the parameters is shown in Table 5.

Table 5: Parameters: range of variations

Parameter	**Min**	**Max**
σ (S/m)	10^4	10^6
d (m)	0.	1.
L (m)	0.	0.5
D (m)	0.	0.5
μ (H/m)	1000.	3000.

The efficiency of the different meta-models is checked in case of 20 randomly selected data points among 243 (3 samples for each of the five parameters). The corresponding values of the LOO and the OSE are shown in Table 6.

Table 6: Comparison of different meta-models

	OSE	**LOO**
Kriging (ordinary trend)	3.2×10^{-3}	$1. \times 10^{-3}$
Kriging (linear trend)	1.7×10^{-4}	4.1×10^{-4}
Kriging (quadratic trend)	8.2×10^{-4}	8.1×10^{-4}
PCE	2.1×10^{-4}	4.2×10^{-6}
PCK	6.3×10^{-3}	1.5×10^{-4}

The influence of the number of samples is described in Table 7. Again, PCK provides the lowest error.

Table 7: LOO values for different number of samples

	15 points	**20 points**	**25 points**
Kriging (ordinary trend)	6.9×10^{-3}	$1. \times 10^{-3}$	8.4×10^{-4}
Kriging (linear trend)	1.1×10^{-2}	4.1×10^{-4}	5.5×10^{-5}
Kriging (quadratic trend)	2.6×10^{-2}	8.1×10^{-4}	3.5×10^{-5}
PCK	1.7×10^{-3}	4.2×10^{-6}	5.2×10^{-7}
PCE	$6. \times 10^{-2}$	1.4×10^{-4}	1.6×10^{-5}

The maximum mean value of the B field recorded on the vertical line shown on Fig. 3 occurs in front of the air gap between the coils. If the number of samples is sufficient (above 20 in the present case) the three meta-models give the same outputs: the relative error between the field obtained but the meta-model and that deduced from the finite element method remains below 0.6% for all the values computed along the vertical line. The predictions remain under the ICNIRP limit of 27 µT.

Table 8 gives the values of the Sobol indices which quantify the impact of uncertain input variables on the output [20]. These indices may be useful in case of a sensitivity analysis. The higher the Sobol index, the stronger the influence of the related input in the output uncertainty. The Sobol indices are directly and analytically extracted from the polynomial chaos expansion [21]. This is a key interest of PCE: the results are obtained sensitivity indices and are computed at almost no additional cost with a computing time which is several orders of magnitude lower compared to a standard Monte Carlo analysis. As expected in this simplified studied case, the distance between the coils has the greatest impact on the magnetic field. Because of the position of the observation point, the physical properties of the plate has negligible effect. The two other parameters which have a significant impact are the shift between the coils and the length of the reception coil. Of course, in the case of a dosimetry analysis involving a realistic human exposure situation, the field has to be evaluated accurately using many observation points near the system (and not only on the vertical line of interest) and in the biological tissues [22-24]. Then the conclusions may be different.

Table 8: Sensitivity of parameters

Parameter	**Sobol Index**
σ (S/m)	$1. \times 10^{-8}$
d (m)	0.83
L (m)	0.3
D (m)	0.15
µ (H/m)	$1. \times 10^{-8}$

IV. CONCLUSION

Predictions of the radiated magnetic field have been obtained from stochastic models based on Kriging and Polynomial chaos expansions in the case of a simplified but realistic wireless power transfer system. This feasibility analysis shows that meta-models provide efficient approaches to consider uncertainties of different physical or geometrical parameters. With a reduced number of samples, the combination of Kriging and Polynomial chaos expansions can be used as a fast predictor to check if reference levels fit the guidelines for human exposure. The work is now extended to investigate more complex configurations, which consider the global structure of the vehicle. Such an approach will also make any sensitivity analysis when designing the system with appropriate shielding structural parts easier.

ACKNOWLEDGMENT

The results here presented are developed in the framework of the 16ENG08 MICEV Project. The latter received funding from the EMPIR program co-financed by the Participating States and from the European Union's Horizon 2020 research and innovation program.

REFERENCES

[1] X. Shi, C. Qi, M. Qu, S. Ye, and G. Wang, "Effects of coil locations on wireless power transfer via magnetic resonance coupling," *ACES Journal*, vol. 31, no. 3, pp. 270-278, 2018.

[2] D.-G. Seo, S.-H. Ahn, J.-H. Kim, S.-T. Khang, S.-C. Chae, J.-W. Yu, and W.-S. Lee, "Power transfer efficiency for distance-adaptive wireless power transfer system," *ACES Journal*, vol. 33, no. 10, pp. 1171-1174, 2018.

[3] Y. Guo, L. Wang, and C. Liao, "A general equivalent model for multi-coil wireless power transfer system analysis and its application on compensation network design," *ACES Journal*, vol. 33, no. 6, pp. 648-656, 2018.

[4] M. Feliziani, S. Cruciani, T. Campi, and F. Maradei, "Near field shielding of a wireless power transfer (WPT) current coil," *Progress In Electromagnetics Research C*, vol. 77, pp. 39-48, 2017.

[5] S. Park, "Evaluation of electromagnetic exposure during 85 kHz wireless power transfer for electric vehicles," *IEEE Trans. on Magnetics*, vol. 53, no. 1, paper 5100208, 2018.

[6] V. Cirimele, F. Freschi, L. Giaccone, L. Pichon, and M. Repetto, "Human exposure assessment in dynamic inductive power transfer for automotive applications," *IEEE Trans. on Magnetics*, vol. 53, no. 6, paper 5000304, 2017.

[7] C. Cimala, M. Clemens, J. Streckert, and B. Schmuelling, "Simulation of inductive power transfer systems exposing a human body with a coupled scaled-frequency approach," *IEEE Transactions on Magnetics*, vol. 53, no. 6, paper 7201804, 2017.

[8] ICNIRP Guidelines for Limiting Exposure to Time Varying Electric and Magnetic Fields (1Hz-100 KHz). Health Physics, 99, pp. 818-836, 2010.

[9] D. Kroese, T. Taimre, and Z. Botev, *Handbook of Monte Carlo Methods*. Wiley Series in Probability and Statistics, 2011.

[10] O. J. Alkhateeb and N. Ida, "Data-driven arbitrary polynomial chaos for uncertainty quantification in filters," *ACES Journal*, vol. 33, no. 9, pp. 1048-1051, 2018.

[11] J. S. Ochoa and A. C. Cangellaris, "Macro-

modeling of electromagnetic domains exhibiting geometric and material uncertainty," *ACES Journal*, vol. 27, no. 2, pp. 80-87, 2012.

[12] S. Lalléchère, P. Bonnet, I. El Baba, and F. Paladian, "An electromagnetic compatibility problem via unscented transform and stochastic collocation methods," *ACES Journal*, vol. 27, no. 2, pp. 94-101, 2012.

[13] S. Bilicz, S. Gyimóthy, J. Pávó, P. Horváth, K. Marák, Uncertainty quantification of wireless power transfer systems, *IEEE Wireless Power Transfer Conference (WPTC)*, May 5-6, 2016, Aveiro, Portugal, 2016.

[14] K. Knaisch and P. Gratzfeld, "Gaussian process surrogate model for the design of circular, planar coils used in inductive power transfer for electric vehicles," *IET Power Electron*., vol. 9, no. 15, pp. 2786-2794, 2016.

[15] P. Lagouanelle, V.-L. Krauth, and L. Pichon, "Uncertainty quantification in the assessment of human exposure near wireless power transfer systems in automotive applications," *Automotive*, Torino, Italy, July 2-5, 2019.

[16] V. Cirimele, "Design and integration of a dynamic IPT system for automotive applications," *Ph.D. Dissertation*, Politecnico di Torino and University Paris-Saclay, 2017.

[17] S. Marelli and B. Sudret, "UQLab: A framework for uncertainty quantification in Matlab," *Proc. 2nd Int. Conf. on Vulnerability, Risk Analysis and Management (ICVRAM2014)*, Liverpool, United Kingdom, 2554-2563, 2014.

[18] W. Abdelli, X. Mininger, L. Pichon, and H. Trabelsi, "Impact of composite materials on the shielding effectiveness of enclosures," *ACES Journal*, vol. 7, no. 4, pp. 369-374, 2012.

[19] G. Al Achkar, L. Pichon, N. Benjelloun, and L. Daniel, "A broadband electromagnetic homogenization method for composite materials," *IEEE Trans. on Magnetics*, vol. 54, no. 3, 9400304, 2018.

[20] I. M. Sobol, "Sensitivity estimates for nonlinear mathematical models," *Mathematical Modelling and Computational Experiments*, vol. 1, no. 4, pp. 407-414, 1993.

[21] B. Sudret, "Global sensitivity analysis using polynomial chaos expansions," *Reliability Engineering & System Safety*, vol. 93, no. 7, pp. 964-97, 2008.

[22] J. Silly-Carette, D. Lautru, M.-F. Wong, A. Gati, J. Wiart, and V. Fouad Hanna, "Variability on the propagation of a plane wave using stochastic collocation methods in a bio electromagnetic application," *IEEE Microwave and Wireless Components Letters*, vol. 19, no. 4, pp. 185-187, 2009.

[23] E. Chiaramello, M. Parazzini, P. Ravazzani, and J. Wiart, "Assessment of fetal exposure to 4G LTE tablet in realistic scenarios using stochastic dosimetry," in *Proc. 2017 International Applied Computational Electromagnetics Society Symposium-Italy (ACES)*, Mar. 2017.

[24] S. Lalléchère, K. El Khamlichi Drissi, P. Bonnet, and D. Poljak, "Stochastic sensitivity in homogeneous electromagnetic-thermal dosimetry model of human brain," *ACES Journal*, vol. 31, no. 6, pp. 644-652, 2016.

Compact Multilayer Substrate Integrated Waveguide Dual-band Filtering Rat-race Coupler Based on Fan-shaped Cavities

Zhigang Zhang, Yong Fan, Yujian Cheng, and Yonghong Zhang

Fundamental Science on Extreme High Frequency Key Laboratory
University of Electronic Science and Technology of China, Chengdu 611731, China
freemanzzg@163.com, yfan@uestc.edu.cn, chengyujian@uestc.edu.cn, zhangyhh@uestc.edu.cn

Abstract ─ A new type of multilayer dual-band filtering rat-race coupler based on fan shaped substrate integrated waveguide (SIW) cavity is first proposed in this paper. Resonant frequencies of SIW fan-shaped cavity (SIFC) have been derived to construct a resonant cell. Magnetic and electric coupling between SIFCs are realized through multiple rectangular and circular slots located on metal layer, respectively. Specifically, the multiple rectangular slots are beneficial to increase coupling bandwidth and achieve better amplitude and phase balance. Moreover, the bandwidth ratio and center frequency of two pass-bands can be flexibly controlled by adjusting the size of band-stop resonators. The detailed analysis and the design method based on coupling matrix have been introduced to realize a dual-band filtering rat-race coupler. The new type of component should be able to provide at least three functions simultaneously, including in-phase and out-of-phase power dividing, filtering, and dual-band operation. Compared with other filtering couplers, the proposed design exhibits good dual-band filtering responses, high *Q* factor, better isolation, amplitude balance, as well as 0° and 180° phase differences.

Index Terms ─ Dual-band, filtering rat-race coupler, multilayer, substrate integrated fan-shaped cavity (SIFC).

I. INTRODUCTION

Rat-race couplers are essential components in transceivers for microwave communication systems, which can operate as an in-phase or out-of-phase power divider by properly choosing the excitation ports. As such, it can be used in the design of numerous components such as power amplifiers, balanced mixers, and antenna array feeding networks.

Meanwhile, the rapid development of various wireless communication systems has also led to the demand of dual-band operations in filters and couplers, which hold the promise for multichannel design. The emerging substrate integrated waveguide (SIW) technology [1-10] provides such a platform that can easily apply the dual-band or multilayer technology to the design of couplers and filters, and facilitate the miniaturization design of couplers and filters [11-12], which is becoming one of the primary trends for SIW components. In [1], synthesis and design techniques of dual-band filters are proposed. On one hand, the use of multilayered topologies [3-6] is known to provide more freedom to design coupling paths between waveguided structures while maintaining a compact circuit size [9]. A compact multilayer dual-mode filter based on the substrate integrated circular cavity (SICC) is developed in [6]. A design method for multiband bandpass filters with multilayer configuration is proposed in [10].

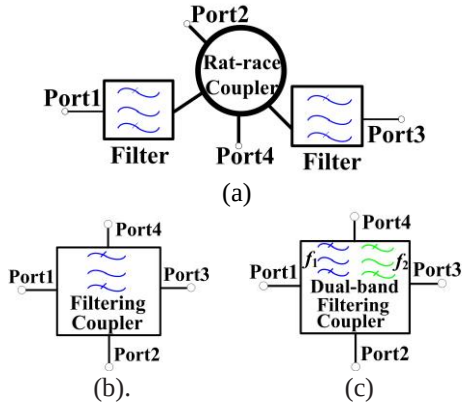

Fig. 1. (a) Cascaded filter and rat-race coupler, (b) single-band filtering rat-race coupler, and (c) dual-band filtering rat-race coupler.

Generally, couplers and filters are cascaded in transceivers front ends with the topology shown in Fig. 1 (a). Two filters are needed to integrate bandpass responses into a rat-race coupler, which leads to a large circuit area, a complex configuration and unwanted loss. On the other hand, to further reduce size, a single device integrated with different functionalities, such as filtering coupler [12-25], has been attracting increasing attention. It also recommends an effective way to avoid the performance degradation due to a cascade connection of two individual components, as shown in Fig. 1 (b).

Submitted On: February 13, 2020
Accepted On: February 28, 2020

Bandpass 90° and 180° directional couplers with coupled resonators have been first proposed in [13]. A compact filtering 180° hybrid is presented in [16]. Based on our knowledge, there are two methods [24-25] to realize the in-phase and out-of-phase operations in SIW rat-race coupler. Four TE_{101}-mode square cavities based on multilayer coupling structures are utilized to construct the filtering rat-race coupler [24]. A SIW filtering rat-race coupler based on TE_{102} and TE_{201} orthogonal degenerate modes is proposed in [25]. However, the above-mentioned filtering couplers can only operate in single frequency band. It is noteworthy that integrating dual-band technology into multifunctional components is a more effective way to realize miniaturization design. As shown in Fig. 1 (c), the dual-band filtering coupler is equivalent to cascading two single-band filtering couplers operating in different frequency band. The new type of component should be able to provide at least three functions simultaneously, including in-phase and out-of-phase power dividing, filtering, and dual-band operation. Moreover, the SIW filtering rat-race couplers with multiple frequency bands are rarely reported.

In this paper, a compact multilayer dual-band filtering rat-race coupler based on substrate integrated fan-shaped cavities (SIFCs) is proposed for the first time. The multilayer SIFC structure is not only compact, but also convenient for the realization of electric and magnetic coupling between resonators. Specifically, the magnetic coupling between SIFCs is obtained by using multiple rectangular slots, which increases the magnetic coupling strength and operation bandwidth, as well as achieves better amplitude and phase balance. Moreover, the bandwidth ratio and center frequency of two pass-bands can be flexibly controlled. What's unique about the analysis process of dual-band filtering rat-race coupler is that the bandwidth and center frequency of the corresponding broadband filtering coupler can be obtained from the specification of dual-band filtering coupler, due to the fact that the two passbands are formed by loading the bandstop resonator. The required coupling coefficient and external quality factor can be obtained by analyzing the topology of the single-band filtering coupler. Afterwards, the coupling matrix method is used to evaluate the initial value of design parameters accurately according to the specifications, which is beneficial to accelerate the later optimization design process. It's a good combination of multilayered topologies, multiband technology and multifunctional component, which realizes the miniaturization design of the coupler while keeping good performance.

II. ANALYSIS AND DESIGN

A. Coupler structure

As shown in Fig. 2, the multilayer SIW dual-band filtering coupler consists of fan-shaped SIW cavities coupled together by means of four rectangular slots and a circular slot etched in the common broad wall of adjacent SIFCs.

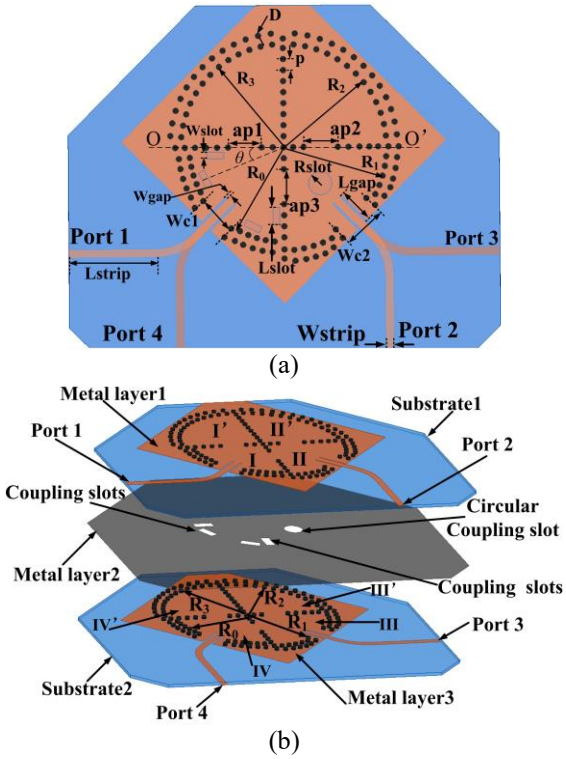

Fig. 2.The proposed multilayer SIFC dual-band filtering coupler: (a) top view and (b) anatomy view.

The configuration of the dual-band filtering coupler is illustrated in Fig. 2 (b).When signals are injected into port 1, the equal magnitude and phase signals are then taken out from port 2 and 4. However, when port 3 is excited, signals reach ports 2 and 4 through electrical and magnetic coupling, respectively. Then, the equal magnitude and opposite phase signals are acquired form port 2 and 4. Furthermore, two pairs TM_{101} SIFC bandstop resonators (Resonator I'~IV') are simultaneously coupling with TM_{101} SIFC bandpass resonators (Resonator I~IV) by the post-wall irises in the common post walls.

B. Analysis of coupler

The topology of the corresponding single-band filtering rat-race coupler is shown in Fig. 3 (a). As we can see, since each port of the coupler is loaded by a resonator, band-pass response can also be realized. Moreover, if each resonator (Resonator 1~4) is replaced by a dual-behavior unit (Unit1~4), a dual-band filtering rat-race coupler can be obtained.

Here, the dual-behavior unit is made up of two coupled resonators, as shown in Fig. 3 (b). Interestingly, the single-band filtering coupler could be regarded as a special case of dual-band filtering coupler by assuming $M11'=M22'=M33'=M44'=0$.

The topology of the dual-band filtering rat-race coupler is shown in Fig. 3 (b). As seen, the dual-band rat-race coupler has following two working states. When signals are injected from port 1, the output signals from ports 2 and 4 are in-phase, equal power allocation (M_{21}=M_{41}), just as an in-phase power divider should do. If port 3 is excited, the out-of-phase responses are obtained in ports 2 and 4 (-M_{23}=M_{43}). In this case, the coupler can be seen as an out-of-phase power divider. Moreover, the output signal has dual-band response characteristics.

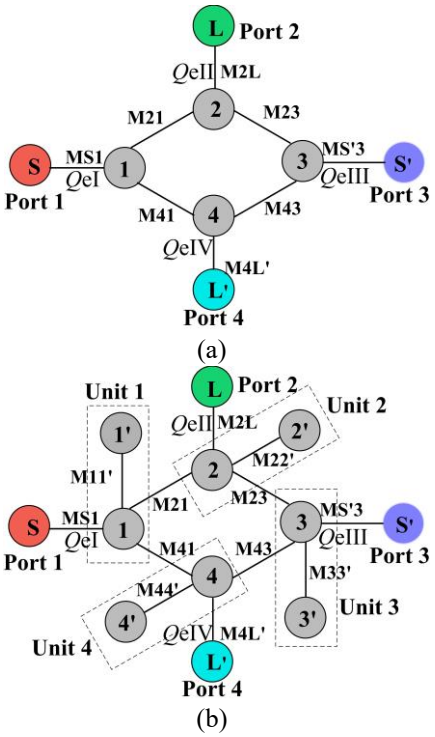

Fig. 3. (a) Topology of the corresponding single-band filtering coupler, (b) Topology of the multilayer dual-band filtering coupler, Unit1~4 represent dual-behavior resonator.

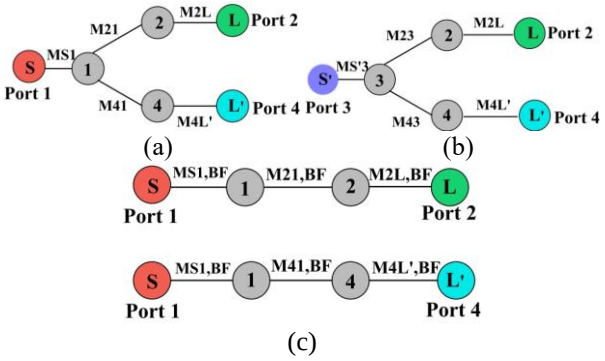

Fig. 4. (a) Topology of the filtering in-phase power divider, (b) topology of the filtering out-of-phase power divider, and (c) topology of two second-order filters.

As depicted in Figs. 4 (a) and (b), in these two working states, the single-band filtering coupler is equivalent to an in-phase filtering power divider and an out-of-phase filtering power divider, respectively. Moreover, divider I and II shown in Figs. 4 (a) and (b) are both designed with 3-dB power split ability and have same passband characteristics but quite different phase characteristic. Therefore, the coupling coefficients between resonators of dividers have the following relationship:

$$M_{21}=M_{41}=-M_{23}=M_{43}, \tag{1}$$

each power divider can be divided into two second-order bandpass filters which have the same operating frequency and passband characteristics, as shown in Fig. 4 (c). The coupling matrix of this second-order coupled-resonator band-pass filter is expressed as:

$$m_{N+2}=\begin{array}{c} \\ S \\ 1 \\ 2 \\ L \end{array}\begin{array}{c} \begin{array}{cccc} S & 1 & 2 & L \end{array} \\ \begin{bmatrix} 0 & m_{S1,BF} & 0 & 0 \\ m_{1S,BF} & 0 & m_{12,BF} & 0 \\ 0 & m_{21,BF} & 0 & m_{2L,BF} \\ 0 & 0 & m_{L2,BF} & 0 \end{bmatrix} \end{array}. \tag{2}$$

And the normalized input impedance of the filtering power divider in Fig. 4 (a) is required to be the same as matrix (2). Thus, the coupling coefficients for the filtering power divider topology in Fig. 4 (a) are determined as:

$$M_{S1,BF}=M_{S1}, \tag{3a}$$

$$M_{2L}=M_{4L'}=M_{2L,BF}=M_{4L',BF}. \tag{3b}$$

According to the filter design theory some elements in the matrix should be reduced by a factor of $\sqrt{2}$ to meet the requirement of input port matching of the power divider [18]:

$$M_{12}=M_{14}=\frac{M_{12,BF}}{\sqrt{2}}. \tag{4}$$

Based on (1), (2), and (4), the coupling matrix for the filtering power divider topology in Fig. 4 (a) is determined as:

$$M_{S1,BF}=M_{S1}, \tag{5a}$$

$$M_{2L}=M_{4L'}=M_{2L,BF}=M_{4L',BF}, \tag{5b}$$

$$M_{21}=M_{41}=-M_{23}=M_{43}=\frac{M_{21,BF}}{\sqrt{2}}=\frac{M_{41,BF}}{\sqrt{2}}. \tag{5c}$$

The required normalized coupling coefficient (m) and external quality factors (Q_e) for the filtering power divider can be calculated by:

$$m_{12}=\frac{M_{21}}{FBW}=\frac{M_{41}}{FBW},\quad m_{12,BF}=\frac{M_{21,BF}}{FBW}, \tag{6}$$

$$Q_e=\frac{FBW}{M_{S1}^2}=\frac{FBW}{M_{2L}^2}=\frac{1}{FBW\times m_{S1}^2}. \tag{7}$$

Generally, external quality factor (Qe) is related to the following two parameters: the length of feeding slot (Lgap), the width of external coupling aperture (Wc). In

order to obtain the same return loss and passband characteristics on each port, we have:

$$Q\text{eI}= Q\text{eII}= Q\text{eIII}= Q\text{eIV}=Q\text{e}. \quad (8)$$

C. Design considerations

Generally, the response of proposed dual-band filtering coupler with different bandwidth ratio can be divided into following three cases (Condition I~III).

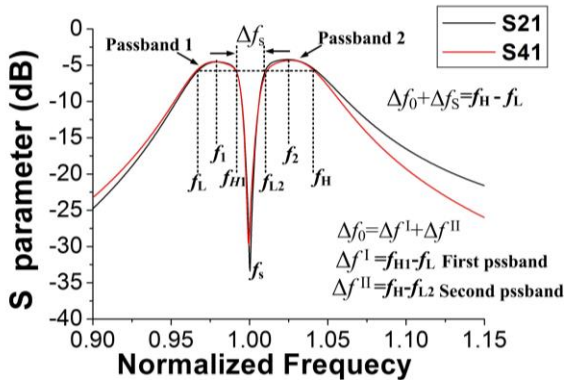

Fig. 5. Response of multilayer dual-band filtering coupler in Condition I ($\Delta f^{I}=\Delta f^{II}$, $f_s=f_0$).

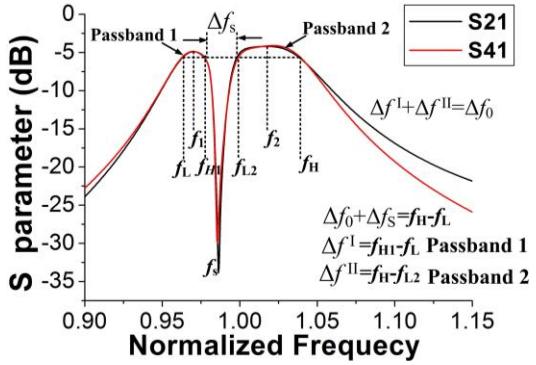

Fig. 6. Response of multilayer dual-band filtering coupler in Condition II ($\Delta f^{I}<\Delta f^{II}$, $f_s<f_0$).

In the first case, the bandwidth of two pass-bands is equal, and the bandwidth ratio equal to 1. Here, Δf^{I} and Δf^{II} represent absolute bandwidths (ABW) of passband 1 and passband 2, respectively. Figure 5 depicts response of the dual-band filtering coupler under Condition I. As seen, the dual-band filtering coupler creates two passbands (f_L, f_{H1}) and (f_{L2}, f_H). Where, f_1 and f_2 are the center frequencies of passband 1 and passband 2, respectively. f_0 and Δf_0 are the center frequency and bandwidth of the corresponding single-band filtering coupler. f_s and Δf_s are the center frequency and bandwidth of the stopband, respectively.

As shown in Fig. 6, the second case is that the bandwidth of the first passband is smaller than that of the second passband. In addition, the center frequency of stopband is less than that of the corresponding single-band filtering coupler.

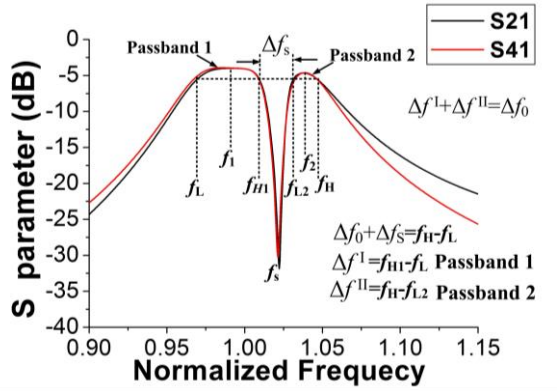

Fig. 7. Response of multilayer dual-band filtering coupler in Condition III ($\Delta f^{I}>\Delta f^{II}$, $f_s>f_0$).

Figure 7 plots the response of dual-band filtering coupler in Condition III, which demonstrates that the bandwidth of the passband 1 is larger than that of the passband 2. Due to the fact the two passbands are formed by splitting the frequency band of a broadband filtering coupler into two parts, combined with the topological structures, the bandwidth (BW) and center frequency of the corresponding single-band filtering coupler are obtained from the specification of the dual-band coupler ($f_0=\sqrt{f_L f_H}$, $\Delta f^{I}+\Delta f^{II}=\Delta f_0$), and the corresponding coupling coefficient and Qe can be obtained by analyzing the single-band filtering coupler, then the initial value of the internal coupling parameters and the length of the feeding slot can be determined.

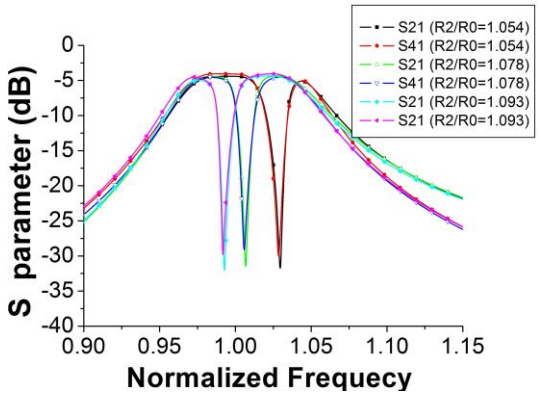

Fig. 8. Variation of stopband center frequency with R2/R0.

The central frequencies of dual-band filtering coupler are determined by the size of the band-pass

resonators (R0, R1). Besides, the radius of the band-stop resonators (R2, R3) is used to control the bandwidth ratio of the two pass-bands. As shown in Fig. 8, with the increase of R2/R0, the center frequency of the stopband decreases, thus the absolute bandwidths (ABW) of the pssband 1 and passband 2 can be adjusted. Throughout the entire procedure, it can be seen that the two passbands of this filtering coupler can be synthesized with prescribed BWs and center frequencies. The resonant frequency of mode for circular cavity with solid wall can be calculated by [34]:

$$f_{mpn}=\begin{cases}\dfrac{c}{2\pi\sqrt{\mu_r\varepsilon_r}}\sqrt{\left(\dfrac{\mu'_{mn}}{R}\right)^2+\left(\dfrac{p\pi}{\Delta h}\right)^2} & TE_{mpn}\\ \dfrac{c}{2\pi\sqrt{\mu_r\varepsilon_r}}\sqrt{\left(\dfrac{\mu_{mn}}{R}\right)^2+\left(\dfrac{p\pi}{\Delta h}\right)^2} & TM_{mpn}\end{cases},(9)$$

where μ_r and ε_r are relative permeability and permittivity of the filling material, μ_{mn} and μ'_{mn} are the nth roots of mth Bessel function of the first kind and its derivative, R is the radius of circular cavity, Δh is the height of the of circular cavity ,and c is the speed of light in free space. According to Equation 9 and by means of the least square method, the resonant frequency of the TM_{101} mode for SIFC can be calculated by the following formula:

$$f_{101}=\frac{0.383c}{\dfrac{1}{b_\theta}R_{eff}\sqrt{\mu_r\varepsilon_r}},\ R_{eff}=R-\frac{D^2}{0.95p}. \quad (10)$$

Where, θ is the central angle of SIFC, R_{eff} is the equivalent radius of the fan-shaped cavity. D and p are the diameter of metallized via-holes and center-to-center pitch between two adjacent via-holes. b_θ is related to the central angle of a fan-shaped resonator. When θ=60°, 90°, 120°, b_θ is approximately equal to 2.7, 2.1, 1.86, respectively.

D. Design example

In this design, the targeted specification of the dual-band filtering coupler is prescribed as follows:

1) Passband 1: 9.205–9.370 GHz (BW:165 MHz);
2) Passband 2: 9.565–9.875 GHz (BW:310 MHz);
3) In-band return loss: 20.0 dB.

According to the above analysis, the bandwidth and center frequency of the corresponding single-band filtering coupler are obtained from the specification of the dual-band coupler. The desired passband of single-band filtering coupler is centered at 9.535 GHz with the 2.9% fractional bandwidth (FBW) of 20-dB equal-ripple return loss (1-dB BW: 475MHz). Based on the advanced coupling matrix synthesis method in [33], the initial normalized coupling matrix of corresponding BPF can be synthesized as:

$$m_{N+2}=\begin{array}{c}\\S\\1\\2\\L\end{array}\begin{array}{c}\begin{array}{cccc}S & 1 & 2 & L\end{array}\\\begin{bmatrix}0 & 1.22474 & 0 & 0\\1.22474 & 0 & 1.65831 & 0\\0 & 1.65831 & 0 & 1.22474\\0 & 0 & 1.22474 & 0\end{bmatrix}\end{array}. \quad (11)$$

From (3)–(7), (11) the desired parameters of the filtering power dividers can be calculated as follows: M_{21}=M_{41}=-M_{23}=M_{43}=0.0343672, Qe,$_{S1}$=22.7465, Qe,$_{2L}$= Qe,$_{4L}$=22.7465. To extract Qe, full-wave simulations using ANSYS HFSS are carried out for the singly loaded SIFC excited by a 50-Ω microstrip line. The coupling strengths are controlled by the feeding slot length Lgap with fixed slot width Wgap = 0.3mm and coupling window width Wc = 5.35 mm. Qe can be extracted from the phase and the group delay response of S11 using [32]:

$$Qe=\frac{f_0}{\Delta f_{\pm 90^\circ}}. \quad (12)$$

Where, f_0 denotes the frequency at which the group delay of S11 reaches the maximum, $\Delta f_{\pm 90^\circ}$ indicates the ABW (absolute bandwidth) between ±90° points with respect to the absolute phase of S11 at f_0.

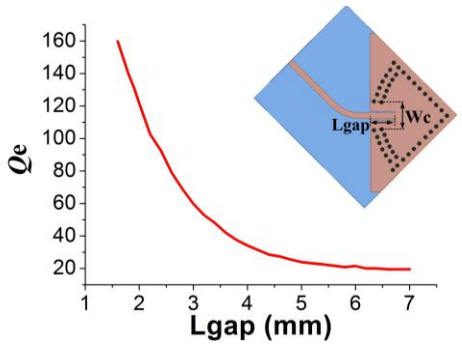

Fig. 9. Simulated external quality factor Qe change with Lgap, Wc=5.35mm.

Figure 9 shows the external quality factor Qe versus the length of feeding slot Lgap. It can be seen that the larger the feeding slots length, the smaller the external quality factor. The adjustment of external quality factor is realized by changing the value of Lgap, as depicted in Fig. 9. Then, the desired Qe (QeI = QeII = QeIII= QeIV= Qe) can be achieved and the initial value of Lgap can also be determined.

In general, the coupling coefficient of two coupled SIW cavities can be extracted by full-wave simulations. For two synchronously tuned coupled resonators, two split resonant frequencies can easily be identified by two resonance peaks, the coupling coefficient can then be evaluated using the formula [32]:

$$M_{ij} = \frac{f_{p2}^2 - f_{p1}^2}{f_{p2}^2 + f_{p1}^2}, \quad (13)$$

where f_{p1} and f_{p2} are the lower and higher resonant frequencies, respectively. Then, the relationship between coupling coefficients and physical structures of coupled resonators should be established.

The coupling coefficient M_{41} versus the rectangular slot length (Lslot) and offset angle (θ) are plotted in Figs. 10 (a) and (b). Obviously, when the lengths of the rectangular coupling slots increase, coupling coefficient also increases accordingly. In addition, the locations of coupling slots also have effect on the coupling strength between two SIW cavities.

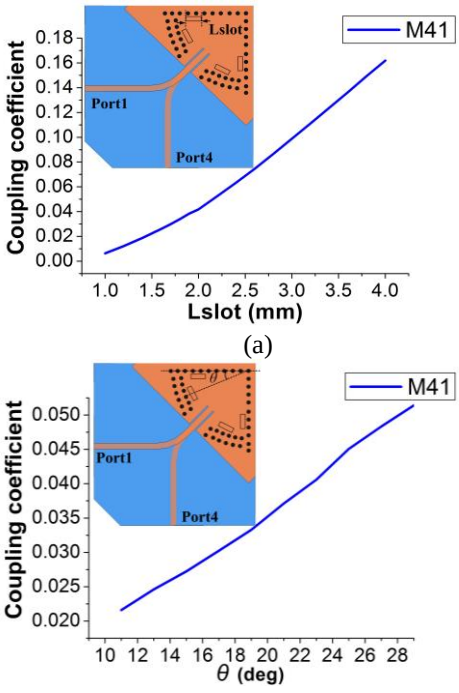

Fig. 10. Coupling coefficients versus the coupling slot: (a) M_{41} versus Lslot, Wslot=0.8mm, and (b) M_{41} versus θ, Lslot =1.85mm.

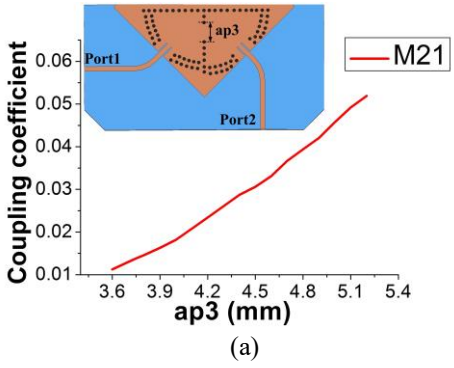

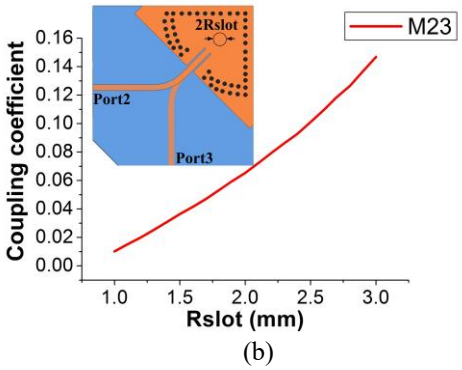

Fig. 11. Coupling coefficients versus the coupling slot: (a) M_{21} versus ap3 and (b) M_{23} versus Rslot.

Figure 11 illustrates the extracted curves of M_{21}, M_{23} which versus the width (ap3) and the radius (Rslot) of coupling slot, respectively.

In summary, the design procedure of the proposed dual-band filtering coupler is listed as follows. Firstly, the bandwidth (Δf_0) and center frequency (f_0) of the corresponding single-band filtering coupler are obtained from the specification of the dual-band filtering coupler. Then, the resonant frequency of the SIFC is calculated by formula (9) ~ (10), to meet the required center frequency f_0. Secondly, a coupling matrix of a second-order BPF is synthesized according to the desired center frequency f_0 and the fractional bandwidth (FBW). Thirdly, according to formulas (3) ~ (8), the coupling matrix and Qe of the corresponding filtering coupler are obtained. Moreover, internal coupling parameters (Lslot, θ, ap3, Rslot) and external coupling parameters (Wc1, Wc2, Lgap) are tuned to meet desired values of coupling coefficients and external quality factor, respectively. Finally, fine tuning of the entire structure is performed to realize good dual-band filtering rat-race coupler performance.

III. SIMULATED AND MEASURED RESULTS

After optimization implemented by HFSS, the geometry parameters of the proposed dual-band filtering coupler are chosen as follows (all in mm): R_0=12.9, R_1=14.15, R_2=R_3=14.2, ap3=4.77, Lgap=5.1, Wgap=0.3, θ=19deg, ap1=4.6 ap2=4.7, Rslot=1.4, Lslot=1.9, Wslot=0.9, Wc1=5.36, Wc2=5.96, Lstrip=11, Wstrip=1.15, D=0.8, p=1.5. To verify the above method, the proposed dual-band filtering coupler was designed and fabricated on a substrate with thickness of 0.508 mm, relative dielectric constant of 3.5 and dielectric loss tangent 0.0018 (at 10 GHz). The measurement is accomplished by using the Agilent N5244A network analyzer.

Figures 12 (a), (b) show the simulated and measured

S-parameters under the in-phase operation. The measured first passband is centered at 9.308 GHz with the 1-dB FBW of 1.62%. The in-band return loss is better than 15 dB. The minimum insertion losses including the 3-dB equal power division loss are (3+1.95) and (3+2.05) dB, with the amplitude imbalance of 0.1 dB.

The second passband is located at 9.738GHz with the 1-dB FBW of 3.12%. The in-band return loss is better than 18.5 dB. The minimum insertion losses including the 3-dB equal power division loss are (3+1.28) and (3+1.33) dB, with the amplitude imbalance of 0.1 dB.

Figures 13 (a), (b) show the simulated and measured S-parameters under the out-of-phase operation. The measured first passband is centered at 9.310GHz with the 1-dB FBW of 1.53%.The in-band return loss is better than 16 dB. The minimum insertion losses including the 3-dB equal power division loss are (3+1.99) and (3+2.08) dB, with the amplitude imbalance of 0.1 dB. The second passband are located at 9.739 GHz with the 1-dB FBW of 3.05%. The in-band return loss is better than 20 dB. The minimum insertion losses including the 3-dB equal power division loss are (3+1.35) and (3+1.4) dB, with the amplitude imbalance of 0.1 dB.

When signals are injected from port 1 and port 3, the measured in-band phase differences between two output ports are nearly 0° and 180°, respectively, with the variation of less than 3.5°, as depicted in Fig. 14.

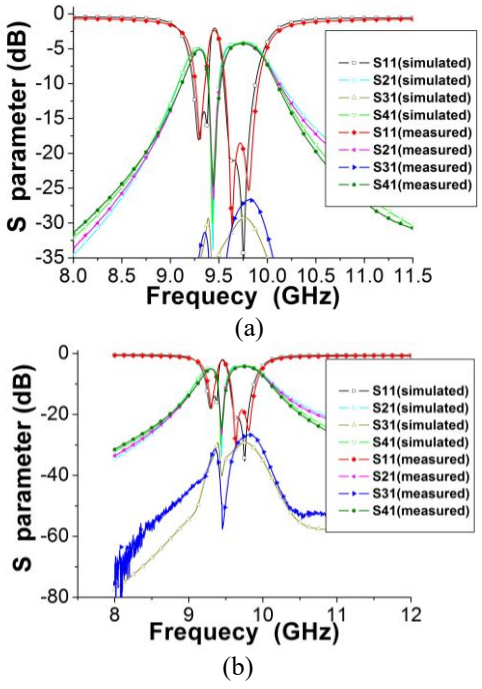

Fig. 12. Simulated and measured results of the fabricated dual-band filtering coupler: (a) and (b) Port 1 is excited.

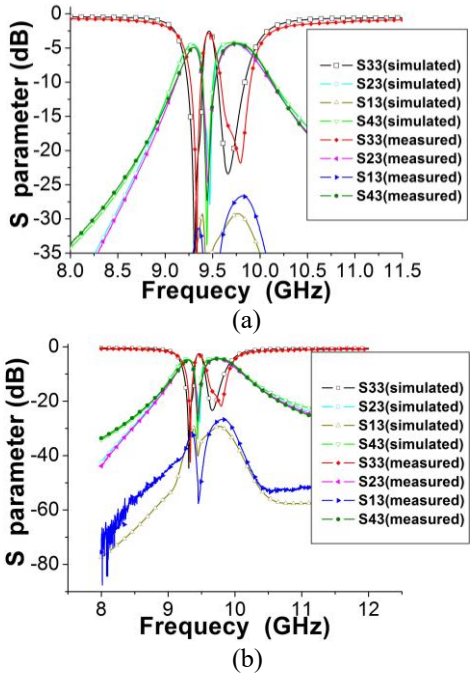

Fig. 13. Simulated and measured results of the fabricated dual-band filtering coupler: (a) and (b) Port 3 is excited.

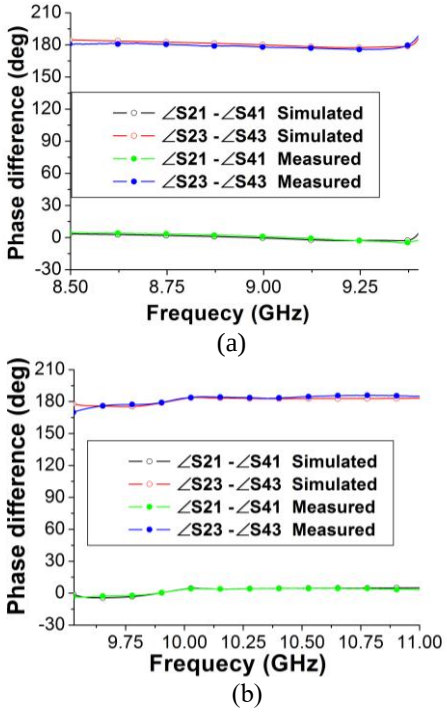

Fig. 14. Phase differences of the fabricated multilayer dual-band filtering coupler: (a) first passband and (b) second passband.

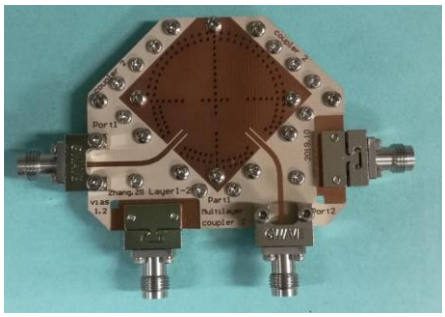

Fig. 15. Photograph of the fabricated multilayer dual-band filtering rat-race coupler.

Figure 15 is the photograph of the fabricated multilayer dual-band filtering rat-race coupler.

A detailed performance comparison with filtering couplers in recent years is shown in Table 1. Compared with [16] and [17], the proposed design has much higher Q factor and self-consistent electromagnetic shielding structure, which is suitable for higher frequency operation. In [19], although the Q factor of the filtering coupler is very high, the 3-D DR structure with large height makes it more difficult to be integrated with other planar circuits. A single-band filtering rat-race coupler based on the orthogonal modes is proposed in [25]. The desired 0° and 180° phase differences are realized by the inherent characteristics of TE_{102} and TE_{201} modes. Therefore, the input port and isolation port, as well as the two output ports, must be kept perpendicular to each other, which makes the phase characteristics and isolation dependent on the port direction. In [26], a novel coupler with arbitrary division, optional phase difference, and alternative input/output impedances is presented for the first time. Based on hybrid couplers, a microwave device able to detect differential-mode to common-mode conversion is proposed in [27]. A dual-mode hybrid coupler, capable of providing distinguished functions as rat-race couplers at two frequency bands, is first demonstrated in [28]. Compared with the works in [16-28], the proposed structure not only has relatively high Q factor, better isolation, flexibly controlled bandwidth ratio, simple structure, but also can be suitable for the application of multiple operation band, which is helpful to achieve high density and miniaturized RF/microwave wave system.

Table 1: Performance comparison of various filtering rat-race couplers

Ref.	f_0 (GHz)/ FBW (%)/ε_r	IL (dB)/ Isolation (dB)/Q factor	Mag.(dB)/ Phase (deg) Imbalance	AOB*	Circuit Size	Techniques/ Layers*
[16]	2.4/10/2.2	0.7/20/80	1/2	1	$0.32\times0.32\lambda_g^2$	Microstrip/1
[17]	0.47/13/3.38	1.17/25/60	0.2/4.5	1	$0.23\times0.12\lambda_g^2$	Microstrip/1
[19]	1.94/0.5/38	1.2/23/2000	0.3/5	1	$0.29\times0.29\lambda_g^2$	DR/-
[22]	20/2.6/2.2	1.63/28/190	0.3/5	1	$2.51\times2.51\lambda_g^2$	SIW/1
[23]	11/3.6/3.5	1.6/20/170	0.6/8	1	$1.59\times1.26\lambda_g^2$	SIW/1
[24]	7.75/2.7/3.5	1.5/25/200	0.6/5	1	$0.79\times0.45\lambda_g^2$	SIW/2
[25]	11.8/3.5/3.5	1.3/18/210	0.1/3	1	$1.18\times1.18\lambda_g^2$	SIW/1
This work	9.30,9.73/1.6,3.1/3.5	1.92,1.35/30,27/210	0.05/3	2 dual-band	$1.19\times1.19\lambda_g^2$	SIW/2

Where λ_g is the guided wavelength on the substrate at the center frequency f_0, FBW represents the fractional bandwidth. **AOB*** represents the number of available operation bands. Layers* represents the number of substrate layers.

IV. CONCLUSION

In this paper, a compact multilayer dual-band filtering rat-race coupler based on substrate integrated fan-shaped cavities (SIFCs) is proposed for the first time. Simulated and measured results have been presented to verify the proposed method. Magnetic and electric coupling between SIFCs are realized through multiple rectangular slots and circular slots etched on metal layer, respectively. What's unique about the analysis process of dual-band filtering rat-race coupler is that the bandwidth and center frequency of the corresponding broadband coupler can be obtained from the specification of dual-band filtering coupler. The required coupling coefficient and external quality factor can be obtained by analyzing the topology of the single-band filtering coupler. Afterwards, the coupling matrix method is used to evaluate the initial value of design parameters accurately according to the specifications. Generally, the proposed designs have shown excellent performance of dual-band filtering responses, isolation, amplitude balance, 0° and 180° phase differences, as well as the compact structure. The proposed multilayer SIFCs dual-band filtering rat-race coupler could be more suitable for the development of high density and miniaturized RF/microwave system.

ACKNOWLEDGMENT

This work was supported in part by the Ministry of Science and Technology of the People's Republic of China under grant 2013YQ200503 and in part by the National Natural Science Foundation of China (NSFC)

under grant 61001028.

REFERENCES

[1] X.-P. Chen, K. Wu, and Z.-L. Li, "Dual-band and triple-band substrate integrated waveguide filters with Chebyshev and quasi-elliptic responses," *IEEE Trans. Microw. Theory Techn*., vol. 55, no. 12, pp. 2569-2578, Dec. 2007.

[2] Y. Dong and T. Itoh, "Miniaturized dual-band substrate integrated waveguide filters using complementary split-ring resonators," *IEEE MTT-S Int. Microw. Symp. Dig*., pp. 1-4, June 2011.

[3] K. Song and Q. Xue, "Novel ultra-wideband (UWB) multilayer slotline power divider with bandpass response," *IEEE Microw. Wirel. Compon. Lett*., vol. 20, no. 1, pp. 13-15, Jan. 2010.

[4] Y. J. Cheng, W. Hong, and K. Wu, "94 GHz substrate integrated monopulse antenna array," *IEEE Trans. Antennas Propag*., vol. 60, no. 1, pp. 121-128, Jan. 2012.

[5] Y. J. Cheng, W. Hong, K. Wu, and Y. Fan, "A hybrid guided-wave structure of half mode substrate integrated waveguide and conductor-backed slotline and its application in directional couplers," *IEEE Microw Wireless Compon Lett*., vol. 21, no. 2, pp. 65-67, Feb. 2011.

[6] Z.-G. Zhang, Y. Fan, Y. J. Cheng, and Y.-H. Zhang, "A compact multilayer dual-mode substrate integrated circular cavity (SICC) filter for X-band application," *Prog. Electromagn. Res*., vol. 122, no. 1, pp. 453-465, Jan. 2012.

[7] H. Zhang, W. Kang, and W. Wu, "Miniaturized dual-band SIW filters using E-shaped slotlines with controllable center frequencies," *IEEE Microw. Wireless Compon. Lett*., vol. 28, no. 4, pp. 311-313, Apr. 2018.

[8] Z.-G. Zhang, Y. Fan, and Y.-H. Zhang, "Compact 3-D multilayer substrate integrated circular and elliptic cavities (SICCs and SIECs) dual-mode filter with high selectivity," *Appl. Comp. Electro. Society (ACES) Journal*, vol. 28, no. 4, pp. 333-340, Apr. 2013.

[9] Q. Chen and J. Xu, "Out-of-phase power divider based on two-layer SIW," *Electron Lett*., vol. 50, no. 14, pp. 1005-1007, July 2014.

[10] X. Guo, L. Zhu and W. Wu, "Design method for multiband filters with compact configuration in substrate integrated waveguide," *IEEE Trans. Microw. Theory Tech*., vol. 66, no. 6, pp. 3011-3018, June 2018.

[11] P.-L. Chi and T.-Y. Chen, "Dual-band ring coupler based on the composite right/left-handed folded substrate-integrated waveguide," *IEEE Microw. Wireless Compon. Lett*., vol. 24, no. 5, pp. 330-332, May 2014.

[12] Y. J. Wang, C.-X. Zhou, K. Zhou, and W. Wu, "Compact dual-band filtering power divider based on SIW triangular cavities," *Electron Lett*., vol. 54, no.18, pp. 1072-1074, Sep. 2018.

[13] H. Uchida, N. Yoneda, and S. Makino, "Bandpass directional couplers with electromagnetically-coupled resonators," *IEEE MTT-S Int. Microwave Symp. Digest*., pp. 1563-1566, June 2006.

[14] L.-S. Wu, B. Xia, W.-Y. Yin, and J. Mao, "Collaborative design of a new dual-bandpass 180° hybrid coupler," *IEEE Trans. Microw. Theory Tech*., vol. 61, no. 3, pp. 1053-1066, Mar. 2013.

[15] P. Li, H. Chu, and R.S. Chen, "SIW magic-T with bandpass response," *Electron Lett*., vol. 51, no. 14, pp. 1078-1080, July 2015.

[16] C.-K. Lin and S.-J. Chung, "A compact filtering 180° hybrid," *IEEE Trans. Microw. Theory Tech*., vol. 59, no. 12, pp. 3030-3036, Dec. 2011.

[17] K.-X. Wang, X.-Y. Zhang, S.-Y. Zheng, and Q. Xue, "Compact filtering rat-race hybrid with wide stopband," *IEEE Trans. Microw. Theory Tech*., vol. 63, no. 8, pp. 2250-2560, Aug. 2015.

[18] J.-X. Xu, X.-Y. Zhang, and H.-Y. Li, "Compact narrowband filtering rat-race coupler using quad-mode dielectric resonator," *IEEE Trans. Microw. Theory Tech*., vol. 66, no. 9, pp. 4029-4039, Sep. 2018.

[19] L.-X. Jiao, Y.-L. Wu, Y.-N. Liu, W.-M. Wang, and J.-X. Chen, "Concept for narrow-band filtering rat-race coupler using dual-mode cross-shaped dielectric," *Electron Lett*., vol. 52, no. 3, pp. 212-213, Feb. 2016.

[20] K.-X. Wang, X.-F. Liu, Y.-C. Li, L.-Z. Lin, and X.-L. Zhao, "LTCC filtering rat-race coupler based on eight-line spatially-symmetrical coupled structure," *IEEE Access*, vol. 6, no. 6, pp. 262-269, June 2018.

[21] Z.-G. Zhang, Y. Fan, and Y.-H. Zhang, "Multilayer half-Mode substrate integrated waveguide wide-band coupler with high selectivity," *Appl. Comp. Electro. Society (ACES) Journal*, vol. 34, no. 9, pp. 1418-1425, Sep. 2019.

[22] S.-Q. Han, K. Zhou, J.-D. Zhang, C.-X. Zhou, and W. Wu, "Novel substrate integrated waveguide filtering crossover using orthogonal degenerate modes," *IEEE Microw. Wireless Compon. Lett*., vol. 27, no. 9, pp. 803-805, Sep. 2017.

[23] U. Rosenberg, M. Salehi, J. Bornemann, and E. Mehrshahi, "A novel frequency-selective power combiner/divider in single-Layer substrate integrated waveguide technology," *IEEE Microw. Wireless Compon. Lett*., vol. 23, no. 8, pp. 406-408, Aug. 2013.

[24] Y.-J. Cheng and Y. Fan, "Compact substrate-integrated waveguide bandpass rat-race coupler and its microwave applications," *IET Microw., Antennas Propag*., vol. 6, no. 9, pp. 1000-1006, June 2012.

[25] H.-Y. Li, J.-X. Xu, and X.-Y. Zhang, "Substrate

integrated waveguide filtering rat-race Coupler based on orthogonal degenerate modes," *IEEE Trans. Microw. Theory Techn*., vol. 67, no. 1, pp. 140-150, Jan. 2019.

[26] Y. L. Wu, L. X. Jiao, Q. Xue, and Y. A. Liu, "A universal approach for designing an unequal branch-line coupler with arbitrary phase differences and input/output impedances," *IEEE Trans. Compon., Packag., Manuf. Technol*., vol. 7, no. 6, pp. 944-955, June 2017.

[27] J. Muñoz-E., P. Vélez, M. G. Barba, J. Mata-C., and F. Martín, "Differential-mode to common-mode conversion detector based on rat-race hybrid couplers: analysis and application to differential sensors and comparators," *IEEE Trans. Microw. Theory Tech*., vol. 68, no. 6, pp. 1-14, June 2020.

[28] H. N. Chu, G.-Y. Li, and T.-G. Ma, "Dual-mode coupler with branch-line/rat-race responses on integrated passive device process," *IEEE MTT-S Int. Microw. Workshop Series on Advanced Materials and Processes. RF, THz. Appl. (IMWS-AMP)*, Bochum, Germany, pp. 82-84, Oct. 2019.

[29] M.-K. Li, C. Chen, and W. Chen, "Miniaturized dual-band filter using dual-capacitively loaded SIW cavities," *IEEE Microw. Wireless Compon. Lett*., vol. 27, no. 4, pp. 344-346, Apr. 2017.

[30] S. Zhang, J.-Y. Rao, J.-S. Hong, and F.-L. Liu, "A novel dual-band controllable bandpass filter based on fan-shaped substrate integrated waveguide," *IEEE Microw. Wireless Compon. Lett*., vol. 28, no. 4, pp. 308-310, Apr. 2018.

[31] Y.-D. Dong and T. Itoh, "Miniaturized substrate integrated waveguide slot antennas based on negative order resonance," *IEEE Trans. Antennas Propag*., vol. 58, no. 12, pp. 3856-3864, Dec. 2010.

[32] J.-S. Hong and M.-J. Lancaster, *Microstrip Filter for RF/Microwave Applications*. New York, NY, USA: Wiley, 2001.

[33] R.-J. Cameron, "Advanced coupling matrix synthesis techniques for microwave filters," *IEEE Trans. Microw. Theory Tech*., vol. 51, no. 1, pp. 1-10, Jan. 2003.

[34] D.-M. Pozar, *Microwave Engineering*, second edition, New York: Wiley, 1998.

Zhigang Zhang was born in Shanxi Province, China. He received the B.S. degree in Electronic Information Engineering and M.S. degree in Wireless Physics from Sichuan University and is currently working toward the Ph.D. degree in Electromagnetic Field and Microwave Technology from The University of Electronic Science and Technology of China (UESTC), Chengdu, Sichuan, China. His current research interests include SIW technology and its application, microwave and millimeter-wave filters and couplers, electromagnetic theory.

Yong Fan received the B.E. degree from the Nanjing University of Science and Technology, Nanjing, Jiangsu, China, in 1985, and the M.S. degree from the University of Electronic Science and Technology of China (UESTC), Chengdu, Sichuan, China, in 1992.

He is currently with the School of Electronic Engineering, UESTC. He has authored or coauthored over 60 papers. From 1985 to 1989, he was interested in microwave integrated circuits. Since 1989, his research interests include millimeter-wave communication, electromagnetic theory, millimeter-wave technology, and millimeter-wave systems. Mr. Fan is a Senior Member of the Chinese Institute of Electronics (CIE).

Yujian Cheng was born in Sichuan, China, in 1983. He received the B.S. degree from University of Electronic Science and Technology of China, in 2005 and the Ph.D. degree from Southeast University, Nanjing, China, in 2010. Since 2010, he has been with University of Electronic Science and Technology of China, and is currently a Professor. His current research interests include microwave and millimeter-wave antennas, arrays and circuits. He has authored or coauthored more than 100 articles in journals and conferences, as well as a book—Substrate Integrated Antennas and Arrays, (CRC Press, 2015). Cheng was the recipient of the National Science Fund for Excellent Young Scholars in 2016, Chang Jiang Scholars Program (Young Scholars) in 2016, and National Excellent Doctorate Dissertation of China in 2012. Now, Cheng serves as an Associate Editor for IEEE Antennas and Propagation Letters

Yonghong Zhang received the B.S., M.S., and Ph.D. degrees from the University of Electronic Science and Technology of China (UESTC), Chengdu, China, in 1992, 1995, and 2001, respectively. From 1995 to 2002, he was a Teacher with the UESTC. In 2002, he joined the Electronic Engineering Department, Tsinghua University, Beijing, China, as a Doctoral Fellow. In 2004, he rejoined the UESTC. His research interests are in the area of microwave and millimeter-wave technology and applications.

Research on Rotor Position Detection Method of Printed PMSM Based on Leakage Magnetic Field of Rotor

Xianming Deng [1], Junhong Zhou [1], Lei Hao [1], Zhihua Fan [1], and Na Liu [2]

[1] Jiangsu Province Laboratory of Mining Electric and Automation, China University of Mining and Technology
Xuzhou, 221116, China

[2] Aerospace Information Research Institute, Chinese Academy of Sciences
Suzhou, 215000, China
xmdengcumt@126.com, Junhongzhou@cumt.edu.cn

Abstract ─ With the merits of simple structure, strong stability and high power factor, the application of Permanent Magnet Synchronous Motor (PMSM) have become more and more widespread. Meanwhile, rotor position information of PMSM is of vital importance to motor driving. This paper is mainly to research the rotor position detection of Printed PMSM, and, by applying fluxgate technology into the detection process, the rotor position is determined based on the leakage magnetic field of the rotor. The simulation of the rotor leakage magnetic field is made using Finite Element Analysis (FEA), which verifies the feasibility of rotor position detection methods based on the Leakage Magnetic Field of Rotor. Finally, through the experimental prototype of Printed PMSM and fluxgate sensor, Printed PMSM can be driven using a rotor position detected by fluxgate sensors. Fluxgate sensors have advantages of high resolution, strong anti-interference ability, good stability, wide measurement range and ability of miniaturization design, making it suitable to detect weak leakage magnetic field at the end of the rotor so that Printed PMSM has advantages of integration and easy maintenance. Meanwhile, methods mentioned in this paper/article are also applicable to other kinds of PMSM and have certain guiding significance for the integration design of PMSM.

Index Terms ─ Finite Element Analysis (FEA), leakage magnetic field of rotor, printed PMSM, rotor position information.

I. INTRODUCTION

In recent years PMSM has received a lot of researches and is widely used in various fields, which has become mainstream of AC speed regulation and servo field [1]. In the closed-loop control system of PMSM, motor rotor position is an indispensable physical quantity for PMSM control. A lot of researches on sensor-less detection technology have been done, but due to its high requirements to motor, it is difficult to accurately control motor under low speed and zero speed. In addition, the control algorithm is complex, which cannot guarantee the accuracy of rotor position estimation [2-3], so position sensors are still irreplaceable in high performance PMSM control systems. Furthermore, PMSM has the advantage of high power-density and its volume is gradually becoming smaller, so additional position sensors are becoming design burdens, resulting in new design that is more likely to integrate position sensor built-in.

Printed PMSM belongs to disk type motor and has merits of short axial distance, simple structure, mature production process, convenient, low cost, small mechanical tolerance. It has great advantage in large-scale applications, and is mainly applied to aerospace, computer peripherals, power tools, electric vehicles, etc. where the requirements for wheelbase are high. For Printed PMSM, this paper proposes a rotor position detection method based on leakage magnetic field, which has better linearity and precision than traditional Hall method.

II. ANALYSIS OF STRUCTURE AND CONTROL TECHNOLOGY

A. Structure of Printed motor

Figure 1 (a) shows the Printed PMSM structure, including rotor, magnetic conductive plate and Printed armature winding [4]. Rotor is composed of a permanent magnet and a stator core. Magnetic steel is magnetized axially and is laid on rotor core. The adjacent magnetic steels are opposite in magnetic polarity, and N poles and S poles are arranged alternately. There are many choices for the shape of magnetic steel: cylindrical, fan-shaped and trapezoidal. Printed windings are applied to stator, and stator windings are fixed on magnetic conductive plate which only functions to constitute a good magnetic loop. The ideal structure of rotor permanent magnet is fan-shaped, but this kind of structure has high cost.

Submitted On: October 27, 2019
Accepted On: January 20, 2020

Therefore, the laboratory designed rotor permanent magnet of the motor adopts a cylindrical structure, as shown in Fig. 1 (b). The prototype of motor designed in laboratory is shown in Fig. 1 (c).

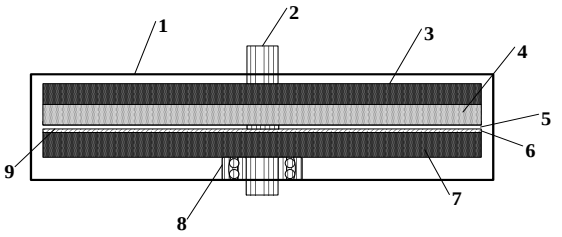

(a)

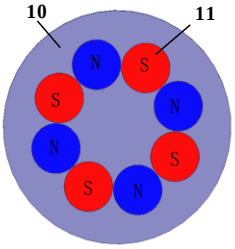

(b)

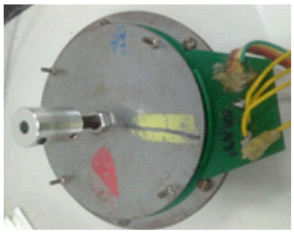

(c)

1-Casing, 2-Shaft, 3-Rotor core, 4-Permanent magnet, 5-Air gap, 6-PCB winding, 7-Stator core, 8-Bearing, 9-Insulating paper, 10-rotor core, 11- Permanent magnet

Fig. 1. (a) Structure of Printed PMSM, (b) rotor structure, and (c) prototype of Printed PMSM.

The conventional Printed PMSM stator adopts a spiral winding structure, as shown in Fig. 2 (a). The winding conducting bar of this structure are compact and three-phase windings are distributed in each layer, so the utilization rate of Printed board is relatively high. The endline is long, and copper loss is high. Stator of Printed PMSM designed by laboratory adopts wave windings structure, as shown in Fig. 2 (b). Compared with spiral winding, Printed circuit board with wave winding structure has a very high utilization rate, and the number of via holes per phase winding is small. Besides, the structure of wave winding is simpler than that of spiral winding. Moreover, at the same speed, the induced electromotive force of wave winding is larger. The parameters of Printed PMSM designed by laboratory are shown in Table 1.

(a)

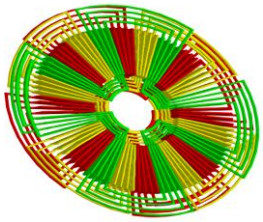

(b)

Fig. 2. (a) Spiral winding and (b) wave winding.

Table 1: Main parameters of Printed PMSM

Parameters	**Value**
Rated power/W	48
Rated voltage/V	5
Rated current/A	4
Rated Torque/ Nm	0.5
Phase number	3
PCB layer number	6
Number of turns per phase	4
Number of poles	4
Rated speed/rpm	750
Diameter of permanent magnet/mm	25
Thickness of permanent magnet/mm	4
Flux linkage/Wb	0.023
Stator diameter/mm	120
Stator resistance/Ω	0.5
Air gap/mm	4
Conducting bar thickness/mm	0.2
Conducting bar width/mm	0.8
Maximum current/A	6
Maximum voltage/V	12

B. Mathematical model of Printed PMSM

The mathematical model of Printed PMSM is the same as that of conventional PMSM. In order to simplify the mathematical model of a Printed PMSM, changing the reference coordinate system is often required. For control system, although the actual parameter is a sinusoid, we still want the system variable to be simple. Therefore, it is possible to convert the sinusoidal quantity to DC quantity by establishing a reference coordinate system whose rotation speed is consistent with the angular velocity of sinusoidal variable, which is called Park transformation in mathematics. The system can be decoupled with Clark and Park transformation performed on motor mathematical equation in ABC stationary coordinate system. The specific equations are as follows.

Clark transformation and its inverse transformation:

$$C_{3s/2s}=\frac{2}{3}\begin{bmatrix}1 & -\frac{1}{2} & -\frac{1}{2}\\ 0 & \frac{\sqrt{3}}{2} & -\frac{\sqrt{3}}{2}\end{bmatrix}, \tag{1}$$

$$C_{2s/3s}=\frac{2}{3}\begin{bmatrix}1 & 0\\ -\frac{1}{2} & \frac{\sqrt{3}}{2}\\ -\frac{1}{2} & -\frac{\sqrt{3}}{2}\end{bmatrix}. \tag{2}$$

Park transformation and its inverse transformation:

$$C_{2s/2r}=\begin{bmatrix}\cos\theta & \sin\theta\\ -\sin\theta & \cos\theta\end{bmatrix}, \tag{3}$$

$$C_{2r/2s}=\begin{bmatrix}\cos\theta & -\sin\theta\\ \sin\theta & \cos\theta\end{bmatrix}. \tag{4}$$

The mathematical model of transformed PMSM in d-q rotating coordinate system is:

$$\begin{cases} u_{\mathrm{d}} = \mathrm{R}_{\mathrm{s}} i_{\mathrm{d}} + p\psi_{\mathrm{d}} - \omega\psi_{\mathrm{q}} \\ u_{\mathrm{q}} = \mathrm{R}_{\mathrm{s}} i_{\mathrm{q}} + p\psi_{\mathrm{q}} + \omega\psi_{\mathrm{d}} \end{cases}, \tag{5}$$

$$\begin{cases} \psi_{\mathrm{d}} = L_{\mathrm{d}} i_{\mathrm{d}} + \psi_{\mathrm{f}} \\ \psi_{\mathrm{q}} = L_{\mathrm{q}} i_{\mathrm{q}} \end{cases}. \tag{6}$$

where u_{d} and u_{q} are respectively the stator voltage component of d and q axis, id and i_{q} are respectively the stator current component of d and q axis, ψ_{d} and ψ_{q} are respectively the main flux component of d and q axis, L_{d} and L_{q} are respectively the inductance of d and q axis, ψ_{f} is flux produced by permanent magnet.

The torque expression of motor is:

$$T_{\mathrm{e}} = 1.5 n_{\mathrm{p}} [\psi_{\mathrm{f}} i_{\mathrm{q}} + (L_{\mathrm{d}} - L_{\mathrm{q}}) i_{\mathrm{d}} i_{\mathrm{q}}]. \tag{7}$$

Since L_{d} and L_{q} are equal in Printed PMSM, equation (7) can be simplified as:

$$T_{\mathrm{e}} = 1.5 n_{\mathrm{p}} \psi_{\mathrm{f}} i_{\mathrm{q}}. \tag{8}$$

C. Control technology of Printed PMSM

Printed PMSM can be controlled by vector control technology. Vector control is also called field oriented control or decoupling control. The principle of rotor-oriented vector control is to transform the motor model from a stationary coordinate system into a rotating coordinate system, and a model similar to a DC machine can be obtained. By controlling stator excitation input, the torque and flux can be separately controlled to achieve torque control.

According to the torque equation (7), the output torque of motor can be controlled by controlling stator current i_{q}. Since the L_{d} and L_{q} are equal in Printed PMSM, i_{d}=0 control is the maximum torque/current ratio control, that is to say, maximum torque output can be obtained with same bus current. Figure 3 shows the i_{d}=0 control vector diagram.

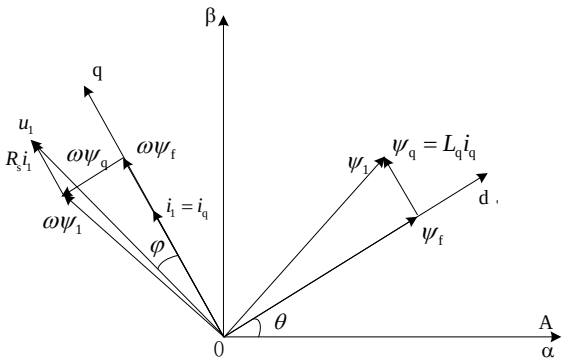

Fig. 3. i_{d}=0 control vector diagram.

Figure 4 shows a control block diagram of id=0 vector control of Printed PMSM. In the figure, θ and n are respectively the rotor position angle and motor speed; i_{a}, i_{b} , i_{c} are three-phase instantaneous currents; id and i_{q} are respectively d and q axis stator current components. The inner loop of system is current loop, and current regulator outputs the reference value of space voltage vector. The outer loop of system is speed loop, and speed regulator outputs the given current. The difference between set value of current and actual value is input to current regulator. The output reference vector of current regulator is sent to the inverter to generate a PWM signal to control inverter power tube, thereby realizing the control of stator current of Printed PMSM. Therefore, rotor position is still important for driving Printed PMSM.

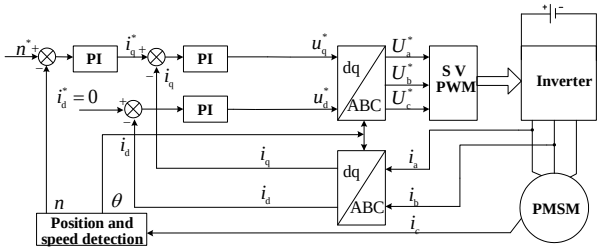

Fig. 4. i_{d}=0 control system block diagram.

III. FEA OF PRINTED PMSM LEAKAGE MAGNETIC FIELD

The direction of the air gap magnetic flux density of Printed PMSM designed by laboratory is axial, so the magnetization direction of permanent magnet is axial, and the main simulation parameters of Printed PMSM are shown in Table 2. The magnetic field generated by permanent magnet passes axially through the air gap, and back to the air gap to the opposite polarity permanent magnet through the stator magnetic plate. However, due to the scattering of magnetic field of permanent magnet, there is leakage magnetic flux directly closed in the air gap at the radial edge of permanent magnet. The simulation model of motor established in the finite element software Ansoft Maxwell is shown in Fig. 5 (a), and for better observation, the rotor core is hidden [5]. When motor is under no-load condition, the magnetic flux density distribution at the radial edge of rotor permanent magnet in which the radius r = 47mm is shown in Fig. 5 (b), and the magnetic flux density distribution and magnetic flux density harmonic histogram in radial direction of this radius are shown in Fig. 5 (c) and Fig. 5 (d), respectively. It can be seen from Fig. 5 (b) that the magnetic field is diverging around the circumference of rotor permanent magnet edge, and the magnetic field of the opposite polarity is reversed. According to the Fig. 5 (c), the radial magnetic field distribution at this circumference is approximately sinusoidal. Since there are 4 pairs of poles in this motor, the number of magnetic field cycles is 4 in one mechanical cycle. By performing harmonic analysis on the magnetic flux density of Fig. 5 (c), result is obtained

which is shown in Fig. 5 (d). It can be seen that except for the fundamental wave, the third harmonic is the highest, and the other harmonic content is very small. Therefore, the third harmonic is the main factor causing distortion of the magnetic field distribution.

Table 2: Main simulation parameters of Printed PMSM

Parameters	**Value**
Rated power/W	36
Phase number	3
PCB layer number	6
Number of turns per phase	4
Number of poles	4
Maximum speed/rpm	2000
Thickness of permanent magnet/mm	4
Outer diameter of PM/mm	92
Inner diameter of PM/mm	40
Air gap/mm	4
Conducting bar thickness/mm	0.2
Conducting bar width/mm	0.8

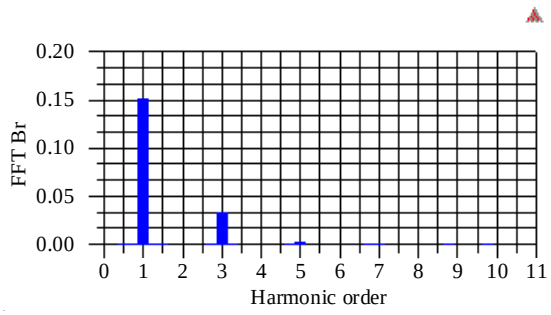

(d)

Fig. 5. (a) Motor simulation model with hidden rotor core, (b) magnetic flux density distribution (r=47mm), (c) magnetic flux density distribution (r=47mm), and (d) magnetic flux density harmonic histogram (r=47mm).

The magnetic field distribution vector at the circumference of radius r = 60mm (the circumference of motor stator edge) is shown in Fig. 6 (a). The magnetic flux density distribution and magnetic flux density harmonic histogram at the radial direction of this circumferential are shown in Fig. 6 (b) and Fig. 6 (c). It can be concluded that the magnetic field at this circumference is substantially sinusoidal in space, and magnetic field starts from the N pole of permanent magnet and returns to the S pole along the air gap in radial direction. In this case, the third harmonic content of radial magnetic field is also higher than other harmonic content, but significantly less than the third harmonic content in the simulation of Fig. 5.

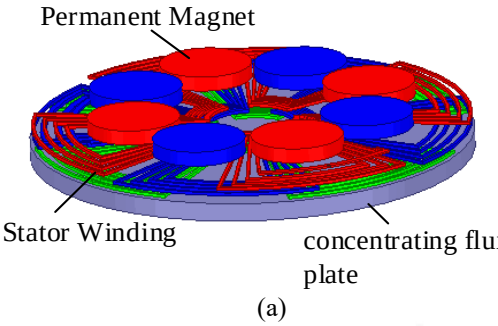

(a)

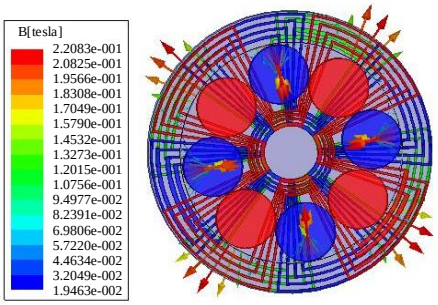

(b)

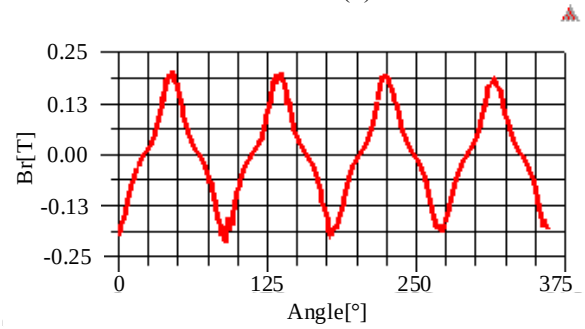

(c)

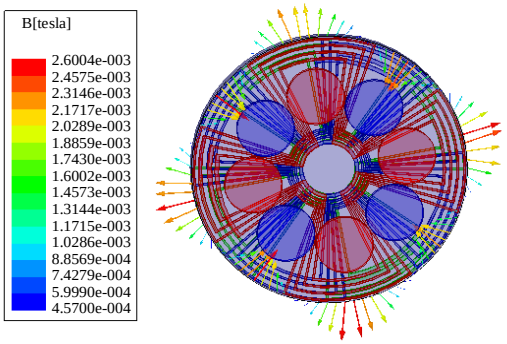

(a)

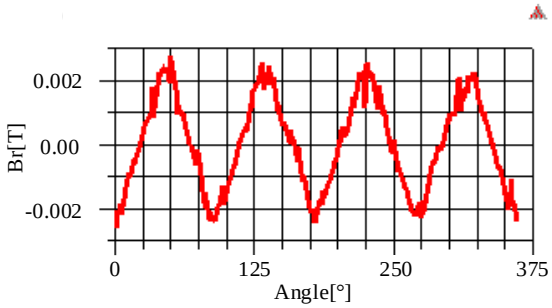

(b)

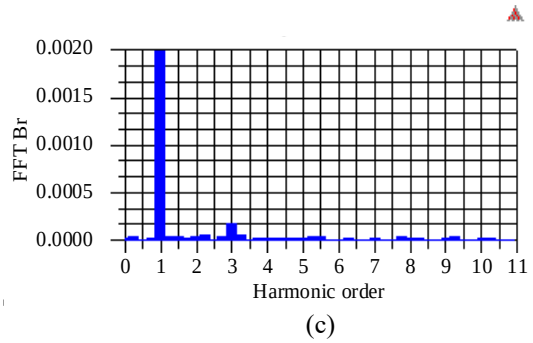

(c)

Fig. 6. (a) Magnetic flux density distribution (r=60mm), (b) magnetic flux density distribution (r=60mm), and (c) magnetic flux density harmonic histogram (r=60mm).

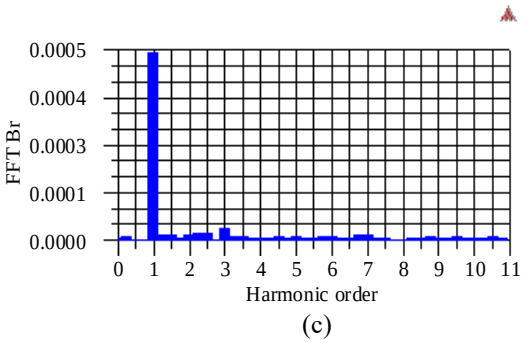

(c)

Fig. 7. (a) Magnetic flux density distribution (r=65mm), (b) magnetic flux density distribution (r=65mm), and (c) magnetic flux density harmonic histogram (r=65mm).

At the circumference of r = 60mm, the vector diagram of magnetic field distribution is shown in Fig. 7 (a), the magnetic flux density distribution and magnetic flux density harmonic histogram in the radial direction of this circumference are shown in Figs. 7 (b) and (c), respectively.

From the simulation, it can be seen that the magnetic field harmonic in this case is slightly more than that in the simulation of Fig. 6, and the magnetic flux density is about 500μT. Therefore, two fluxgate detectors can be mounted on the circumference of the air gap between the stator and rotor of motor with a radius r = 65 mm, that is, a circumference of 5 mm from the edge of stator.

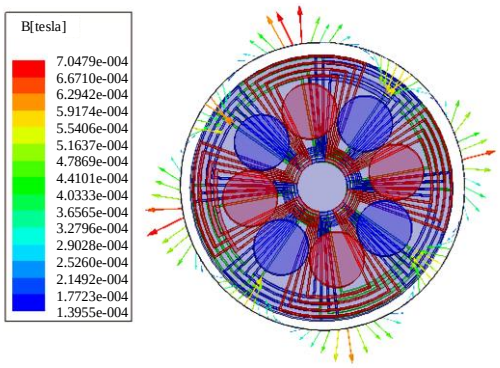

(a)

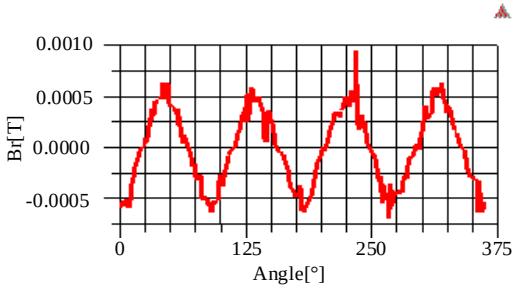

(b)

The above simulations are all carried out under no-load condition of the motor. When motor is running under rated state, stator current will generate stator magnetic field. In this case, the magnetic flux density distribution and the harmonic histogram in the radial direction at the circumference of radius r = 65 mm are as shown in Figs. 8 (a) and 8 (b), respectively. It can be seen that, compared with the magnetic leakage distribution of no-load motor, the symmetry of leakage magnetic flux distribution of each pair of poles is deteriorated because the motor running in rated state is affected by stator magnetic field, and not only leakage magnetic flux amplitudes are different, but also the harmonics are different, which increase the difficulty of leakage magnetic flux detection.o

According to the above simulation analysis, the leakage magnetic flux intensity of permanent magnets is different at different positions, and so is the magnetic field distribution under no-load and rated operating conditions. In no-load mode, on the circumference of the air gap of radius r = 47mm, sinusoidal distribution of magnetic flux density is better, the harmonic law is obvious, and the signal intensity is large. While in rated mode, on the air gap circumference with radius r = 60mm and r = 65mm, the magnetic flux density distribution still has a good sinusoidally degree, but harmonics become more complicated and signal intensity get smaller with the increase of radius. In Printed disc type motor, the radial outer end of permanent magnet is relatively wide, and in general motor, motor end space is also relatively rich, which is a preferred position for installing magnetic sensor.

However, at the end of motor, leakage magnetic flux density of permanent magnet is weak. A generally magnetic sensor cannot detect the magnetic field at this position, so magnetic sensor needs to be installed at a suitable position inside the motor. For example, Hall

sensor has a generally detectable magnetic field intensity range of ± (0.1~0.15) T. According to the above simulation, this leakage flux intensity is inside the motor of this simulation, so installing Hall sensor can be very troublesome and difficult to repair and replace. The fluxgate sensor can detect weak magnetic fields, and its magnetic field detection has a wide range of intensity and high resolution. According to the range of leakage magnetic flux intensity at the end of motor, the requirement of leakage magnetic field intensity detection at this position can be satisfied by rationally designing structure of fluxgate sensor. Therefore, compared with other magnetic sensors, the fluxgate sensor is more suitable for determining the rotor position of motor due to its special performance. Therefore, compared with other magnetic sensors, fluxgate sensor is more suitable for determining the rotor position of motor due to its special performance.

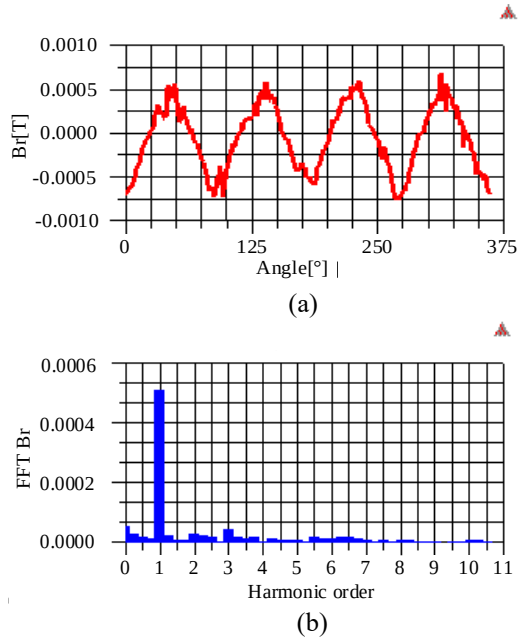

Fig. 8. (a) Magnetic flux density distribution under rated condition (r=65mm), (b) and magnetic flux density harmonic histogram under rated condition (r=65mm).

IV. ROTOR POSITION DETECTION METHOD BASED ON LEAKAGE MAGNETIC FIELD

A. Working principle of fluxgate sensor

The fluxgate sensor is a device sensitive to external magnetic field, which made by utilizing the property that magnetic core material has a nonlinear change in periodic supersaturation state, and is mainly composed of an iron core, an excitation coil and an induction coil. The working principle can be described by Fig. 9.

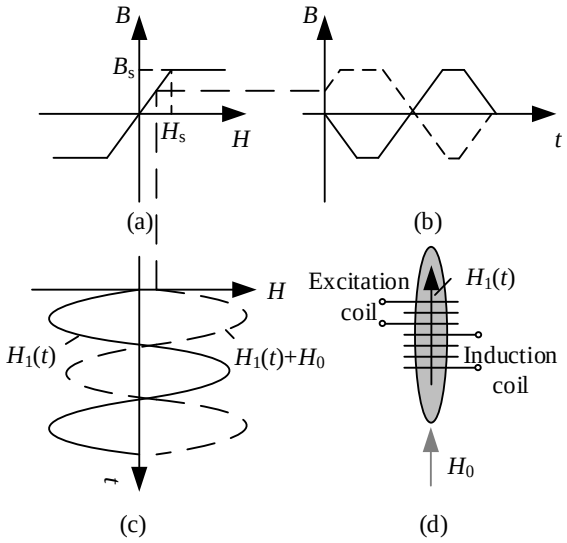

Fig. 9. (a) Magnetization curve of ferromagnetic material, (b) magnetic flux density curve, (c) magnetic field strength curve, and (d) coil structure diagram.

Figure 9 (a) shows the magnetization curve of ferromagnetic material. When the magnetic field intensity $H_1(t)$ generated by excitation coil periodically changes and its amplitude is greater than the saturation magnetic field intensity H_s of core material, core material is in periodic supersaturation state, when the magnetic flux density changes as shown by solid line in Fig. 9 (b). Since the magnetization curve of core material is symmetrical, the magnetic induction signal shown by solid line in Fig. 9 (b) contains only the odd harmonics of magnetic field intensity $H_1(t)$, and the induced voltage of induction coil contains only odd harmonics. When there is an external magnetic field intensity H_0, magnetic field strength changes as shown by dashed line in Fig. 9 (c). The magnetic flux density curve at this time is as shown by broken line in Fig. 9 (b), and the upper half is wider than the lower half, which will cause even harmonics of induced voltage signal of induction coil in Fig. 9 (d). In even harmonic of the signal, because the second harmonic content is proportional to the magnitude of external magnetic field within a certain range of external magnetic field intensity, second harmonic signal is often used to detect the magnitude of external magnetic field intensity H_0 [6].

Second harmonic signal that the single-core flux sensor of single-core core outputs is small, and there are a large number of useless odd harmonic signals, resulting in difficult useful signal extraction. Therefore, a double-core sensor is generally selected. The excitation coil of double-core sensor is wound on two cores in the same polarity and the number of turns of two coils is equal, and induction coil wraps two core windings. When excitation coil applies AC excitation and the core of

sensor reaches a periodic supersaturation state, the odd harmonics in voltage signal induced by induction coil cancel each other, and the even harmonics overlap each other.

B. Mathematical model of fluxgate detection

The fluxgate of double iron core structure can effectively suppress useless signal and increase useful signal. The structure diagram is shown in Fig. 10.

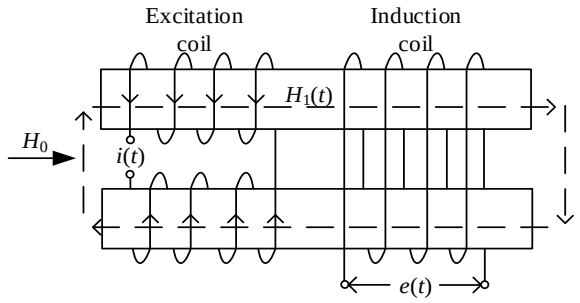

Fig. 10. Structural sketch of dual-core fluxgate.

In Fig. 10, N_1 is the number of excitation coils of two cores, N_2 is the number of turns of induction coil, S is the cross-sectional area of core, and μ is magnetic permeability. The excitation coil is supplied with an alternating current of which the frequency is f_{ex}, which produces the internal magnetic field intensity $H_1(t)$ having equal magnitude and opposite direction on two cores, while iron core is in a periodic supersaturation state. The internal magnetic field intensity $H_1(t)$ can be described by:

$$H_1(t) = H_m \sin(2\pi f_{ex} t), \tag{9}$$

where H_m is the amplitude of internal magnetic field intensity $H_1(t)$.

If there is no external magnetic field, it can be known from Faraday law of electromagnetic induction that the alternating magnetic field in two cores changes the magnitude of the induced voltage generated on induction coil, and the direction is opposite, so the fluxgate sensor has no voltage signal output.

If there is an external magnetic field intensity H_0, the magnetic fields inside two cores are:

$$\begin{cases} H'(t) = H_1(t) + H_0 \\ H''(t) = H_1(t) - H_0 \end{cases}, \tag{10}$$

where $H'(t)$ is the internal magnetic field of one core, and $H''(t)$ is the internal magnetic field of the other core.

The induced voltage on fluxgate sensor induction coil is:

$$e(t) = -N_2 S \frac{d[\mu'(t)H'(t)]}{dt} + N_2 S \frac{d[\mu''(t)H''(t)]}{dt}, \tag{11}$$

where $\mu'(t)$ and $\mu''(t)$ are the magnetic permeability functions of two cores, respectively. The direction of magnetic field generated by excitation signal is periodically changed, but magnetic permeability has no polarity, that is, the excitation of magnetic field in both directions produces two changes in magnetic permeability. Therefore, the frequency of magnetic permeability change is twice that of the magnetic field, which is an even function in time. Equation (12) shows the magnetic permeability expanded according to the Fourier series:

$$\begin{aligned} \mu(t) &= \mu_{0m} + \mu_{2m} \cos 4\pi f_{ex} t + \mu_{4m} \cos 8\pi f_{ex} t + \ldots \\ &= \sum_{n=0}^{\infty} \mu_{2n\times m} \cos 4n\pi f_{ex} t. \end{aligned} \tag{12}$$

Because of the existence of external magnetic field, the saturation and magnetic permeability of two cores are different. By substituting equations (9), (10), (12) into equation (11), it can be concluded that:

$$\begin{aligned} e(t) = -N_2 S H_m [& 2\pi f_{ex} \Big(\sum_{n=0}^{\infty} \mu'_{2n\times m} \cos 4n\pi f_{ex} t \cdot \sin 2\pi f_{ex} t \\ & - \sum_{n=0}^{\infty} \mu''_{2n\times m} \cos 4n\pi f_{ex} t \cdot \sin 2\pi f_{ex} t\Big) \\ & - \cos 2\pi f_{ex} t \cdot \Big(\sum_{n=0}^{\infty} 4n\pi f_{ex} \mu'_{2n\times m} \sin 4n\pi f_{ex} \\ & - \sum_{n=0}^{\infty} 4n\pi f_{ex} \mu''_{2n\times m} \sin 4n\pi f_{ex}\Big)] \\ & + N_2 S H_0 f_{ex} \sum_{n=0}^{\infty} 4n\pi \mu'_{2n\times m} \sin 4n\pi f_{ex} \\ & + N_2 S H_0 f_{ex} \sum_{n=0}^{\infty} 4n\pi \mu''_{2n\times m} \sin 4n\pi f_{ex}, \end{aligned} \tag{13}$$

where $\mu'_{2n\times m}$ and $\mu''_{2n\times m}$ are the Fourier decomposition coefficients of magnetic permeability of two cores. Generally, the strength of external magnetic field detected by fluxgate sensor is much smaller than the saturation magnetic field of iron core, so the difference of the total magnetic field after superimposing external magnetic field in two cores is small, that is, the difference in magnetic permeability between two cores is small. In order to simplify the analysis, assuming that changes in the magnetic permeability of two cores are both $\mu(t)$, then equation (13) can be simplified as:

$$e(t) = 2N_2 S H_0 f_{ex} \sum_{n=0}^{\infty} 4n\pi \mu_{2n\times m} \sin 4n\pi f_{ex}. \tag{14}$$

Comparing equation (14) with equation (13), it can be seen that in double core structure, voltage signals independent of the external magnetic field are mutually suppressed, and the related voltage signals are superimposed on each other, thereby effectively reducing the difficulty of extracting useful signals.

C. Advantages of fluxgate sensor

A comparison of three common commercial position sensors is shown in Table 3.

Table 3: Comparison of three position sensors

	Photoelectric Encoder	Resolver	Hall Sensor
Volume	Little small	Large	Small
Structure	Simple	Complicate	Simple
Resolution	High	Little high	Low
Precision	High	Little high	Low
Range of operation	Small	Large	Small
Temperature	High	Low	High
Speed range	High	Low	High
Request to working environment	High	Low	Low
Cost	High	Little high	low

The fluxgate sensor is a magnetic sensor capable of detecting a weak magnetic field, of which the basic structure is composed of an iron core, an induction coil and excitation coil wound around iron core, and belongs to an induction transformer structure. When fluxgate sensor is working, it is necessary to apply an alternating current power to its excitation coil to make the core of fluxgate in a state of periodic supersaturation. When there exist an external magnetic field, the induction coil of fluxgate will induce an electromotive force related to the strength of external magnetic field. Fluxgate sensor has the advantages of high resolution, strong anti-interference ability, good stability, wide measurement range, and ability of miniaturized design [7-11], making it can be designed as a sensor to detect the position of PMSM rotor.

D. Analysis of detection method based on leakage magnetic field of rotor

The detection method based on leakage magnetic field of rotor is simple in structure and can be integrated with motor. However, this method has high requirements on design, manufacture and control of motor, and its accuracy is also affected by motor operating conditions. In the case where the position of motor space is strictly required, the volume and mounting position of fluxgate sensor must also be considered [12]. This section will analyze the effects of motor system on rotor position detection.

a) Leakage flux distribution under the influence of working conditions

According to the analysis of Printed permanent magnet synchronous motor, the magnetic field distribution on the circumference of the radius r = 65 mm at the air gap between stator and motor rotor is approximately sinusoidal under no-load conditions, and leakage flux distribution of each pair is similar. However, when motor is running under rated conditions, it can be seen from Fig. 8 (a) that the leakage magnetic flux distribution of each pair of poles changes and is no longer the same. However, when motor is running under rated conditions, it can be seen from Fig. 8 (a) that the leakage magnetic flux distribution of each pair of poles changes and is no longer the same. Influenced by stator magnetic field, compared with Fig. 7 (b), the leakage flux distribution of four pairs of poles in Fig. 8 (a) is different, and the amplitude of magnetic field intensity is obviously asymmetrical. It can be seen that the leakage flux distribution of motor is affected by operating conditions of the motor, which affects the accuracy of rotor position detection of motor.

b) Leakage flux distribution under the influence of rotor permanent magnet migration

The motor model designed by laboratory is little rough. During the manufacturing process, the installation of permanent magnet will be inevitably deviated, that is, center positions of permanent magnets are not on one circumference. Taking no-load operation of motor as an example, the simulation analyzes distribution of leakage magnetic flux when permanent magnet is deviated. Taking two permanent magnets on the same diameter as an example, the permanent magnets of motor simulation model are offset, that is, one permanent magnet is shifted inward by 1 mm, and one permanent magnet is shifted outward by 1 mm, as shown in Fig. 11(a). The magnetic flux density distribution in radial direction on the circumference of radius r = 65 mm at the air gap between stator and rotor of motor is as shown in Fig. 11 (b). It can be seen that the leakage magnetic flux distribution of four pairs of poles is significantly different, and the amplitude is no longer symmetrical. By analyzing harmonic of leakage magnetic flux, the magnetic flux density harmonic histogram is obtained in Fig. 11 (c), and harmonic content is significantly increased. This is the result of the migration of two permanent magnets. During the motor manufacturing process, there may be cases where centers of eight permanent magnets are all offset. The distortion of leakage magnetic flux caused by permanent magnet migration significantly increases the error of motor rotor position detection.

According to the above analysis, the magnetic flux detection method includes the detection error of fluxgate sensor itself, and also has additional detection error caused by motor system. Since the motor is a four-pole structure, the leakage magnetic flux distribution of each pair is easily affected by motor manufacturing and operation conditions, so that the leakage magnetic flux distribution of four pairs of poles is different, which increases the difficulty of detecting rotor position of motor.

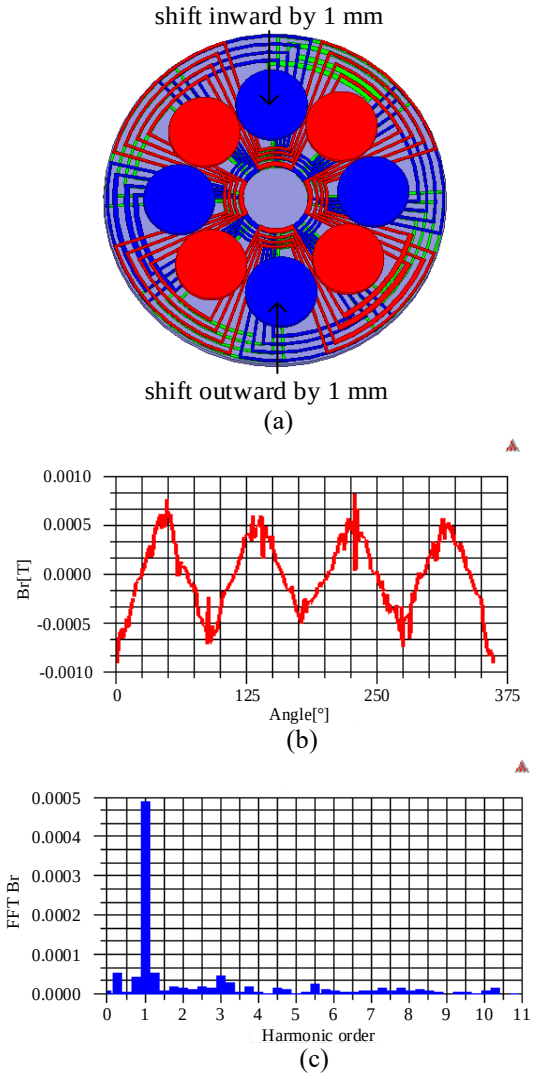

Fig. 11. (a) Permanent magnet shift diagram (r=65mm), (b) magnetic flux density distribution with shifted permanent magnet (r=65mm), and (c) magnetic flux density harmonic histogram with shifted permanent magnet (r=65mm).

V. PROTOTYPE EXPERIMENT ANALYSIS

A. Production and testing of fluxgate sensors

According to the principle of fluxgate, fluxgate sensor core needs to use a soft magnetic material with a small coercive force. However, in the sensor structure designed herein, the strip 1J85 does not have sufficient physical support capability, so it is necessary to design a skeleton support material. The core skeleton model designed by Soildworks software is shown in Fig. 12 (a).The core material 1J85 is cut and then attached to the groove of core frame and fixed with glue. Its physical picture is shown in Fig. 12 (b). The excitation coil is wound directly on both sides of core frame. In order to facilitate the winding of induction coil, induction coil winding skeleton is designed, and model and physical map are respectively shown in Figs. 12 (c) and (d).

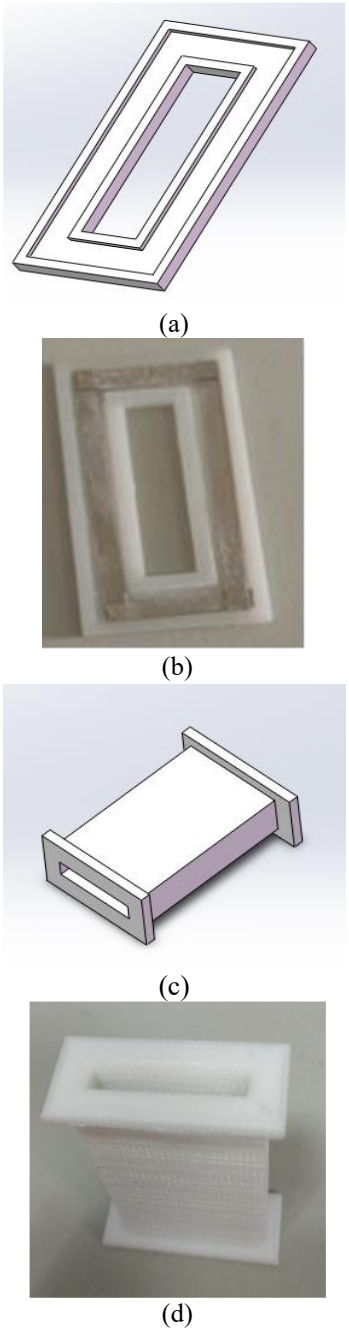

Fig. 12. (a) Core skeleton model, (b) core skeleton actual picture, (c) induction coil winding skeleton model, and (d) induction coil winding skeleton actual picture.

Induction coil winding skeleton and iron core skeleton are matched structures, and iron core skeleton can be inserted into the groove of induction coil winding skeleton. Induction coil winding skeleton total length is 35mm, width is 25mm, and wall thickness is 2mm. In

order to enable core skeleton after winding excitation coil to be inserted into the rectangular groove of induction coil winding skeleton, the designed rectangular groove has a certain margin, of which the length is 17.5 mm and width is 3 mm. Both the core skeleton and induction coil winding skeleton are Printed by a 3D printer, and printing consuming materials are made of PLA (polylactic acid) material having good mechanical and physical properties.

After skeleton model is designed, the excitation coil and induction coil need to be wound on skeleton. The total turns of excitation coil is 110, and copper enameled wire with a diameter of 0.29mm is selected. The total turns of induction coil is 400. For easy winding, a copper enameled wire with a diameter of 0.2 mm is selected. The number of turns of excitation coil and induction coil can be adjusted according to the actual situation, and the physical diagram of fluxgate detector is shown in Fig. 13.

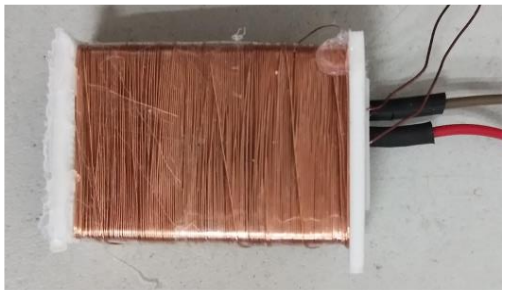

Fig. 13. Fluxgatae detector actual picture.

B. Rotor position detection of Printed PMSM

Position detection method based on rotor leakage flux is based on a laboratory-designed Printed PMSM. The main magnetic flux direction of motor is axial, and leakage magnetic flux direction of rotor permanent magnet is almost radial. It can be seen from Fig. 6 that the radial magnetic field strength at the circumference of motor stator is about 0.002T, and the magnetic field intensity exceeds designed detection range of fluxgate detector. Therefore, fluxgate detector needs to be installed at a circumference larger than stator radius. Two fluxgate detectors are tangentially placed on the stator of Printed PMSM, as shown in Fig. 14. The motor is a four-pole motor, so two fluxgate detectors are placed with an angular difference of 22.5°. It can be seen that two fluxgate detectors are placed at the end of motor, which is convenient for installation and maintenance, and does not affect the internal structure of motor.

The Printed PMSM designed by laboratory is rough, the air gap length is about 1cm, and this is too large, resulting in uneven air gap. There are only 4 turns per phase winding in motor stator and no stator core. So, the inductance is very small, about 7.8μH, which is difficult to control. In order to facilitate the control, a 1.5mH compensation inductor is connected to each three-phase stator winding of motor in the experiment.

Fig. 14. Installation position of fluxgate detector.

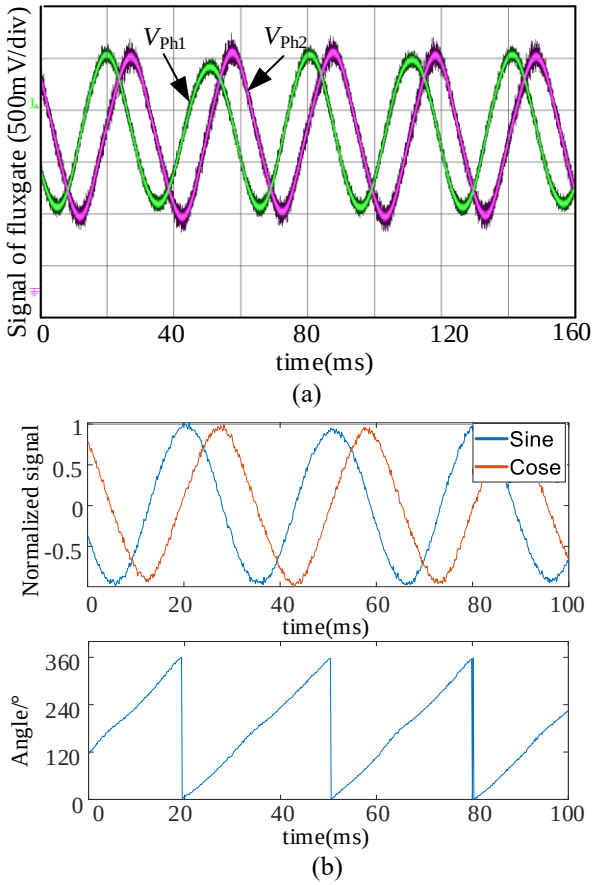

Fig. 15. (a) Output waveform of fluxgate hardware circuit, and (b) angle solving.

When motor is in driving mode and its speed is 500 rpm, waveforms of fluxgate hardware circuit output

signals V_{Ph1} and V_{Ph2} are as shown in Fig. 15 (a). In a mechanical angular cycle, the amplitudes of V_{Ph1} and V_{Ph2} are deviated because the eight rotor permanent magnets of motor have a certain positional deviation during installation, resulting in a difference in flux leakage distribution of four pairs of permanent magnets. Save oscilloscope data and perform signal processing in MATLAB. Then normalize the amplitude of signal and remove DC offset, and solve angle using atan2 function. The result is shown in Fig. 15 (b). Motor is in driving mode, and stator winding is open, and there is no influence of stator current. In this case, fluxgate sensor can accurately identify the rotor position of motor by detecting leakage flux of permanent magnet of motor, and the linearity of angle waveform is good. The motor rotor position detected by leakage flux detection method is an electrical angle. When speed is 500 rpm, the frequency of magnetic field change is four times that of motor rotation.

Using VF control to start Printed PMSM with no load, Phase A current i_A of motor in no-load start-up process and the operation state are shown in Figs. 16 (b) and (c), respectively. No-load start-up current of motor is about 2.8A. The current amplitude after operation state is about 1A, and the current waveform is distorted. Due to the fact that motor production is rough, the air gap of motor is too large and uneven, and harmonics are large, which causes the current to be distorted.

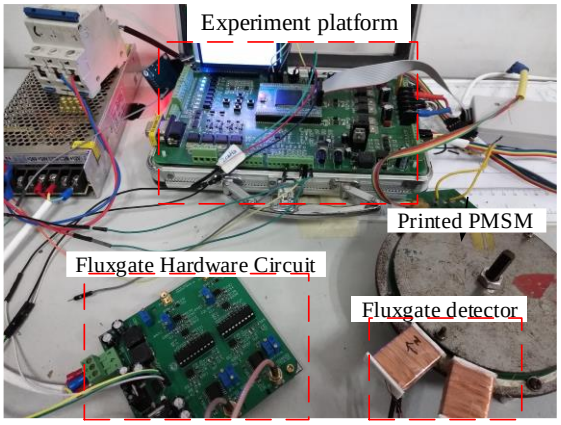

(a)

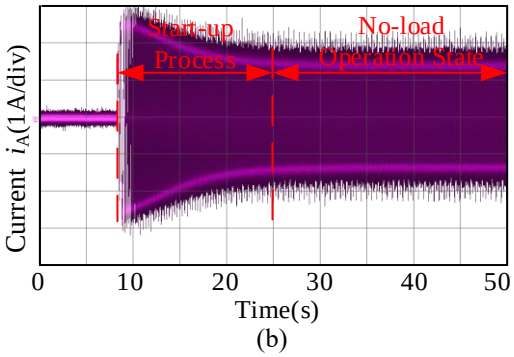

(b)

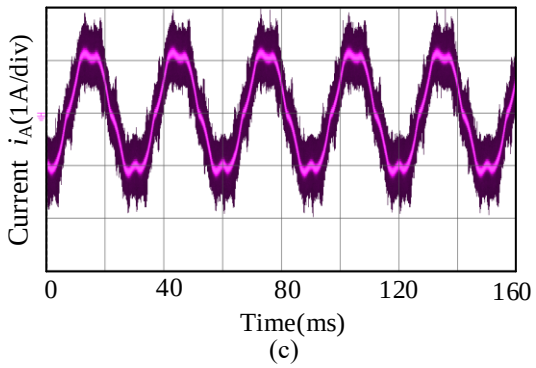

(c)

Fig. 16. (a) Experiment platform, (b) Phase A motor current during VF no-load start-up, and (c) Phase A current in no-load motor.

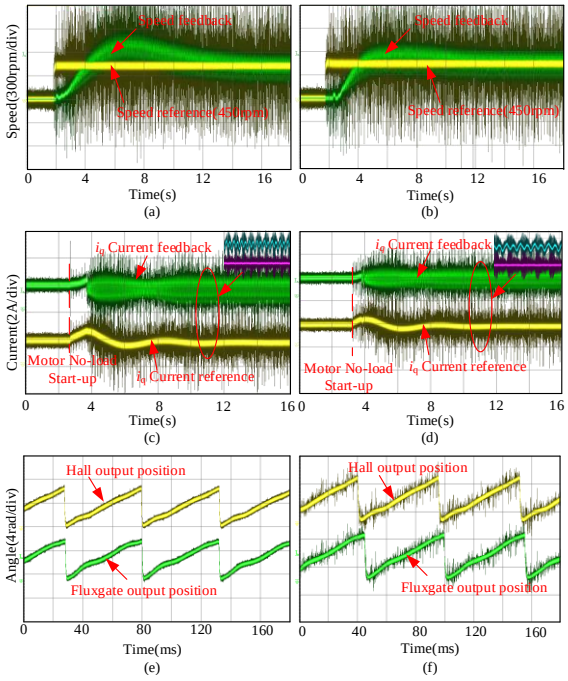

Fig. 17. (a) Motor speed based on Hall sensor, (b) motor speed based on fluxgate sensor, (c) i_q reference and feedback based on Hall control, (d) i_q reference and feedback based on fluxgate control, (e) output position based on Hall control, and (f) output position based on Hall control.

According to the above analysis, the Printed motor laboratory designed causes distortion of current due to manufacturing problems, and motor vibration and torque ripple is large during operation. During the start-up process of motor, the presence of starting current will inevitably affect leakage flux distribution of rotor permanent magnet, thus increasing the difficulty of leakage flux detection. This section still takes id=0 motor

control experiment as an example. Motor is given a speed of 450 rpm and runs at no-load. The motor control experiment waveform based on Hall sensor and fluxgate sensor is shown in Fig. 17. It can be seen from Figs. 17 (a) and (b) that in two sets of experiments, when motor is in steady operation, speed feedback can track the given speed well. Comparing Figs. 17 (e) and (f), in the two sets of experiments, the linearity difference of output angle waveform of fluxgate sensor is smaller than that of Hall sensor. The reason is that manmade sensor is rough, but it has the equivalent performance of a mature Hall sensor. If fluxgate sensor is precision-produced, its performance will exceed Hall sensor.

VI. CONCLUSION

In this paper, the structural characteristics of Printed PMSM are briefly introduced. At the same time, the basic control method and relevant parameters of PMSM used in the experiment are given. In addition, in order to verify the feasibility of detecting rotor position of Printed PMSM based on leakage flux detection, this paper simulates leakage flux distribution around the air gap of Printed PMSM with different radius. The simulation results show that the larger the radius, the smaller leakage magnetic flux and the more complex harmonics is. But fundamental frequency content is always high, that is, the sinusoidally degree is good, which means it is suitable for rotor position detection. In order to detect the weak rotor leakage flux, this paper introduces fluxgate technology, compares the advantages and disadvantages of existing position sensors, and analyzes the influence of motor system error on rotor position detection. Finally, the fluxgate position sensor is designed and fabricated, and it is used to drive Printed PMSM. Feasibility of the method described in this paper is verified by finishing the experiment using this sensor to drive Printed PMSM. The rotor position detection method proposed in this paper is based on the example of Printed PMSM, but it is also applicable to rotor position detection of most traditional PMSM, which means it has good reference value for integrated design of PMSM.

ACKNOWLEDGMENT

This work has been supported by the Postgraduate Research & Practice Innovation Program of Jiangsu Province (KYCX19_2191), Postgraduate Research & Practice Innovation Program of China University of Mining and Technology (ZGKD19_2191) and Natural Science Foundation of Jiangsu Province Grant No. BK20190634.

REFERENCES

[1] Q. N. Ni, M. Yang, X. Dong, X. S. Liu, and D. G. Xu, “State estimation error suppression for PMSM speed observer based on Hall position sensor,” *Transactions of China Electrotechnical Society*, vol. 32, no. 17, pp. 189-198, Sep. 2017.

[2] J. Zhu, L. L. Han, and X. D. Wang, “Status and trends of sensorless control algorithm for PMSM,” *Micromotors*, vol. 46, no. 9, pp. 11-16, Sep. 2013.

[3] J. L. Liu, F. Xiao, Y. Shen, Z. Q. Mai, and C. R. Li, “Position-sensorless control technology of permanent-magnet synchronous motor-A review,” *Transactions of China Electrotechnical Society*, vol. 32, no. 16, pp. 76-88, Aug. 2017.

[4] S. Neethu, P. N. Saurabh, S. Sumeet, P. Saumitra, K. W. Ashok, and B. G. Fernandes, “High-speed coreless axial-flux permanent-magnet motor with printed circuit board winding,” *IEEE Transactions on Industry Applications*, vol. 55, no. 2, pp. 1954-1962, Mar-Apr. 2019.

[5] A. Athavale, K. Sasaki, B. S. Gagas, T. Kato, and R. D. Lorenz, “Variable flux permanent magnet synchronous machine (VF-PMSM) design methodologies to meet electric vehicle traction requirements with reduced losses,” *IEEE Transactions on Industry Applications*, vol. 53, no. 5, Sep-Oct. 2017.

[6] *Handbook of Magnetic Measurements*, ver. 1, Mechanical Industry Press, Beijing, BJ, 2014.

[7] A. H. Guo and J. M. Fu, “Measurement technology of magnetic flux and its application,” *Journal of Transducer Technology*, vol. 19, no. 4, pp. 1-4, Mar. 2000.

[8] D. M. Miles, B. B. Narod, D. K. Milling, I. R. Mann, and D. Barona, “A hybrid fluxgate and search coil magnetometer concept using a racetrack core,” *Geoscientific Instrumentation & Methods and Data Systems*, vol. 7, no. 4, pp. 265-276, Oct. 2018.

[9] N. Murata, H. Karo, I. Sasada, and T. Shimizu, “Fundamental mode orthogonal fluxgate magnetometer applicable for measurements of DC and low-frequency magnetic fields,” *IEEE Sensors Journal*, vol. 18, no. 7, pp. 2705-2712, Apr. 2018.

[10] Z. Q. Chu, H. D. Shi, M. J. PourhosseiniAsl, J. E. Wu, W. L. Shi, X. Y. Gao, X. T. Yuan, and S. X. Dong, “A magnetoelectric flux gate: new approach for weak DC magnetic field detection,” *Scientific Reports*, vol. 7, no. 1, pp. 8592, Aug. 2017.

[11] M. F. Snoeij, V. Schaffer, S. Udayashankar, and M. V. Ivanov, “Integrated fluxgate magnetometer for use in isolated current sensing,|” *IEEE Journal of Solid-State Circuits*, vol. 51, no. 7, pp. 1684-1694, May. 2016.

[12] A. F. Morabito, L. D. Donato, and T. Isernia, “Orbital angular momentum antennas: Understanding actual possibilities through the aperture antennas theory,” *IEEE Antennas and Propagation Magazine*, vol. 60, no. 2, pp. 59-67, Feb. 2018.

Xianming Deng was born in Sichuan, China. He received his B.S., M.S., and Ph.D. in Electrical Engineering from China University of Mining and Technology, Jiangsu, China. He is currently a Professor in the School of Electrical and Power Engineering of China University of Mining and Technology. His current research fields include power electronics and motor drive.

Junhong Zhou was born in Hunan, China. He received his B.S. in Information Engineering from China University of Mining and Technology, Jiangsu, China. He is currently receiving a Master education at China University of Mining and Technology. His current research interests include power electronics and motor drive.

Lei Hao was born in Shandong, China. He received his B.S. in Electrical Engineering from Shandong University of Technology, Shandong, China. He is currently receiving a Master education at China University of Mining and Technology. His current research interests include power electronics and motor drive.

Zhihua Fan was born in Shanghai, China. He received the B.S. degree in Electrical Engineering from Nanjing Institute of Technology, Jiangsu, China. He is currently receiving a Master education at China University of Mining and Technology. His current research interests include power electronics and motor drive.

Na Liu was born in Anhui, China. She received her B.S. and M.S. in Electrical Engineering from China University of Mining and Technology, Jiangsu, China. She is currently a Hardware Engineer at Institute of Electronics, Chinese Academy of Science. Her current research interests include power electronics and motor drive.